Oceanologia

Official Journal of the Polish Academy of Sciences

This journal is supported by the Ministry of Science and Higher Education, Warsaw, Poland

Indexed in: ISI Journal Master List, Science Citation Index Expanded, Scopus, Current Contents, Zoological Record, Thomson Scientific SSCI, Aquatic Sciences and Fisheries Abstracts, DOAJ

IMPACT FACTOR ANNOUNCED FOR 2021 IN THE 'JOURNAL CITATION REPORTS' IS 2.526; 5-year IF is 2.778. CITESCORE ANNOUNCED FOR 2021 IS 4.7

Publisher
Elsevier B.V.
Radarweg 29
1043 NX Amsterdam
The Netherlands

Senior Publisher
Tobias Wesselius
+31 6 5370 3539

ISSN 0078-3234

Oceanologia 64 (2022) 405—416

Available online at www.sciencedirect.com

ScienceDirect

journal homepage: www.journals.elsevier.com/oceanologia

ORIGINAL RESEARCH ARTICLE

Detecting food limitation of bacterial growth during dilution experiments

Krzysztof Rychert*

Institute of Biology and Earth Sciences, Pomeranian University, Słupsk, Poland

Received 25 December 2020; accepted 7 February 2022
Available online 22 February 2022

KEYWORDS
Bacterial growth;
Bacterivory;
Organic matter;
Oxygen consumption;
Coastal zone;
Baltic Sea

Abstract The dilution method is typically applied to estimate the growth and mortality rates of phytoplankton, but it is also used to study bacterioplankton. The method comprises creating a gradient of dilutions to reduce the encounter rates between bacterivores and bacteria, thus allowing for estimations of bacterial growth and grazing pressure exerted on the bacteria. However, the manipulations involved in the method can lead to biased results. In this study, 12 dilution experiments performed in the coastal zone of the Baltic Sea were accompanied by additional measurements capable of detecting possible artefacts. Only six measurements performed during spring and summer (March—August) produced results that were free of artefacts and were statistically significant. During fall and winter (October—February) measurements were unsuccessful because of food limitation of bacterial growth during experimental incubation. Twice (in September and October) bacterial growth and grazing mortality rates were underestimated because grazing pressure was not successfully removed. The study demonstrated that 24-hour and five-day oxygen consumption measurements incorporated into dilution experiments permitted estimating the fraction of biodegradable organic matter used during incubation, and, thus, detecting the food limitation of bacterial growth.

* Corresponding author at: Institute of Biology and Earth Sciences, Pomeranian University, Słupsk, ul. Arciszewskiego 22b, 76-200 Słupsk, Poland.
E-mail address: krychert@wp.pl
Peer review under the responsibility of the Institute of Oceanology of the Polish Academy of Sciences.

Production and hosting by Elsevier

https://doi.org/10.1016/j.oceano.2022.02.001

1. Introduction

Because of their high metabolic versatility and adaptability, bacteria play an important role in the energy flow through aquatic ecosystems, oxygen consumption, and nutrient regeneration (Cole, 1999; del Giorgio and Cole, 2000; Stocker, 2012; Våge et al., 2018; Zoccarato et al., 2016). Thus, studies on bacterial growth and mortality are essential in ecological research as they provide necessary data for the construction of budgets and models describing ecosystem functioning (Miki and Yamamura, 2005; Tett and Wilson 2000; Våge et al., 2018; Witek et al., 1997; Zoccarato et al., 2016). Consequently, methods for estimating bacterial growth and mortality must be improved continuously (Bochdansky and Clouse, 2015; Pree et al., 2016). This paper contributes to the development of the dilution method applied to measuring bacterial dynamics in pelagic waters.

Dilution experiments (Landry and Hassett, 1982), which permit relaxing grazing pressure, were originally developed to measure the production and grazing mortality of phytoplankton (Landry and Hassett, 1982; Shinada et al., 2000). Later, the dilution technique was adapted to estimate the growth and mortality rates of bacteria (Anderson and Rivkin, 2001; Jochem et al., 2004; Murrell and Hollibaugh, 1998; Pree et al., 2016; Sakka et al., 2000; Sommer et al., 2002; Zoccarato et al., 2016). Further modifications also made it possible to measure bacterial mortality caused by viral lysis (Evans et al., 2003; Taira et al., 2009), and even the growth of protozoa (Rychert, 2016; and references therein). The dilution technique comprises whole-community manipulation by creating a gradient of dilutions using unfiltered water and particle-free filtrate (0.2 μm). In dilution gradients from undiluted to the most diluted the encounter rates between predators and prey are gradually reduced (Landry and Hassett, 1982). Consequently, grazing pressure exerted on prey is gradually reduced too, which permits estimating it. Moreover, the specific growth rate of the prey can also be measured. The dilution method is superior to size fractionation, another method based on whole community manipulation (Kuuppo-Leinikki, 1990; Landry and Hassett, 1982; Pree et al., 2016). Unfortunately, numerous studies report that a fraction of dilution experiments are unsuccessful when the method is applied both to phytoplankton (Latasa, 2014) and bacterioplankton (e.g., Jochem et al., 2004; Murrell and Hollibaugh, 1998). Typically, experiments are unsuccessful because method assumptions are violated.

The key assumption of the dilution method is that the availability of inorganic nutrients necessary for algal growth and inorganic nutrients and the dissolved organic matter necessary for bacterial growth remain unchanged as they are not reduced by 0.2-μm filtration (Landry et al., 1995). However, 0.2-μm filtration can enrich the pool of available organic matter by protistan cell breakage on the filters (Ferguson et al., 1984) that releases cytoplasm containing labile organic matter fueling bacterial growth. Experimental incubation of water typically lasts 24 hours (Anderson and Rivkin, 2001; Pree et al., 2016; Zoccarato et al., 2016), to include diel rhythms of algal or (possibly) bacterial growth, but such a long incubation could result in the depletion of resources. In contrast, filtration can result in the release of metabolites from toxic algal blooms that inhibit bacterial growth (Pree et al., 2016).

When algal growth and grazing are studied, resource limitation could be avoided by the addition of nutrients (Landry and Hassett, 1982; Zoccarato et al., 2016). Similar preventive measure cannot be taken when studying bacterial growth and grazing, because the composition of dissolved organic matter in particular water sample is unique and actually cannot be reproduced during environmental studies. Obviously, the addition of non-native organic matter changes the growth rate and composition of a bacterial community (Pinhassi et al., 1999). Thus, no additional organic matter is applied in dilution experiments measuring bacterial dynamics (e.g., Anderson and Rivkin, 2001; Murrell and Hollibaugh, 1998).

In this study, the dilution experiments were accompanied by additional measurements estimating the impact of filtration on organic matter content and also the share of organic matter available to bacteria that is used during experimental incubations. The latter were introduced to detect possible food limitation during experimental incubation. Additional measurements were based on respiration, i.e., oxygen consumption by organisms present in the water. Oxygen consumption measured during experimental incubations that lasted for 24 hours were compared to oxygen consumption observed over five days — a widely accepted proxy for the bioavailable organic matter content (=biochemical oxygen demand, BOD). However, in this study incubations were performed at *in situ* temperature and not at 20°C like standard BOD measurements. Oxygen consumption measurements were chosen because total organic carbon (TOC) estimates or even resolving the general composition of organic matter, that is, the content of proteins, carbohydrates, etc., did not provide information regarding the availability of organic matter to the bacteria. Bacteria are the main oxygen consumers in aquatic environments. They are responsible for about 40% of total community respiration in open oceans (del Giorgio and Duarte, 2002; Robinson and Williams, 2005; Williams, 2000). In coastal zones, as in the present study, bacteria are additionally fueled by allochthonous organic matter of terrestrial origin (Ameryk et al., 2005; Andersson et al., 2018; Cole, 1999), and, consequently, bacterial respiration contributes 50% or more to total community respiration (del Giorgio and Duarte, 2002; Griffith et al., 1990; Preen and Kirchman, 2004). In conclusion, oxygen consumption primarily estimates the metabolism of bacteria, which are the organisms in question.

The hypothesis posted in this study was that the failure of dilution experiments, i.e., no detection of bacterial growth and grazing rates, was caused primarily by food limitation occurring during experimental incubation. The second possible cause of experimental failure could be the violation of the second key assumption of the dilution method that grazing pressure is gradually relaxed in subsequent dilutions. This assumption has been discussed in detail previously (Dolan et al., 2000; Gallegos, 1989; Gifford, 1988; Landry, 1993; Landry et al., 1995). In this study, the relaxation of grazing pressure was also evaluated. To do this, the abundance of nanoflagellates, the main bacterivores

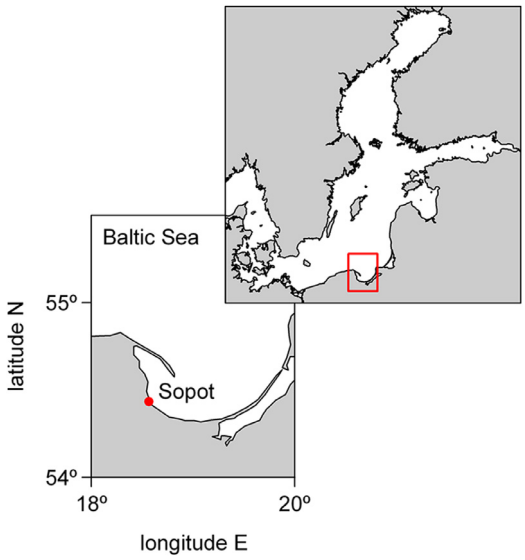

Figure 1 Location of the sampling site in Sopot (Gulf of Gdańsk, Baltic Sea).

(Sherr and Sherr, 2002) and its dynamics during incubation was assessed in crucial dilutions. Additionally, changes in bacterial communities observed after grazing pressure was relaxed permitted evaluating the impact of grazing on these communities.

It was mentioned above that Pree et al. (2016) reported dilution experiments that were unsuccessful due to inhibitory metabolites released by toxic phytoplankters. In this study, samples were studied under an inverted microscope in order to detect toxic blooms.

2. Material and methods

2.1. Sampling site

The experiments were conducted monthly between April 2003 and March 2004 in the coastal zone of the Gulf of Gdańsk (Baltic Sea). The sampling site was located at the end of a 450 m wooden pier in Sopot (Baltic Sea, 54°27′N 18°34′E, Figure 1). The water temperature ranged from 1°C in March to 21°C in August. Salinity (PSU) ranged from 6.4 to 7.4‰ at a mean of 7.1‰, which was slightly lower than the mean value for the southern Baltic of 7.5‰ (Matthäus et al., 2008). The water at the sampling site was well-oxygenated year round with the lowest value of 8.2 mg O_2 l^{-1} observed in August and the highest value of 15.84 mg O_2 l^{-1} observed in March. Secchi depth ranged from 4.5 to 6.5 m in winter to 2.0—2.5 m during the spring phytoplankton bloom and during the summer. The average chlorophyll concentration was 3.56 mg m^{-3} (range: 1.0—15.9 mg m^{-3}). Microscopic observations of concentrated samples did not detect blooms of toxic organisms.

2.2. Dilution experiments

The dilution experiments were conducted according to Landry and Hassett (1982) and Landry (1993). Before each experiment all the equipment (bottles, tubings, etc.) was acid-washed and thoroughly rinsed with deionized water. For each experiment, subsurface water (60 l) was collected from the sampling site and taken to the laboratory. Part of the water was filtered through glass fiber pre-filter and 0.2-μm cellulose filter (filters and holder of diameter 142 mm, Sartorius) to produce the 0.2-μm-filtrate, which was subsequently used to prepare the dilutions in which the fractions of unfiltered seawater were 25%, 50%, 75%, and 100% (undiluted water). All dilutions were prepared in triplicate in one-liter bottles (12 in total). Since the oxygen consumption was to be measured, the bottles were filled completely (without air space) using gas-tight tubing. No substrates or nutrients were added. Each bottle was mixed gently by rotating it 100 times, and then the water from each one-liter bottle was siphoned using tubing into a half-liter bottle. The remaining water from each one-liter bottle was fixed for bacterial and flagellate counts and was used for initial oxygen measurements (three standard Winkler flasks for each measurement). The water in the half-liter bottles (12 in total) was then incubated for 24 hours in the dark at *in situ* temperature and with gentle mixing (3 rpm). Dark incubation was necessary to exclude photosynthesis that liberates oxygen and interferes with respiration measurements. After incubation, the water from each half-liter bottle was fixed for bacterial and flagellate counts and oxygen measurements as described above. Samples for bacteria and flagellate counts, taken before and after incubation, permitted evaluation of dynamics of their biomass during incubation. The difference between the initial and final concentrations of oxygen in a particular treatment permitted calculation of 24-hour oxygen consumption.

2.3. Estimation of the biodegradable organic matter

In order to detect possible food limitation of bacterial growth during the experiments, 24-hour oxygen consumption in each dilution (described above) was compared to oxygen consumption measured over five days. For the latter measurement, the water was incubated in the same conditions (*in situ* temperature, darkness, gentle mixing — 3 rpm), and the estimate was a non-standard biochemical oxygen demand measurement (BOD5-*in situ*), which, according to Witek et al. (2001), is an estimate of the temperature-dependent, actual pool of biodegradable organic matter. At first, unfiltered water and the 1:1 mixture of unfiltered water and the 0.2-μm-filtrate were siphoned to one-liter bottles (two bottles for unfiltered water and two bottles for the mixture). Bottles were gently mixed by rotating them 100 times. Next, water from each one-liter bottle was siphoned into a half-liter bottle and the remaining water was used for initial oxygen measurements (three standard Winkler flasks for each bottle). Next, half-liter bottles were incubated over five days to determine BOD5-*in situ* for unfiltered water (two bottles) and BOD5-*in situ* for the 1:1 mixture of unfiltered water and the 0.2-μm-filtrate (another two bottles). After incubation, final oxygen concentrations were measured (three Winkler flasks for each bottle). BOD5-*in situ* values were calculated as the difference between the initial and final concentrations of oxy-

gen. Since BOD5-*in situ* measurements were performed with unfiltered water and the dilution containing 50% unfiltered seawater, it was also possible to interpolate the BOD5-*in situ* value for the dilution containing 75% unfiltered seawater and to extrapolate the same for the dilution containing 25% unfiltered seawater.

As was mentioned above, the 24-hour oxygen consumption in each dilution was compared to oxygen consumption measured over five days (in the same dilution). The coefficient of (I) 24-hour oxygen consumption by (II) BOD5-*in situ* for the appropriate dilution was used as a measure of the fraction of easily biodegradable (labile) matter used up during 24 hours of incubation.

Directly comparing the BOD5-*in situ* measured for unfiltered water and the 1:1 mixture of unfiltered water and the 0.2-μm-filtrate permitted evaluating the impact of filtration on the fraction of easily biodegradable organic matter.

2.4. Bacterial and protozoan counts

The bacterial abundance, biomass, and morphological composition (shape of the bacterial cells) were determined during observations under an epifluorescence microscope of bacteria that had been fixed with formalin (1%) and mounted on 0.2-μm polycarbonate, membrane, irgalan-black-dyed filters (Osmonics). Next, bacteria were stained with acridine orange and observed under an epifluorescence microscope (Hobbie et al., 1977). The bacteria were observed in 30 fields of view. To estimate bacterial abundance, a minimum of 400 cells, and typically more than 1,000, were counted per sample. Each time 50 bacterial cells selected at random were measured to estimate volume (V, μm^3) and then carbon content (CC, fg C). The following allometric formula was used (Posch et al., 2001):

$$CC = 120 \times V^{0.72} \quad (1)$$

The mean carbon content of bacterial cells and bacterial abundance permitted calculating the bacterial biomass (Posch et al., 2001).

Nanoflagellates were fixed with glutaraldehyde (0.5%) and mounted on 0.8-μm polycarbonate, membrane, irgalan-black-dyed filters (Osmonics) (Caron, 1983). Next, nanoflagellates were stained with primulin and analyzed under an epifluorescence microscope (Caron, 1983). Under excitation with UV light primulin-stained nanoflagellates were observed as blue objects. Switching to blue light-excitation permitted detection of autofluorescence of chlorophyll inside cells, which emitted red light (Caron, 1983). Chlorophyll autofluorescence permitted separation of auto- (ANF) and heterotrophic nanoflagellates (HNF). At least 20 fields of view, or minimum of 100 flagellates of size 1–8 μm, were counted; 50 cells chosen at random – ANF and HNF separately – were measured to calculate their volume. The volume (V, μm^3) was recalculated onto carbon content (CC, fg C) according to Børsheim and Bratbak (1987):

$$CC = 220 \times V \quad (2)$$

2.5. Oxygen measurements

Oxygen concentration was determined with the standard Winkler method using a Metrohm Titrino 702SM titrator that permitted potentiometric end-point detection. Determinations were performed each time on three Winkler flasks; thus, a single measurement was the mean value of three independent titrations.

2.6. Analysis of dilution experiments

To determine bacterial growth (μ) and mortality rates caused by grazing (g), the apparent bacterial growth rate (k, d^{-1}) was calculated for each dilution (Landry and Hassett, 1982):

$$k = \ln(FBB/IBB) \quad (3)$$

where IBB and FBB were initial and final bacterial biomasses. The dynamics of bacterial biomass were analyzed according to Landry and Hassett (1982), and apparent growth rates were drawn against the fraction of unfiltered seawater to estimate the specific growth rate (μ, d^{-1}, intercept) and the grazing rate (g, d^{-1}, slope of the curve). The grazing rate was written as a positive number (modulus) even though the slope was negative. Of course, the dependence had to be statistically significant. Four times measurements demonstrated non-linear dynamics, or the so-called saturated feeding effect (Evans and Paranjape, 1992; Gallegos, 1989), in which the relaxation of grazing pressure was only observed in higher dilutions. In these cases, the grazing curve was calculated for higher dilutions only. This procedure was applied if it produced higher statistical significance than did linear regression. In this method, the grazing rates were computed using the formula proposed by Elser and Frees (1995) and Shinada et al. (2000):

$$g = s \times (TH/100\%) \quad (4)$$

where s was the slope of the grazing curve and TH was the threshold (breaking point) expressed as the fraction of unfiltered water (0% < TH < 100%). In experiments in which the saturated feeding effect was observed, simple linear plots were also statistically significant.

2.7. Statistical analyses

Calculation of R^2 coefficients and statistical significances of regression lines were carried out using Statistica software (Statsoft).

3. Results and discussion

3.1. Bacterial standing stocks

The bacterial community was studied between April 2003 and March 2004. To obtain well-documented results, three environmental samples were analyzed and averaged each time. Bacterial abundance ranged from 4.4×10^9 cells l^{-1} (standard deviation, SD = 0.9×10^9 cells l^{-1}) to 17.1×10^9 cells l^{-1} (SD = 2.4×10^9 cells l^{-1}) and the mean value was 8.2×10^9 cells l^{-1}. The mean annual bacterial biomass was 82.8 μg C l^{-1} (Figure 2). Two bacterial biomass peaks were observed: the first was in late spring-early summer and the second was in summer (Figure 2) corresponding to seasonal changes in primary production in the Gulf of Gdańsk

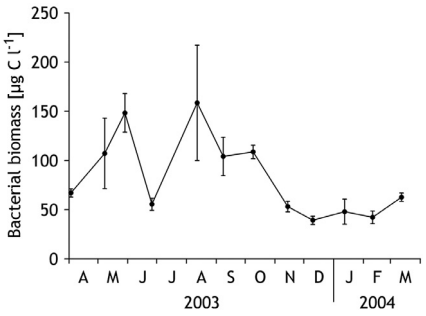

Figure 2 Bacterial biomass at the sampling site in the coastal zone of the Gulf of Gdańsk (Baltic Sea) between April 2003 and March 2004. At each sampling date, three replicates of environmental samples were analyzed and whiskers represent standard deviation. The experiment was planned to be conducted in July 2003 was carried out a few days ahead of schedule (see graph), but for the sake of simplicity, it was described as having been done in July.

Table 1 Bacterial growth and grazing rates measured with the dilution method in the coastal zone of the Gulf of Gdańsk (Baltic Sea).

Experiment	Growth rate [μ, d^{-1}]	Grazing rate [g, d^{-1}]
April 2003	0.52	0.58
May 2003	0.66	0.63
June 2003	1.34	1.37
July 2003	0.99	1.03
August 2003	0.83	0.78
September 2003	0.65	0.65
October 2003	insignificant	insignificant
November 2003	insignificant	insignificant
December 2003	insignificant	insignificant
January 2004	insignificant	insignificant
February 2004	insignificant	insignificant
March 2004	0.96	0.76

(Renk and Ochocki, 1999). Seasonal changes in bacterial abundance and the ranges of values observed corresponded well with measurements that were done at the same site in 1993 (Witek et al., 1997) and in the coastal zone of other regions of the Baltic Sea (Jost and Ballin, 1984; Kuuppo-Leinikki, 1990). During the spring phytoplankton bloom (May and June), mean bacterial cell volume was larger (0.062 μm^3) than during the rest of the year (0.028—0.046 μm^3), which was a typical observation (e.g., Kuparinen, 1988) confirming that algal exudates produced during the spring phytoplankton bloom efficiently fueled bacterial growth (del Giorgio and Cole, 2000). The mean cell volume of bacteria corresponded well with values noted in the Baltic Proper (0.033—0.053 μm^3; Kuuppo et al., 2003).

3.2. Bacterial growth and mortality

Of the 12 dilution experiments, statistically significant bacterial growth was observed in 7 experiments (between April and September and in March, Figure 3). In the experiments conducted in October and November, the grazing curves for bacterial biomass were flat and statistically insignificant (Figure 3). In the experiments performed in December, January, and February, the preliminary studies on dynamics of bacterial biomass did not indicate any statistical significance and further analyzes were abandoned. The bacterial growth rates ranged from 0.52 to 1.34 d^{-1} and grazing rates ranged from 0.58 to 1.37 d^{-1} (Table 1). The highest values were observed in June and July. It was statistically documented that growth rates (μ) were tightly coupled with grazing rates (g): $\mu = 1.02 \times g$, $R^2 = 0.90$, $p = 0.001$).

Bacterial growth rates were comparable to those reported by Blackburn et al. (1998) from the northern Baltic Sea (about 0.1 d^{-1} in winter to 1.2 d^{-1} in summer). Growth rates were also comparable to those reported for other waters, e.g., Porsangerfjord in northern Norway (0.58 d^{-1} and 0.75 d^{-1}; Pree et al., 2016), the San Francisco Bay (up to ~1 d^{-1}; Murrell and Hollibaugh, 1998), the Gulf of Mexico (0.2—0.9 d^{-1}; Jochem et al., 2004), Arctic and Antarctic waters (up to ~1 d^{-1}; Anderson and Rivkin, 2001), and the Gulf of Aqaba and the Red Sea (0.61—1.30 d^{-1}; Sommer et al., 2002). It should be emphasized that, regardless of latitude, similar ranges of bacterial growth rates are reported (reviewed by Anderson and Rivkin, 2001). Bacterial growth rates seem to be low when compared to those in cultures; however, it should emphasized that the availability of resources in the environment is much lower and bacterial growth and metabolism per cell is underestimated since their rates are scaled to all bacteria, both active (growing) and inactive (non-growing) (Ducklow, 2000; reviewed by Jochem et al., 2004).

As was mentioned above, bacterial growth rates and their grazing mortality were tightly coupled. The equilibrium between the production and elimination of bacteria is expected in steady-state periods (Ducklow, 2000). Using dilution experiments, balanced bacterial growth and grazing mortality were also reported by Anderson and Rivkin (2001), Jochem et al. (2004), Murrell and Hollibaugh (1998), Sommer et al. (2002), and Zoccarato et al. (2016). This balance was observed directly or could be demonstrated based on averaged data.

The main bacterivores in aquatic environments are protozoa (= heterotrophic protists; Sherr and Sherr, 2002). The analysis of protozoan communities at the sampling site (described in Rychert et al., 2013) revealed that the main bacterivores were heterotrophic nanoflagellates with a mean annual biomass of 9.7 $\mu g\ C\ l^{-1}$. Bacterivorous ciliates (only bacterivorous) were of minor importance with a mean annual biomass of 3.6 $\mu g\ C\ l^{-1}$. Both heterotrophic nanoflagellates and bacterivorous ciliates peaked during spring. During the rest of the year (summer, fall, and winter), bacteria could be also ingested by abundant mixotrophic nanoflagellates (described in Rychert, 2006).

In this study, the maximum bacterial growth rate observed in June (1.34 d^{-1}, Table 1) corresponded with spring phytoplankton bloom, which was detected during sampling conducted in May and June. As was mentioned above elevated biomass of bacterivorous protists was also observed at that time. As a result of strong grazing pressure, bacterial biomass decreased between samplings in May and June despite a high growth rate (Figure 2). Next year, during sam-

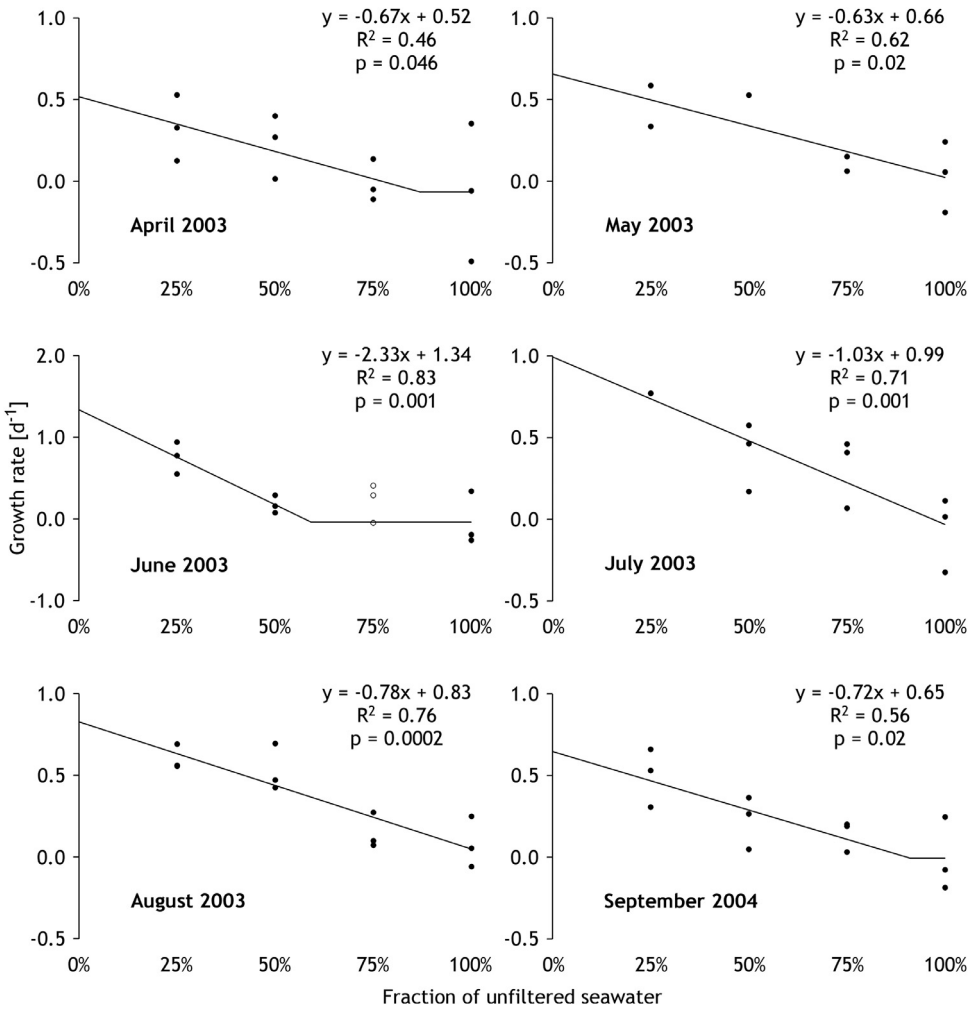

Figure 3 Changes in bacterial biomass observed during dilution experiments. Apparent growth rates observed in dilutions permitted extrapolating the specific growth rate (μ, intercept). The slope, essentially its modulus, corresponded to the grazing rate (g). In April, June, September, and March the increase of bacterial biomass demonstrated non-linear dynamics; therefore, grazing curves in these experiments were calculated for higher dilutions only (see Material and methods). In June and March data from dilution 75% (marked with open circles) were not taken into account. Several treatments were lost; however, all dependencies were statistically significant ($p < 0.05$).

pling occasion in March, an unexpectedly high value of bacterial growth rate was observed (0.96 d^{-1}, Table 1). During that sampling occasion also the highest chlorophyll *a* concentration was observed (15.9 mg m^{-3}), which indicated early phytoplankton bloom. Such phenomenon was previously observed at the sampling site by Witek et al. (1997).

3.3. Food resources during dilution experiments

The main assumption of dilution experiments is that the growth of the organisms studied remains unaltered. Bacterial growth depends primarily on the pool of available organic matter, which can be changed by filtration, and, further, decreased by incubation conditions that restrict its supply. Filtration can enrich the pool of available organic matter by protistan cell breakage on filters (Ferguson et al., 1984; Nagata and Kirchman, 1990; Pree et al., 2016). Conversely, the pool of organic matter can also decrease from filtration that removes detrital particles (Güde, 1986) that are degraded by bacteria (Chróst, 1991; Miki and Yamamura, 2005).

The impact of filtration on the pool of available organic matter was estimated directly by comparing BOD5-*in situ* in unfiltered water and in a 1:1 mixture of unfiltered water and 0.2-μm-filtrate. This mixture was used to provide the appropriate inoculum of bacteria for BOD5-*in situ* incubation (it was absent in the 0.2-μm-filtrate). The comparison demonstrated (Figure 4) that the mixture contained an average of 87% of the biodegradable organic matter present in the unfiltered water. Since the mixtures contained equal volumes of whole water and 0.2-μm-filtrate, it was calculated that the filtrate typically contained 74% of the organic matter present in the whole water. Surprisingly, no differences between experiments were observed (the R^2 value and statistical significance were both high, Figure 4). In conclusion, filtration decreased the pool of organic matter by 26%, which indicated the moderate importance of detrital particles as a source of biodegradable organic matter.

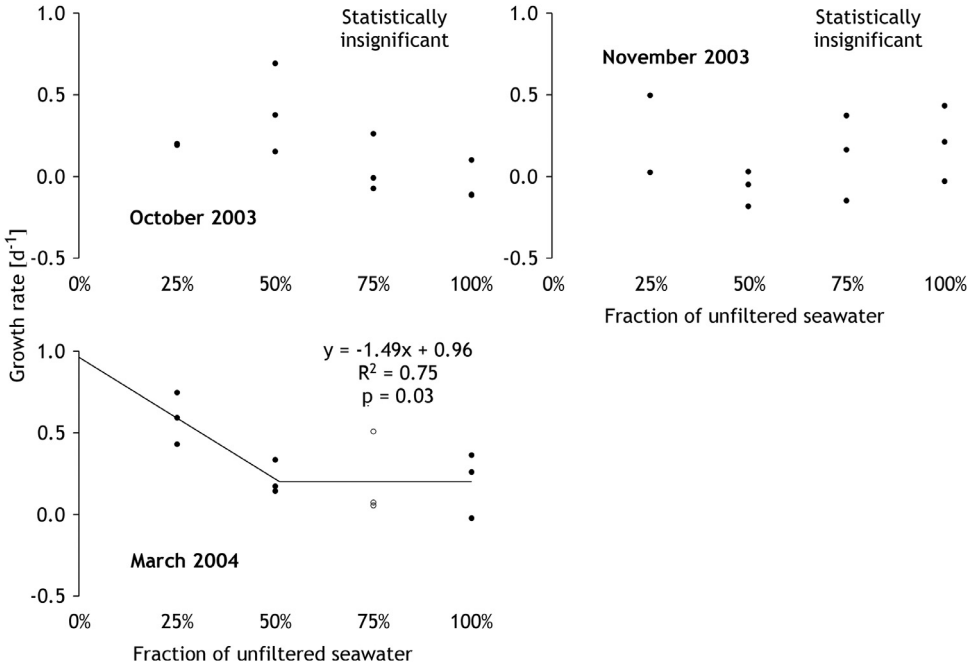

Figure 3 *Continued.*

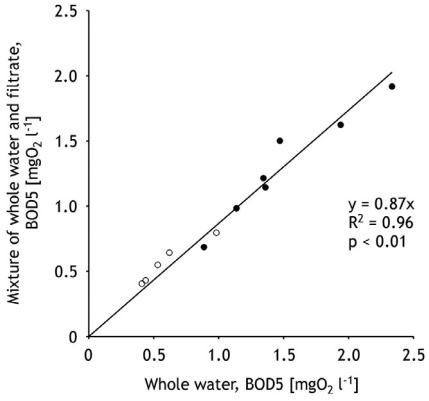

Figure 4 The impact of filtration on the pool of available organic matter estimated by comparing BOD5-*in situ* in unfiltered water and in a 1:1 mixture of unfiltered water and 0.2-μm-filtrate. The mixture contained an average of 87% of the biodegradable organic matter present in the unfiltered water. The relationship was highly statistically significant ($p < 0.01$). Filled circles represent measurements carried out between April and August and in March, i.e., during successful dilution experiments. Open circles represent measurements carried out between October and February, i.e., in experiments that were unsuccessful due to food limitation of bacterial growth during experimental incubation.

As mentioned above, the rate of resource supply decreased because of the incubation conditions. Producers (algae) and consumers (protozoa and metazoa) both excrete organic matter (Landry, 1993), and during the experiments they starved because of dark incubation (which affects producers) or dilution (which affects consumers). In addition, the water confinement cut off the supply of allochthonous organic matter that occurs in the coastal zone (as reviewed in the Introduction). This food limitation might have caused insignificant increases in bacterial biomass in the experiments done between October and February. To demonstrate the possible limitation of bacterial growth, the respiration values measured in all dilutions were compared with BOD5-*in situ* values (Table 2). Since BOD5-*in situ* measurements were performed with unfiltered water and the dilution containing 50% unfiltered seawater, it was possible to interpolate the BOD5 value for the dilution containing 75% unfiltered seawater and to extrapolate the same for the dilution containing 25% unfiltered seawater. The literature lacks recommendations on how to detect such food limitations, which is a particularly difficult problem, because organic matter consists of a few fractions that differ in terms of their value for sustaining bacterial growth (del Giorgio and Cole, 2000), and BOD5 measurements provide no information regarding this. However, the data presented in Table 2 indicated that in the experiments conducted between October and February, for which insignificant growth of bacterial biomass was observed, (24-hour respiration)/(BOD5-*in situ*) coefficients exceeded 60% in some dilutions. Thus, I propose this criterion for the detection of resource limitation of bacterial growth.

Generally, bacteria are limited by the labile carbon source, that is, organic matter. In some environments and periods, e.g., in offshore waters of the Baltic Sea Proper, bacterial growth could also be limited by the availability of inorganic phosphorus or nitrogen compounds (Kuuppo et al., 2003; Zweifel et al., 1993). Similarly, in the northern Baltic Sea during summer periods, bacterial growth is limited by the availability of inorganic phosphorus (Pinhassi and Hagström, 2000). However, in the southern Baltic Sea, and particularly in the Gulf of Gdańsk, bacterial growth does not depend on inorganic nutrients, i.e., bacteria utilizes organic phosphorus and nitrogen (Ameryk et al., 2005). Previous studies (Ameryk et al., 2005; Witek et al., 1997) in-

Table 2 Comparison between 24-hour and 5-day respirations (both incubated at *in situ* temperature) measured during dilution experiments in the coastal zone of the Gulf of Gdańsk (Baltic Sea). The highest values of the coefficient (24-hour respiration exceeded 60% of 5-day respiration, underlined) were observed in experiments done between October and February, for which insignificant increases of bacterial biomass were observed indicating that these experiments were resource limited.

Experiment	Dilutions			
	100%	75%	50%	25%
	24 hour respiration / 5 day respiration			
April 2003	50%	44%	47%	43%
May 2003	31%	30%	30%	26%
June 2003	52%	54%	56%	52%
July 2003	39%	35%	37%	41%
August 2003	38%	30%	33%	36%
September 2003	51%	47%	51%	58%
October 2003	39%	51%	68%	83%
November 2003	69%	64%	52%	55%
December 2003	45%	46%	49%	68%
January 2004	52%	56%	63%	37%
February 2004	50%	53%	70%	72%
March 2004	40%	42%	23%	36%

dicated that in the Gulf of Gdańsk, both autochthonous and allochthonous organic matter was important for fueling bacterial growth. In this study, only experiments performed during the growing season were successful, whereas bacterial growth was resource-limited in experiments conducted during the cold period of the year (October—February). It indicated that a considerable amount of labile organic matter, especially autochthonous phytoplankton exudate, is necessary to measure bacterial growth rates using the dilution method. A prerequisite of a sufficient amount of labile organic matter is also suggested by the value of BOD5-*in situ* measured in the whole water taken for experiments. Successful dilution experiments were carried out with water, for which BOD5-*in situ* value ranged from 0.89 to 2.33 mg O_2 l^{-1} (Figure 4, filled circles), whereas BOD5-*in situ* value of water collected for resource-limited experiments ranged from 0.41 to 0.98 mg O_2 l^{-1} (Figure 4, open circles).

3.4. Grazing pressure during dilution experiments

The second assumption of dilution experiments is that grazing pressure is gradually relaxed in subsequent dilutions. To examine this, I checked whether the 0.2-μm filtration was efficient, that is, the dilutions contained the expected abundance of bacteria and bacterivores. The main bacterivores were studied — heterotrophic nanoflagellates (HNF) and autotrophic nanoflagellates (ANF). The latter were taken into account because a significant part of them are mixotrophic, that is, they can simultaneously conduct photosynthesis and graze on bacteria. The presence of numerous mixotrophs among nanoflagellates at the study site was discussed by another study by Rychert (2006). The bacterial and flagellate biomasses observed in the dilutions before incubation were compared to the values expected from the biomasses recorded in the unfiltered water and the dilution factor. In the case of the bacteria, the values observed corresponded to 107%, on average, of the expected values (27 comparisons, $R^2 = 0.88$, $p < 0.01$). Values exceeding 100% suggest counting errors or indicated that, in the majority of experiments, some bacteria had passed through the 0.2-μm-filter. Such observation was reported by Li and Dickie (1985) and Haller et al. (1999). However, the discrepancy between the expected and observed values was small. In the case of the flagellates, that discrepancy was larger (HNF — the observed biomass corresponded to 115% of the expected biomass, 12 comparisons, $R^2 = 0.94$, $p < 0.01$; ANF — 122%, 12 comparisons, $R^2 = 0.91$, $p < 0.01$). Nanoflagellates were larger (1—8 μm) than bacteria (typically below 1 μm) thus, the discrepancy between the expected and observed biomasses should be identified as a systematic counting error, which is explained below. Nanoflagellate analysis was much more difficult and less precise than that of bacteria. Because of lower abundance, nanoflagellates had to be counted in larger samples (i.e. in larger volumes of water), which resulted in larger amounts of detritus present on filters inspected under an epifluorescence microscope. Most probably, some of the nanoflagellates were not detected in the unfiltered water, because they were covered by detrital particles. The problem was less likely in dilutions, in which a fraction of detrital particles were excluded by filtration. In conclusion, flagellate biomass in the unfiltered water and thus biomass that was expected in the dilutions could be underestimated, whereas flagellate biomass in dilutions was estimated precisely. Generally, the filtration procedure demonstrated satisfactory efficiency, and there was no experiment in which filtration was unsuccessful.

Generally during dilution experiments, it is expected that the growth of predators is gradually restricted in subsequent dilutions. Dolan and McKeon (2005) and Agis et al. (2007) suggest that the growth of predators indicates that the relaxation of grazing pressure is unsuccessful. However, Landry and Calbet (2005) argue that dilution restricts both the grazing activity and mortality of bacterivores, as their predators are diluted as well; there-

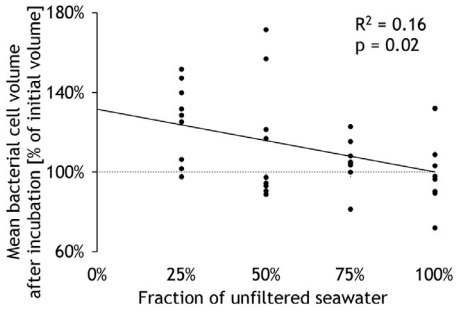

Figure 5 The gradual relaxation of grazing pressure along the dilution gradient (i.e., 100%, whole water → 0%, i.e., complete dilution) resulted in a gradual increase of bacterial cell volume during 24-hour incubation. Please note that the increase was not observed in undiluted whole water (100%) and rose proportionally to the degree of dilution (to 0%, i.e., complete dilution).

fore, the biomass of bacterivores should not obligatorily decrease. To check the possible growth of bacterivores, I assessed changes in the biomass of nanoflagellates, which were the main bacterivores, during the incubation of unfiltered seawater and the dilution containing 25% unfiltered seawater. Because some chlorophyll-containing flagellates (ANF) tended to lose their pigments during dark incubation, and the number of ANF should be treated as mixotrophs (Caron, 2000; Rychert, 2006), the biomass of HNF and ANF was combined. Generally, flagellate biomass (HNF + ANF) decreased slightly during incubation in both unfiltered seawater (decrease to 91% of the initial flagellate biomass, 12 comparisons, $R^2 = 0.77$, $p < 0.01$) and in the 25% dilution of unfiltered seawater (decrease to 92% of the initial flagellate biomass, 12 comparisons, $R^2 = 0.76$, $p < 0.01$). Among the results analyzed, the flagellate biomass increased during incubation only twice — in September and October in both undiluted (100%) and diluted seawater (25%). In September in undiluted seawater flagellate biomass (HNF + ANF) increased to 124% of the initial value and in diluted seawater (25%) to 134% of the initial value. In October the increases in flagellate biomass were higher — 165% and 173%, respectively. In conclusion, grazing pressure was not successfully removed during the experiments performed in September and October. During both months bacterial biomass was high (Figure 2); that is, in September 104.0 μg C l^{-1} (SD = 19.5 μg C l^{-1}) and in October 108.7 μg C l^{-1} (SD = 6.8 μg C l^{-1}). In the following months, bacterial biomass was roughly twice lower. Thus, during this period, especially in October, grazing pressure exerted on bacteria seemed to be stronger than bacterial growth rates.

3.5. Change within the bacterial community during incubation

Bacterial counts before and after incubation demonstrated that the mean volume of bacterial cells increased after grazing pressure was relaxed (Figure 5); that is, the increase was not observed in undiluted water and rose proportionally to the degree of dilution (Figure 5). This indicated that it was not an artefact caused by the confinement of water in bottles but a response to relaxed grazing pressure. Similar increases of mean bacterial cell volume are also reported by Kuuppo-Leinikki (1990) and Šimek and Chrzanowski (1992), and they are considered to be evidence that protozoa graze preferentially on larger bacteria (Ammerman et al., 1984; Gonzalez et al., 1993; Šimek and Chrzanowski, 1992; Sherr et al., 1992). It should be mentioned that limnological studies (reviewed by Hahn and Höfle (2001); Jürgens and Güde (1994); but see reports from marine environments — Epstein and Shiaris (1992), Lebaron et al. (1999)) indicated that protozoa preferentially graze medium-sized bacteria, whereas the largest bacteria are grazing-resistant forms such as filaments or aggregates (microcolonies and flocs). These forms were not observed in the current study, which was not unusual, because, according to reviews by Sherr and Sherr (2002) and Pernthaler (2005), such grazing-resistant forms are observed rarely in marine waters. Bacterial communities consist of cells that differ in metabolic activity and growth rate (e.g., Morán et al., 2007; Vaqué et al., 2001) and after the relaxation of grazing pressure, the fraction of metabolically-active bacteria, indicated by the high content of nucleic acids, increases significantly (Pree et al., 2016). In summary, relaxing grazing pressure resulted in a shift to larger bacterial cells because of the growth of larger, metabolically-active bacteria. This was suggested by Stevenson (1978) and demonstrated in a considerable number of studies (Anderson and Rivkin, 2001; and references therein; Gasol et al., 1995; Gonzalez et al., 1993; Koton-Czarnecka and Chróst, 2003; Sherr et al., 1992; Søndergaard and Danielsen, 2001; and references therein; but see Bouvier et al., 2007).

Changes in bacterial cell volumes confirmed that biomass, not numerical abundance, is the proper parameter to assess the growth of the ungrazed bacterial community Kuuppo-Leinikki (1990). reports an increased fraction of rod-shaped cells in the ungrazed bacterial community. In the present study, coccoid bacteria prevailed (56—73%, mean: 63%) over rods, vibrios, and other elongated forms, and no changes in the morphological composition of the bacterial community were demonstrated during incubation. It is well known that the taxonomic composition of the ungrazed bacterial community can change (e.g., Agis et al., 2007; Massana et al., 2001). In this study the taxonomic composition of the community was not assessed.

3.6. Concluding remarks

Only 6 (April—August and March) of the 12 dilution experiments measuring bacterial growth and grazing mortality were successful. During five experiments, conducted during the cold period of the year (October—February), food limitation was detected, and during two experiments (September and October) grazing pressure was not successfully relaxed. This means that one experiment (October) was unsuccessful because of both food limitation and the unsuccessful relaxation of grazing pressure. Thus, the hypothesis posed in the Introduction was confirmed, and the main cause of the unsuccessful dilution experiments was food limitation during experimental incubation. The food limitation of bacterial growth can be detected by 24-hour oxygen consumption exceeding 60% of the BOD5-*in situ* value in any dilution. The production of the 0.2-μm filtrate did not in-

crease but moderately decreased the pool of biodegradable organic matter in the water.

It should be emphasized that the dilution experiment performed with the 0.2-μm-filtrate only measured grazing mortality. Bacterial mortality from viral lysis was not reduced because viruses pass freely through 0.2-μm filters (Evans et al., 2003; Li and Dickie, 1985). To exclude mortality from viral lysis, filtrate for dilutions must be prepared with ultrafiltration (Evans et al., 2003; Kimmance et al., 2007). A couple of dilution experiments performed with 0.2-μm-filtrate and 10-kDa-filtrate permitted differentiation between the mortality induced by predators and viruses (Evans et al., 2003). Such studies are crucial for clarifying the impact of viruses on bacterial community composition (Våge et al., 2018) and are an interesting new line of research.

The constraint of the dilution method is that bacteria attached to detrital particles are not diluted (Murrell and Hollibaugh, 1998), and their mortality rates may be reduced only partially, because the rate of colonization of detritus particles by protozoa is obviously reduced by dilution, but protozoa already attached to particles can graze as before. According to the best of my knowledge this problem has yet to be quantified. It is worth noting that size fractionation, which is a competing method based on whole community manipulation, is inferior to the dilution method because filtration removes almost all detritus particles and almost all attached organisms.

Acknowledgments

This study was supported by the Polish Ministry of Science and Higher Education (grant No. 2 P04F 074 27). The preparation of the manuscript was supported by a grant for young scientists I received from the Pomeranian University in Słupsk. Thanks are due to Marcus Reckermann and Zbigniew Witek for initial training on the dilution technique. The help of Mariusz Zalewski, Anetta Ameryk, Antoni Kurowicki, and Bartosz Witalis from the National Marine Fisheries Research Institute in Gdynia (formerly the Sea Fisheries Institute) with chlorophyll measurements and assistance during sampling is also appreciated. I would like to thank two anonymous reviewers for their valuable comments and suggestions.

References

Agis, M., Granda, A., Dolan, J.R., 2007. A cautionary note: examples of possible microbial community dynamics in dilution grazing experiments. J. Exp. Mar. Biol. Ecol. 341, 176—183. http://doi.org/10.1016/j.jembe.2006.09.002

Ammerman, J.W., Fuhrman, J.A., Hagström, Å., Azam, F., 1984. Bacterioplankton growth in seawater: I. Growth kinetics and cellular characteristics in seawater cultures. Mar. Ecol. Prog. Ser. 18, 31—39.

Ameryk, A., Podgórska, B., Witek, Z., 2005. The dependence between bacterial production and environmental conditions in the Gulf of Gdańsk. Oceanologia 47 (1), 27—45.

Anderson, M.R., Rivkin, R.B., 2001. Seasonal patterns in grazing mortality of bacterioplankton in polar oceans: a bipolar comparison. Aquat. Microb. Ecol. 25, 195—206.

Andersson, A., Brugel, S., Paczkowska, J., Rowe, O.F., Figueroa, D., Kratzer, S., Legrand, C., 2018. Influence of allochthonous dissolved organic matter on pelagic basal production in a northerly estuary. Estuar. Coast. Shelf Sci. 204, 225—235. https://doi.org/10.1016/j.ecss.2018.02.032

Blackburn, N., Hagström, Å., Wikner, J., Cuadros-Hansson, R., Bjørnsen, P.K., 1998. Rapid determination of bacterial abundance, biovolume, morphology, and growth by neural network-based image analysis. Appl. Environ. Microbiol. 64, 3246—3255.

Bochdansky, A.B., Clouse, M.A., 2015. New tracer to estimate community predation rates of phagotrophic protests. Mar. Ecol. Prog. Ser. 524, 55—69. https://doi.org/10.3354/meps11209

Børsheim, K.Y., Bratbak, G., 1987. Cell volume to carbon conversion factors for a bacterivorous *Monas* sp. enriched from seawater. Mar. Ecol. Prog. Ser. 36, 171—175.

Bouvier, T., del Giorgio, P.A., Gasol, J.M., 2007. A comparative study of cytometric characteristics of high and low nucleic acid bacterioplankton cells from different aquatic ecosystems. Environ. Microbiol. 9, 2050—2066. https://doi.org/10.1111/j.1462-2920.2007.01321.x

Caron, D.A., 1983. Technique for enumeration of heterotrophic and phototrophic nanoplankton, using epifluorescence microscopy, and comparison with other procedures. Appl. Environ. Microbiol. 46, 491—498.

Caron, D.A., 2000. Symbiosis and mixotrophy among pelagic microorganisms. In: Kirchman, D.L. (Ed.), Microbial ecology of the oceans. John Wiley & Sons, New York, 495—523.

Chróst, R.J., 1991. Environmental control of the synthesis and activity of aquatic microbial ectoenzymes. In: Chróst, R.J. (Ed.), Microbial enzymes in aquatic environments. Springer Verlag, New York, 22—59.

Cole, J., 1999. Aquatic microbiology for ecosystem scientists: new and recycled paradigms in ecological microbiology. Ecosystems 2, 215—225.

del Giorgio, P.A., Cole, J.J., 2000. Bacterial energetics and growth efficiency. In: Kirchman, D.L. (Ed.), Microbial ecology of the oceans. John Wiley & Sons, New York, 289—325.

del Giorgio, P.A., Duarte, C.M., 2002. Respiration in the open ocean. Nature 420, 379—384. http://doi.org/10.1038/nature01165

Dolan, J.R., Gallegos, Ch.L., Moigis, A., 2000. Dilution effects on microplankton in dilution grazing experiments. Mar. Ecol. Prog. Ser. 200, 127—139.

Dolan, J.R., McKeon, K., 2005. The reliability of grazing rate estimates from dilution experiments: have we over-estimated rates of organic carbon consumption by microzooplankton? Ocean. Sci. 1, 1—7. http://doi.org/10.5194/os-1-1-2005

Ducklow, H., 2000. Bacterial production and biomass in the oceans. In: Kirchman, D.L. (Ed.), Microbial ecology of the oceans. John Wiley & Sons, New York, 85—120.

Elser, J.J., Frees, D.L., 1995. Microconsumer grazing and sources of limiting nutrients for phytoplankton growth: application and complications of a nutrient-depletion/dilution-gradient technique. Limnol. Oceanogr. 40, 1—16.

Epstein, S.S., Shiaris, M.P., 1992. Size selective grazing of coastal bacterioplankton by natural assemblages of pigmented flagellates, colorless flagellates, and ciliates. Microb. Ecol. 23, 211—225.

Evans, C., Archer, S.D., Jacquet, S., Wilson, W.H., 2003. Direct estimates of the contribution of viral lysis and microplankton grazing to the decline of a *Micromonas* spp. population. Aquat. Microb. Ecol. 30, 207—219. https://doi.org/10.3354/ame030207

Evans, G.T., Paranjape, M.A., 1992. Precision of estimates of phytoplankton growth and microzooplankton grazing when the functional response of grazers may be nonlinear. Mar. Ecol. Prog. Ser. 80, 285—290.

Ferguson, R.L., Buckley, E.N., Palumbo, A.V., 1984. Response of ma-

rine bacterioplankton to differential filtration and confinement. Appl. Environ. Microbiol. 47, 49—55.
Gallegos, Ch.L., 1989. Microzooplankton grazing on phytoplankton in the Rhode River, Maryland: nonlinear feeding kinetics. Mar. Ecol. Prog. Ser. 57, 23—33.
Gasol, J.M., del Giorgio, P.A., Massana, R., Duarte, C.M., 1995. Active versus inactive bacteria: size-dependence in a coastal marine community. Mar. Ecol. Prog. Ser. 128, 91—97.
Gifford, D.J., 1988. Impact of grazing by microzooplankton in the Northwest Arm of Halifax Harbour, Nova Scotia. Mar. Ecol. Prog. Ser. 47, 249—258.
Gonzalez, J.M., Sherr, E.B., Sherr, B.F., 1993. Differential feeding by marine flagellates on growing versus starving and on motile versus non-motile bacterial prey. Mar. Ecol. Prog. Ser. 102, 257—267.
Griffith, P.C., Douglas, D.J., Wainright, S.C., 1990. Metabolic activity of size-fractionated microbial plankton in estuarine, nearshore, and continental shelf waters of Georgia. Mar. Ecol. Prog. Ser. 59, 263—270.
Güde, H., 1986. Loss processes influencing growth of planktonic bacterial populations in Lake Constance. J. Plankton Res. 8, 795—810.
Hahn, M.W., Höfle, M.G., 2001. Grazing of protozoa and its effect on population of aquatic bacteria. FEMS Microbiol. Ecol. 35, 113—121. https://doi.org/10.1111/j.1574-6941.2001.tb00794.x
Haller, C.M., Rolleke, S., Vybiral, D., Witte, A., Velimirov, B., 1999. Investigation of 0.2 μm filterable bacteria from the Western Mediterranean Sea using a molecular approach: dominance of potential starvation forms. FEMS Microbiol. Ecol. 31, 153—161.
Hobbie, J.E., Daley, R.J., Jasper, S., 1977. Use of nucleopore filters for counting bacteria by fluorescence microscopy. Appl. Environ. Microbiol. 33, 1225—1228.
Jochem, F.J., Lavrentyev, P.J., First, M.R., 2004. Growth and grazing rates of bacteria groups with different apparent DNA content in the Gulf of Mexico. Mar. Biol. 145, 1213—1225. https://doi.org/10.1007/s00227-004-1406-7
Jost, G., Ballin, G., 1984. Seasonal changes in bacteriological parameters at a station in the chain of shallow waters (boddens), south of the Darss-Zingst Peninsula (South Baltic). Limnologica 15, 597—603.
Jürgens, K., Güde, H., 1994. The potential importance of grazing-resistant bacteria in planktonic systems. Mar. Ecol. Prog. Ser. 112, 169—188.
Kimmance, S.A., Wilson, W.H., Archer, S.D., 2007. Modified dilution technique to estimate viral versus grazing mortality of phytoplankton: limitations associated with method sensitivity in natural waters. Aquat. Microb. Ecol. 49, 207—222. https://doi.org/10.3354/ame01136
Koton-Czarnecka, M., Chróst, R.J., 2003. Protozoans prefer large and metabolically active bacteria. Pol. J. Environ. Stud. 12, 325—334.
Kuparinen, J., 1988. Development of bacterioplankton during winter and early spring at the entrance to the Gulf of Finland, Baltic Sea. Verh. Internat. Verein. Limnol. 23, 1869—1878.
Kuuppo, P., Samuelsson, K., Lignell, R., Seppälä, J., Tamminen, T., Andersson, A., 2003. Fate of increased production in late-summer plankton communities due to nutrient enrichment of the Baltic Proper. Aquat. Microb. Ecol. 32, 47—60. https://doi.org/10.3354/ame032047
Kuuppo-Leinikki, P., 1990. Protozoan grazing on planktonic bacteria and its impact on bacterial population. Mar. Ecol. Prog. Ser. 63, 227—238.
Landry, M.R., 1993. Estimating rates of growth and grazing mortality of phytoplankton by the dilution method. In: Kemp, P.F., Sherr, B.F., Sherr, E.B., Cole, J.J. (Eds.), Handbook of methods in aquatic microbial ecology. Levis Publ., Boca Raton, 715—722.
Landry, M.R., Calbet, A., 2005. Reality checks on microbial food web interactions in dilution experiments: responses to the comments of Dolan and McKeon. Ocean. Sci. 1, 39—44. https://doi.org/10.5194/os-1-39-2005
Landry, M.R., Hassett, R.P., 1982. Estimating the grazing impact of marine micro-zooplankton. Mar. Biol. 67, 283—288.
Landry, M.R., Kirshtein, J., Constantinou, J., 1995. A refined dilution technique for measuring the community grazing impact of microzooplankton, with experimental tests in the central equatorial Pacific. Mar. Ecol. Prog. Ser. 120, 53—63.
Latasa, M., 2014. Comment: A potential bias in the databases of phytoplankton growth and microzooplankton grazing rates because of the improper formulation of the null hypothesis in dilution experiments. Limnol. Oceanogr. 59, 1092—1094. https://doi.org/10.4319/lo.2014.59.3.1092
Lebaron, P., Servais, P., Troussellier, M., Courties, C., Vives-Rego, J., Muyzer, G., Bernard, L., Guindulain, T., Schäfer, H., Stackebrandt, E., 1999. Changes in bacterial community structure in seawater mesocosms differing in their nutrient status. Aquat. Microb. Ecol. 19, 255—267.
Li, W.K.W., Dickie, P.M., 1985. Growth of bacteria in seawater filtered through 0.2 μm Nucleopore membranes: implications for dilution experiments. Mar. Ecol. Prog. Ser. 26, 245—252.
Massana, R., Pedrós-Alió, C., Casamayor, E.O., Gasol, J.M., 2001. Changes in marine bacterioplankton phylogenetic composition during incubations designed to measure biogeochemically significant parameters. Limnol. Oceanogr. 46, 1181—1188. https://doi.org/10.4319/lo.2001.46.5.1181
Matthäus, W., Nehring, D., Feistel, R., Nausch, G., Mohrholz, V., Lass, H.-U., 2008. The inflow of highly saline water in the Baltic Sea. In: Feistel, R., Nausch, G., Wasmund, N. (Eds.), State and Evolution of the Baltic Sea. Wiley & Sons, Hoboken, 265—309.
Miki, T., Yamamura, N., 2005. Theoretical model of interactions between particle-associated and free-living bacteria to predict functional composition and succession in bacterial communities. Aquat. Microb. Ecol. 39, 35—46. https://doi.org/10.3354/ame039035
Morán, X.A.G., Bode, A., Suárez, L.Á., Nogueira, E., 2007. Assessing the relevance of nucleic acid content as an indicator of marine bacterial activity. Aquat. Microb. Ecol. 46, 141—152. https://doi.org/10.3354/ame046141
Murrell, M.C., Hollibaugh, J.T., 1998. Microzooplankton grazing in northern San Francisco Bay measured by the dilution method. Aquat. Microb. Ecol. 15, 53—63.
Nagata, T., Kirchman, D.L., 1990. Filtration-induced release of dissolved free amino acids: application to cultures of marine protozoa. Mar. Ecol. Prog. Ser. 68, 1—5.
Pernthaler, J., 2005. Predation on prokaryotes in the water column and its ecological implications. Nat. Rev. Microbiol. 3, 1—10. https://doi.org/10.1038/nrmicro1180
Pinhassi, J., Azam, F., Hemphälä, J., Long, R.A., Martinez, J., Zweifel, U.L., Hagström, Å., 1999. Coupling between bacterioplankton species composition, population dynamics, and organic matter degradation. Aquat. Microb. Ecol. 17, 13—26.
Pinhassi, J., Hagström, Å., 2000. Seasonal succession in marine bacterioplankton. Aquat. Microb. Ecol. 21, 245—256.
Posch, T., Loferer-Krößbacher, M., Gao, G., Alfreider, A., Pernthaler, J., Psenner, R., 2001. Precision of bacterioplankton: a comparison of two fluorescent dyes, and of allometric and linear volume-to-carbon conversion factors. Aquat. Microb. Ecol. 25, 55—63. https://doi.org/10.3354/ame025055
Pree, B., Kuhlisch, C., Pohnert, G., Sazhin, A.F., Jakobsen, H.H., Paulsen, M.L., Frischer, M.E., Stoecker, D., Nejstgaard, J.C., Larsen, A., 2016. A simple adjustment to test reliability of bacterivory rates derived from the dilution method. Limnol. Oceanogr.-Methods 14, 114—123. https://doi.org/10.1002/lom3.10076
Preen, K., Kirchman, D.L., 2004. Microbial respiration and produc-

tion in the Delaware Estuary. Aquat. Microb. Ecol. 37, 109—119. https://doi.org/10.3354/ame037109

Renk, H., Ochocki, S., 1999. Primary production in the southern Baltic Sea determined from photosynthetic light curves. Bull. Sea Fish. Inst. Gdynia 148, 23—40.

Robinson, C., Williams, P., 2005. Respiration and its measurement in surface marine waters. In: del Giorgio, P.A., Williams, P.J. le B. (Eds.), Respiration in aquatic ecosystems. Oxford University Press, Oxford, New York, 147—180.

Rychert, K., 2006. Nanoflagellates in the Gdańsk Basin: coexistence between forms belonging to different trophic types. Oceanologia 48 (2), 323—330.

Rychert, K., 2016. Growth rates of common pelagic ciliates in a highly eutrophic lake measured with a modified dilution method. Oceanol. Hydrobiol. Stud. 45, 216—229. https://doi.org/10.1515/ohs-2016-0020

Rychert, K., Spich, K., Laskus, K., Pączkowska, M., Wielgat-Rychert, M., Sojda, G., 2013. Composition of protozoan communities at two stations in the coastal zone of the southern Baltic Sea. Oceanol. Hydrobiol. Stud. 42, 268—276. https://doi.org/10.2478/s13545-013-0083-x

Sakka, A., Legendre, L., Gosselin, M., Delesalle, B., 2000. Structure of the oligotrophic planktonic food web under low grazing of heterotrophic bacteria: Takapoto Atoll, French. Mar. Ecol. Prog. Ser. 197, 1—17.

Sherr, E.B., Sherr, B.F., 2002. Significance of predation by protists in aquatic microbial food webs. Antonie Leeuwenhoek 81, 293—308.

Sherr, B.F., Sherr, E.B., McDaniel, J., 1992. Effect of protistan grazing on the frequency of dividing cells in bacterioplankton assemblages. Appl. Environ. Microbiol. 58, 2381—2385.

Shinada, A., Ikeda, T., Ban, S., Tsuda, A., 2000. Seasonal changes in micro-zooplankton grazing on phytoplankton assemblages in the Oyashio region, western subarctic Pacific. Plankton Biol. Ecol. 47, 85—92.

Šimek, K., Chrzanowski, T.H., 1992. Direct and indirect evidence of size-selective grazing on pelagic bacteria by freshwater nanoflagellates. Appl. Environ. Microbiol. 58, 3715—3720.

Sommer, U., Berninger, U.G., Böttger-Schnack, R., Cornils, A., Hagen, W., Hansen, T., Al-Najjar, T., Post, A.F., Schnack-Schiel, S.B., Stibor, H., Stübing, D., Wickham, S., 2002. Grazing during early spring in the Gulf of Aqaba and the northern Red Sea. Mar. Ecol. Prog. Ser. 239, 251—261.

Søndergaard, M., Danielsen, M., 2001. Active bacteria (CTC+) in temperate lakes: temporal and cross-system variations. J. Plankton Res. 23, 1195—1206. https://doi.org/10.1093/plankt/23.11.1195

Stevenson, L.H., 1978. A case for bacterial dormancy in aquatic systems. Microb. Ecol. 4, 127—133.

Stocker, R., 2012. Marine microbes see a sea of gradients. Science 338, 628—633. https://doi.org/10.1126/science.1208929

Taira, Y., Uchimiya, M., Kudo, I., 2009. Simultaneous estimation of viral lysis and protozoan grazing on bacterial mortality using a modified virus-dilution method. Mar. Ecol. Prog. Ser. 379, 23—32. https://doi.org/10.3354/meps07820

Tett, P., Wilson, H., 2000. From biogeochemical to ecological models of marine microplankton. J. Mar. Syst. 25, 431—446.

Våge, S., Bratbak, G., Egge, J., Heldal, M., Larsen, A., Norland, S., Paulsen, M.L., Pree, B., Sandaa, R.-A., Skjoldal, E.F., Tsagaraki, T.M., Øvreås, L., Thingstad, T.F., 2018. Simple models combining competition, defence and resource availability have broad implications in pelagic microbial food webs. Ecol. Lett. 21, 1440—1452. https://doi.org/10.1111/ele.13122

Vaqué, D., Casamayor, E.O., Gasol, J.M., 2001. Dynamics of whole community bacterial production and grazing losses in seawater incubations as related to the changes in the proportions of bacteria with different DNA content. Aquat. Microb. Ecol. 25, 163—177.

Williams, P.J.leB., 2000. Heterotrophic bacteria and the dynamics of dissolved organic matter. In: Kirchman, D.L. (Ed.), Microbial ecology of the oceans. WileyLiss, New York, 153—200.

Witek, Z., Drgas, A., Ameryk, A., Ochocki, S., 2001. Production and mineralization of organic matter in the Pomeranian Bay. Bull. Sea Fish. Inst. Gdynia 3, 49—69.

Witek, Z., Ochocki, S., Maciejowska, M., Pastuszak, M., Nakonieczny, J., Podgórska, B., Kownacka, J.M., Mackiewicz, T., Wrzesińska-Kwiecień, M., 1997. Phytoplankton primary production and its utilization by the pelagic community in the coastal zone of the Gulf of Gdańsk (southern Baltic). Mar. Ecol. Prog. Ser. 148, 169—186.

Zoccarato, L., Malusà, A., Fonda Umani, S., 2016. Major contribution of prokaryotes to carbon fluxes in the pelagic microbial food webs of the Mediterranean Sea. Adv. Oceanogr. Limnol. 7, 51—66. https://doi.org/10.4081/aiol.2016.5799

Zweifel, U.L., Norrman, B., Hagström, Å., 1993. Consumption of dissolved organic carbon by marine bacteria and demand for inorganic nutrients. Mar. Ecol. Prog. Ser. 101, 23—32.

Oceanologia 64 (2022) 417—432

Available online at www.sciencedirect.com

ScienceDirect

journal homepage: www.journals.elsevier.com/oceanologia

ORIGINAL RESEARCH ARTICLE

Shoreline change rate dynamics analysis and prediction of future positions using satellite imagery for the southern coast of Kuwait: A case study

Najeeb S. Aladwani*

Department of Earth and Environmental Sciences, Faculty of Science, Kuwait University, Kuwait

Received 24 September 2021; accepted 8 February 2022
Available online 24 February 2022

KEYWORDS
Shoreline change rates;
Shoreline position extraction;
Future shoreline position;
EPR and LRR models;
Al-Khiran project

Abstract The studied shoreline extends 73 kilometers, starting from the Kuwait-Saudi Arabia borders northward. This work represents a limited work that analyses the historical shoreline positions. Five-dates satellite images along a period of 35 years between 1986 and 2021 were used to calculate the historical shoreline change rates and predict future shoreline positions in 2030 and 2050. First, the historical shoreline was extracted using the Normalized Difference Wader index (WI 2015). Then, the shoreline change rates were quantified statistically using the End Point Rate (EPR) and the Linear Regression Rate (LRR) models of the Digital Shoreline Analysis System (DSAS) tool in ArcMap. It has been found that the maximum erosion rate is −9.73 m/year, and the highest accretion is 10.88 m/year. Also, the positions of shorelines in the year 2030 and 2050 were predicted and defined on the map, with mapping of gain and loss surfaces. The results defined the most stable areas for future development and the areas needing urgent protection. It has been found that the resulting model can be affected by the topographical changes of the beaches due to human activities, where the coast alongside the Al-Khiran project will be eroded and accreted less than predicted because of the presence of protection facilities.

* Corresponding author at: Department of Earth and Environmental Sciences, Faculty of Science, Kuwait University, P.O. Box 5969, Safat 13060, Kuwait. Tel: +96597833332.
E-mail address: Najeeb.aladwani@ku.edu.kw
Peer review under the responsibility of the Institute of Oceanology of the Polish Academy of Sciences.

Production and hosting by Elsevier

https://doi.org/10.1016/j.oceano.2022.02.002

1. Introduction

The impact of natural factors on shoreline movement occupies the minds of governments, especially during the implementation of large tourism projects on the coasts. The short-term and long-term shoreline changes are controlled by various factors such as sediment supply, sea-level change, river mouth interaction with the shoreline, the strength of wind, tidal currents, and the height of waves (Ding and Wang, 2008; Hakkou et al., 2018; Kumar and Jayappa, 2009). Therefore, understanding the shoreline movement mechanism either by erosion or accretion and determining the quantitative rates of progradation/degradation are essential elements for the engineers and decision-makers (Boak and Turner, 2005).

Many approaches can be used to detect shoreline changes, such as field survey and integration method between remote sensing and Geographic Information System (GIS). However, the conventional field survey method is very intensive work, costly, and time-consuming, especially in the case of the extensive study area as in this work (Natesan et al., 2015). On the other hand, remote sensing provides global repetitive coverage and multispectral satellite imagery, which is associated with developing some applications more powerful for shoreline change analysis on ArcGIS which supports us with impressive results for shoreline change (Ruiz-Beltran et al., 2019). In addition, the accessibility of satellite images increases the use of remote sensing and GIS techniques in shoreline position assessment and monitoring (Qiao et al., 2018; Salmon et al., 2019).

Kuwait is a desert bounded from north and west by Iraq, from the south by Saudi Arabia, and The Arabian Gulf to the east. It has low to moderate relief with a topographic surface that rises gently from the shoreline of the Arabian Gulf toward the southwest, ranging between −20 m at the north-eastern coast and 300 m in the southwest corner (Khalaf et al., 1984). It has no permanent surface water, such as lakes or rivers, and just some valleys are located in interior desert basins. It has a low precipitation rate, little is absorbed beyond the surface level, with most being lost to evaporation. Kuwait has a coast of about 499 km in length, and 94% of the population (4.5 million) living on the coast (see the world factbook, https://www.cia.gov/the-world-factbook/field/coastline). In the last decades, human activities increased rapidly in industrial, tourism, and living constructions along the coast. Hassan (2016) explained ten types of human activities along the Kuwaiti coasts, including seven commercial and oil seaports, four of which are located on the southern coast. There are also oil refineries such as the Mina Abdullah refinery and the Shuaiba area for the oil products industry. He also referred to recreational facilities such as the Green Island and military facilities such as Sobah Al Ahmed and Muhammad Al Ahmed military bases. The formation and topography of the coastline were excavated and changed by preparing concrete sidewalks and bridges.

Moreover, a new city (Al-Khiran) built on five phases last 15 years since 2003 and occupied about 10 kilometers from the lower part of the Kuwaiti shoreline. Hassan (2018) states that Al-Khiran city constructions vanished some natural geomorphological phenomena and were replaced by artificial forms. For example, the natural Creeks (Khors) have turned into artificial ones, and new artificial beaches have been created in tidal flats by replacing the old beaches with washed desert sand. Also, new residential areas and entertainment resorts have been built in the sabkhas areas.

This study was conducted to understand the historical shoreline change for better management for the current and future development activities in the studied area. The study used the satellite images for five dates along 35 years period (1986, 1995, 2005, 2015, and 2021) for the area of study. We calculated the amount of shoreline progradation and degradation over the study period to predict the relative (2030) and far (2050) shoreline positions based on a statistical analysis of the historical data on the shoreline. Besides, we determined the areas which need urgent protection and the most area for safe future coastal constructions. In addition to that, the study aims to obtain the effect of human activities in the area mentioned above on the natural progress of erosion and accretion mechanisms along the shoreline. The research methodology presented in this study can be useful for investigations of any long-term coastline changes worldwide.

2. Study area

The study area is part of the Kuwait coast on the Arabian Gulf; it represents the southern part of the coastal line extending about 73 km from the Kuwait-Saudi Arabia borders northward (Figure 1). It lies between latitudes 28°30′ and 29°N and longitudes 48°5′ and 48°30′E. The area of study has two tongues of shoreland extending to the sea, making them more susceptible to natural factors and climatic changes.

2.1. Climate and wave-dominated energy

The climate of Kuwait is a desert, with intensely hot summers and short cool winters. The heat in summer reaches 111°F (44°C) and on occasion approaches 130°F (54°C) through the daytime. The rainfall averages from 25 to 180 mm/year, and most of it is observed by the valleys in the interior desert without any drainage water to the Arabian Gulf. The Arabian Gulf is considered the third largest bay globally, with 237,473 km^2. The maximum depth of the Arabian Gulf is 93 m, and the shallowest waters are about 10 m at the western coast, which is a leading factor in the wave energy strength Goharnejad et al. (2021). provide a study for the wave energy and wave height over 30 years ranging from 1988 to 2017 depending on the reading from six stations (P1−P6) using buoy data. The distributions of the wave energy directions and wave height in the Arabian Gulf according to the six stations through 30 years (1988−2017) are demonstrated in Figure 2A and showed that the mean wave height ranges from 0.2 to over 1.75 m, while the mean historical wave power plotted in Figure 2B, ranging from 0.18 to 0.62 kW/m (Average of 0.4 kW/m) (Alizadeh et al., 2020; Vieira et al., 2020). The wave periods in the area range from 2 to 3 seconds at all stations except station (P6) that exceed up to 4 seconds (Goharnejad et al. 2021).

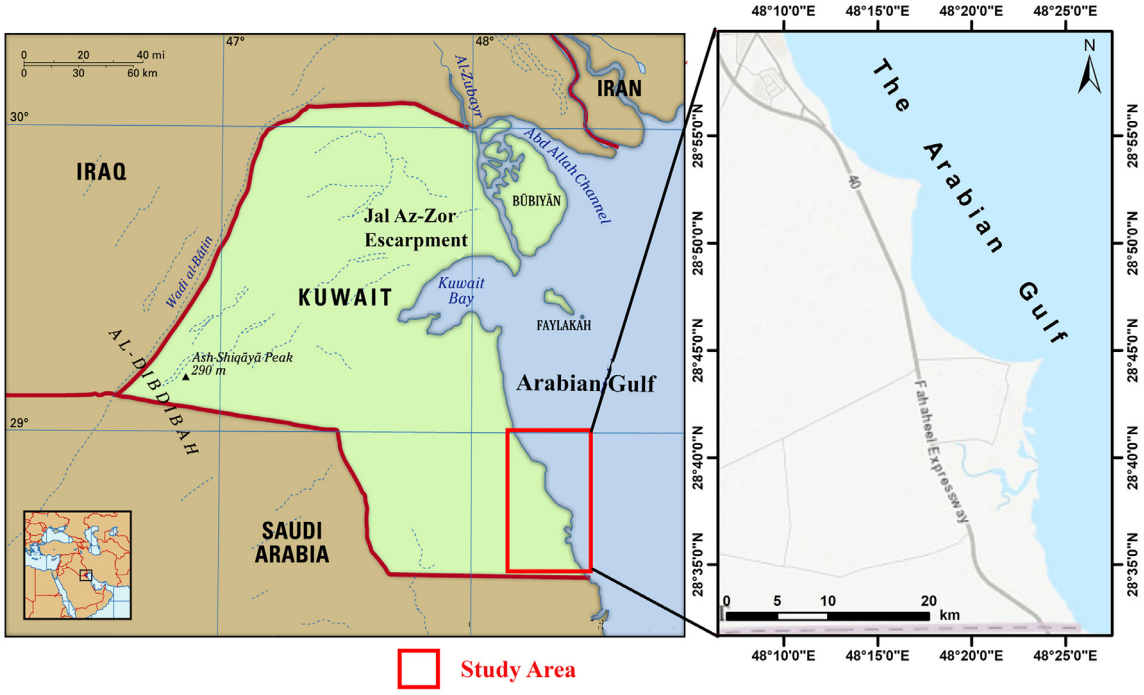

Figure 1 Location map of the studied area.

Table 1 Specifications of the used satellite datasets.

Satellite	Sensor	Spatial Resolution (m)	Year	Acquisition date D/M/YYYY
Sentinel-2	MSI	10	2021	6/6/2021
		10	2015	12/8/2015
Landsat 7	ETM+	15	2005	5/6/2005
Landsat 5	TM	30	1995	18/6/1995
	TM	30	1986	9/6/1986

Taebi et al. (2008) estimated 100-years wave height depending on 30 years of data (1975—2004) and provided that the wave heights range from below 2 m to above 5 m in the Arabian Gulf. Rakha et al. (2007) confirmed the model of Taebi et al. (2008) by calculating the wave height over the Arabian Gulf for 12 years (1993—2004) using European Centre for Medium-Range Weather Forecast (ECMWF) wind data. According to Rakha's model, the wave height ranged from (0—0.5 m) at the western coast of the Gulf to over 5 m at the southeast of the Gulf.

3. Material and methods

For the present work to be achieved, five satellite images in a time range of 35 years from 1986 to 2021 were used to extract the shorelines for these five temporal images (Table 1). The used datasets are two Landsat TM images (1986 and 1995), Landsat ETM+ (2005), and two Sentinel-2 images (2015 and 2021). This study followed the methodological approaches (Figure 3) to evaluate the shoreline change rate and provide the results to guide future development in the area.

3.1. Image processing

All images are acquired in level-1 processing, which is georeferenced to the World Geodetic System (WGS84) datum and the Universal Transverse Mercator (UTM) projection and fall in the zone (38 N). This level of image processing provides raw image data with pixels having only digital numbers (DN's) without correction of the atmospheric effects. The Dark Subtraction atmospheric correction method was applied to all the datasets to retrieve surface reflectance data. This atmospheric correction method is preferred for satellite images containing large water surfaces because it corrects the atmospheric errors due to water vapor and dust particles suspended in the atmosphere that badly affect data. First, the raw satellite data with digital number format is radiometrically calibrated to Top of Atmosphere (TOA) reflectance using the radiometric calibration tool in ENVI v. 5.3. Then, the TOA reflectance data is input to the Dark Subtraction tool in ENVI, and the output is the surface reflectance that is a precise measure for the Earth's surface without any artifacts caused by the atmosphere and illumination. Sentinel-2 and Landsat's images under level-2 processing can provide a good possibility for comparability be-

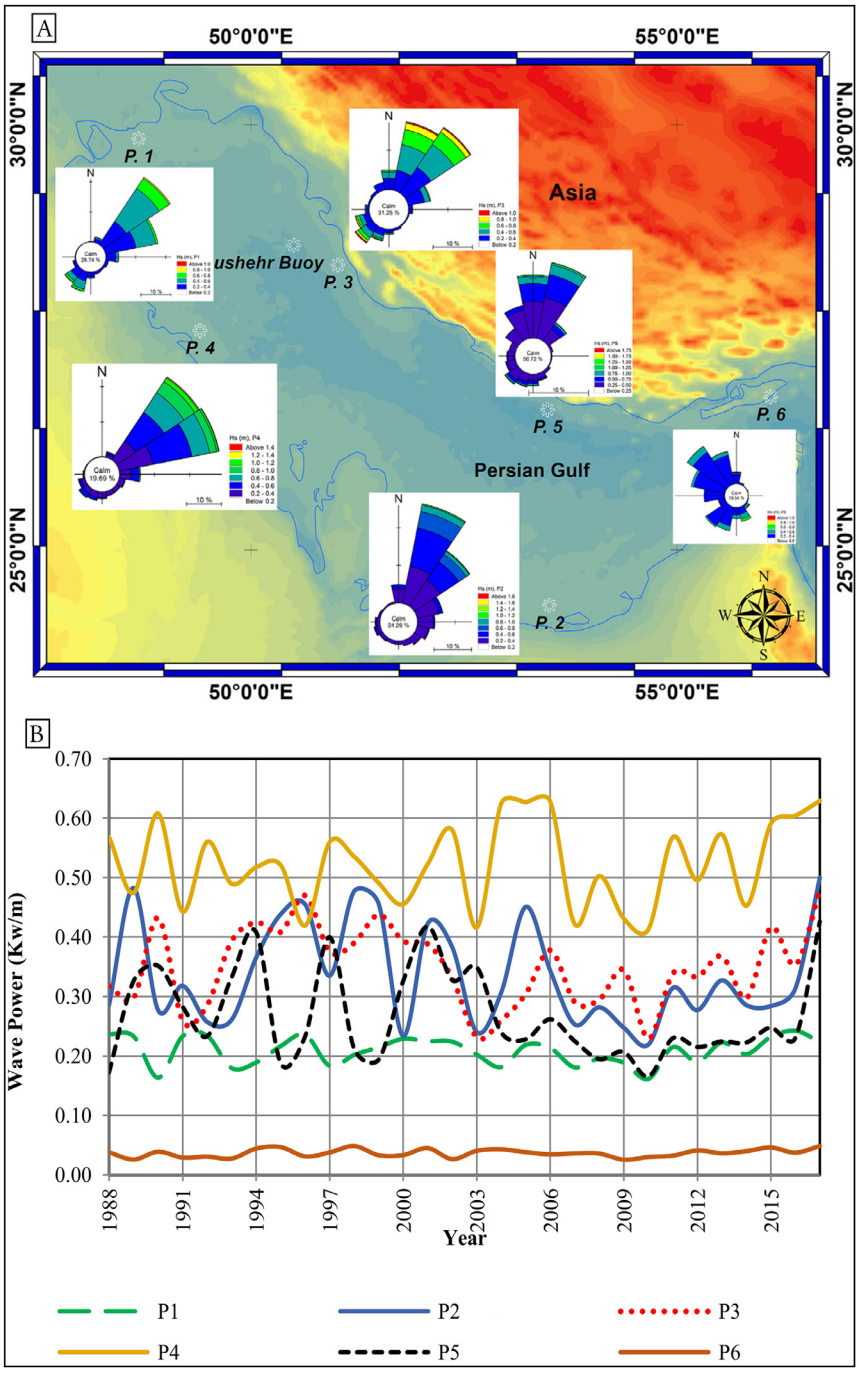

Figure 2 A) Directional distributions for wave energy at six buoy stations distributed in the Arabian Gulf; B) the historical mean wave energy for 30 years period (1988—2017); A and B are taken from Goharnejad et al. (2021) study in the Arabian Gulf.

tween these images if taken at different times (Masek et al., 2006; Vermote et al., 2016). After having all the acquired images are checked for any radiometric defects or errors, mosaicked together, and clipped using ArcGIS v.10.5 to outline the study area. The total uncertainty values for each satellite image were estimated based on the pixel size error (E_p) only, as mentioned in Table 1, which equals 10 m for Sentinel-2, 15 m for Landsat-7, and 30 m for Landsat-5. The calculation of total error percentage is based on some factors; first, the study area is not subjected to vigorous tidal changes as it is part of the shoreline on a gulf area known with low current rates. Second, the selected satellite data were acquired in similar or nearly similar seasonal conditions. Also, the satellite geometric error was not considered as it is deficient and almost constant, so it was neglected.

3.2. Shoreline extraction

The shoreline position is usually in dynamic change due to natural factors (Huang et al., 2019), and many terms have defined its position to determine the shore-water boundary (Boak and Turner, 2005). The baseline was created us-

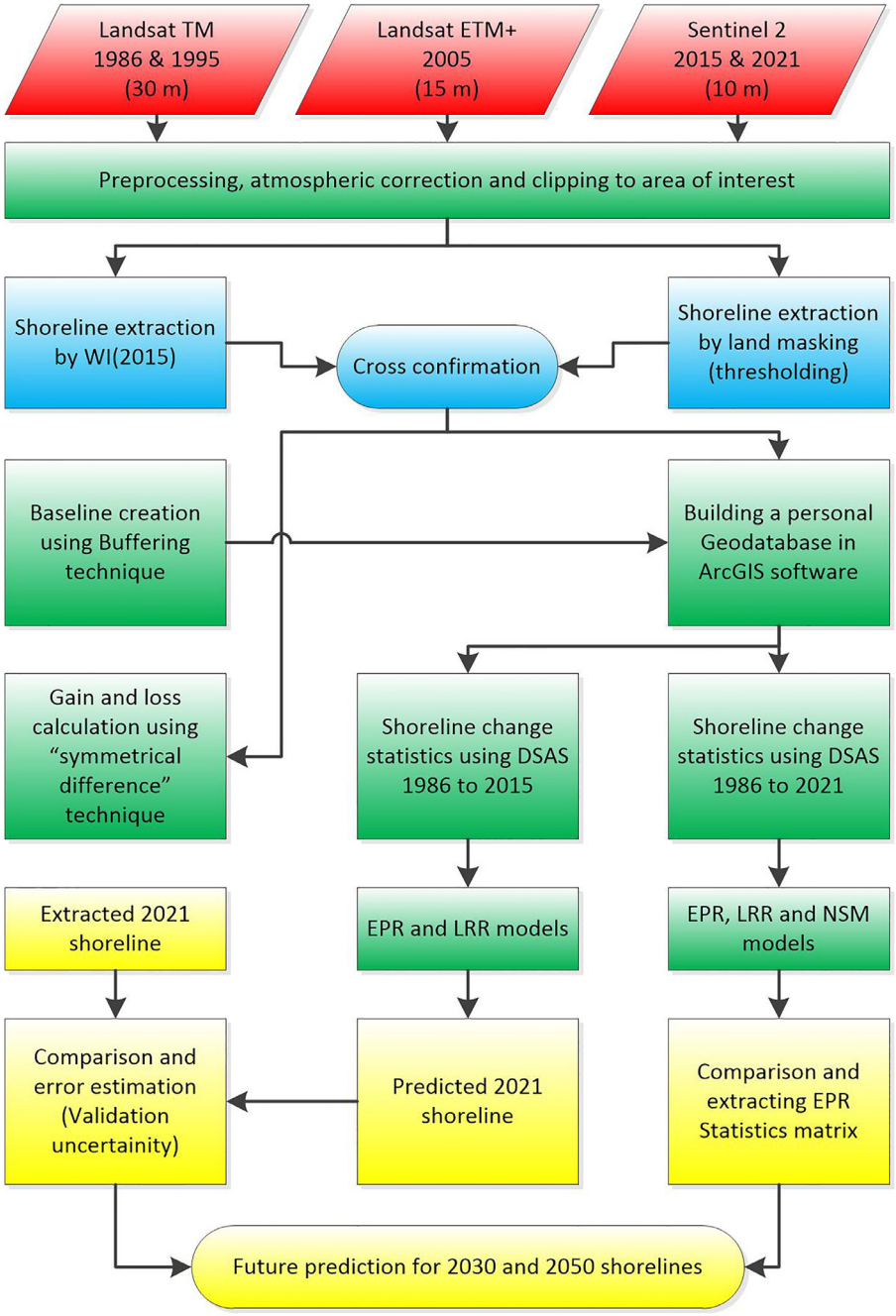

Figure 3 Methodology flow chart.

ing the buffering technique in the environment of ArcGIS software. This line represents a dray/water line, or High-Water Line (HWL), approved by many researchers as a shore-water boundary line because it is visible on images and easy to find in the field (Gokceoglu et al., 2015; Moore, 2000). On the other hand, the shoreline was extracted from these data sets using the Normalized Difference Wader index (WI 2015) (Fisher et al., 2016) and using the land/water masking threshold technique in the study period (Figure 4). The extracted shorelines were confirmed and validated against the ESRI high-resolution base map imagery in ArcMap software. The optimal shoreline was extracted from comparing the automatically extracted shoreline from water indices to the reference shoreline digitized from the buffering technique (Atiquzzaman and Kandasamy, 2015; Tong and Granat, 1999).

3.3. Shoreline change rates and prediction of the future positions

U.S. Geological survey developed Digital Shoreline Analysis System (DSAS) module as an extension in ArcGIS software, which calculates the difference between the baseline and extracted shorelines as a standard method for calculating the shoreline change statistics (Nandi et al., 2016; Thieler et al., 2009). Thieler et al. (2009) discuss the

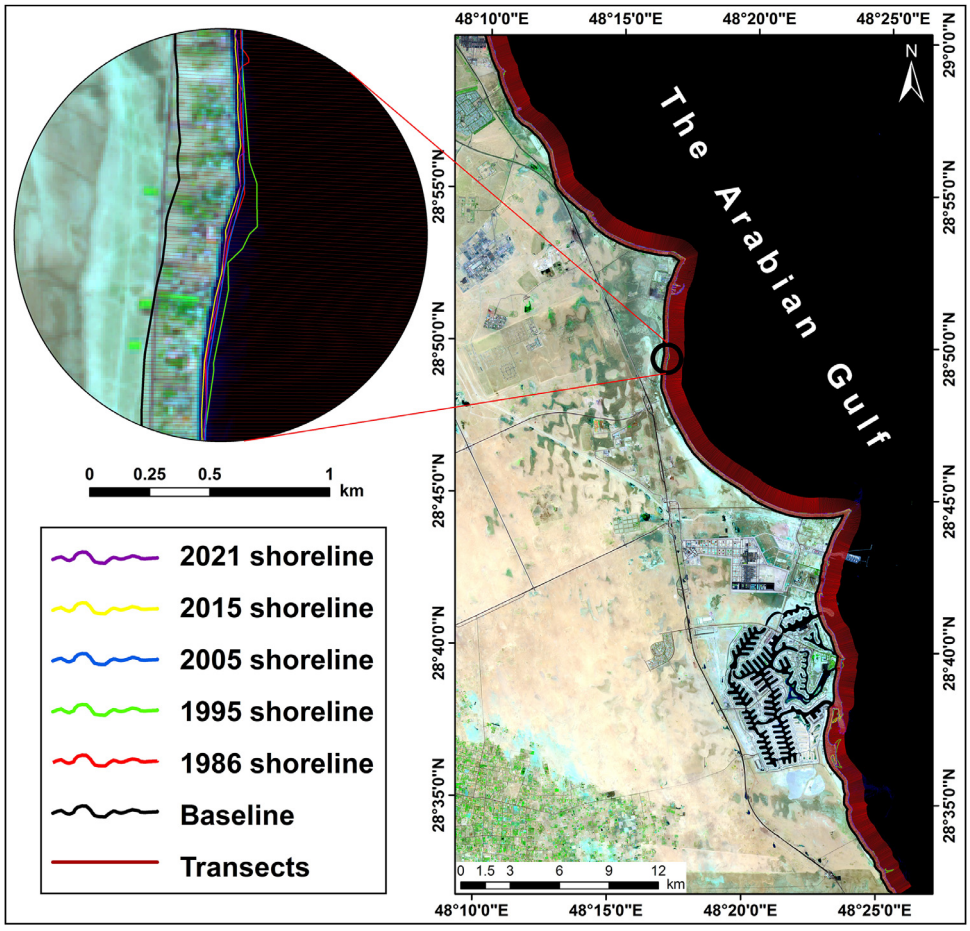

Figure 4 Multi-temporal shoreline positions extracted from five different dates over 35 years (1986—2021).

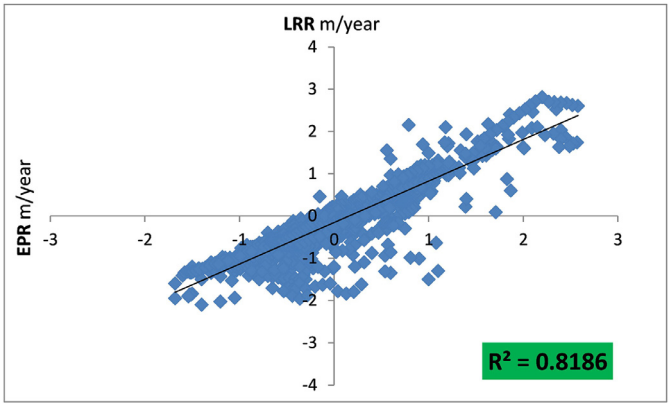

Figure 5 Shoreline change rates obtained from EPR against those of LRR, the results show very close readings.

different DSAS algorithms and their application in shoreline statistics calculation; Net Shoreline Movement (NSM) for determining the total position movement of shoreline within a specific period, Shoreline Change Envelop (SCE) for future prediction of the shoreline position, End Point Rate (EPR) and Linear Regression Rate (LRR) are using for calculation the change rate in the shoreline. In this work, the shoreline change rates were quantified statistically using the End Point Rate (EPR) and the Linear Regression Rate (LRR) models of the Digital Shoreline Analysis System (DSAS) tool in ArcMap. Both EPR and LRR results showed a high correlation with R2=0.81 (Figure 5). The very high correlation between EPR and LRR results was also reported by Esmail et al. (2019), Kanwal et al. (2020), and Nassar et al. (2018). Hence, EPR was used to evaluate the change rates for the 1986—2021 period and predict 2030 and 2050 shoreline positions. In addition, surface analysis was carried out using the "symmetrical difference" tool of ArcGIS to quantify the gain and loss surface areas along the whole shoreline. EPR and LRR have been widely

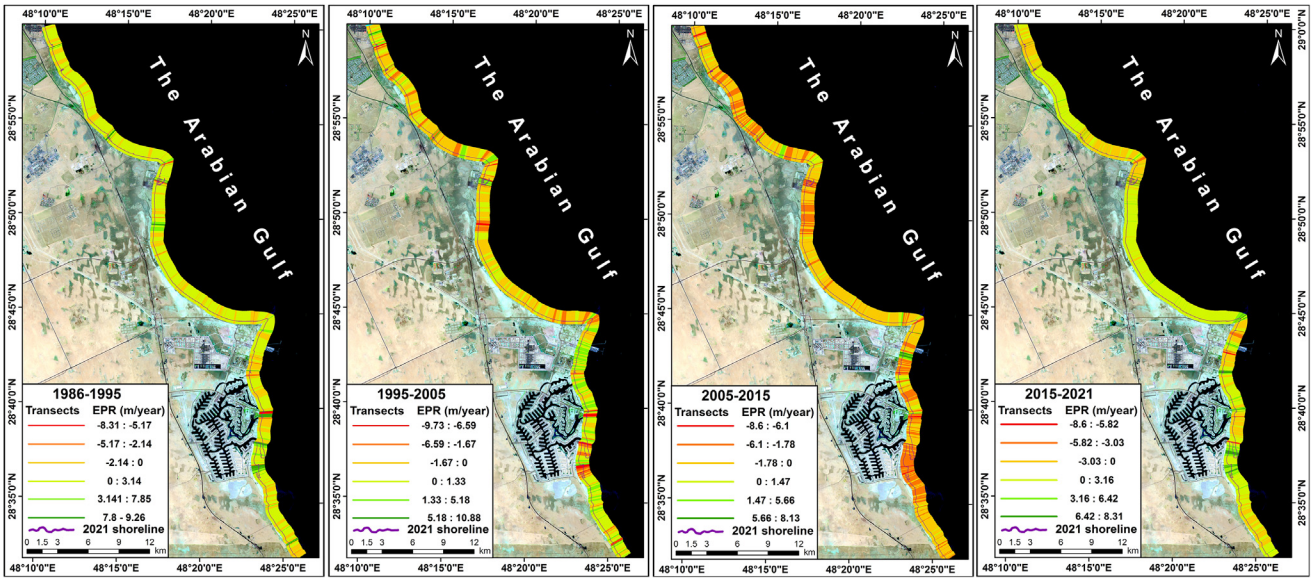

Figure 6 Shoreline change rates by EPR model over the four periods separately.

used to predict future temporal changes of the shoreline (Fenster et al., 1993) along each transect in the study area. The estimated position of the future shoreline can be calculated from Eq. (1), depending on the rate and intercept:

$$Y = mX + B \quad (1)$$

where Y denotes shoreline position, X is the date, B is the intercept, and m is the rate of shoreline movement. The EPR intercept can be calculated from the Eq. (2):

$$B_{(EPR)} = Y_n - m_{(EPR)} * X_n \quad (2)$$

4. Results and discussion

4.1. Analysis of shoreline change rates

The shoreline change rates statistics were retrieved from 4499 transect lines perpendicular to the baseline and intersecting the five extracted shorelines, with 15 m spacing intervals and covering the coast's whole length (about 73 km). EPR and LRR statistical models were used to calculate the change rates over the study area in five periods: (1986—1995), (1995—2005), (2005—2015), (2015—2021) (Figure 6), and the global period of (1986—2021) (Figure 7). Based on the analysis of the change rates of the historical data, 25 alternating erosion-accretion shoreline segments were identified (Figure 7). The statistics of shoreline change rates along the four periods are presented in Tables 2 and 3, while the descriptive statistics of change rates using EPR and LRR models in DSAS across the global period (1986—2021) are presented in Table 4 and illustrated in Figure 8. Generally, the beach was not exposed to a fixed mechanism type, but it was switching between erosion and accretion from one period to another through the studied period of the last 35 years, depending on the direction of wave-driven longshore currents in the studied area. However, each shoreline segment has a dominant mechanism in the global period between 1986 and 2021 Figure 9.

4.1.1. Areas of erosion

Erosion areas are concentrated in the segments with odd numbers (1, 3, ⋯, 23) and represent 59.59% (43.5 km) of the total length of the studied shoreline. This length studied by 2681 transects dominated by erosion ranged from −3.67 m/year to zero for the global period and sometimes increased to −9.7 m/year in the entire periods (see Figures 6 and 7). The erosion reached its maximum in the central area, which extends to the sea (segments 9, 11, 13, 15, 17, and 19) with an average of −3.246 m/year, while the moderate rate of erosion found in the northern part (segments 1 and 3) with an average −0.376 m/year. On the other hand, the lowest erosion rate and most stable shoreland concentrated in the southern part of the shoreline (segments 21, 23, and 25) with an average erosion rate of −0.265 m/year (see Table 4). The areas that dominance by erosion exposed to erosion in the second period (1995—2005) with an average −0.205 m/year, and the erosion rate increased in the third period (2005—2015) to reaches −1.313 m/year, while in the first period (1986—1995) and the fourth period (2015—2021) exposed to accretion with rates 1.1346 and 1.4923 m/year, respectively (Figure 6) and Tables 2 and 3.

4.1.2. Areas of accretion

Accretion areas are characterized by short length and represented by the even segment's number (2, 4, 6, …, 24) with some sediment accretion interspersed with erosion areas such as segments 1, 3, 24, and 25 (see Figures 7 and 8). The total number of transects that represent the accretion process along the study area is 1818, representing 49.41% (29.5 km) of the shoreline. Also, the central part of the studied shoreline (segments from 10 to 18) represents the area of strong accretion mechanism because of the sand accumulated in three periods: the first period (1986—1995) with an

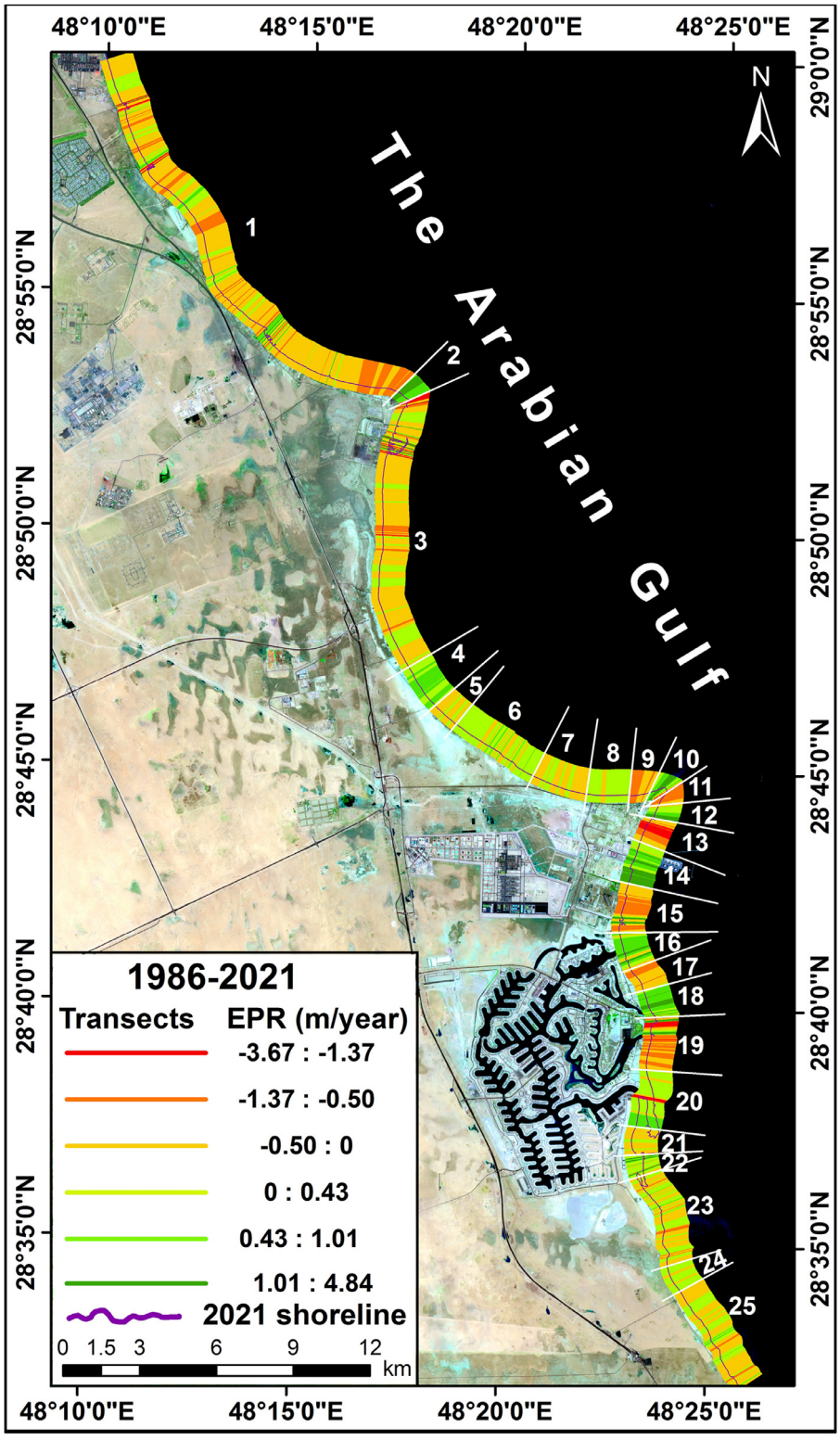

Figure 7 Shoreline change rates by EPR model over the global period 1986—2021 with the shoreline segments plotted.

average accretion rate of 0.75 m/year, the second period (1995—2005) with average accretion rate 0.56 m/year, and the fourth period (2015—2021) with average 1.64 m/year, while it eroded with a rate of —0.93 m/year in the third period (2005—2015). It has been found that the segments 18, 20, 22, and 24 accreted with 0.66, 0.25, 0.29, and 0.104 m/year, respectively, as an average of the total period (see Table 4 and Figure 8). Most of these areas, in detail, eroded in the periods (1995—2005) and (2005—2015) with average rates of —0.20 m/year and —1.31 m/year, respec-

Table 2 Shoreline change rates along the periods (1986—1995) and (1995—2005).

Segment number	EPR 1986–1995			EPR 1995–2005		
	min	max	mean	min	max	mean
1	-28.81	20.29	**0.799**	-16.63	29.96	**-0.378**
2	0.18	4.99	**2.27**	-1.89	0.29	**-0.584**
3	-15.24	23.65	**1.036**	-29.15	10.88	**-0.597**
4	-0.11	2.6	**0.783**	-1.27	1.02	**-0.102**
5	-1.18	1.04	**-0.046**	-1.92	1.18	**-0.194**
6	-0.28	2.02	**0.632**	-3.25	0.95	**-0.379**
7	-0.68	2.19	**0.436**	-3.36	0.13	**-0.8**
8	-1.88	1.94	**0.749**	-4.81	3.44	**-0.377**
9	-2.14	1.5	**-0.291**	-1.15	0.58	**-0.368**
10	-1.2	4.25	**1.093**	-0.43	1.79	**0.552**
11	0.62	4.18	**1.729**	-0.75	1.56	**-0.052**
12	1.42	5.01	**2.713**	-2.44	-0.12	**-0.533**
13	-1.17	4.15	**0.179**	-2.39	3.65	**0.672**
14	-2.24	2.83	**0.97**	-4.71	4.4	**0.029**
15	-3.49	12.08	**-0.615**	-0.47	4.7	**1.446**
16	-1.42	1.84	**0.67**	-4.59	3.18	**0.14**
17	-1.96	0.48	**-0.509**	-2.22	4.28	**2.021**
18	-15.07	9.22	**0.572**	-0.66	2.73	**0.84**
19	-13.3	21.38	**1.237**	-12.56	12.12	**-1.323**
20	-1.69	47.58	**3.237**	-46.7	5.41	**-2.402**
21	-1.46	5.42	**1.178**	-11.19	2.33	**-2.454**
22	-15.03	37.37	**7.498**	-32.62	5.06	**-1.62**
23	-2.52	4.41	**0.521**	-3.69	3.12	**0.222**
24	0.01	1.43	**0.83**	0.13	2.05	**0.957**
25	-2.22	25.16	**0.694**	-20.55	3.29	**0.152**

tively, while the sediments accreted in the periods (1986—2005) and (2015—2021) with an average 1.13 m/year and 1.49 m/year, respectively (see Tables 2 and 3). The very high erosion and accretion rates through the third and fourth periods, in the southern part of the studied shoreline, can be attributed to the construction of the Al-Khiran city constructions and other tourist and military facilities alongside the shoreline of this part.

4.2. Evaluation of gain and loss surfaces

The calculation of shoreline changes rates obtained the distances and the directions of shoreline movement along the study part of the shoreline. The gain and loss mapping support us with the amount of beach lost to the sea or gained, which is a significant factor in determining the future and sustainable plans for exploiting the beaches in the study area. The gain and loss mapping results (Figure 10 and Supplementary I) are presented to highlight and prioritize the areas that would require protection structures. The gain areas have grown in their beaches and are mainly found in areas of accretion. The loss areas have erosion in their beaches and are found in areas of erosion, and the lost surface increase as the erosion rate increase. Segments 14 and 2 have the maximum gain areas with 2.58 ha and 2.09 ha, respectively. The segments 11, 13, and 17 have the maximum loss areas with —0.01 ha, —0.06 ha, and —0.03 ha, respectively (see Table 4, Figure 8, and Supplementary I). By comparing the gain and loss maps for the beach along the study area, we will find that the area that most needs protection from the waves is the area that extends between segments 9 and 19, at the extended tongue of land to the sea, where the rates of gain and loss are the maximum followed by the northern part of the area (segments 1, 2, and

Table 3 Shoreline change rates along the periods (2005—2015) and (2015—2021).

Segment number	EPR 2005–2015			EPR 2015–2021		
	min	max	mean	min	max	mean
1	-24.22	13.11	**-1.273**	-33.61	41.18	**1.135**
2	-0.95	1.91	**-0.033**	-0.78	1.37	**0.233**
3	-42.55	11.69	**-1.587**	-94.3	35.11	**1.164**
4	-2.15	0.86	**-0.714**	-1.61	8.04	**1.344**
5	-2.53	-0.39	**-1.102**	-1.18	3.19	**0.422**
6	-2.79	0.91	**-0.882**	-1.52	3.21	**0.841**
7	-1.69	0.5	**-0.993**	-2.15	3.27	**0.98**
8	-1.47	2.8	**-0.377**	0.52	3.62	**2.068**
9	-3.3	-0.9	**-1.81**	1.76	3.62	**2.53**
10	-1.83	1.67	**-0.384**	0.81	3.28	**1.629**
11	-8.64	0.12	**-1.685**	0.8	2.71	**1.675**
12	-1.77	-1	**-1.331**	0.81	2.15	**1.345**
13	-3.02	0.41	**-1.274**	0.95	2.48	**1.787**
14	-3.06	10.13	**1.078**	-5.39	8.61	**1.082**
15	-8.72	1.75	**-1.833**	-4.3	6.82	**1.616**
16	-3.27	1.93	**-0.684**	-8.13	3.75	**0.461**
17	-4.72	6.57	**-2.05**	-0.79	3.55	**1.912**
18	-2.83	13.27	**-0.232**	-1.24	9.24	**3.279**
19	-6.33	0.63	**-2.18**	-20.15	4.5	**-0.668**
20	-37.07	0.44	**-2.239**	-2.05	4.84	**1.11**
21	-9.61	-0.63	**-3.401**	0.72	48.85	**7.172**
22	-25.13	-1.02	**-3.593**	0.67	11.69	**3.044**
23	-5.47	0.81	**-2.124**	-2.24	5.43	**0.619**
24	-2.19	-0.29	**-1.2**	-0.61	1.28	**0.397**
25	-3.42	1.38	**-0.94**	-3.05	6	**0.131**

3). On the other hand, the most stable coastlands are found between segments 4 and 8 at the north and among segments 20 and 25 in the southern part of the shoreline, where the gain and loss rates are minimum and allow for long suitability for building and infrastructures.

4.3. Prediction of future shoreline changes

The future shoreline positions for 2030 and 2050 were calculated related to its position in 2021 using the EPR model. The prediction was based on the historical EPR rates calculated between 1986 and 2021, which reflect the dominant trend of accretion and erosion along the studied shoreline. It found that the erosion concentrated in the odd segments from 1 to 25 as the historical change rate trend. The predicted minimum erosion rate is —0.835 m/year in segments 23 and 25, and the maximum rate is —8.16 m/year in segments 11, 13, and 15, and an average of —3.94 m/year in the rest eroded areas. Also, the model shows that the historical rates of accretion extend to the future with a minimum rate of 0.665 m/year in segments 6, 22, and 24, and a maximum rate in segments 4, 10, 12, and 14 of 8.53 m/year. The rest areas of sand accumulation advanced by a rate of 4.79 m/year. The results from this model mapped for all 25 segments (Figure 11 and Supplementary II). Generally, the areas of loss along the shoreline obtained in Figure 10 and Supplementary I will show prediction shoreline on the land, while the areas of gain will show future shorelines in the sea. The recession and progradation of shoreline concerning its position in 2021 may break the previous and logical rule of nature if humans interfere with constructions and tourism work on the beaches (Deepika et al., 2014). It has been found that the Al-Khiran project's constructions in south Kuwait, which is equivalent to the segments from 16

Table 4 Shoreline change rates using EPR and LRR models in DSAS across the global period 1986—2021.

Seg. No.	Transects		NO. of transect lines	EPR			LRR		
	from	to		min	max	mean	min	max	mean
1	1	1252	1252	-1.3	1.2	-0.222	-2.03	1.55	-0.365
2	1253	1283	31	0.09	2.09	1.022	-0.06	2.08	1.04
3	1284	2000	717	-1.6	1.1	-0.154	-1.74	1.49	-0.362
4	2001	2139	139	-0.02	0.82	0.394	-0.27	0.72	0.256
5	2140	2212	73	-0.31	0.3	-0.065	-0.52	1.49	-0.22
6	2213	2462	250	-0.46	0.75	0.161	-0.64	0.55	0.003
7	2463	2616	154	-0.21	0.2	-0.048	-0.46	0.05	-0.271
8	2617	2729	113	-0.02	0.51	0.157	-0.02	0.37	0.096
9	2730	2769	40	-1.08	0.18	-0.609	-1.2	0.08	-0.835
10	2770	2799	30	0.06	1.68	0.797	-0.62	1.68	0.515
11	2800	2829	30	-1.68	-0.01	-0.587	-1.6	-0.1	-0.907
12	2830	2857	28	0.02	1.68	0.712	-0.31	1.72	0.633
13	2858	2913	56	-1.58	-0.06	-0.856	-1.34	-0.16	-0.832
14	2914	3037	124	-0.06	2.58	0.993	-0.2	2.81	0.927
15	3038	3178	141	-0.94	1.47	-0.302	-1.72	1.3	-0.364
16	3179	3278	100	-0.35	1.55	0.612	-0.34	1.66	0.606
17	3279	3348	70	-0.9	-0.03	-0.424	-0.99	-0.09	-0.582
18	3349	3433	85	-0.73	1.87	0.664	-1.21	2.15	0.528
19	3434	3556	123	-1.68	1.71	-0.468	-2.1	0.4	-0.724
20	3557	3719	163	-0.15	0.85	0.25	-0.86	0.35	0.013
21	3720	3793	74	-0.33	0.27	-0.038	-1.02	-0.07	-0.323
22	3794	3874	81	-0.46	1.64	0.295	-1.87	1.09	0.12
23	3875	4119	245	-0.74	0.95	-0.066	-0.95	0.73	-0.232
24	4120	4194	75	-0.05	0.41	0.104	-0.11	0.41	0.046
25	4195	4499	305	-0.82	0.61	-0.048	-1.63	0.53	-0.124

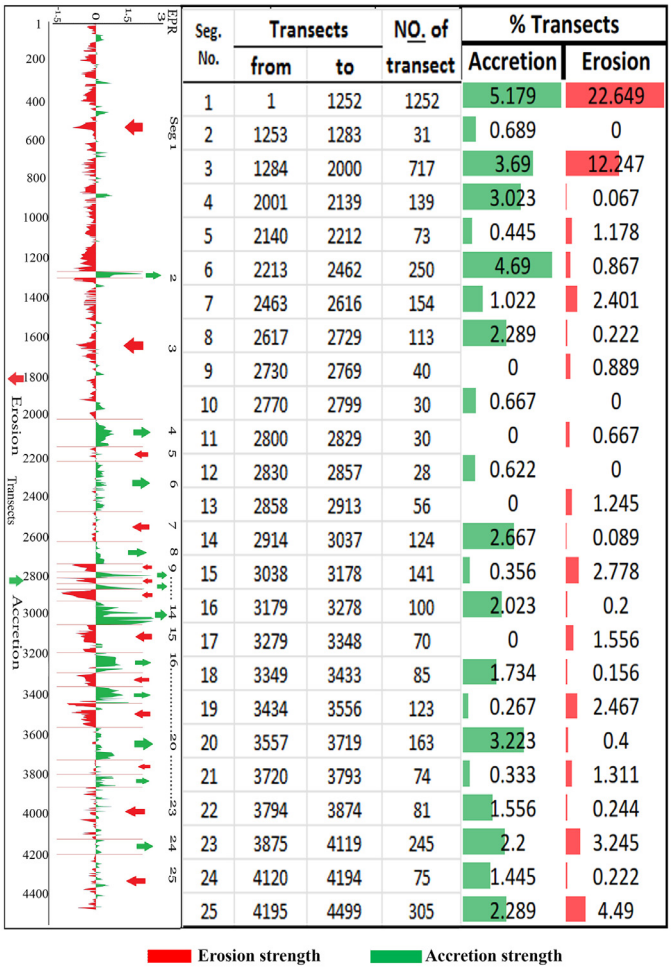

Figure 8 Shoreline change rates using EPR and LRR models in DSAS across the global period 1986—2021, and the dominant shoreline change rate, either erosion or accretion, in all segments of the studied area.

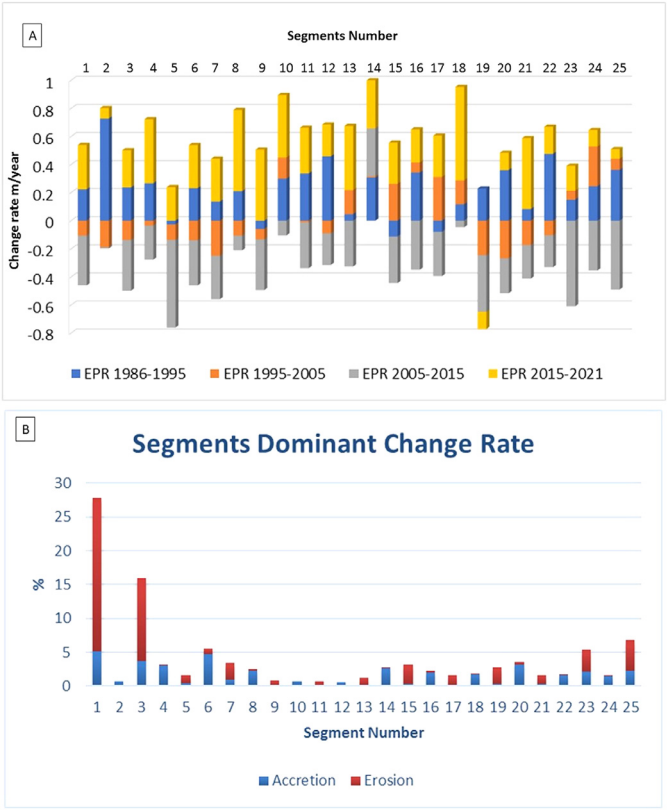

Figure 9 A) The shoreline changes rates range of each segment plotted in the four-time periods; B) The dominant change rate, either erosion or accretion, in each segment.

to 22, led to the disappearance of the dynamic change rate mechanism because of the replacement of the beach sand and building wave breakers along the coastline of Al-Khiran city. The historical shoreline alongside this length characterizes by a high rate of erosion and accretion, but the future shorelines by 2030 and 2050 usually coincide with the current shoreline position in 2021.

4.4. Sustainable development in the study area

The shoreline recession and progradation analysis is an essential study for identifying the areas of significant erosion that require protection to avoid the beach's land loss (Frihy, 2009; Rady, 2011). Segments 1 and 3 suffer from erosion rate ranges between −3.67 and −1.37 m/year that must be considered when planning for future constructions on the beaches by adding one of the beach protection methods. The shoreline at the two tongues of land that extended to the sea and surrounding areas shows a wide range of gain and loss ranges between 4.84 and −3.67 m/year, which forces the decision-maker to be very careful when planning for future construction projects in this area. The recession and progradation in segments from 4 to 8 are low, with rates ranging between −0.50 and 0.43 m/year, making it safe for future development. The segments from 16 to 22 are characterized by high erosion and accretion rates in the last 35 years, but it is protected today by the Al-Khiran project facilities that extend along with these segments. These human constructions affect the future shoreline position, reducing the predicted gain and loss rates (Supplementary II), where it found that the current shoreline coincides with 2030 and 2050 prediction shorelines without any gain or loss. Also, these facilities acted as a shield protecting the southern part, among the segments 23 and 25, from possible severe impacts, which make it safe for future development due to the low rate of recession and progradation.

5. Discussion

We studied along part of the southern coastline of Kuwait in the present study that traced the dynamic behaviour of the beach sand related to the erosion and accretion processes at a temporal time scale. The study shows that the historical rates of beach change were natural in response to erosion processes, which were affected by the extension of two parts of the beach into the water. Since 2000, many projects for the development and exploitation of beaches began, such as establishing Al-Khiran city, on an extension of about 10 km from the coast and other ports and naval military bases. Consequently, the coastline morphology is changed, and its nature affects the rates of beach change. As a result, this part of the coast became more stable land and protected, which vanished the future continuing of shoreline erosion and accretion. This approach used, for calculating the historical shoreline change rate and predicting the future position of the coastline,

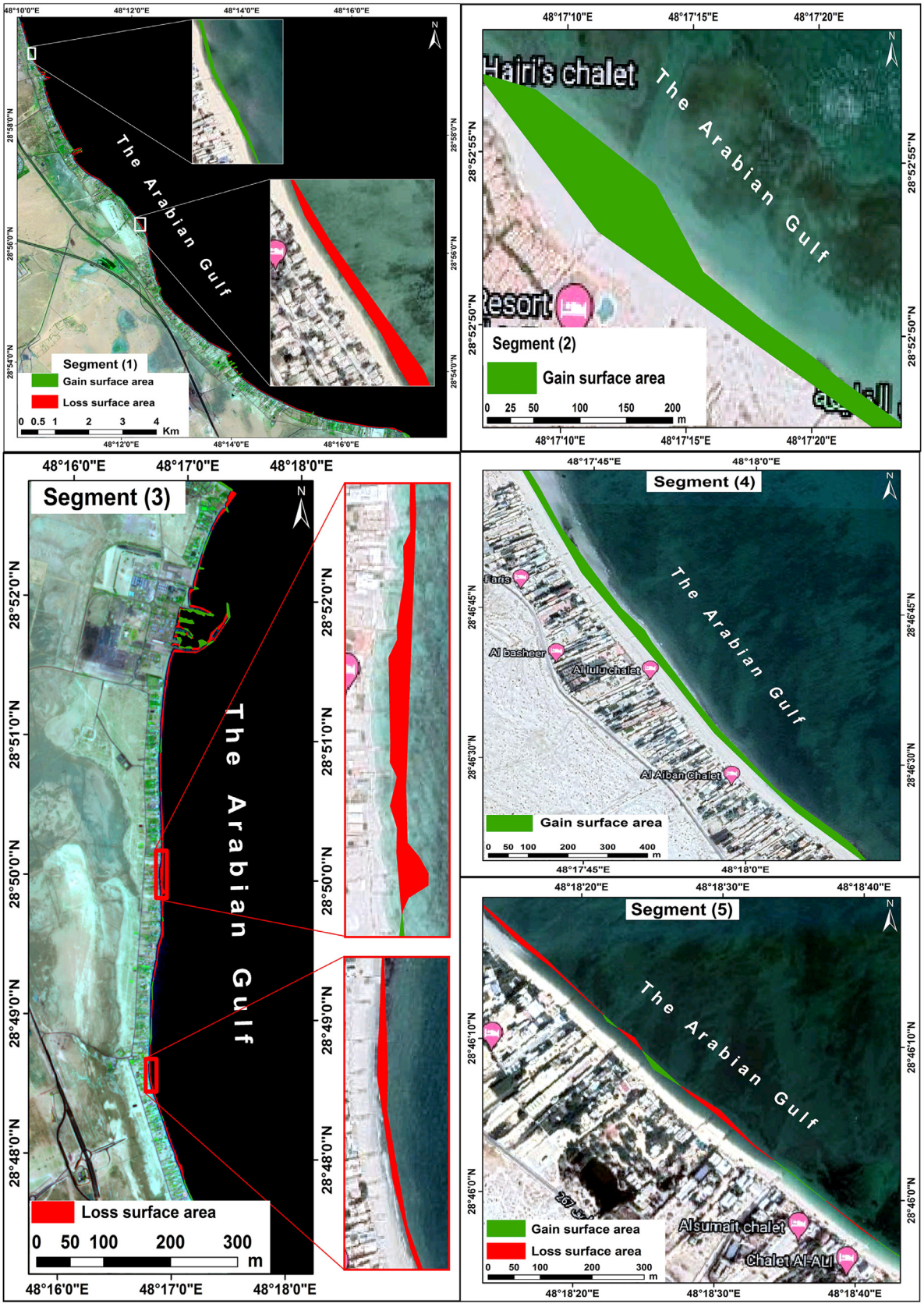

Figure 10 Mapping for gain and loss surfaces in segments from 1 to 5 result from the processes of accumulation and erosion, respectively.

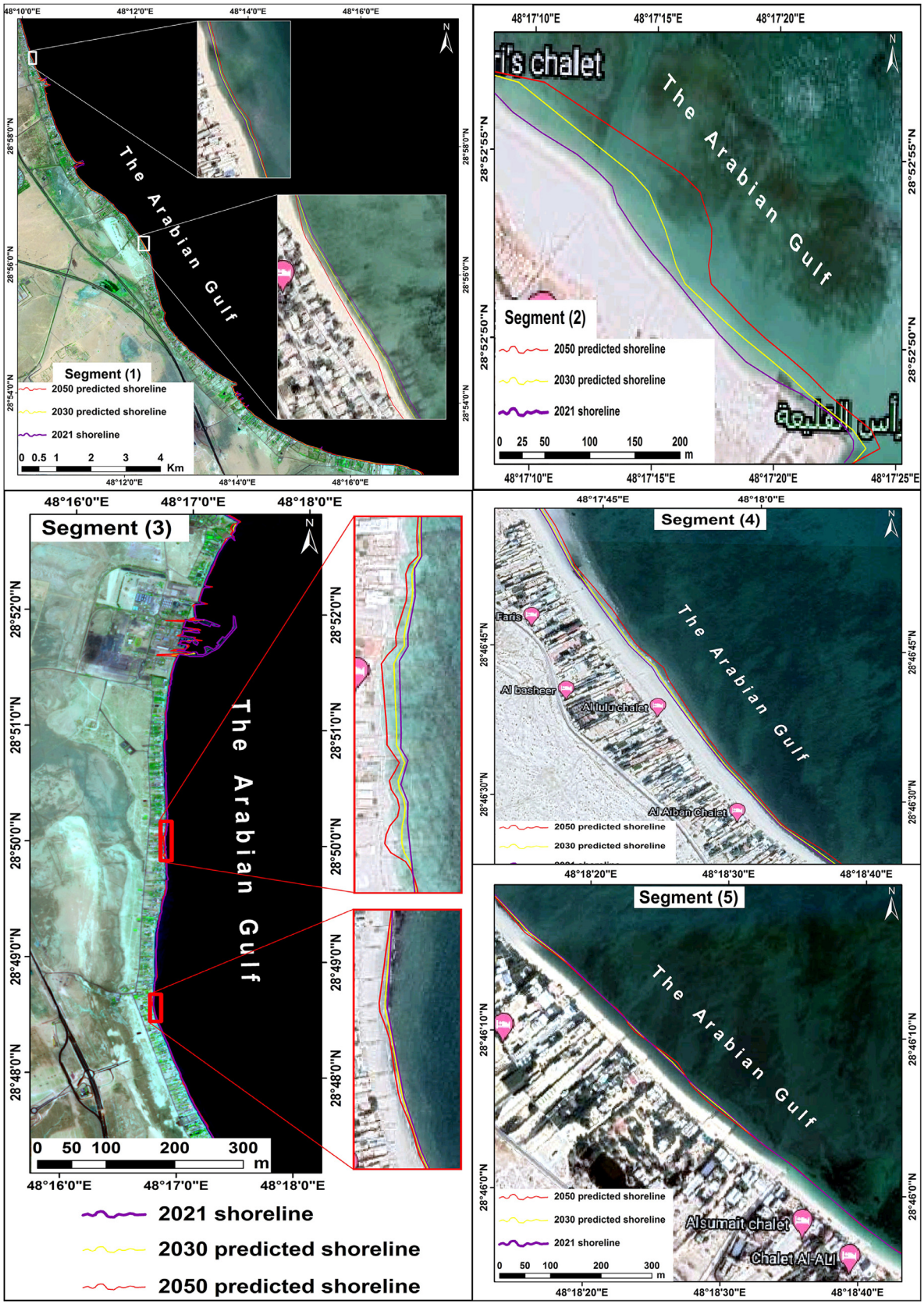

Figure 11 Mapping for the shoreline in segments from 1 to 5: the current shoreline position (2021) with the predicted shoreline positions for 2030 (9 years) and 2050 (29 years).

by many such as Barik et al. (2019) for assessment long-term shoreline changes along the Odisha Coast, and Pardo-Pascual et al. (2012) present a high precision geometric method for automated shoreline detection from Landsat TM and ETM+ imagery. However, what distinguishes this work is that a large part of the beach in the study area was wholly changed geomorphologically during the study period, which is equivalent to Al-Khiran city (see also Žilinskas et al., 2020). The implementers of the Al-Khiran project took complete control of the length of 10 kilometers alongside the city coast. As a result, the model tracks the shoreline change rate which is characterized historically by a high level of erosion and accretion and expected to disappear the effects of the erosion and accretion in the future. This is considered proof of the model's success in tracking the impact of human interactions with the environment, which can be used to maintain the course of natural processes affecting the environment.

6. Conclusion

The analysis of shoreline changes over 35 years along the south coast of Kuwait, using GIS and statistical methods, has contributed to a better understanding of the movement mechanism of the sand along the coast by identifying the areas of accretion and erosion. The historical changes in the shoreline were extracted using EPR and LRR models over the studied period and found that the shoreline exhibited alternation between erosion and accretion at various rates. The future predictions of shoreline position revealed that the parts of the coast that will suffer from significant loss by erosion would guide the area management to provide urgent protection for safe future constructions. The study reported the effect of human activity at the southern part of the studied area and its role in shoreline changes by comparing shorelines' historical and future predictions at the segments from 16 to 22, which is equivalent to Al-Khiran city. It found that the constructions of the Al-Khiran project and the associated infrastructure that extended to the sea will vanish the high rate of accretion and erosion along this area. The automated EPR model report that the area of the coast that extends alongside the human facilities gave up the natural high gain and loss in the last decade, at the beginning of the Al-Khiran project. The results of this study are significant for obtaining that the automated EPR and LRR models can trace the effect of human activities on the coasts. This approach will help map the best scenario for the sustainable development of coasts and obtaining the areas will have negative implications for tourism due to the loss of beaches. This approach can be applied in different regions around the world that have the same development history to show the response of the resulting model to human interventions in changing the topography of beaches.

Declaration of competing interest

No known competing financial interests or personal relationships could have influenced the work reported in this paper. Finally, this paper is not considered for publishing elsewhere.

Supplementary materials

Supplementary material associated with this article can be found, in the online version, at https://doi.org/10.1016/j.oceano.2022.02.002.

References

Alizadeh, M.J., Alinejad-Tabrizi, T., Kavianpour, M.R., Shamshirband, S., 2020. Projection of spatiotemporal variability of wave power in the Persian Gulf by the end of 21st century: GCM and CORDEX ensemble. J. Cleaner Prod. 256, 120400. https://doi.org/10.1016/j.jclepro.2020.120400

Atiquzzaman, M., Kandasamy, J., 2015. Prediction of hydrological time-series using extreme learning machine. J. Hydroinf. 18 (2), 345—353. https://doi.org/10.2166/hydro.2015.020

Boak, E.H., Turner, I.L., 2005. Shoreline definition and detection: a review. J. Coast Res. 21 (4), 688—703. https://doi.org/10.2112/03-0071.1

Barik, K.K., Annaduari, R., Mohanty, P.C., Mahendra, R.S., Tripathy, J.K., Mitra, D., 2019. Statistical assessment of long-term shoreline changes along the Odisha coast. Indian J. Geo Mar. Sci. 48 (12), 1990—1998.

Deepika, B., Avinash, K., Jayappa, K.S., 2014. Shoreline change rate estimation and its forecast: remote sensing, geographical information system and statistics-based approach. Int. J. Environ. Sci. Technol. 11, 395—416. https://doi.org/10.1007/s13762-013-0196-1

Ding, Y., Wang, S.S.Y., 2008. Development and application of a coastal and estuarine morphological process modeling system. J. Coast Res. 52, 127—140. https://doi.org/10.2112/1551-5036-52.sp1.127

Esmail, M., Mahmod, W.E., Fatha, H., 2019. Assessment and prediction of shoreline change using multi-temporal satellite images and statistics: a case study of Damietta coast. Egypt. Appl. Ocean Res. 82, 274—282. https://doi.org/10.1016/j. apor.2018.11.009

Fenster, M.S., Dolan, R., Elder, J.F., 1993. A new method for predicting shoreline positions from historical data. J. Coast Res. 9 (1), 147—171.

Fisher, A., Flood, N., Danaher, T., 2016. Comparing Landsat water index methods for automated water classification in eastern Australia. Rem. Sens. Environ. 175, 167—182. https://doi.org/10.1016/j.rse.2015.12.055

Frihy, O.E., 2009. Morphodynamic implications for shoreline management of the western Mediterranean sector of Egypt. Environ. Geol. 58, 1177—1189. https://doi.org/10.1007/s00254-008-1595-3

Gokceoglu, C., Nefeslioglu, H.A., Turer, D., Akgun, A., Ayas, Z., Temimhan, M., 2015. Determination of coastal border line: an integrated approach for a part of Antalya coast (Turkey). Arab. J. Geosci. 8, 1145—1154. https://doi.org/10.1007/s12517-014-1287-0

Goharnejad, H., Nikaein, E., Perrie, W., 2021. Assessment of wave energy in the Persian Gulf: An evaluation of the impacts of climate change. Oceanologia 63 (1), 27—39. https://doi.org/10.1016/j.oceano.2020.09.004

Hakkou, M., Maanan, M., Belrhaba, T., El khalidi, K., El Ouai, D., Benmohammadi, A., 2018. Multi-decadal assessment of shoreline changes using geospatial tools and automatic computation in Kenitra coast. Morocco. Ocean Coast Manage. 163, 232—239. https://doi.org/10.1016/j.ocecoaman.2018.07.003

Hassan, A., 2018. The Environmental Geomorphological Assessment of the Urban Expansion in Al-Khiran Marine City. Kuwait. J. Social Sci. 46 (1), 31—54.

Hassan, A., 2016. Human encroachments and their environmental geomorphological effects on the sustainable development for coastal areas in Kuwait. Ph.D. thesis, Geograph. Dep., Faculty of Social Sciences, Kuwait University.

Huang, C., Wu, M., Sun, W., Bian, G., He, J., Deng, K., Zhai, G., 2019. Improving the definition and algorithms of China's coastline considering the diversity of tidal characteristics. Mar. Geodes. 42 (4), 382—405. https://doi.org/10.1080/01490419.2019.1610816

Kanwal, S., Ding, X., Sajjad, M., Abbas, S., 2020. Three decades of coastal changes in Sindh, Pakistan (1989—2018): a geospatial assessment. Rem. Sens. 12 (1), 8. https://doi.org/10.3390/rs12010008

Khalaf, F.I., Gharib, I.M., Al-Hashash, M.Z., 1984. Types and characteristics of the recent surface deposits of Kuwait, Arabian Gulf. J. Arid Environ. 7, 9—33.

Kumar, A., Jayappa, K.S., 2009. Long and short-term shoreline changes along Mangalore coast. India. Int. J. Environ. Res. 3, 177—188.

Masek, J.G., Vermote, E.F., Saleous, N.E., Wolfe, R., Hall, F.G., Huemmrich, K.F., Gao, F., Kutler, J., Lim, T., 2006. A Landsat surface reflectance dataset for North America, 1990—2000. IEEE Geosci. Rem. Sens. Lett. 3, 68—72. https://doi.org/10.1109/LGRS.2005.857030

Moore, L., 2000. Shoreline mapping techniques. J. Coast Res. 16, 111—124 https://www.jstor.org/stable/4300016 (accessed 18 February 2021).

Nandi, S., Ghosh, M., Kundu, A., Dutta, D., Baksi, M., 2016. Shoreline shifting and its prediction using remote sensing and GIS techniques: a case study of Sagar Island, West Bengal (India). J. Coast Conserv. 20, 61—80. https://doi.org/10.1007/s11852- 015-0418-4

Natesan, U., Parthasarathy, A., Vishnunath, R., Kumar, G.E.J., Ferrer, V.A., 2015. Monitoring longterm shoreline changes along Tamil Nadu, India using geospatial techniques. Aquat. Procedia 4, 325—332. https://doi.org/10.1016/j. aqpro.2015.02.044

Nassar, K., Fath, H., Mahmod, W.E., Masria, A., Nadaoka, K., Negm, A., 2018. Automatic detection of shoreline change: case of North Sinai coast. Egypt. J. Coast Conserv. 22, 1057—1083. https://doi.org/10.1007/s11852-018-0613-1

Pardo-Pascual, J.E., Almonacid-Caballer, J., Ruiz, L.A., Palomar-Vázquez, J., 2012. Automatic extraction of shorelines from Landsat TM and ETM+ multi-temporal images with subpixel precision. Remote Sens. Environ. 123, 1—11.

Qiao, G., Mi, H., Wang, W., Tong, X., Li, Z., Li, T., Liu, S., Hong, Y., 2018. 55-year (1960—2015) spatiotemporal shoreline change analysis using historical DISP and Landsat time series data in Shanghai. Int. J. Appl. Earth Obs. Geoinf. 68, 238—251. https://doi.org/10.1016/j.jag.2018.02.009

Rady, A., 2011. Profile of Sustainability in Some Mediterranean Tourism Destinations. Case Studies in Egypt: Marsa Matrouh, Al Alamein, Siwa Oasis (Matrouh Governorate). Final Report. UNEP/MAP Regional Activity Centre, Plan Bleu, Sophia Antipolis.

Rakha, K., Al-Salem, K., Neelamani, S., 2007. Hydrodynamic atlas for the Arabian Gulf. J. Cost. Res. 550—554.

Ruiz-Beltran, A.P., Astorga-Moar, A., Salles, P., Appendini, C.M., 2019. Short-term shoreline trend detection patterns using SPOT-5 image fusion in the northwest of Yucatan. Mexico. Estuar. Coast 42, 1761—1773. https://doi.org/10.1007/s12237-019-00573-7

Salmon, C., Duvat, V.K.E., Laurent, V., 2019. Human- and climate-driven shoreline changes on a remote mountainous tropical Pacific island: Tubuai, French Polynesia. Anthropocene 25, 100191. https://doi.org/10.1016/J.ANCENE.2019.100191

Taebi, S., Golshani, A., Chegini, V., 2008. An approach towards wave climate study in The Persian Gulf and the Gulf of Oman: simulation and validation 11—26.

Tong, K., Granat, M., 1999. A practical gait analysis system using gyroscopes. Med. Eng. Phys. 21, 87—94. https://doi.org/10.1016/S1350-4533(99)00030-2

Thieler, E.R., Himmelstoss, E.A., Zichichi, J.L., Ayhan, E., 2009. Digital Shoreline Analysis System (DSAS) Version 4.0 (Updated for Version 4.3) — an ArcGIS Extension for Calculating Shoreline Change: U.S. Geological Survey. Open-File Report 2008—1278. https://cmgds.marine.usgs.gov/publications/DSAS/of20081278/data/DSASv4_3.pdf (accessed 21 July 2020).

Vermote, E., Justice, C., Claverie, M., Franch, B., 2016. Preliminary analysis of the performance of the Landsat 8/OLI land surface reflectance product. Rem. Sens. Environ. 185, 46—56. https://doi.org/10.1016/j.rse.2016.04.008

Vieira, F., Cavalcante, G., Campos, E., 2020. Analysis of wave climate and trends in a semi-enclosed basin (Persian Gulf) using a validated SWAN model. Ocean Eng. 196, 106821. https://doi.org/10.1016/j.oceaneng.2019.106821

Žilinskas, G., Janušaitė, R., Jarmalavičius, D., Pupienis, D., 2020. The impact of Klaipėda Port entrance channel dredging on the dynamics of coastal zone. Lithuania. Oceanologia 62 (4A), 489—500. https://doi.org/10.1016/j.oceano.2020.08.002

Oceanologia 64 (2022) 433—444

Available online at www.sciencedirect.com

ScienceDirect

journal homepage: www.journals.elsevier.com/oceanologia

ORIGINAL RESEARCH ARTICLE

Distribution of benthic macroinvertebrates across a reed stand in a brackish Baltic lagoon

Krzysztof Pawlikowski*, **Ryszard Kornijów**

National Marine Fisheries Research Institute, Gdynia, Poland

Received 12 October 2021; accepted 21 February 2022
Available online 7 March 2022

KEYWORDS
Vistula Lagoon;
Littoral zone;
Zoobenthos;
Trophic guilds;
Macrophytes

Abstract The role of reeds in the functioning of ecosystems and their significance for zoobenthos in the coastal lagoons is poorly understood. We hypothesise that next to the spatial zonal differentiation of abiotic factors in the apparently homogeneous habitat of reeds, benthic macroinvertebrate fauna is also unevenly distributed, and differs in taxonomic and functional diversity, as well as density and biomass across the reed stand. The research was carried out in the Vistula Lagoon (southern Baltic) along three designated sectors arranged parallel to the shoreline and differing in distance from the shore and depth. Mean density of reed stems in the analysed stand was within the range of values reported from different American and European wetlands. Regardless of the location within the reeds and the season, the fauna was dominated by detritivorous Tubificinae and larvae of Chironomidae. The highest diversity, density, and biomass of fauna were found in the middle littoral zone, and the lowest in the outer zone adjacent to the open water. The presented data support our hypothesis predicting the existence of a spatial variation pattern in the composition and distribution of macroinvertebrates in response to the changing zonal habitat conditions within the reed stand.

1. Introduction

Common reed, *Phragmites australis* (Cav.) Trin. ex Steud, is believed to be one of the most widespread riparian plants in a wide range of wetland habitats worldwide. Although the common reed is considered a freshwater species (Ostendorp, 1993), it is well adapted to brackish water conditions (Karstens et al., 2019; Lissner and Schierup, 1997). The plant is considered native to Europe. Beyond the continent, it is often treated as an invasive species (Swearingen and Saltonstall, 2012). There-

* Corresponding author at: National Marine Fisheries Research Institute, Kołłątaja 1, 81—332 Gdynia, Poland.
E-mail address: kpawlikowski@mir.gdynia.pl (K. Pawlikowski).
Peer review under the responsibility of the Institute of Oceanology of the Polish Academy of Sciences.

Production and hosting by Elsevier

https://doi.org/10.1016/j.oceano.2022.02.004

fore, depending on where the reed occurs, its environmental significance and role in wetland vegetation communities may be perceived differently (Gabriel and Bodensteiner, 2011). European literature emphasises the multiple ecosystem functions and services of reeds (Karstens et al., 2019; Mancinelli et al., 2005; Okun and Mehner, 2005; Pawlikowski and Kornijów, 2019). They constitute feeding and breeding places, shape habitat conditions, and determine sediment and water quality for animals and other plants. They also play a role in matter circulation, damp wave energy, and stabilise bottom sediments and banks. In countries where the reed has emerged as an invasive species, particularly in disturbed habitats, its rapid rate of colonisation and tendency to replace other plant and animal species is often considered a nuisance, negatively affecting local biodiversity (Gabriel and Bodensteiner, 2011; Warren et al., 2001). In both cases, however, although for a different reason, it is important to know the role of reeds in the functioning of ecosystems and their significance as a habitat for other organisms. As pointed out by Ostendorp (1993), the latter issue is barely investigated. This is especially true of benthic macroinvertebrates living in sediments overgrown by reeds. One of the reasons could be methodological difficulties in sampling bottom sediments among the tangle of roots and rhizomes (Moss, 1998). The most frequently used methods of sampling include sweeping by hand nets, or collecting a littoral section together with sediments and macrophytes by means of e.g. Surber, Wisconsin, Macan, or Ekman box-samplers (Arnold and Ormerod, 1997; Fell et al., 1998; James et al., 1998; Jayawardana et al., 2006; Jayawardana and Westbrooke, 2010; Miler et al., 2018; Olson et al., 1995; Sychra et al., 2010). Various types of traps are also sometimes used (Fell et al., 1998; Oertli, 1995; Raichel et al., 2003). While such studies provide valuable insight into the general diversity of macroinvertebrates within a stand, they do not reflect the real distribution and quantitative proportions between various invertebrate communities with their distinctive feeding behaviour and diet, such as sediment-living, plant-associated, and free-swimming animals (Moss, 1998). Consequently, such data offer little information on the relationships and drivers that potentially structure truly benthic communities, i.e. those inhabiting bottom sediments. Moreover, the use of different sampling approaches makes it difficult to compare results and draw general conclusions.

Only several papers employ quantitative methods that take into account selective sampling of sediments and, importantly, sampling to a known depth (Cardinale et al., 1998; Kornijów and Gulati, 1992; Okun and Mehner, 2005; Yozzo and Osgood, 2013). These publications focus on benthic invertebrates in reed beds of lakes or rivers. Coastal wetlands have not yet been subject to similar research. The purpose of this work is to fill this gap, and to find a pattern in the distribution of benthic macroinvertebrates within the reed stand.

The structure and processes in lagoon environments are primarily maintained by physical forces, including wave action that can be mediated by dense patches of emergent macrophytes such as reeds (Karstens et al., 2019; Kornijów, 2018; Pawlikowski and Kornijów, 2019; Perez-Ruzafa et al., 2011; Viaroli et al., 1996). This can lead to a spatial gradient of organic matter content in the sediments, and through the consumption of oxygen in decaying processes, also of water oxygenation. The research on abiotic factors in the reeds of the Vistula Lagoon in fact showed low oxygenation of water in the near-shore zone compared to the middle and peripheral part of the patch, adjacent to the open water zone. On the one hand, that was most likely due to the horizontal distribution of sediment organic matter, and on the other hand due to a different rate of water exchange with the pelagic zone (Pawlikowski and Kornijów, 2019). Similar horizontal zonation of oxygen conditions, and other physical and chemical properties of water or sediment, such as pH or salinity within stands of emergent vegetation, were found in various aquatic ecosystems. This suggests the universal character of the phenomenon (Dvorak, 1970; Howard-Williams and Lenton, 1975; Kłosowski, 1992; Suzuki et al., 1995). However, there are exceptions, e.g. water throughout the stand of emergent vegetation in Lake Huron was typically supersaturated with dissolved oxygen, and there was never any evidence of anoxia (Cardinale et al., 1997).

It can be assumed that due to the spatial zonal differentiation of abiotic factors in the apparently homogeneous habitat of reeds, also benthic macroinvertebrate fauna is not evenly distributed, and differs across the reed stand in terms of taxonomy and functional diversity, as well as density and biomass. In order to verify this hypothesis, we carried out seasonal research in the Vistula Lagoon — one of the most important and well-known ecosystems in the southern Baltic coast with extensive reed beds (Karstens et al., 2019).

2. Material and methods

2.1. Study site

The Vistula Lagoon is a brackish coastal lagoon adjacent to the Gulf of Gdansk of the Baltic Sea. The lagoon has a surface area of 838 km^2, including 328 km^2 on the Polish side of the border. The Vistula Lagoon is shallow, with a depth not exceeding 5.2 m in the Russian, and 4 m in the Polish part. The hydrological dynamics of the waters of the lagoon are determined by the inflow of freshwater masses from its extensive catchment area, mixed with salty water inflowing from the Gulf of Gdańsk through the Baltiysk Strait. Salinity varies from 0 to 6.5 PSU. No tides occur, although wind action causes daily water level fluctuations reaching 1 m. The concentrations of total nitrogen and phosphorus in water are high, reaching 1.1—4.4 mg dm^{-3} and 0.06—0.19 mg dm^{-3}, respectively. The most frequently recorded water transparency, measured as Secchi disc depth, fluctuates around 40 cm (Kornijów, 2018). Bottom sediments are primarily composed of silt and sand (Zachowicz, 1985). The lagoon is very productive, with advanced eutrophic processes (Kownacka et al., 2020). It is influenced by both maritime and continental climates, with ice cover persisting for several days in mild winters, and from December until March in the coldest years (Herman, 2018).

The research was conducted in a reed patch with a length of 200 m and width of approximately 60 m (54.33360°N, 19.54700°E), located approximately 2 km north-east of the

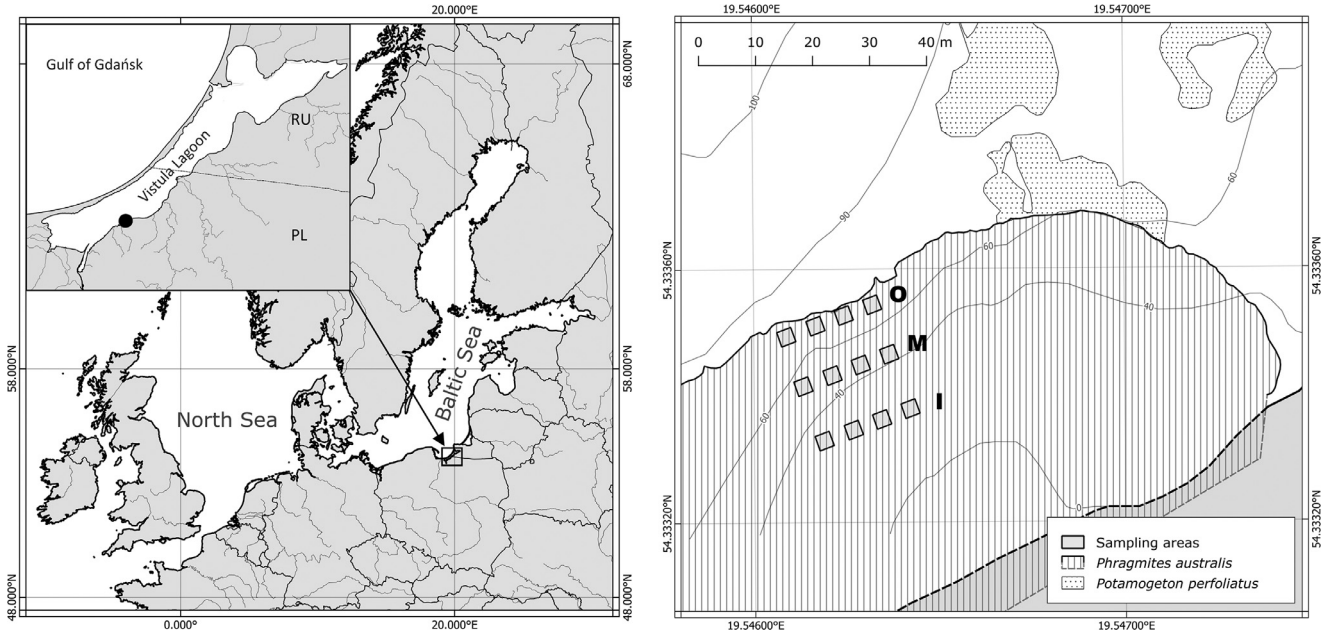

Figure 1 Location of the study area on the map of Northern Europe (left side, marked with a dot). On the right side — detailed map of the analysed reed stand in the Vistula Lagoon. Note that the coastline was drawn conventionally — its range varied as the water level changed. Depths are expressed in centimetres. I — inner zone, M — middle zone, O — outer zone. GIS layers sources for the map of Northern Europe: Europe coastline and rivers: Natural Earth (2020); Country borderlines: NOAA GSHHG (2014); Polish coastline: SIPAM (2020) simplified; Rivers of Vistula Lagoon catchment: OpenStreetMap (2021) modified; Coastline of the Russian part of the Vistula Lagoon: digitized scanned map from Domnin and Chubarenko (2008).

municipality of Tolkmicko at the southern shore of the lagoon (Figure 1). No local changes resulting from human activity such as shoreline alteration were recorded which could potentially interfere with the obtained results (Brauns et al., 2007; Miler et al., 2013). Growth of the macrophytes was seasonal, with regeneration from rhizomes after winter ice-scour. Seasonal changes in reed density involved a gradual increase in the number of stems during the vegetative season, lasting from April until October. The highest and spatially relatively even values of reed density (132—158 stems m^{-2}) in the analysed patch were observed in late summer (Pawlikowski and Kornijów, 2019).

Measurements of physico-chemical properties conducted in 2011 revealed no trends in salinity across the stand (Pawlikowski and Kornijów, 2019). Water oxygenation at the time was generally lower in the near-shore area than in the periphery adjacent to open water. The opposite pattern was observed for water temperature. Water level fluctuations were characterized by high dynamics, with an amplitude of approximately 40 cm (Pawlikowski and Kornijów, 2019).

2.2. Field survey and laboratory analyses

The study was conducted in spring (April), summer (August), and autumn (October) 2011. The width of the analysed reed stand exceeded 60 m, but the sampling area covered a much smaller strip (approx. 30 m wide) due to the shallow depth in the near-shore area and strong water fluctuations. Samples from the reed stand were collected along three designated sectors arranged parallel to the shoreline, at a distance of around 10 m from one another, differing in depth and distance from the shore, depending on geographic distribution and changing water level: inner (depth 0—40 cm, distance from the shore of approximately 30—40 m), middle (depth 40—60 cm, distance from the shore of 40—50 m), and outer (depth 60—90 cm, distance from the shore of 50—60 m) (Figure 1).

Four sampling locations, each of approximately 9 m^2 and spaced 3 m from one another, were established in each sector, referred to as zones. In each sampling location, 3 pooled sediment cores were collected by means of a transparent acrylic tube (length 1.5 m; diameter 4.4 cm) closed from the top with a stopper. In our opinion, the sampler used is appropriate not only for the sampling of sedentary invertebrates, but also for mobile gammarids, and even free-living mysids in turbid lagoon water (Linkowski et al., 2021). The tube was pushed into the bottom to a depth of 25 cm. No fauna occurred deeper in the sediment, as suggested by studies on the vertical distribution of macroinvertebrates in sediments (Pawlikowski and Kornijów, 2022). A total of 36 samples consisting of 108 sediment cores were collected on all sampling occasions. Each sample was washed separately through a net with 0.3 mm mesh size, and transported to the laboratory in plastic containers with no water. We chose such fine mesh to provide accurate community and population estimates given the relatively small size of macro-invertebrates living in estuarine and lagoon ecosystems (Schlacher and Wooldridge, 1996). Invertebrates were sorted live by hand on a white tray filled with water, and preserved with 4% formaldehyde solution. Oligochaeta were treated with Amman's lactophenol solution, and Chironomidae larvae with Faure liquid, and identified to the lowest possible taxon according to Timm (1999) and Andersen et al. (2013), respectively. The nomenclature of Naididae was adopted after

WoRMS (2021). Macrobenthic taxa were assigned to trophic groups based on food preferences documented in the literature (Armitage et al., 1995; Pellan et al. 2016; Savage, 1982; Vaughn, 1982). Categorisation of macroinvertebrates into groups allows a better understanding of the processes of the material cycle and ecosystem function (Cummins, 1973).

Measurements of reed density were carried out in 10 random 0.5 × 0.5 m quadrats within each location, expressed as the number of shoots per square meter and averaged (Pawlikowski and Kornijów, 2019).

Granulometric analyses involved the collection of additional sediment cores with a length of 25 cm in each sampling location in August. The collected sediments were dried and manually ground in a mortar, and then sieved on a set of geological sieves with a mesh of 2 mm, 1 mm, 0.5 mm, 0.25 mm, 0.125 mm, and 0.063 mm. The obtained data were processed with the application of GRADISTAT software version 8 (Blott and Pye, 2001). Organic matter content in sediment was determined by the direct method as a mass loss on ignition (LOI) at a temperature of 500°C for 24 hours.

Bathymetric measurements were performed by means of a ranging rod with an accuracy of 1 cm on 2014.09.04. Depth was measured in 154 points with geographic coordinates determined by means of a GPS receiver (Garmin GPSMAP 60CSx). The memory of the receiver also recorded the course of the shoreline (zero depth). The data matrix was loaded to Surfer 10 software in which a detailed bathymetric map of the studied water body was generated by means of the kriging method. The map was then visually processed by means of QGIS software (Figure 1).

Due to unequal variances or non-normal distribution, the following non-parametric statistics were applied:

- Kruskal-Wallis test (H) was applied for the determination of the effect of different locations within the reed patch on the density and biomass of fauna.
- Friedman test (Chi-Square) was applied for the determination of differences in the density and biomass of fauna between sampling occasions.

T-test was applied for the determination of differences in the density of fauna between 2011 and 2013. For this comparison, we used data from 2013 in zone M on the vertical distribution of macroinvertebrates in sediments (Pawlikowski and Kornijów, 2022), obtained in a similar way as in 2011. Statistical calculations were performed by means of Statistica 10 software (StatSoft, 2011).

3. Results

3.1. Zoobenthos

The material showed the presence of 31 taxa belonging to Chironomidae, Naididae, Hirudinea, Chrysomelidae, Amphipoda, Bivalvia, and Nematoda (Table 1). The highest diversity (24 taxa) was determined in the middle littoral zone, and lowest in the outer zone (16 taxa), adjacent to open water. Depending on the season, the diversity of fauna considerably changed in the middle and outer zones and was relatively stable in the inner zone (Figure 2).

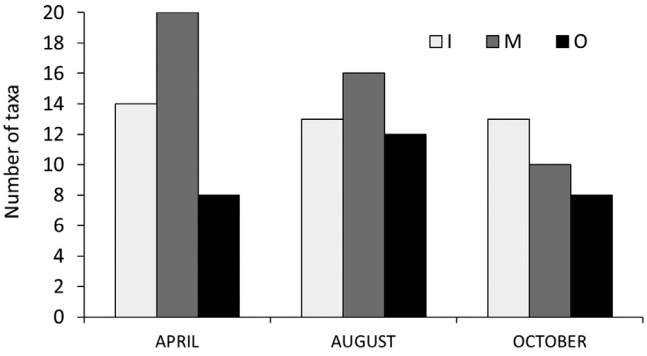

Figure 2 Number of zoobenthos taxa in the inner (I), middle (M), and outer zone (O) of the reed stand in the Vistula Lagoon.

The highest total density of fauna was reached in spring and summer in the middle zone (12 057—15 510 ind. m^{-2}), and lowest, irrespective of the season in the outer zone (4 165—4 658 ind. m^{-2}) (Kruskal-Wallis test H (n = 12) = 6.06 and 7.38; p = 0.04 and 0.02, respectively) (Figure 3). Differences in total density between the zones in autumn were at the threshold of significance (Kruskal-Wallis test H (n = 12) = 5.80; p = 0.06).

Biomass values in spring and autumn were the highest in the middle littoral zone (42—107 g ww m^{-2}), and lowest in the outer zone (8—10 g ww m^{-2}) (Kruskal-Wallis test H (n = 12) = 7.73 and 6.73; p = 0.02 and 0.03, respectively). In summer, differences in biomass between the zones were at the threshold of significance (Kruskal-Wallis test H (n = 12) = 5.54; p = 0.06) (Figure 3).

In terms of percent share, irrespective of the location within the reed stand (with the exception of the middle and outer zone in April), Tubificinae usually dominated (46—79%), and among them particularly *Limnodrilus hoffmeisteri* (Figure 4, Table 1). The second group with the most considerable share were Chironomidae (15—76%) larvae with dominant *Glyptotendipes* sp. (Figure 4, Table 1). The proportions of percent shares between the most abundant taxa varied in particular seasons with no discernible patterns.

Next to Chironomidae and Tubificinae (2—51% and 10—73%, respectively), the biomass contained a high share of Chrysomelidae (*Donacia* sp.) (up to 60%) and Amphipoda (1—42%) (Figure 4). Their contribution varied depending on the study term: in April, the majority of sites were dominated by larvae of *Donacia* sp. (up to 60%) and Chironomidae (22—51%), in August Tubificinae (48—73%) and *Donacia* sp. (23—30%), and in October Amphipoda (up to 42%) and Tubificinae (37—56%).

A large majority of the recorded taxa belonged to detritivores, constituting more than 58% of the fauna abundance (Table 1, Figure 5). The second major trophic group were omnivores constituting up to 34% of the fauna abundance. The percent share of particular trophic groups varied depending on the season and zone. A considerable share of herbivores was observed in spring in the middle zone, and a clear increase in omnivores in summer and autumn in the middle and outer zones.

For the purpose of verification of the stability of benthic communities in the reed belt, their abundances were compared in zone M in 2011 and 2013 (Figure 6). In the second year of the study, the density of zoobenthos was more than

Table 1 Density [ind. m^{-2}] of zoobenthos in the inner (I), middle (M), and outer (O) zones of the reed stand in the Vistula Lagoon in 2011. DETR – detritivores, CARN – carnivores, HERB – herbivores, OMNI – omnivores, n. d. – not determined. Mean values ± SE (Standard Error).

	Taxa	Trophic group	I	M	O
NAIDIDAE					
TUBIFICINAE					
	n. det. without hair chaetae (juvenile or damaged), probably *Limnodrilus* sp.	DETR	3 416 ± 591	5 974 ± 1 463	1 206 ± 346
	n. det. with hair chaetae (juvenile or damaged), probably: *Tubifex* sp., *Potamothrix* sp., *Psammoryctides* sp.	DETR	786 ± 397	877 ± 124	55 ± 39
	Tubifex tubifex (Müller)	DETR	219 ± 127	110 ± 63	0 ± 0
	Limnodrilus hoffmeisteri Clapar.	DETR	1 151 ± 443	347 ± 103	420 ± 116
	Limnodrilus claparedeianus Ratz.	DETR	365 ± 199	512 ± 228	18 ± 18
	Limnodrilus profundicola (Verill)	DETR	110 ± 50	128 ± 63	55 ± 39
	Limnodrilus udekemianus Claparède	DETR	37 ± 25	91 ± 74	0 ± 0
	Potamothrix hammoniensis (Mich.)	DETR	0 ± 0	37 ± 37	0 ± 0
	Potamothrix moldaviensis Vejd.	DETR	0 ± 0	55 ± 55	18 ± 18
	Potamothrix heuscheri (Bretscher)	DETR	18 ± 18	146 ± 87	0 ± 0
	Enchytraeidae n. det.	DETR	0 ± 0	37 ± 37	0 ± 0
NAIDINAE					
	Naidinae n. det.	HERB	0 ± 0	18 ± 18	0 ± 0
TOTAL Naididae			**6 102 ± 1 369**	**8 330 ± 1 652**	**1 772 ± 467**
CHIRONOMIDAE					
	Chironomus sp.	DETR	475 ± 117	183 ± 59	18 ± 18
	Glyptotendipes sp.	DETR	694 ± 134	2 503 ± 454	475 ± 299
	Dicrotendipes sp.	DETR	110 ± 43	91 ± 50	274 ± 90
	Polypedilum scalaneum (Schr.)	DETR	37 ± 25	37 ± 25	0 ± 0
	Cladotanytarsus mancus (Walker)	DETR	18 ± 18	347 ± 128	457 ± 305
	Microchironomus tener (Kieff.)	DETR	0 ± 0	0 ± 0	37 ± 25
	Endochironomus albipennis (Mg.)	DETR	0 ± 0	18 ± 18	0 ± 0
	Parachironomus varus (Goetgh.)	CARN	0 ± 0	0 ± 0	37 ± 37
	Cryptochironomus sp.	CARN	55 ± 29	292 ± 102	201 ± 69
	Procladius sp.	CARN	37 ± 25	73 ± 31	18 ± 18
	Orthocladiinae n. det.	HERB	0 ± 0	0 ± 0	18 ± 18

(*continued on next page*)

Table 1 (*continued*)

	Taxa	Trophic group	I	M	O
TOTAL Chironomidae			**1 425 ± 234**	**3 544 ± 536**	**1 535 ± 567**
CRUSTACEA, MALACOSTRACA					
	Gammaridae n. det. (probably: *G. tigrinus* and *G. duebeni*)	OMNI	201 ± 87	1 754 ± 370	1 005 ± 341
	Asellus sp.	DETR	0 ± 0	37 ± 25	0 ± 0
INSECTA, CHRYSOMELIDAE					
	Donacia sp.	HERB	183 ± 53	457 ± 227	37 ± 25
HIRUDINEA					
	Hirudinea n. det.	CARN	37 ± 37	0 ± 0	0 ± 0
BIVALVIA					
	Dreissena polymorpha (Pallas)	DETR	18 ± 18	37 ± 37	55 ± 39
OTHERS					
	Diptera larvae n. det.	n. d.	91 ± 57	55 ± 39	0 ± 0
	Nematoda n. det.	DETR	18 ± 18	37 ± 25	0 ± 0
TOTAL DENSITY			**8 075 ± 1 449**	**14 249 ± 1 449**	**4 403 ± 811**
NUMBER OF TAXA			**19**	**24**	**16**

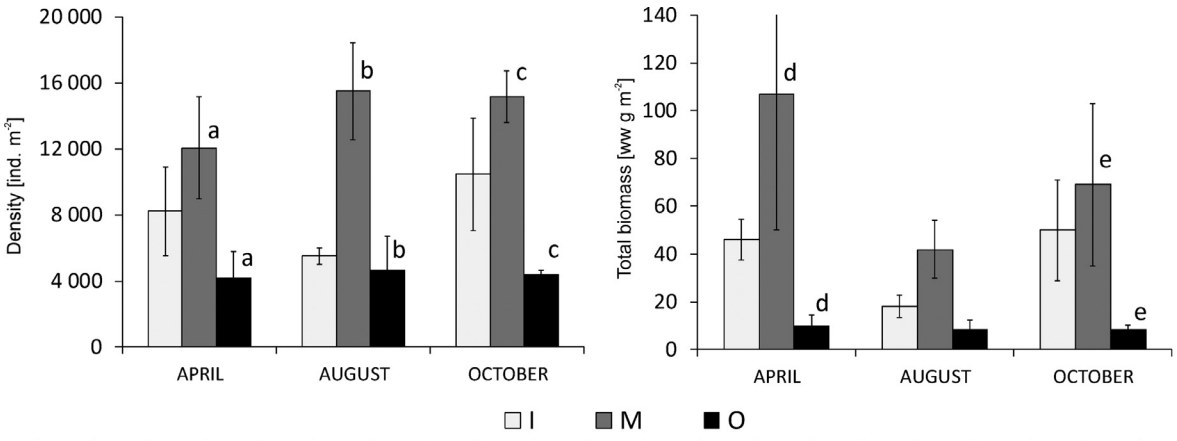

Figure 3 Density [ind. m^{-2}] and total biomass [ww g m^{-2}] of zoobenthos in the inner (I), middle (M), and outer zone (O) of the reed stand in the Vistula Lagoon. Small letters denote significant difference (Post-hoc Kruskal-Wallis test, $p < 0.05$) between areas marked with the same letter. No letter aside bar means no significant difference in density or biomass. Whiskers denote Standard Error.

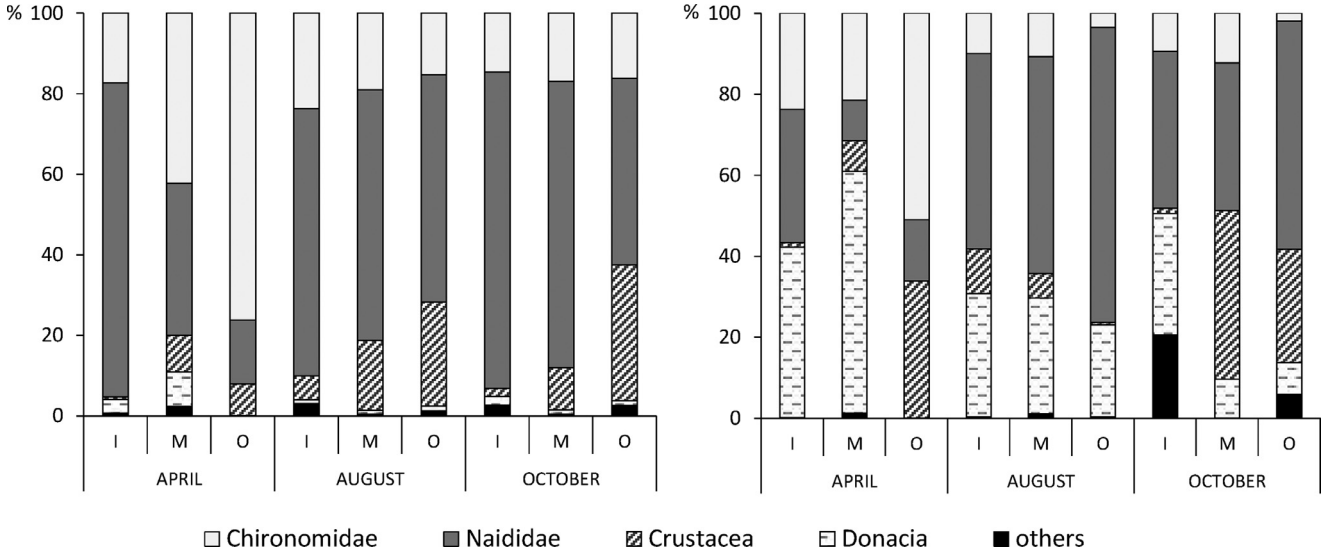

Figure 4 Percent share of the main groups of taxa in total density (left) and total biomass (right) of zoobenthos in the inner (I), middle (M), and outer zone (O) of the reed stand in the Vistula Lagoon.

twice higher (test $t = -3.12$; $p = 0.004$). The quantitative proportions between groups did not change, with evident dominance of Tubificinae and Chironomidae in both years.

3.2. Sediments

Reed grew on sandy-muddy sediments (textural group: slightly gravelly muddy sand) (Table 2). In the inner zone, fine muddy fractions were considerably more abundant (17.4%) than in the middle and outer zones located further from the shore (11.3% and 11.7%, respectively). A similar pattern was recorded in reference to the content of organic matter in the sediment (Table 2).

Table 2 Characteristics of sediments in the inner (I), middle (M), and outer (O) zones of the reed stand in the Vistula Lagoon. LOI — organic matter determined as loss on ignition.

	I	M	O
gravel	0.1%	0.3%	0.5%
sand	82.5%	88.4%	87.7%
mud	17.4%	11.3%	11.7%
LOI	3.1%	1.3%	1.1%

4. Discussion

The diversity of macroinvertebrates found in the lagoon's reed stand was much higher (31 taxa) than that in the open water central part of the lagoon, where only 6 taxa were reported (Kornijów et al., 2021b). It was, however, still much lower than in the littoral of freshwater ecosystems, where many other groups not found in the Vistula Lagoon inhabit the sediments, e.g. Odonata, Ephemeroptera, Trichoptera, Ceratopogonidae, and Gastropoda (Arnold and

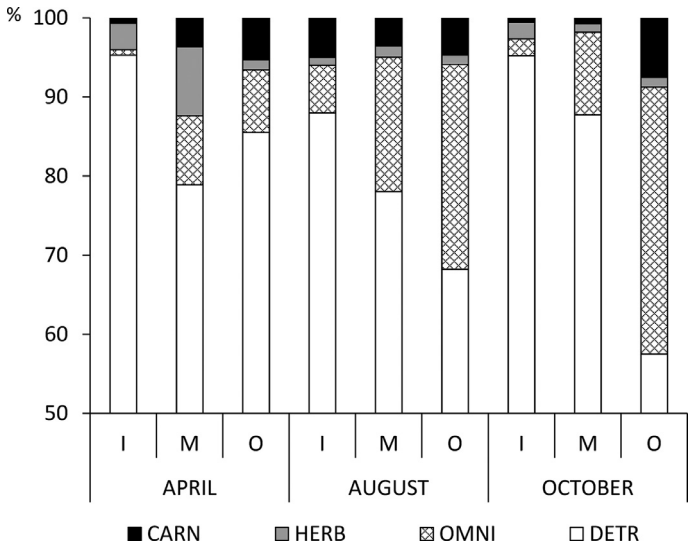

Figure 5 Percent share of particular trophic groups in the total abundance of zoobenthos in the inner (I), middle (M), and outer zone (O). DETR — detritivores, CARN — carnivores, HERB — herbivores, OMNI — omnivores. Note: Y-axis truncated to 50—100% range for clarity.

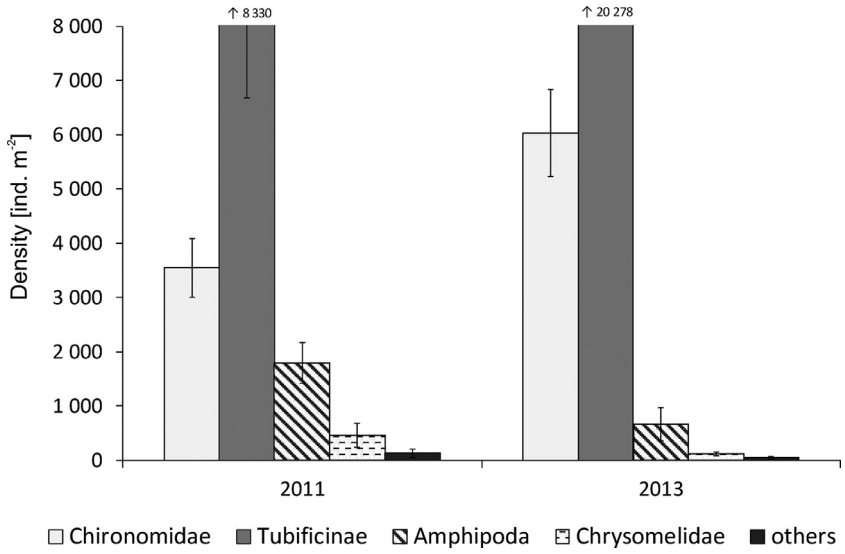

Figure 6 Density [ind. m^{-2}] of the most abundant groups of zoobenthos in the middle zone in 2011 and 2013. The values are means for three sampling occasions. Whiskers denote Standard Error.

Ormerod, 1997; Cardinale et al., 1998; James et al., 1998; Kornijów et al., 2010; Kornijów and Gulati, 1992; Sychra et al., 2010; Yozzo and Osgood, 2013). The reason for this might be elevated salinity which adversely affects some freshwater invertebrates (Arnold and Ormerod, 1997; Brucet et al., 2012; Kornijów et al., 2021a).

In both habitats of the lagoon, namely the littoral and open waters, Tubificinae and chironomid larvae showed the highest abundance. In the reed stand, Tubificinae were dominated by *L. hoffmeisteri*, like in the central part of the lagoon. *Potamothrix hammoniensis*, very abundant in the central part, barely marked its presence in the littoral. Among Chironomidae, the larvae of *Glyptotendipes* sp. were the most abundant in the littoral. As typical dwellers of sediments overgrown with vegetation (Kornijów and Gulati, 1992; Pinder, 1995), they were not present in the central lagoon, where chironomid larvae were instead dominated by *Chironomus balatonicus* Devai, Wuelker & Scholl (Kornijów et al., 2021b). Mean total density was comparable (2 806—16 269 ind. m^{-2} in the central part vs. 4 165—15 510 ind. m^{-2} in the reed stand). Functional feeding groups were dominated by detritus eaters in both habitats.

In the inner littoral zone, the highest densities were reached by a tubificid *L. hoffmeisteri* and *Chironomus* sp. larvae, known for tolerating oxygen deficits and coexisting under such conditions (Kornijów et al., 2021b). A significant percentage of omnivores (mainly *Gammarus* sp.) and herbivores also occurred. The latter were represented almost exclusively by larvae of the root-piercing beetle *Donacia* sp.

The mean density of reed stems in the analysed stand (132—158 stems m^{-2}) was within the mean range of values (60—250 stems m^{-2}) reported from different wetland European habitats (Haslam, 1973), and corresponded with the top determined values, e.g. in freshwater and brackish ecosystems of the North America (Meyerson et al., 2000). Although the reed zones designated in the Vistula Lagoon were separated by a short distance of approx. 10 m, they differed remarkably in terms of habitat conditions. It particularly concerned afternoon water oxygenation the values of which were proportional to the distance from the shoreline and ranged from 59% (5.4 mg dm^{-3}) to 109% (9.5 mg dm^{-3}) (Pawlikowski and Kornijów, 2019).

The relationship between the oxygen conditions and the diversity and density of bottom fauna, regardless of the type of aquatic environment, is a generally known pattern (Berezina and Golubkov, 2008; Jacobsen, 2020; Maasri et al., 2019; Verberk et al., 2011). It was also evident in our research. The highest diversity, density, and biomass were found in the middle zone, where oxygenation was clearly higher than in the inner near-shore zone. The exception was autumn, when the highest diversity was found in the inner zone. It can be assumed that at low water temperature and at plant density too low to impede water circulation, the oxygenation conditions could be aligned across the reed stand, and oxygenation might be no longer the structuring factor for the occurrence of some, at least less oxygen-demanding taxa (Warfe and Barmuta, 2004). A proportion of Amphipoda, known to be sensitive to hypoxia (Meijering, 1991), in the inner zone remained negligible in autumn. The larvae of *Donacia* sp. which rely on the plant for oxygen (Houlihan, 1969) showed the highest biomass in the inner and middle zones, regardless of the season.

Oxygen shortage can be partially compensated by the release of oxygen by macrophyte roots (Reddy et al., 1990; Sand-Jensen et al., 1982) that may support the development of some benthic macroinvertebrates (Sagova-Mareckova and Kvet, 2002). The process, however, was probably insufficient in the stand studied, particularly in summer under the conditions of increased temperature and drying out of the bottom.

A characteristic feature of the littoral of freshwater ecosystems with periodic hypoxia is the occurrence of a high number of invertebrates that respire atmospheric oxygen, such as pulmonate snails or beetles (Dvorak, 1970). They were, however, not present in the brackish waters of the Vistula Lagoon.

Temporary oxygen shortage in shallow coastal Baltic waters seems to be a common phenomenon not only in the reed stand. It can also be the result of the decomposition of drifting algal mats, leading to a strong depletion of benthic macrofauna (Berezina and Golubkov, 2008; Conley et al., 2011).

In the reed stand, a much higher content of organic matter in the sediments of the inner zone was not accompanied by the highest densities of all detritivores, with the exception of *L. hoffmeisteri* and *Chironomus* sp. The probable reason was the astatic nature of this habitat, associated with periodic drying, and the aforementioned strong fluctuations in oxygenation with periodic hypoxia, favoured by the elevated content of sediment organic matter, and limited water exchange with the open water (Cardinale et al., 1997; Dvorak, 1970; Pawlikowski and Kornijów, 2019).

According to Żbikowski et al. (2021), the occurrence and rate of growth of *L. hoffmeisteri* may be determined by the content of the sand fraction with a diameter of 60—160 μm in mud. Swallowed by worms, it may accelerate digestion and nutrient assimilation. Due to the different classification of sand grain size adopted in this paper, however, we could not verify this theory.

The relatively lowest total density and biomass, as well as the diversity of macroinvertebrates in the outer zone adjacent to the well-oxygenated open water, could have resulted from predation pressure by fish migrating here by day from the free water area in search for refugia from predators (Macneil et al., 1999; Okun et al., 2005). An additional factor might be the instability of the habitat conditions due to the strong and frequent wave action that could not damp by the vegetation sufficiently (Kairesalo, 1983). Interestingly, we found no pattern in terms of distribution of invertebrate predators, as previously pointed out by e.g. Dvorak (1970).

In conclusion, with some minor exceptions, the presented data support our hypothesis predicting the existence of a spatial variation pattern in the composition and distribution of macroinvertebrates in response to the changing zonal habitat conditions within the reed stand.

Our main research program lasted for one year. Therefore, in order to verify the long-term stability of the fauna composition, we repeated the research two years later in the middle zone (Pawlikowski and Kornijów, 2022). We recorded a more than double increase in density, but the proportions between the main faunal components did not change much. This suggests that while the density may fluctuate from year to year, the specificity of the assemblage composition remains relatively constant. Our results are generally in agreement with Cardinale et al. (1998), who claimed that distance from open water may be of primary importance for the spatial distributions of macroinvertebrates throughout coastal emergent vegetation.

Declaration of competing interest

The authors declare that they have no conflicts of interest.

Acknowledgements

The work was conducted as a part of the National Marine Fisheries Research Institute statutory research project P1-3 “Ecology of the Vistula Lagoon Benthos”, supported by the Polish Ministry of Science and Higher Education. The authors wish to thank Ms. Sławomira Gromisz for assistance in Gammaridae identification.

References

Andersen, T., Cranston, P.S., Epler, J.H., 2013. The larvae of Chironomidae (Diptera) of the Holarctic region — Keys and diagnoses. Insect Syst. Evol. Supplement 66, 573 pp.

Armitage, P.D., Cranston, P.S., Pinder, L.C.V., 1995. THE CHIRONOMIDAE. Biology and ecology of non-biting midges. Chapman and Hall, London-Madrid, 447 pp. https://doi.org/10.1007/978-94-011-0715-0.

Arnold, S.L., Ormerod, S.J., 1997. Aquatic macroinvertebrates and environmental gradients in *Phragmites* reedswamps: implications for conservation. Aquat. Conserv. 7 (2), 153—163. https://doi.org/10.1002/(SICI)1099-0755(199706)7:2⟨153::AID-AQC234⟩3.0.CO;2-E

Berezina, N.A., Golubkov, S.M., 2008. Effect of drifting macroalgae *Cladophora glomerata* on benthic community dynamics in the easternmost Baltic Sea. J. Marine Syst. 74, 80—85. https://doi.org/10.1016/j.jmarsys.2008.03.027

Blott, S.J., Pye, K., 2001. GRADISTAT: a grain size distribution and statistics package for the analysis of unconsolidated sediments. Earth Surf. Proc. Land. 26 (11), 1237—1248. https://doi.org/10.1002/esp.261

Brauns, M., Garcia, X.F., Walz, N., Pusch, M.T., 2007. Effects of human shoreline development on littoral macroinvertebrates in lowland lakes. J. Appl. Ecol. 44 (6), 1138—1144. https://doi.org/10.1111/j.1365-2664.2007.01376.x

Brucet, S., Boix, D., Nathansen, L.W., Quintana, X.D., Jensen, E., Balayla, D., Meerhoff, M., Jeppesen, E., 2012. Effects of temperature, salinity and fish in structuring the macroinvertebrate community in shallow lakes: Implications for effects of climate change. Plos One 7 (2), 1—11. https://doi.org/10.1371/journal.pone.0030877

Cardinale, B.J., Brady, V.J., Burton, T.M., 1998. Changes in the abundance and diversity of coastal wetland fauna from the open water/macrophyte edge towards shore. Wetl. Ecol. Manag. 6 (1), 59—68. https://doi.org/10.1023/a:1008447705647

Cardinale, B.J., Burton, T.M., Brady, V.J., 1997. The community dynamics of epiphytic midge larvae across the pelagic-littoral interface: do animals respond to changes in the abiotic environment? Can. J. Fish. Aquat. Sci. 54 (10), 2314—2322. https://doi.org/10.1139/cjfas-54-10-2314

Conley, D.J., Carstensen, J., Aigars, J., Axe, P., Bonsdorff, E., Eremina, T., Haahti, B.M., Humborg, C., Jonsson, P., Kotta, J., Lannegren, C., Larsson, U., Maximov, A., Medina, M.R., Lysiak-Pastuszak, E., Remeikaite-Nikiene, N., Walve, J., Wilhelms, S., Zillen, L., 2011. Hypoxia is increasing in the coastal zone of the Baltic Sea. Environ. Sci. Technol. 45, 6777—6783. https://doi.org/10.1021/es201212r

Cummins, K.W., 1973. Trophic relations of aquatic insects. Annu. Rev. Entomol. 18, 183—206. https://doi.org/10.1146/annurev.en.18.010173.001151

Domnin, D.A., Chubarenko, B.V., 2008. Watershed and administrative division of the Kaliningrad Oblast. In: Chubarenko, B. (Ed.), Transboundary waters and basins in the South-East Baltic. Terra Baltica, Russ. Acad. Sci., P.P. Shirshov Inst. Oceanol., Atlantic Branch, Kaliningrad, 306 pp.

Dvorak, J., 1970. Horizontal zonation of macrovegetation, water properties and macrofauna in a littoral stand of *Glyceria aquatic* (L.) Wahlb. in a pond in South Bohemia. Hydrobiologia 15, 17—30.

Fell, P.E., Weissbach, S.P., Jones, D.A., Fallon, M.A., Zeppieri, J.A., Faison, E.K., Lennon, K.A., Newberry, K.J., Reddington, L.K., 1998. Does invasion of oligohaline tidal marshes by reed grass, *Phragmites australis* (Cav) Trin ex Steud, affect the availability of prey resources for the mummichog, *Fundulus heteroclitus* L.? J. Exp. Mar. Biol. Ecol. 222 (1—2), 59—77. https://doi.org/10.1016/S0022-0981(97)00138-X

Gabriel, A.O., Bodensteiner, L.R., 2011. Ecosystem functions of mid-lake stands of common reed in Lake Poygan. Wisconsin. J. Freshw. Ecol. 26 (2), 217—229. https://doi.org/10.1080/02705060.2011.555202

Herman, A., 2018. The ice cover of the Vistula Lagoon. In: Bolałek, J. (Ed.), The Vistula Lagoon. PWN, Warsaw, 129—133 (in Polish).

Haslam, S.M., 1973. Some aspects of the life history and autecology of *Phragmites communis* Trin. — A review. Pol. Arch. Hydrobiol. 29 (1), 79—100.

Houlihan, D.F., 1969. Respiratory physiology of larva of *Donacia simplex*, a root-piercing beetle. J. Insect Physiol. 15 (9), 1517—1536. https://doi.org/10.1016/0022-1910(69)90173-5

Howard-Williams, C., Lenton, G.M., 1975. The role of the littoral zone in the functioning of a shallow tropical lake ecosystem. Freshw. Biol. 5 (5), 445—459. https://doi.org/10.1111/j.1365-2427.1975.tb00147.x

Jacobsen, D., 2020. The dilemma of altitudinal shifts: caught between high temperature and low oxygen. Front. Ecol. Environ. 18 (4), 211—218. https://doi.org/10.1002/fee.2161

James, M.R., Weatherhead, M., Stanger, C., Graynoth, E., 1998. Macroinvertebrate distribution in the littoral zone of Lake Coleridge, South Island, New Zealand — effects of habitat stability, wind exposure, and macrophytes. N. Z. J. Mar. Freshw. Res. 32 (2), 287—305. https://doi.org/10.1080/00288330.1998.9516826

Jayawardana, J.M.C.K., Westbrooke, M., 2010. Potential effects of riparian vegetation changes on functional organisation of macroinvertebrates in central Victorian streams. Vic. Nat. (Blackburn) 127 (2), 36—48.

Jayawardana, J.M.C.K., Westbrooke, M., Wilson, M., Hurst, C., 2006. Macroinvertebrate communities in *Phragmites australis* (Cav.) Trin. ex Steud. reed beds and open bank habitats in central Victorian streams in Australia. Hydrobiologia 568, 169—185. https://doi.org/10.1007/s10750-006-0103-6

Kairesalo, T., 1983. Dynamics of epiphytic communities on *Equisetum fluviatile* L. In: Wetzel, R.G. (Ed.), Periphiton of freshwater ecosystems, 17. Springer, Dordrecht, 153—160.

Karstens, S., Inacio, M., Schernewski, G., 2019. Expert-based evaluation of ecosystem service provision in coastal reed wetlands under different management regimes. Front. Environ. Sci. 7. https://doi.org/10.3389/fenvs.2019.00063

Kłosowski, S., 1992. Temporal and spatial variation of habitat conditions in the zonation of littoral plant communities. Aquat. Bot. 43 (2), 199—208. https://doi.org/10.1016/0304-3770(92)90043-I

Kornijów, R., 2018. Ecosystem of the Polish part of the Vistula Lagoon from the perspective of alternative stable states concept, with implications for management issues. Oceanologia 60 (3), 390—404. https://doi.org/10.1016/j.oceano.2018.02.004

Kornijów, R., Dukowska, M., Leszczynska, J., Smith, C., Jeppesen, E., Hansson, L.A., Ketola, M., Irvine, K., Noges, T., Sahuquillo, M., Miracle, M.R., Gross, E., Kairesalo, T., van Donk, E., de Eyto, E., Garcia-Criado, F., Grzybkowska, M., Moss, B., 2021a. Distribution patterns of epiphytic reed-associated macroinvertebrate communities across European shallow lakes. Sci. Total Environ. 760, 144117. https://doi.org/10.1016/j.scitotenv.2020.144117

Kornijów, R., Gulati, R.D., 1992. Macrofauna and its ecology in Lake Zwemlust, after biomanipulation. I. Bottom fauna. Arch. Hydrobiol. 123 (3), 337—347.

Kornijów, R., Pawlikowski, K., Błędzki, L.A., Drgas, A., Piwosz, K., Ameryk, A., Całkiewicz, J., 2021b. Co-occurrence and potential resource partitioning between oligochaetes and chironomid larvae in a sediment depth gradient. Aquat. Sci. 83 (51), 1—10. https://doi.org/10.1007/s00027-021-00800-z

Kornijów, R., Strayer, D.L., Caraco, N.F., 2010. Macroinvertebrate communities of hypoxic habitats created by an invasive plant (*Trapa natans*) in the freshwater tidal Hudson River. Fund. Appl. Limnol. 176 (3), 199—207. https://doi.org/10.1127/1863-9135/2010/0176-0199

Kownacka, J., Całkiewicz, J., Kornijów, R., 2020. A turning point in the development of phytoplankton in the Vistula Lagoon (southern Baltic Sea) at the beginning of the 21st century. Oceanologia 62 (4 Pt. A), 538—555. https://doi.org/10.1016/j.oceano.2020.08.004

Linkowski, T.B., Kornijów, R., Karpowicz, M., 2021. Comparison of three methods for nocturnal sampling of predatory zooplankters in shallow waters. Oceanologia 63 (1), 71—79. https://doi.org/10.1016/j.oceano.2020.10.001

Lissner, J., Schierup, H.H., 1997. Effects of salinity on the growth of *Phragmites australis*. Aquat. Bot. 55, 247—260. https://doi.org/10.1016/S0304-3770(96)01085-6

Maasri, A., Schechner, A.E., Erdenee, B., Dodds, W.K., Chandra, S., Gelhaus, J.K., Thorp, J.H., 2019. Does diel variation in oxygen influence taxonomic and functional diversity of stream macroinvertebrates? Freshw. Sci. 38 (4), 692—701. https://doi.org/10.1086/705916

Macneil, C., Dick, J.T.A., Elwood, R.W., 1999. The dynamics of predation on *Gammarus* spp. (Crustacea: Amphipoda). Biol. Rev. (Camb.) 74 (4), 375—395. https://doi.org/10.1017/S0006323199005368

Mancinelli, G., Sabetta, L., Basset, A., 2005. Short-term patch dynamics of macroinvertebrate colonization on decaying reed detritus in a Mediterranean lagoon (Lake Alimini Grande, Apulia, SE Italy). Mar. Biol. 148 (2), 271—283. https://doi.org/10.1007/s00227-005-0091-5

Meijering, M.P.D., 1991. Lack of oxygen and low pH as limiting factors for *Gammarus* in Hessian brooks and rivers. Hydrobiologia 223, 159—169. https://doi.org/10.1007/bf00047637

Meyerson, L.A., Saltonstall, K., Windham, L., Kiviat, E., Findlay, S.A., 2000. A comparison of *Phragmites australis* in freshwater and brackish marsh environments in North America. Wetl. Ecol. Manag. 8, 89—103. https://doi.org/10.1023/A:1008432200133

Miler, O., Czarnecka, M., Garcia, X.F., Jager, A., Pusch, M., 2018. Across-shore differences in lake benthic invertebrate communities within reed stands (*Phragmites australis* (Cav.) Trin. ex Steud.). Int. Rev. Hydrobiol. 103 (5-6), 99—112. https://doi.org/10.1002/iroh.201801955

Miler, O., Porst, G., McGoff, E., Pilotto, F., Donohue, L., Jurca, T., Solimini, A., Sandin, L., Irvine, K., Aroviita, J., Clarke, R., Pusch, M.T., 2013. Morphological alterations of lake shores in Europe: A multimetric ecological assessment approach using benthic macroinvertebrates. Ecol. Indic. 34, 398—410. https://doi.org/10.1016/j.ecolind.2013.06.002

Moss, B., 1998. Ecology of freshwaters. Man and medium, past to future, 3rd edn. Blackwell Science, Oxford, 572 pp.

Natural Earth, 2020. Natural Earth — Free vector and raster map data, https://www.naturalearthdata.com/ (access 2020.12.16).

NOAA GSHHG, 2014. Global self-consistent hierarchical high-resolution geography, https://www.ngdc.noaa.gov/mgg/shorelines/data/gshhg/latest/ (access 2014.12.30).

Oertli, B., 1995. Spatial and temporal distribution of the zoobenthos community in a woodland pond (Switzerland). Hydrobiologia 300, 195—204. https://doi.org/10.1007/Bf00024461

Okun, N., Lewin, W.C., Mehner, T., 2005. Top-down and bottom-up impacts of juvenile fish in a littoral reed stand. Freshw. Biol. 50 (5), 798—812. https://doi.org/10.1111/j.1365-2427.2005.01361.x

Okun, N., Mehner, T., 2005. Distribution and feeding of juvenile fish on invertebrates in littoral reed (*Phragmites*) stands. Ecol. Freshw. Fish. 14 (2), 139—149. https://doi.org/10.1111/j.1600-0633.2005.00087.x

Olson, E.J., Engstrom, E.S., Doeringsfeld, M.R., Bellig, R., 1995. Abundance and distribution of macroinvertebrates in relation to macrophyte communities in a prairie marsh, Swan-Lake, Minnesota. J. Freshw. Ecol. 10 (4), 325—335. https://doi.org/10.1080/02705060.1995.9663455

OpenStreetMap Contributors, 2021. OpenStreetMap — OpenTopoMap. Accessed by OSM plugin in QGIS.

Ostendorp, W., 1993. Reed bed characteristics and significance of reed in landscape ecology. In: Ostedorp, W., Krumsheid—Plankert, P. (Eds.), Lakeshore deterioration and restoration works in Central Europe. Fischer-Verlag, Stuttgart, 149—161.

Pawlikowski, K., Kornijów, R., 2019. Role of macrophytes in structuring littoral habitats in the Vistula Lagoon (southern Baltic Sea). Oceanologia 61 (1), 26—37. https://doi.org/10.1016/j.oceano.2018.05.003

Pawlikowski, K., Kornijów, R., 2022. Patterns of macroinvertebrates distribution in a sediment depth gradient in habitats dominated by emergent and submerged vegetation. Oceanologia Submitted for publication.

Pellan, L., Médoc, V., Renault, D., Spataro, T., Piscart, C., 2016. Feeding choice and predation pressure of two invasive gammarids, *Gammarus tigrinus and Dikerogammarus villosus*, under increasing temperature. Hydrobiologia 781, 43—54. https://doi.org/10.1007/s10750-015-2312-3

Perez-Ruzafa, A., Marcos, C., Perez-Ruzafa, I.M., Perez-Marcos, M., 2011. Coastal lagoons: "transitional ecosystems" between transitional and coastal waters. J. Coast. Conserv. 15 (3), 369—392. https://doi.org/10.1007/s11852-010-0095-2

Pinder, L.C.V., et al., 1995. The habitats of chironomid larvae. In: Armitage, P.S., et al. (Eds.), Chironomidae: biology and ecology of non-biting midges. Chapman & Hall, London, 107—135.

Raichel, D.L., Able, K.W., Hartman, J.M., 2003. The influence of *Phragmites* (common reed) on the distribution, abundance, and potential prey of a resident marsh fish in the Hackensack Meadowlands, New Jersey. Estuaries 26 (2b), 511—521. https://doi.org/10.1007/Bf02823727

Reddy, K.R., Dangelo, E.M., Debusk, T.A., 1990. Oxygen transport through aquatic macrophytes — the role in waste-water treatment. J. Environ. Qual. 19 (2), 261—267. https://doi.org/10.2134/jeq1990.00472425001900020011x

Sagova-Mareckova, M., Kvet, J., 2002. Impact of oxygen released by the roots of aquatic macrophytes on composition and distribution of benthic macroinvertebrates in a mesocosm experiment. Arch. Hydrobiol. 155 (4), 567—584.

Sand-Jensen, K., Prahl, C., Stokholm, H., 1982. Oxygen release from roots of submersed aquatic macrophytes. Oikos 38 (3), 349—354. https://doi.org/10.2307/3544675

Savage, A.A., 1982. The survival and growth of *Gammarus tigrinus* Sexton (Crustacea: Amphipoda) in relation to salinity and temperature. Hydrobiologia 94 (3), 201—212.

Schlacher, T.A., Wooldridge, T.H., 1996. How sieve mesh size affects sample estimates of estuarine benthic macrofauna. J. Exp. Mar. Biol. Ecol. 201, 159—171. https://doi.org/10.1016/0022-0981(95)00198-0

SIPAM, 2020. System informacji przestrzennej administracji morskiej. https://sipam.gov.pl/

StatSoft, 2011. Statistica software version 10. StatSoft Inc., http://www.statsoft.com

Suzuki, N., Endoh, S., Kawashima, M., Itakura, Y., McNabb, C.D., D'Itri, F.M., Batterson, T.R., 1995. Discontinuity bar in a wet land of Lake Huron's Saginaw Bay. J. Freshwater Ecol. 10 (2), 111—123.

Swearingen, J., Saltonstall, K., 2012. *Phragmites* field guide: distinguishing native and exotic forms of common reed (*Phragmites australis*) in the United States. USDA — Natural Resources Conservation Service Boise, TN Plant Materials NO 56 , Idaho. https://www.nrcs.usda.gov/Internet/FSE_PLANTMATERIALS/publications/idpmctn11494.pdf

Sychra, J., Adamek, Z., Petrivalska, K., 2010. Distribution and diversity of littoral macroinvertebrates within extensive reed beds

of a lowland pond. Ann. Limnol. - Int. J. Lim. 46 (4), 281—289. https://doi.org/10.1051/limn/2010026

Timm, T., 1999. A guide to the Estonian Annelida. Estonian Academy Publishers, Tallinn, 208 pp.

Vaughn, C.C., 1982. Distribution of Chironomids in the littoral-zone of Lake Texoma, Oklahoma and Texas. Hydrobiologia 89 (2), 177—188. https://doi.org/10.1007/Bf00006170

Verberk, W., Bilton, D.T., Calosi, P., Spicer, J.I., 2011. Oxygen supply in aquatic ectotherms: Partial pressure and solubility together explain biodiversity and size patterns. Ecology 92 (8), 1565—1572. https://doi.org/10.1890/10-2369.1

Viaroli, P., Bartoli, M., Bondavalli, C., Christian, R.R., Giordani, G., Naldi, M., 1996. Macrophyte communities and their impact on benthic fluxes of oxygen, sulphide and nutrients in shallow eutrophic environments. Hydrobiologia 329 (1—3), 105—119. https://doi.org/10.1007/Bf00034551

Warfe, D.M., Barmuta, L.A., 2004. Habitat structural complexity mediates the foraging success of multiple predator species. Oecologia 141 (1), 171—178. https://doi.org/10.1007/s00442-004-1644-x

Warren, R.S., Fell, P.E., Grimsby, J.L., Buck, E.L., Rilling, G.C., Fertik, R.A., 2001. Rates, patterns, and impacts of *Phragmites australis* expansion and effects of experimental *Phragmites* control on vegetation, macroinvertebrates, and fish within tidelands of the lower Connecticut River. Estuaries 24 (1), 90—107. https://doi.org/10.2307/1352816

WoRMS Editorial Board, 2021. World Register of Marine Species. VLIZ. Available from https://doi.org/10.14284/170

Yozzo, D.J., Osgood, D.T., 2013. Invertebrate communities of low-salinity wetlands: overview and comparison between *Phragmites* and *Typha* marshes within the Hudson River Estuary. Estuar. Coast. 36 (3), 575—584. https://doi.org/10.1007/s12237-012-9543-6

Zachowicz, I.M., 1985. From biostratigraphical studies of sediments from the Vistula Lagoon. Petrobalticum 3, 97—111 (in Polish).

Żbikowski, J., Żbikowska, E., Kobak, J., 2021. The presence of fine sand in the muddy sediments affects habitat selection and accelerates the growth rate of *Limnodrilus hoffmeisteri* and *Limnodrilus claparedianus* (Oligochaeta). Hydrobiologia 848 (11), 2761—2771. https://doi.org/10.1007/s10750-021-04595-w

Oceanologia 64 (2022) 445—456

Available online at www.sciencedirect.com

ScienceDirect

journal homepage: www.journals.elsevier.com/oceanologia

ORIGINAL RESEARCH ARTICLE

Tropical cyclone intensity modulated by the oceanic eddies in the Bay of Bengal

Navaneeth Kodunthirapully Narayanaswami[a,b,*], **Venkatesan Ramasamy**[a]

[a] *Ocean Observation Systems, National Institute of Ocean Technology (NIOT), Chennai, India*
[b] *Anna University, Guindy Campus, Chennai, India*

Received 22 June 2021; accepted 20 February 2022
Available online 7 March 2022

KEYWORDS
Phailin;
Fani;
Eddy feedback factor;
Cold-core eddy;
Warm-core eddy

Abstract The Bay of Bengal, an affluent region for mesoscale oceanic eddies, is also home to devastating tropical cyclones. The intensity modulation of two cyclones, Phailin (2013) and Fani (2019), in the Bay of Bengal by the oceanic eddies is studied. The intensities of both the cyclones rapidly changed after transiting over mesoscale eddies. The surface and subsurface oceanic conditions before and during the passage of the two cyclones were analysed. During Phailin (Fani), the cyclonic (anticyclonic) eddy resulted in significant (weak) sea surface temperature cooling due to the shallow (deep) D26 isotherm. Wind shear estimates revealed that it had no (minor) effect on the weakening (intensification) of Phailin (Fani). The analysis of enthalpy fluxes during the two cyclones has shown that during Phailin (Fani), the latent heat flux supply was reduced (enhanced) by 20 W m^{-2} (30 W m^{-2}) over the regions of the cyclonic (anticyclonic) eddy due to significant (weak) sea surface temperature cooling. The case study of cyclone interaction with mesoscale oceanic eddies has shown that a thorough understanding of mesoscale eddies is vital for improving the accuracy of the cyclone intensity forecasts.

1. Introduction

Tropical cyclones (TCs) affect millions of people annually across the globe. TCs cause significant damage to life and property because of strong winds, heavy precipitation, and storm surge. Global warming has resulted in an increase in the frequency and intensity of TCs (Emanuel, 2013). The accurate forecast of TC, both in terms of its intensity and track, is highly critical for mitigating socio-economic impacts. Rappaport et al. (2012) reported that even though forecasting skills have improved in accurately predicting

* Corresponding author at: Ocean Observation Systems, National Institute of Ocean Technology (NIOT), Chennai 600025, India.
E-mail address: nkn968@gmail.com (N. Kodunthirapully Narayanaswami).
Peer review under the responsibility of the Institute of Oceanology of the Polish Academy of Sciences.

Production and hosting by Elsevier

https://doi.org/10.1016/j.oceano.2022.02.005

TC's track over the past few decades, intensity prediction remains challenging. The intensity change of a TC is governed by a multitude of atmospheric and oceanic processes. Emanuel et al. (2004) reported that air-sea interactions are highly crucial in controlling the intensity of TC. Sea Surface Temperature (SST) cooling induced by the strong TC winds can curtail the supply of enthalpy fluxes and impede the further intensification of TC (Cione and Uhlhorn, 2003; Halliwell et al., 2015). However, studies (Lloyd and Vecchi, 2011; Mei and Pasquero, 2013) have documented that the SST response to a TC is not entirely dependent on TC characteristics but also depends on the oceanic environment.

The oceanic environment is non-homogeneous. The mesoscale oceanic eddies have a significant role in determining the ocean's vertical temperature and salinity structure. Cyclonic (anticyclonic) eddies promote (restrain) SST cooling (Jaimes and Shay, 2009; Lin et al., 2005). Hence, the cyclonic (anticyclonic) eddies are referred to as cold (warm) core eddies. The intensification (weakening) of TCs over anticyclonic (cyclonic) eddies has been documented in several studies (Demaria and Kaplan, 1994; Liang et al., 2018, 2016; Lin et al., 2005; McTaggart-Cowan et al., 2006; Shay et al., 2000). Lin et al. (2005) have reported on Typhoon Maemi's rapid intensification over a giant warm-core eddy. Similarly, Ma et al. (2020) documented the mechanisms responsible for the unusual rapid weakening of typhoon Francisco over a cold-core eddy using observations and modelling studies.

The Bay of Bengal (BoB), a semi-closed marginal sea located in the tropical north-eastern Indian Ocean, is rich in mesoscale eddies (Babu et al., 2003; Chen et al., 2012; Cheng et al., 2013; Hacker et al., 1998; Kurien et al., 2010; Prasanna Kumar et al., 2004, 2007). Chen et al. (2012) reported that the majority of eddies in the BoB are generated in the eastern and western boundaries. Cheng et al. (2018) utilised the synergy of observations and models to understand eddy generation in the central BoB. They reported that equatorial zonal winds mainly drive eddies generated near the eastern BoB boundary. However, the eddy formation in the western BoB is attributed to the instability of flow in the East India Coastal Current (EICC) (Kurien et al., 2010). Vinayachandran (2013) also reported the formation of cold-core and warm-core eddies, especially during April, May, October, and November. The BoB is also home to the deadliest cyclones in history. High SSTs (~28–31°C) and weak vertical wind shear during pre-monsoon (Neetu et al., 2019) and high relative humidity during post-monsoon (Li et al., 2013) provide a conducive environment for TC formation in the BoB. Due to the funnel-shaped coastline, high storm surges generated during TC result in a high death toll. For example, the Orissa Super Cyclone resulted in the deaths of approximately 10,000 people. Hence, any errors in the forecasts of TC can have widespread socio-economic impacts.

The interaction between pre-existing mesoscale eddies and TCs in the BoB is a thrust area of research. Lin et al. (2009) investigated the intensification of Nargis over the warm ocean and reported that the pre-existing deep, warm subsurface layer decreased SST cooling induced by the TC. As a result, the enthalpy fluxes have been shown to increase by 300%. Sadhuram et al. (2012) documented the intensification of TC Aila by 43% over a warm-core eddy. Recently, Liu et al. (2021) documented the influence of pre-existing cold and warm-core eddies on the intensity of tropical storm Roanu in the BoB. Here, we investigate the intensity modulation of two intense TCs, Phailin (2013) and Fani (2019), in the BoB. Both the TCs interacted with pre-existing mesoscale eddies in the BoB before landfall. Phailin, a category-5 TC, encountered a cyclonic eddy and weakened to a category-3 TC before landfall. Contrastingly, Fani intensified to a category-4 TC from category-3 when it passed over an anticyclonic eddy. The role of pre-existing mesoscale eddies in the intensity modulation of these two intense TCs, Phailin (2013) and Fani (2019), in the BoB, was analysed and presented.

2. Data and methodology

The gridded daily global estimates of sea level anomaly (SLA) based on Ssalto/Duacs altimeter products produced and distributed by Copernicus Marine and Environment Monitoring Service (CMEMS) (http://www.marine.copernicus.eu) are used for the detection of mesoscale features. The six-hour interval tracks of Phailin (2013) and Fani (2019) were obtained from Joint Typhoon Warning Centre (https://www.metoc.navy.mil/jtwc/jtwc.html?north-indian-ocean). The high-resolution (1 km) daily-mean foundation SST (SSTfnd) from the Group for High-Resolution Sea Surface Temperature (GHRSST) Level 4 gridded products (Donlon et al., 2007) is utilised. Subsurface temperature data products at 1/12° resolution from CMEMS(http://marine.copernicus.eu/getting-started/) are used for the estimation of the depth of 26°C isotherms (D26) and Tropical Cyclone Heat Potential (TCHP). CMEMS products utilise the synergy of advanced modelling and data assimilation techniques.

The TCHP is calculated using the formula

$$\mathrm{TCHP} = \rho Cp \int_0^{D26} (Tz - 26)dz \quad (1)$$

Hourly datasets of relative humidity at 700 hPa (MTRH), zonal and meridional winds at 200 and 850 hPa, Latent Heat Flux (LHF) and Sensible Heat Flux (SHF) from ERA5 reanalysis products (Hersbach and Dee, 2016) were also utilised. The in-situ observations of Sea Level Pressure (SLP), wind speed, and temperature profiles during TCs Phailin and Fani from moored buoys deployed by the National Institute of Ocean Technology (Venkatesan et al., 2013) are used for understanding the temporal evolution. Vertical Wind Shear (VWS) is calculated as the vector difference between the 200- and 850-hPa winds.

3. Results and discussion

3.1. Synopsis of cyclone Phailin (2013) and Fani (2019)

The track of the two intense TCs, Phailin (category-5) and Fani (category-4), developed over the BoB overlaid on TRMM rainfall along with the location of moored buoys deployed by the NIOT is shown in Figure 1a–b, respectively. North-central BoB received cumulative precipitation of ~20 cm

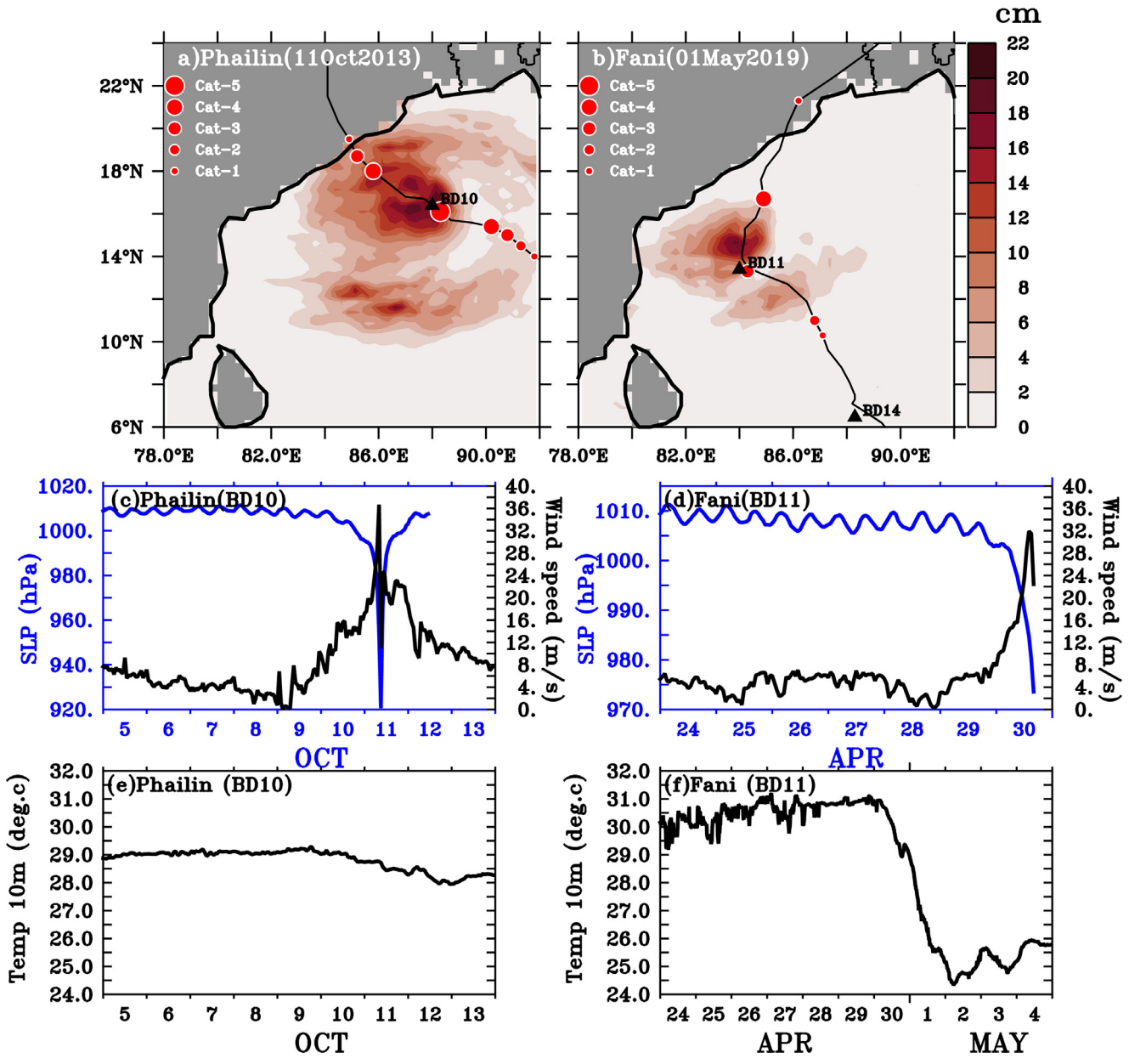

Figure 1 TRMM cumulative precipitation (cm) in the Bay of Bengal on (a) 11 October 2013 (Phailin), (b) 01 May 2019 (Fani). SLP and Wind speed at 10 m height (c) for Phailin, (d) for Fani. Subsurface temperature at 10 m from (e) BD10 for Phailin (f) BD11 for Fani. The black triangular shaped markers in panels a and b represent the mooring deployed by NIOT. The red circle-shaped markers in panels a and b indicate the intensity of the cyclone on Saffir-Simpson scale.

during Phailin. Phailin was the strongest post-monsoon cyclone (09—13 October 2013), making landfall at the Odisha coast after the Orissa Super Cyclone in 1999. Phailin developed as a tropical storm over the northern Andaman Sea on October 9, 2013 and intensified into a category-1 on October 10, 2013. Moving north-westwards, it further intensified into a category-3 TC and finally reached maximum intensity with a central pressure of 940 hPa and wind speed of 115 knots (category-5) on October 11, 2013 at 16.0°N, 88.5°E. It crossed Odisha near Gopalpur on 12 October 2013 as a category-3 cyclone. Fani (27 April—03 May 2019) was one of the strongest pre-monsoon TCs in the BoB after 1994, developed near the equator in the north Indian Ocean. Fani covered 3030 km in the open ocean from the south BoB to the north Odisha coast and maintained a wind speed of ≥100 knots for 36 hours (Singh et al., 2021). Heavy rainfall (~20 cm) occurred in the western BoB near the BD11 mooring (Figure 1b). It made landfall on the Odisha coast near Puri as a category-4 cyclone with ~105 knots.

3.2. In situ observations from moored buoys in the vicinity of cyclone track

The significant observations of meteorological parameters and SST from the moored buoys during Phailin and

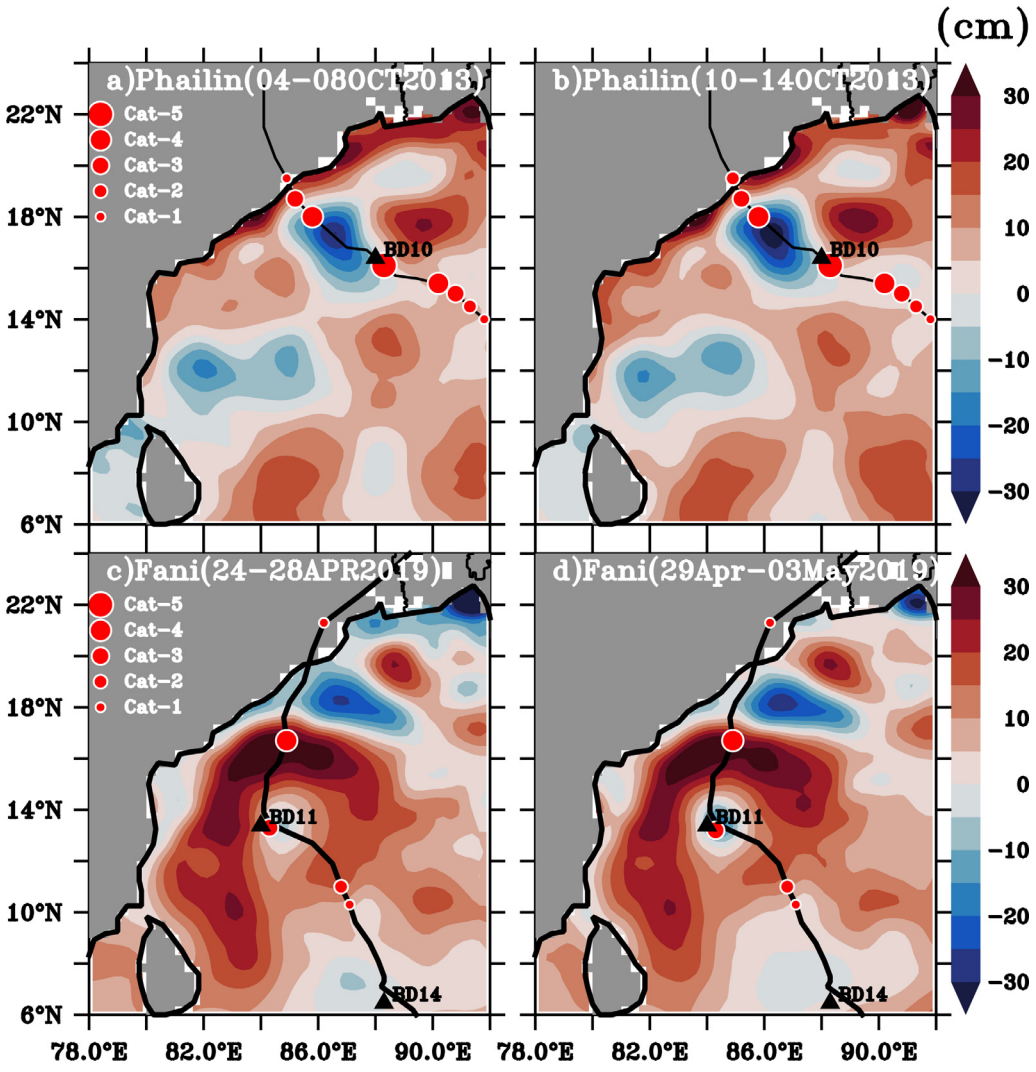

Figure 2 Five-day average AVISO SLA data (a) during 04—08 October 2013 before the passage of Phailin, (b) during 10—14 October 2013 during the passage of Phailin, (c) during 24—28 April 2019 before the passage of Fani, and (d) during 29 April—03 May 2019 during the passage of Fani. The black triangular shaped markers represent the moorings deployed by NIOT. The red circle-shaped markers indicate the intensity of the cyclone on the Saffir-Simpson scale.

Fani in the vicinity of the TC tracks were shown in Figure 1c—f. The average SLP was ~1010 hPa with wind speed in the range of 5—10 m s^{-1} before the passage of Phailin (Figure 1c). The SLP in the moored buoy BD10 (88°E/16.5°N) dropped to 920 hPa, and wind speeds increased to 37 m s^{-1} on 11 October 2013. The observations from remote sensing platforms also estimated the SLP to be around 910 hPa during Phailin. Note that Phailin was a category-5 cyclone near BD10. Two of the NIOT buoys, namely BD14 (88°E/7°N) and BD11 (84°E/13.5°N) along the track, recorded the significant anomalies of Fani (Figure 1d). BD14, located 35 km from the track, observed a maximum wind speed of 21 m s^{-1}, and SLP dropped to 997 hPa on 27 April 2019 during the genesis stage of Fani. The SLP dropped to 973.5 hPa, and the wind speed increased up to 32 m s^{-1} in BD11 (located 12 km from the track) on 30 April 2019, when Fani reached the intensity of category-3.

The temperature at 10 m from BD10 and BD11 during Phailin and Fani is shown in Figures 1e and f, respectively. The temperature measured at 10 m by the NIOT buoys can be considered Foundation SST (SSTfnd) since it is free from diurnal variability (GHRSST-PP). The SSTfnd from BD10 before Phailin was ~29—29.5°C (Figure 1e), whereas a high SSTfnd of ~30—31°C was observed at BD11 prior to the formation of Fani (Figure 1f). Intense cooling of ~6°C was observed at BD11 after the passage of Fani. However, SST cooling of ~1°C was observed at BD10 after Phailin's passage. Significant wave height of 6.8 m, 3.8 m and 5 m was recorded by the moored buoys BD11, BD14 and BD08, respectively, during Fani (Figures not shown). The synoptic conditions during the two TCs were analysed using remote sensing observations in the following section.

3.3. Surface oceanic conditions during Phailin and Fani

3.3.1. Pre-existing oceanic eddies

The presence of mesoscale oceanic eddies characterises the surface oceanic conditions before and during the passage of

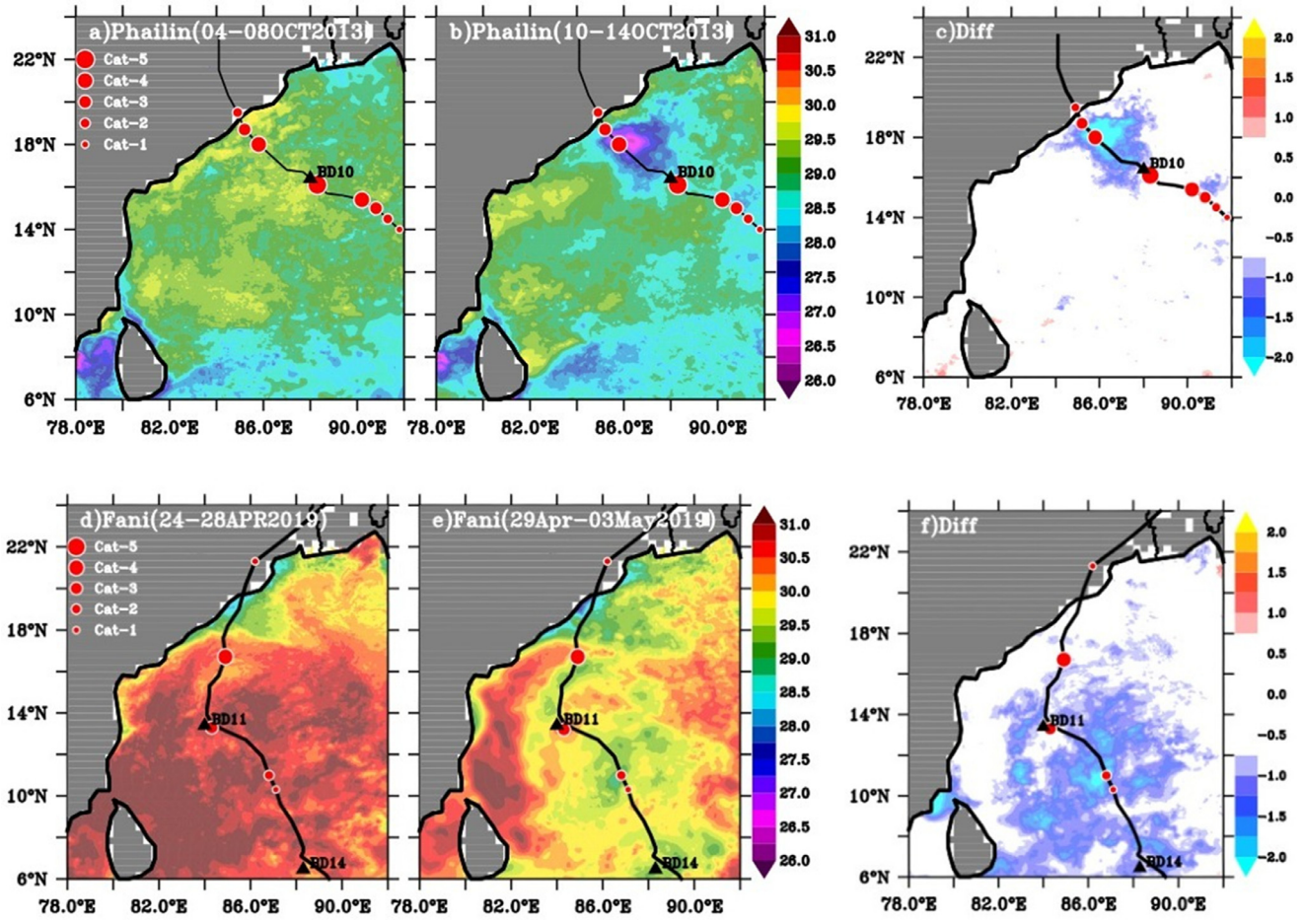

Figure 3 Five-day mean SST from GHRSST in the Bay of Bengal during (a) pre-Phailin days (04—08 October 2013), (b) Phailin days (10—14 October 2013), (d) pre-Fani days (24—28 April 2019), and (e) Fani days (29 April—03 May 2019). (c) SST changes caused by cyclone Phailin are calculated by subtracting SST data in (a) from (b). (d) The same as 3(c), but the SST changes after Fani's passage. The black triangular-shaped markers represent the moorings deployed by NIOT. The red circle-shaped markers indicate the intensity of the cyclone on the Saffir-Simpson scale.

Phailin and Fani. Mesoscale eddies are an integral part of ocean circulation in the BoB. Intense eddy activity is observed throughout the year in the BoB (Chen et al., 2012; Cheng et al., 2018). Eddies that are generated in the eastern BoB due to the interactions of wind, nonlinear processes, and coastline geometry get embedded in the Rossby waves and propagate westwards. The eddy also gets generated in the western BoB due to flow instabilities in the EICC (Kurien et al., 2010). Hence, the circulation in the western BoB is primarily dominated by eddy—mean flow interactions (Chen et al., 2012). TCs are most active in the BoB during the post-monsoon (October—December) and pre-monsoon seasons (April—May). The TCs generated in the BoB generally move in a north-westerly direction during the post-monsoon season and northerly or north-easterly direction during the pre-monsoon season. The intensity of TCs gets modulated by mesoscale eddies. Hence, we have analysed the daily SLA data from AVISO to detect eddies and their interaction with Phailin and Fani. Figure 2a and b shows the five-day average SLA before (04—08 October 2013) and during (10—14 October 2013) the passage of Phailin.

A pre-existing cyclonic eddy evident in a closed-contour negative SLA can be seen in the western BoB near 86.5°E/17°N (Figure 2a). Phailin attained its peak intensity of category-5 TC near the BD10 mooring. It encountered a cyclonic eddy and subsequently weakened to a category-3 TC. However, in the case of Fani, a pre-existing anticyclonic eddy with a closed-contour positive SLA is present in the region of 82—87°E/15—17°N. Fani was a category-3 TC before encountering the anticyclonic eddy and intensified to a category-4 TC when it passed over the anticyclonic eddy. Mesoscale oceanic eddies can alter the surface SST signatures (Gaube et al., 2019). Also, SST plays a crucial role in determining TC intensity (Fisher, 1958). Hence, the role of the cyclonic and anticyclonic eddies on SST during the two TCs was investigated further.

3.3.2. SST

The energy required for the TCs comes from surface enthalpy fluxes (Emanuel, 1986), which depend on SST. Several studies (for example, Demaria and Kaplan, 1994) have documented the relationship between SST and the intensity of TC. Furthermore, SST uncertainty has been shown to play a significant role in errors in estimating and predicting TC intensity. The five-day averaged SSTfnd from GHRSST for Phailin and Fani is shown in Figure 3a—b and d—e, re-

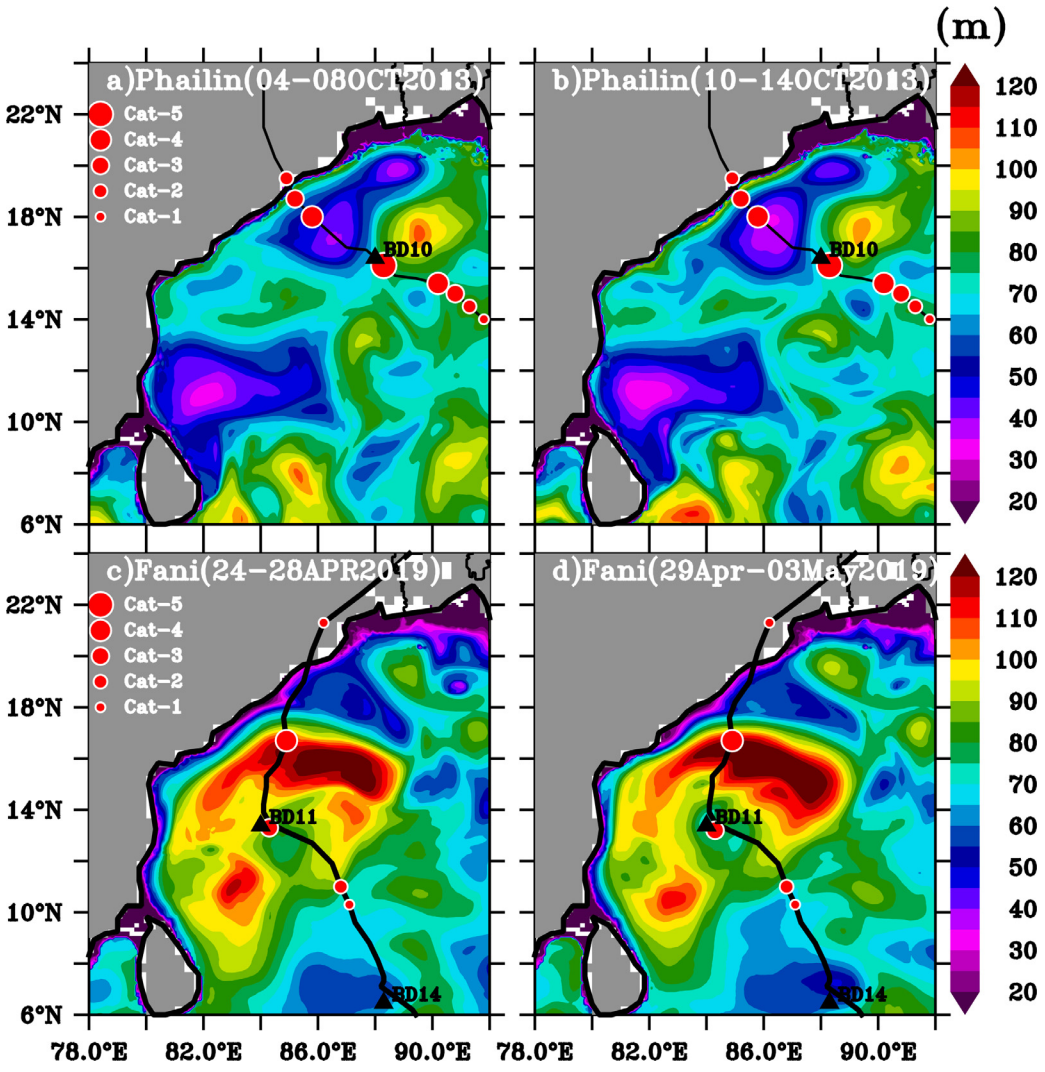

Figure 4 Five-day average D26 isotherm estimated from CMEMS data (a) during 04—08 October 2013, before the passage of Phailin, (b) during 10—14 October 2013, during the passage of Phailin, (c) during 24—28 April 2019, before the passage of Fani, and (d) during 29 April—03 May 2019, during the passage of Fani. The black triangular-shaped markers represent the moorings deployed by NIOT. The red circle-shaped markers indicate the intensity of the cyclone on the Saffir-Simpson scale.

spectively. The SST in the BoB prior to Phailin was greater than 29°C, which was consistent with moored buoy observations (Figures 3a and 1e). During Phailin, the SST cooling in the BoB was very small, 0.5°C (Figures 3b—c). Studies (Chaudhuri et al., 2019; Navaneeth et al., 2019) reported that the less cold wake during Phailin is due to salinity stratification. Sengupta et al. (2008) also reported that the SST cooling induced by the post-monsoon cyclones in the open north BoB is minimal. However, there was a significant cooling of 2.5°C in the areas where a cyclonic eddy was present (Figure 3c). Phailin weakened to a category-4 TC after passing through the cold wake. The entire BoB had a very warm SST (>30.5°C) prior to Fani (Figure 3d). The SST cooling was more pronounced in the regions south of 15°N (Figures 3e—f) during Fani. However, SST cooling was minimal in areas above 15°N (0.75°C). Also, note that Fani intensified into a category-4 TC in this region. To summarise, the passage of Phailin over the cyclonic eddy caused a significant SST cooling. The intensity of Phailin was found to be reduced from category-5 to category-3 during its passage over a cyclonic eddy. Contrastingly, Fani's passage over an anticyclonic eddy caused a weak cold wake. Also, Fani strengthened to category-4 from category-3 over the anticyclonic eddy. Gaube et al. (2019) documented that the cyclonic (anticyclonic) eddies result in shoaling (deepening) of mixed layers by eddy upwelling (downwelling). These subsurface changes induced by eddies can vary the TCHP and thereby affect the intensity of TC. Therefore, the subsurface ocean conditions during Phailin and Fani were investigated further to determine the causes of the intensity modulation of Phailin and Fani over eddies.

3.4. Subsurface ocean conditions

The energy required for a TC's intensification is provided by the ocean from the surface up to a depth in the range of 100—200 m (Lloyd & Veechi, 2011; Price, 1981; Shay et al.,

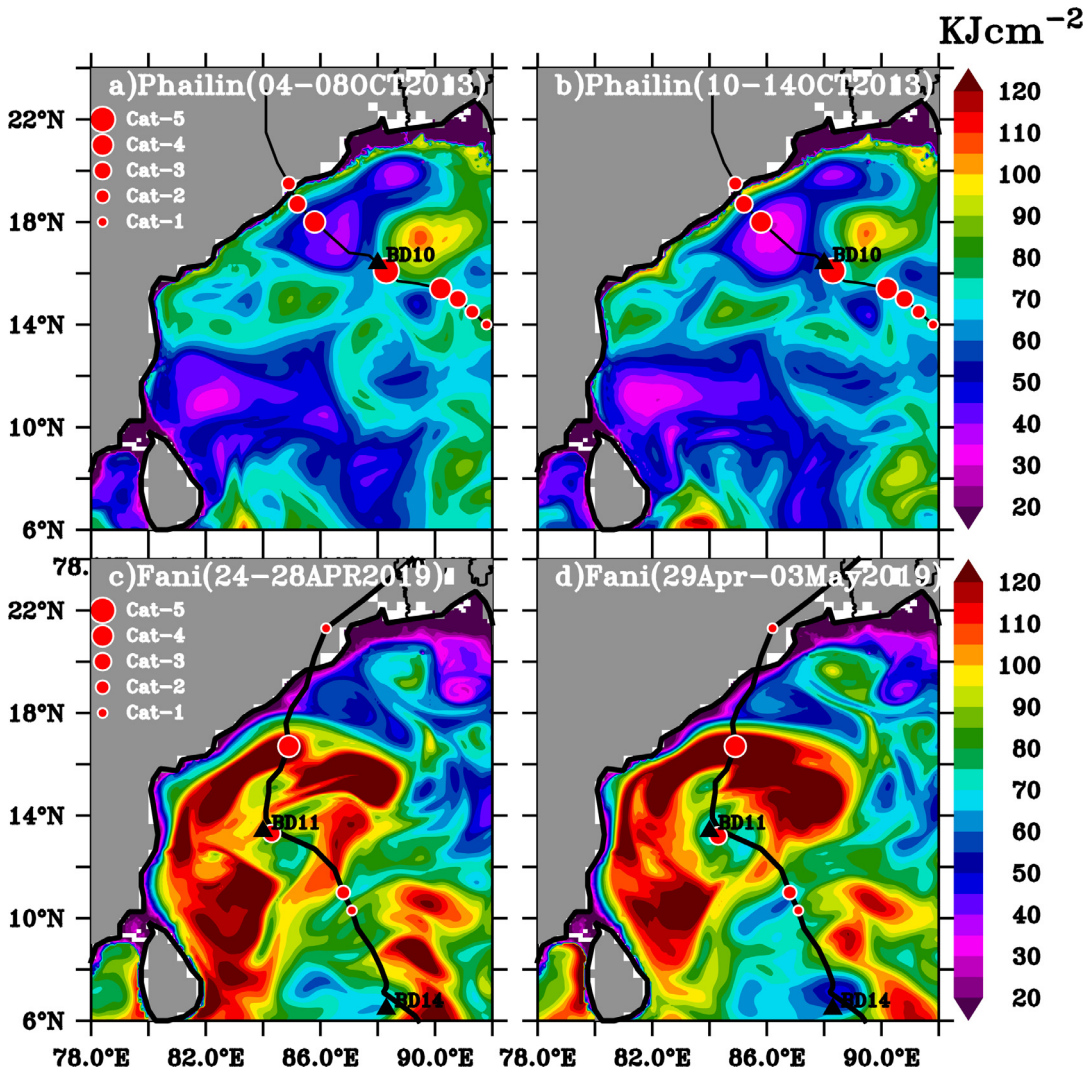

Figure 5 Five-day average TCHP estimated from CMEMS data (a) during 04—08 October 2013, before the passage of Phailin, (b) during 10—14 October 2013, during the passage of Phailin, (c) during 24—28 April 2019, before the passage of Fani, and (d) during 29 April—03 May 2019, during the passage of Fani. The black triangular-shaped markers represent the mooring deployed by NIOT. The red circle-shaped markers indicate the intensity of the cyclone on the Saffir-Simpson scale.

2000). The TCHP quantifies the thermal energy available below the ocean surface for the intensification of TC. TCs do not form in oceanic regions with SSTs less than 26°C. Hence, TCHP is estimated as the vertical integration of ocean temperatures above 26°C. Intensification of TC occurs in the regions of high TCHP (Wang and Wu, 2018). NOAA's Hurricane Centre has been using altimeter-derived TCHP data for operational forecasts since 2004 (Mainelli et al., 2008) and has reported that the forecasts are more accurate when using TCHP than SST alone. The D26 and TCHP values for Phailin and Fani, estimated from CMEMS, are shown in Figures 4 and 5, respectively.

The D26 isotherm can be considered as mid-thermocline depth, and the deepening (shoaling) of the D26 isotherm indicates downwelling (upwelling). The D26 isotherm was shallow (<40 m) in the cyclonic eddy region before Phailin (Figure 4a). When Phailin passed over the region of the cyclonic eddy, the cooler thermocline water is entrained into the mixed layer, lowering the SST (Figure 3c) compared to others. The shallow D26 also resulted in low TCHP values (<40 kJ cm^{-2}) before Phailin in the cyclonic eddy regions (Figures 4a and 5a). In situ temperature profiles from BD10 mooring also revealed a shallow D26 (~60 m) before the passage of Phailin cyclone (Figure 6a). The shallow D26 isotherm resulted in low TCHP values and significant SST cooling during the passage of Phailin over the cyclonic eddy. The cool SST and low TCHP over the regions of the cyclonic eddy supported the dampening of Phailin's intensity. However, during Fani, the region of the anticyclonic eddy was characterised by a deep D26 isotherm (>120 m) (Figure 4b) which indicates that the extension of the warmer temperature approaches 26°C up to 120 m depth, resulting in high TCHP values of ~140—180 kJ cm^{-2} (Figure 5b). Prior to Fani's passage, a deep D26 isotherm (90 m) was observed in the BD11 mooring (Figure 6b). The deep D26 isotherm resulted in high TCHP values and less cold wake over the anticyclonic eddy. The weak SST cooling and high TCHP provided a conducive environment for the intensification of Fani. SST

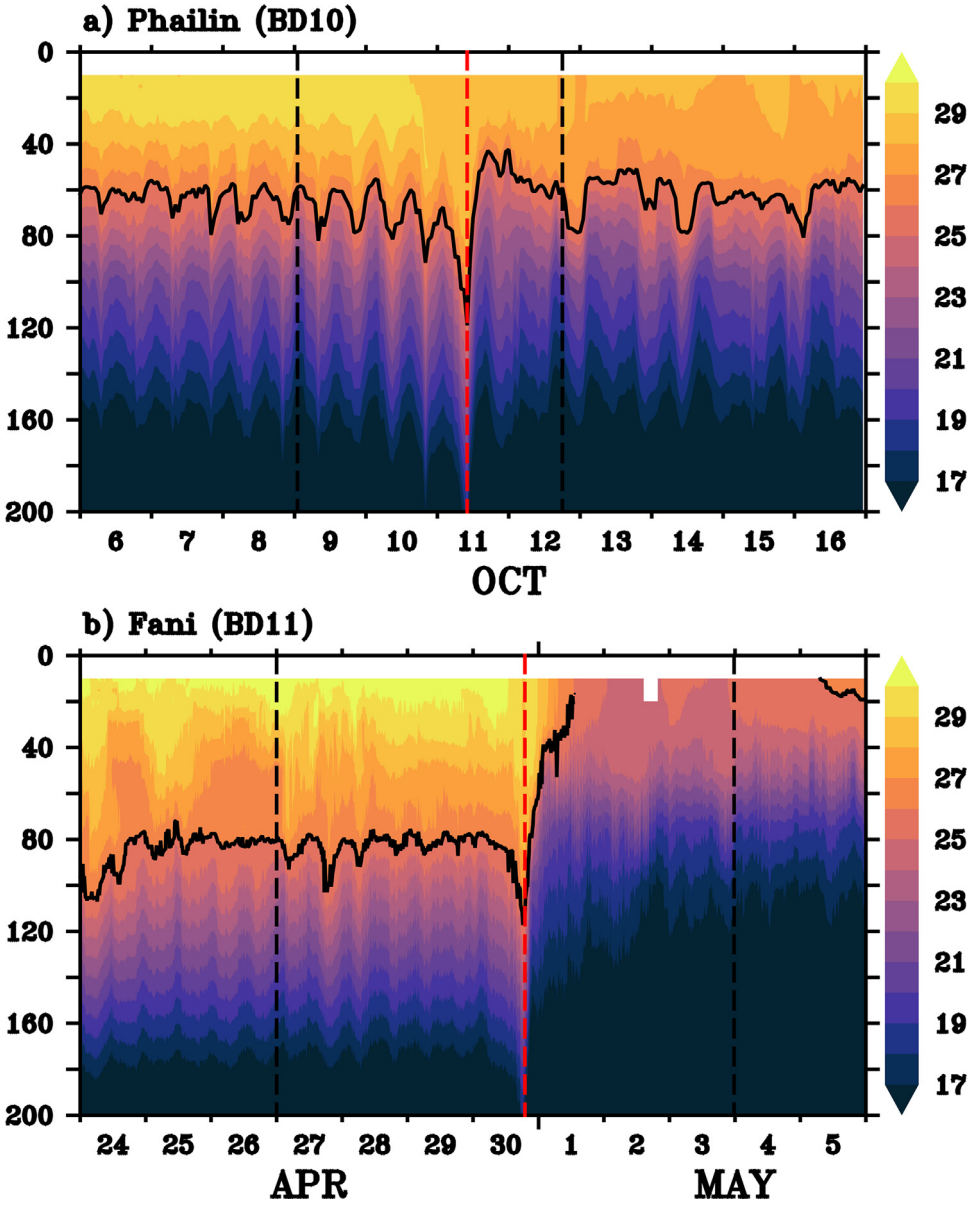

Figure 6 Temporal evolution of the vertical profile of temperature based on hourly moored buoy observations at a) BD10 during Phailin (2013) and b) BD11 during Fani (2019). The black line indicates the depth of the D26 isotherm in metres. The black dashed vertical lines represent the cyclone period and the red dashed lines indicate the time period where the cyclones were closest to the mooring locations.

patterns modulated by the oceanic eddies due to subsurface temperature variations can change the enthalpy fluxes at the air-sea interface. As the enthalpy fluxes control TC intensity (Emanuel, 1986; Emanuel et al., 2004; Riehl, 1954), the influence of the oceanic eddies on the enthalpy fluxes was further investigated.

3.5. LHF during Phailin and Fani

SST modulates the enthalpy fluxes (LHF + SHF) at the air-sea interface. The moisture and thermal disequilibrium at the air-sea interface are controlled by SST response. Studies by Cione and Uhlhorn (2003) revealed that SST cooling of approximately 1°C within the inner core of a TC could effectively change the maximum total enthalpy flux by 40% or more. Studies Ma et al. (2015) and Ma (2018) reported that the LHF rather than SHF has a significant role in fuelling storm intensification. The oceanic eddies modulated SST patterns during Phailin and Fani, which in turn could lead to variations in enthalpy fluxes. Hence, LHF and SHF variation during the two TCs was analysed. In order to study the eddy-TC interaction, ERA5 LHF and SHF data were temporally filtered using a 3–10 day Lanczos band-pass filter. Furthermore, a 2-D Gaussian high-pass filter with a cut-off wavelength of 600 km. The filtered LHF (LHF_{filt}) and SHF (SHF_{filt}) on October 12, 2013 and May 02, 2019 during Phailin and Fani were shown in Figures 7a–d. These two days were selected since the cyclones were located over eddies. The LHF_{filt} and SHF_{filt} showed positive values of ~20–30 W m^{-2} and ~3 W m^{-2} in the vicinity of the cyclone track located

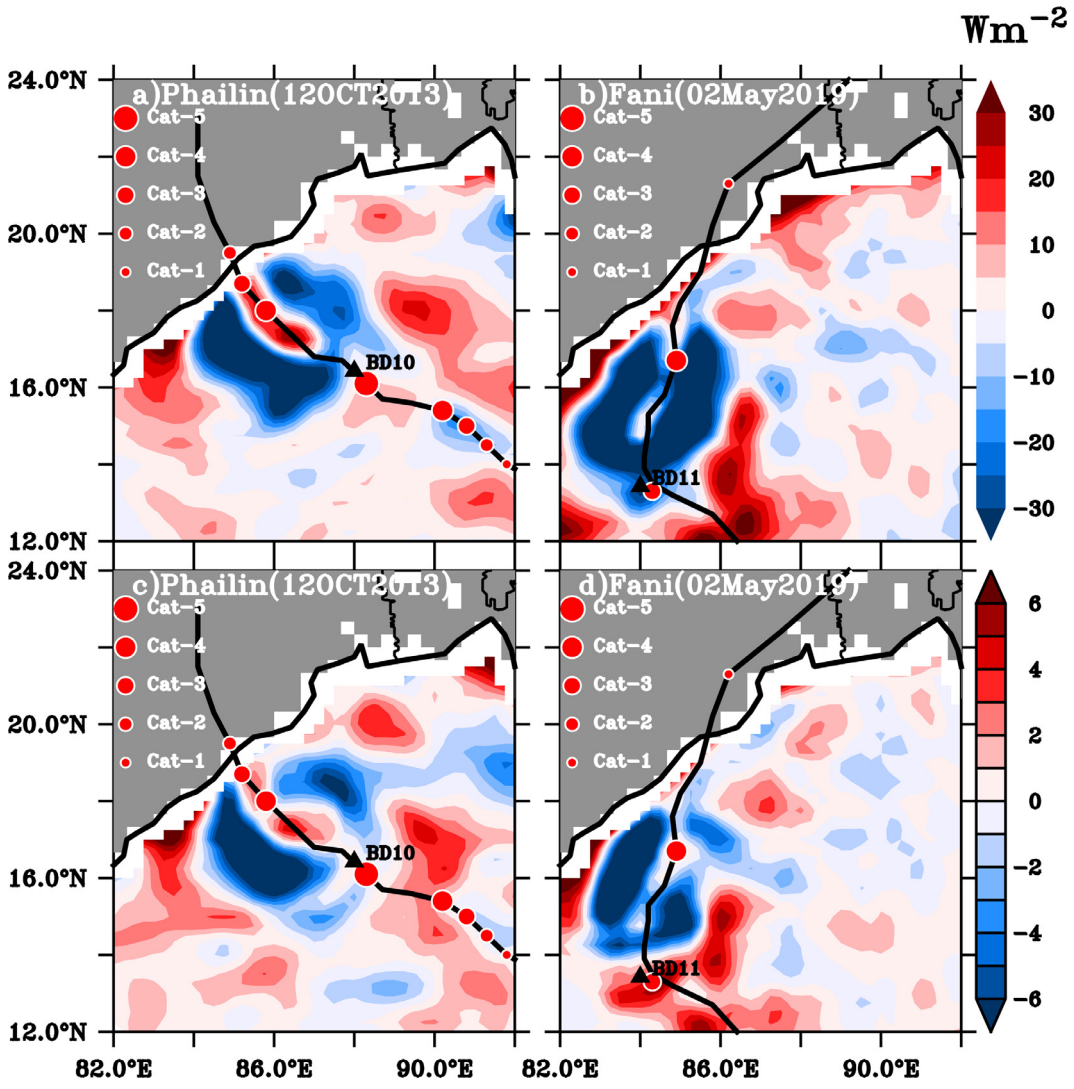

Figure 7 Filtered-LHF (LHF_{filt}) on (a) October 12th, 2013 (Phailin); (b) May 02, 2019 (Fani). Filtered-SHF (SHF_{filt}) on (c) October 12, 2013 (Phailin) and (d) May 2, 2019 (Fani).

within the cyclonic eddy on October 12th, 2013 (Figures 7a—c). The cold wake (Figure 3c) created due to the cyclonic eddy curtailed enthalpy fluxes and resulted in the weakening of Phailin. However, during Fani, LHF_{filt} showed negative values (~30 W m^{-2}) in the vicinity of the cyclone track situated within the anticyclonic eddy (Figure 7b). The meagre SST cooling (Figure 3f) due to the presence of anticyclonic eddy enhanced the LHF, which supported the intensification of Fani.

3.6. Atmospheric parameters (VWS, MTRH and Divergence at 200 hPa)

TC intensities are greatly affected by VWS (DeMaria and Kaplan 1999; Fitzpatrick 1997; Hanley et al. 2001). The low VWS between 950 and 200 hPa levels reduces the 'ventilation effect' of latent heat released in the cumulonimbus clouds in the core region of the TC. For intensification, VWS values less than ~10 m s^{-1} is conducive, with values between ~2 and 4 m s^{-1} favouring rapid intensification (Paterson et al., 2005). Hence, the role of VWS in modulating the intensity of Phailin and Fani is being investigated.

The Central Pressure (CP) and Maximum Sustained Winds (MSW) of Phailin and Fani, obtained from JTWC six-hourly track data, are shown in the Figure 8a and b respectively.

Phailin was a category-5 TC with a CP and MSW of ~922 hPa and 140 knots on October 11, 2013 before encountering the cyclonic eddy. The CP increased to 948 hPa and the MSW decreased to 100 knots on October 12, 2013, equivalent to a category-4 TC, after encountering the cold-core eddy. The VWS along Phailin's track is shown in Figure 8e. The VWS values were less than 9 m s^{-1}, after October 10, 2013, making them conducive for intensification. Also, the intensity of Phailin was at its maximum (category-5) during this time. Phailin encountered the cold-core eddy on October 11, 2013. Despite the fact that the VWS values were favourable for intensification (10 m s^{-1}), Phailin weakened to a category-4 TC. Figure 8c shows the SST cooling averaged over a 1° × 1° box centred on Phailin's track. Significant SST cooling (3°C) occurred in the vicinity of Phailin's

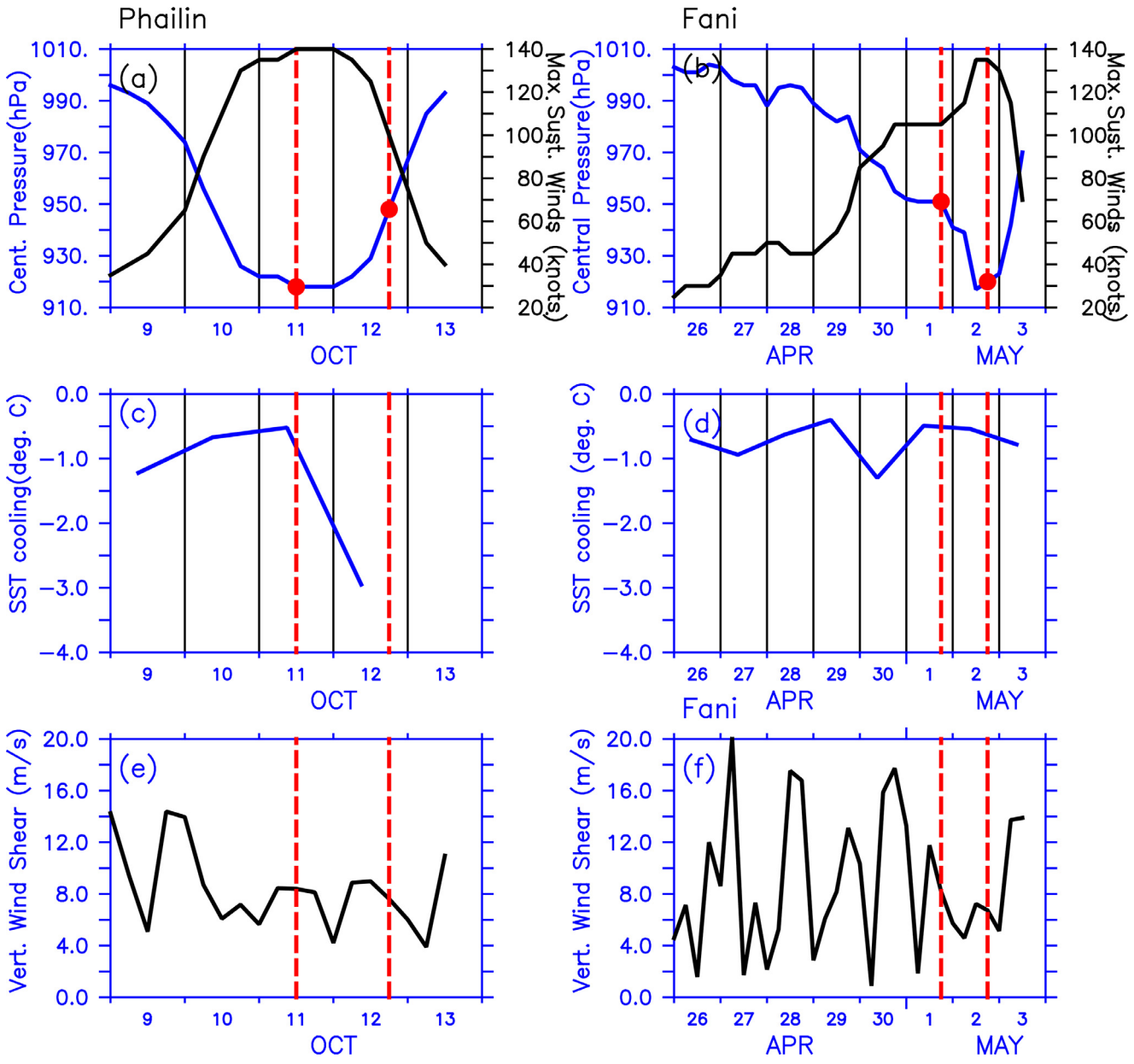

Figure 8 Central Pressure and Maximum Sustained Wind Speeds from JTWC track data (a) for Phailin and (b) for Fani. SST cooling averaged over a 1° × 1° box along the TC track (c) for Phailin and (d) for Fani. Vertical wind shear along the TC track (e) for Phailin (f) for Fani. The vertical red lines indicate the time of TC entering and leaving the eddy.

track in the areas of the cold-core eddy (Figures 3c and 8c). Strong cooling curtailed the supply of enthalpy fluxes (Figures 7a and c) dampening the intensity of Phailin.

Fani, on the other hand, was a Category 3 TC with a CP of ∼951 hPa and a MSW of ∼110 knots on May 01, 2019 (Figure 8b). The CP dropped to 917 hPa and the MSW increased to ∼135 knots after encountering the warm-core eddy. The VWS was ∼8 m s^{-1} when Fani encountered the warm-core eddy and remained less than ∼8 m s^{-1} favouring intensification (Figure 8f). Paterson et al. (2005) reported that values of VWS in this range will result in an intensification of ∼3 hPa. However, Fani experienced an intensification of ∼34 hPa. This suggests that VWS has only a minor effect on the intensification of Fani. The SST cooling averaged over a 1° × 1° box centred on the Fani's track is shown in Figure 8d. Weak SST cooling in the regions of warm-core eddy favoured the intensification of Fani (Figures 3f and 8d). The analysis of MTRH and divergence at 200 hPa during the pre-cyclonic days of Phailin and Fani has shown that these parameters have no significant contribution to modulating the intensity (Supplementary Figure S1).

4. Conclusions

The intensity modulation of TCs Phailin (2013) and Fani (2019) in the BoB is analysed in this study. Both the cyclones interacted with pre-existing mesoscale eddies before their landfall. The mesoscale eddies modulated the intensity of the two TCs. Phailin weakened to a category-3 TC

from a category-5 after encountering a cyclonic eddy. Contrastingly, Fani transected over an anticyclonic eddy and intensified. The surface and subsurface oceanic conditions in the BoB during the two TCs were analysed. The analysis revealed a pre-existing cyclonic eddy (SLA<25 cm) before the passage of Phailin. However, an anticyclonic eddy was present before the passage of Fani. Before Phailin, the SST in the BoB was 29.5°C. However, SST was much higher (>31°C) in the BoB before the onset of Fani. During Phailin, SST cooling in the BoB was minimal (1°C), with significant SST cooling (>2°C) restricted to cyclonic eddy regions. During Fani, significant SST cooling (>1°C) occurred south of 16°N. In contrast, the SST cooled very little (0.75°C) in the anticyclonic eddy regions.

The D26 isotherm and TCHP in the BoB during two TC periods were analysed to characterise the subsurface oceanic conditions. The D26 isotherm was observed to be shallower in the regions of cyclonic eddy compared to other regions in the BoB before the passage of Phailin. The TCHP values were also lower in the regions bounded by the cyclonic eddy due to shallow D26. Hence, significant SST cooling occurred in the regions confined by cyclonic eddy during the passage of Phailin, which favoured the weakening of Phailin. However, before Fani, the subsurface oceanic conditions in the regions of anticyclonic eddies were characterised by deep D26, which resulted in high TCHP. Hence, a weak SST cooling occurred in these regions during the passage of Fani. The weak SST cooling provided a conducive environment for the intensification of Fani over the anticyclonic eddy.

The enthalpy fluxes, especially LHF, play a significant role in controlling the TC intensity. Hence, LHF and SHF variations during the passage of two TCs over eddies were analysed. The LHF and SHF decreased by ∼20—30 W m^{-2} and ∼3 W m^{-2} respectively, in the region of the cyclonic eddy during Phailin on October 12, 2013. The analysis of VWS has shown that even though the shear was favourable for the intensification of Phailin, the strong SST cooling due to the cyclonic eddy curtailed the supply of enthalpy fluxes (especially LHF) and favoured the weakening of Phailin. Contrastingly, in the case of Fani, the weak SST cooling in the regions of anticyclonic eddy enhanced LHF supply from the ocean and favoured intensification. The estimates of VWS have shown that it played a minor role in Fani's intensification. The case study of the two TCs in the BoB has shown that the mesoscale oceanic eddies can modulate the intensity of TC. Hence, a thorough understanding of mesoscale eddies is vital for improving the accuracy of the TC intensity forecast.

Declaration of competing interest

The authors declare that they have no known competing financial interests or personal relationships that could have appeared to influence the work reported in this paper.

Acknowledgements

The authors thank the Ministry of Earth System Sciences, Govt. of India, for the support extended towards the moored buoy program. The authors are grateful to the Director, NIOT for the facilities and encouragement. The NIOT technical team is also acknowledged for maintaining the moored buoys.

Supplementary materials

Supplementary material associated with this article can be found, in the online version, at https://doi.org/10.1016/j.oceano.2022.02.005.

References

Babu, M.T., Sarma, Y.V.B., Murty, V.S.N., Vethamony, P., 2003. On the circulation in the Bay of Bengal during Northern spring intermonsoon (March—April 1987). Deep Sea Res. Pt. II 50, 855—865. https://doi.org/10.1016/S0967-0645(02)00609-4

Chaudhuri, D., Sengupta, D., D'Asaro, E., Venkatesan, R., Ravichandran, M., 2019. Response of the Salinity-Stratified Bay of Bengal to Cyclone Phailin. J. Phys. Oceanogr. 49, 1121—1140. https://doi.org/10.1175/JPO-D-18-0051.1

Chen, G., Wang, D., Hou, Y., 2012. The features and interannual variability mechanism of mesoscale eddies in the Bay of Bengal. Cont. Shelf Res. 47, 178—185. https://doi.org/10.1016/j.csr.2012.07.011

Cheng, X., McCreary, J.P., Qiu, B., Qi, Y., Du, Y., Chen, X., 2018. Dynamics of Eddy Generation in the Central Bay of Bengal. J. Geophys. Res. - Ocean 123, 6861—6875. https://doi.org/10.1029/2018JC014100

Cheng, X., Xie, S.-P., McCreary, J.P., Qi, Y., Du, Y., 2013. Intraseasonal variability of sea surface height in the Bay of Bengal. J. Geophys. Res. - Ocean 118, 816—830. https://doi.org/10.1002/jgrc.20075

Cione, J.J., Uhlhorn, E.W., 2003. Sea surface temperature variability in hurricanes: Implications with respect to intensity change. Mon. Waether Rev. 131, 1783—1796.

Demaria, M., Kaplan, J., 1994. Sea Surface Temperature and the Maximum Intensity of Atlantic Tropical Cyclones. J. Clim. 7, 1324—1334. https://doi.org/10.1175/1520-0442(1994)007<1324:SSTATM>2.0.CO;2

DeMaria, M., Kaplan, J., 1999. An updated statistical hurricane intensity prediction scheme (SHIPS) for the Atlantic and eastern North Pacific basins. Weather Forecast 14 (3), 326—337.

Donlon, C., Robinson, I., Casey, K.S., Vazquez-Cuervo, J., Armstrong, E., Arino, O., Gentemann, C., May, D., LeBorgne, P., Piollé, J., Barton, I., Beggs, H., Poulter, D.J.S., Merchant, C.J., Bingham, A., Heinz, S., Harris, A., Wick, G., Emery, B., Minnett, P., Evans, R., Llewellyn-Jones, D., Mutlow, C., Reynolds, R.W., Kawamura, H., Rayner, N., 2007. The Global Ocean Data Assimilation Experiment High-resolution Sea Surface Temperature Pilot Project. Bull. Am. Meteorol. Soc. 88, 1197—1214. https://doi.org/10.1175/BAMS-88-8-1197

Emanuel, K.A., 1986. An Air-Sea Interaction Theory for Tropical Cyclones. Part I: Steady-State Maintenance. J. Atmos. Sci. 43, 585—605. https://doi.org/10.1175/1520-0469(1986)043<0585:AASITF>2.0.CO;2

Emanuel, K.A., DesAutels, C., Holloway, C., Korty, R., 2004. Environmental Control of Tropical Cyclone Intensity. J. Atmos. Sci. 61, 843—858. https://doi.org/10.1175/1520-0469(2004)061<0843:ECOTCI>2.0.CO;2

Emanuel, K.A., 2013. Downscaling CMIP5 climate models shows increased tropical cyclone activity over the 21st century. PNAS 110 (30), 12219—12224. https://doi.org/10.1073/pnas.1301293110

Fisher, E.L., 1958. Hurricanes and the Sea-Surface Temperature Field. J. Atmos. Sci. 15, 328—333. https://doi.org/10.1175/1520-0469(1958)015<0328:HATSST>2.0.CO;2

Fitzpatrick, P.J., 1997. Understanding and forecasting tropical cyclone intensity change with the Typhoon Intensity Prediction Scheme (TIPS). Weather Forecast 12 (4), 826—846.

Gaube, P., J. McGillicuddy Jr., D., Moulin, A.J., 2019. Mesoscale Eddies Modulate Mixed Layer Depth Globally. Geophys. Res. Lett. 46, 1505—1512. https://doi.org/10.1029/2018GL080006

Hacker, P., Firing, E., Hummon, J., Gordon, A.L., Kindle, J.C., 1998. Bay of Bengal currents during the Northeast Monsoon. Geophys. Res. Lett. 25, 2769—2772. https://doi.org/10.1029/98GL52115

Halliwell, G.R., Gopalakrishnan, S., Marks, F., Willey, D., 2015. Idealized Study of Ocean Impacts on Tropical Cyclone Intensity Forecasts. Mon. Weather Rev. 143, 1142—1165. https://doi.org/10.1175/MWR-D-14-00022.1

Hanley, D., Molinari, J., Keyser, D., 2001. A composite study of the interactions between tropical cyclones and upper-tropospheric troughs. Mon. Weather Rev. 129 (10), 2570—2584.

Hersbach, H., Dee, D., 2016. ERA5 reanalysis is in production. ECMWF Newsl. 147, 5—6.

Jaimes, B., Shay, L.K., 2009. Mixed layer cooling in mesoscale oceanic eddies during Hurricanes Katrina and Rita. Mon. Weather Rev. 137, 4188—4207.

Kurien, P., Ikeda, M., Valsala, V.K., 2010. Mesoscale variability along the east coast of India in spring as revealed from satellite data and OGCM simulations. J. Oceanogr. 66, 273—289. https://doi.org/10.1007/s10872-010-0024-x

Li, Z., Yu, W., Li, T., Murty, V.S.N., Tangang, F., 2013. Bimodal character of cyclone climatology in the Bay of Bengal modulated by monsoon seasonal cycle. J. Climate 26 (3), 1033—1046.

Liang, J., Wu, L., Gu, G., 2018. Rapid Weakening of Tropical Cyclones in Monsoon Gyres over the Tropical Western North Pacific. J. Climate 31, 1015—1028. https://doi.org/10.1175/JCLI-D-16-0784.1

Liang, J., Wu, L., Gu, G., Liu, Q., 2016. Rapid weakening of Typhoon Chan-Hom (2015) in a monsoon gyre. J. Geophys. Res. Atmos. 121, 9508—9520. https://doi.org/10.1002/2016JD025214

Lin, I.-I., Chen, C.-H., Pun, I.-F., Liu, W.T., Wu, C.-C., 2009. Warm ocean anomaly, air sea fluxes, and the rapid intensification of tropical cyclone Nargis (2008). Geophys. Res. Lett. 36. https://doi.org/10.1029/2008GL035815

Lin, I.-I., Wu, C.-C., Emanuel, K.A., Lee, I.-H., Wu, C.-R., Pum, I.-F., 2005. The interaction of Supertyphoon Maemi with a warm ocean eddy. Mon. Waether Rev. 133, 2635—2649. https://doi.org/10.1175/MWR3005.1

Liu, Y., LÜ, H., Zhang, H., Cui, Y., Xing, X., 2021. Effects of ocean eddies on the tropical storm Roanu intensity in the Bay of Bengal. Plos one 16 (3), e0247521.

Lloyd, I.D., Vecchi, G.A., 2011. Observational Evidence for Oceanic Controls on Hurricane Intensity. J. Climate 24, 1138—1153. https://doi.org/10.1175/2010JCLI3763.1

Ma, Z., Fei, J., Huang, X., Cheng, X., 2015. Contributions of surface sensible heat fluxes to tropical cyclone. Part I: Evolution of tropical cyclone intensity and structure. J. Atmos. Sci. 72, 120—140. https://doi.org/10.1175/JAS-D-14-0199.1

Ma, Z., 2018. Examining the contribution of surface sensible heat flux induced sensible heating to tropical cyclone intensification from the balance dynamics theory. Dyn. Atmos. Oceans 84, 33—45. https://doi.org/10.1016/j.dynatmoce.2018.09.001

Ma, Z., Fei, J., Huang, X., Cheng, X., Liu, L., 2020. A Study of the Interaction between Typhoon Francisco (2013) and a Cold-Core Eddy. Part II: Boundary Layer Structures. J. Atmos. Sci. 77, 2865—2883. https://doi.org/10.1175/JAS-D-19-0339.1

Mainelli, M., DeMaria, M., Shay, L.K., Goni, G., 2008. Application of Oceanic Heat Content Estimation to Operational Forecasting of Recent Atlantic Category 5 Hurricanes. Weather Forecast 23, 3—16. https://doi.org/10.1175/2007WAF2006111.1

McTaggart-Cowan, R., Bosart, L.F., Davis, C.A., Atallah, E.H., Gyakum, J.R., Emanuel, K.A., 2006. Analysis of Hurricane Catarina (2004). Mon. Weather Rev. 134, 3029—3053.

Mei, W., Pasquero, C., 2013. Spatial and Temporal Characterization of Sea Surface Temperature Response to Tropical Cyclones. J. Climate 26, 3745—3765. https://doi.org/10.1175/JCLI-D-12-00125.1

Navaneeth, K.N., Martin, M.V, Joseph, K.J., Venkatesan, R., 2019. Contrasting the upper ocean response to two intense cyclones in the Bay of Bengal. Deep Sea Res. Pt. I 147, 65—78. https://doi.org/10.1016/j.dsr.2019.03.010

Neetu, S., Lengaigne, M., Vialard, J., Samson, G., Masson, S., Krishnamohan, K.S., Suresh, I., 2019. Premonsoon/postmonsoon Bay of Bengal tropical cyclones intensity: Role of air-sea coupling and large-scale background state. Geophys. Res. Lett. 46 (4), 2149—2157.

Paterson, L.A., Hanstrum, B.N., Davidson, N.E., Weber, H.C., 2005. Influence of environmental vertical wind shear on the intensity of hurricane-strength tropical cyclones in the Australian region. Mon. Weather Rev. 133 (12), 3644—3660.

Prasanna Kumar, S., Nuncio, M., Narvekar, J., Kumar, A., Sardesai, S., de Souza, S.N., Gauns, M., Ramaiah, N., Madhupratap, M., 2004. Are eddies nature's trigger to enhance biological productivity in the Bay of Bengal? Geophys. Res. Lett. 31, L07309. https://doi.org/10.1029/2003GL019274

Prasanna Kumar, S., Nuncio, M., Ramaiah, N., Sardesai, S., Narvekar, J., Fernandes, V., Paul, J.T., 2007. Eddy-mediated biological productivity in the Bay of Bengal during fall and spring intermonsoons. Deep Sea Res. Pt. I 54, 1619—1640. https://doi.org/10.1016/J.DSR.2007.06.002

Price, J.F., 1981. Upper ocean response to a hurricane. J. Phys. Oceanogr. 11 (2), 153—175.

Rappaport, E.N., Jiing, J.-G., Landsea, C.W., Murillo, S.T., Franklin, J.L., 2012. The Joint Hurricane Testbed: Its first decade of tropical cyclone research-to-operations activities reviewed. Bull. Amer. Meteor. Soc. 93, 371—380.

Riehl, H., 1954. Variations of energy exchange between sea and air in the trades. Weather 9, 335—340. https://doi.org/10.1002/j.1477-8696.1954.tb01706.x

Sadhuram, Y., Maneesha, K., Ramana Murty, T.V., 2012. Intensification of Aila (May 2009) due to a warm core eddy in the north Bay of Bengal. Nat. Hazards 63, 1515—1525. https://doi.org/10.1007/s11069-011-9837-1

Sengupta, D., Goddalehundi, B.R., Anitha, D.S., 2008. Cyclone-induced mixing does not cool SST in the post-monsoon north Bay of Bengal. Atmos. Sci. Lett. 9, 1—6. https://doi.org/10.1002/asl.162

Shay, L.K., Goni, G.J., Black, P.G., 2000. Effects of a Warm Oceanic Feature on Hurricane Opal. Mon. Weather Rev. 128, 1366—1383. https://doi.org/10.1175/1520-0493(2000)128<1366:EOAWOF>2.0.CO;2

Singh, V.K., Roxy, M.K., Deshpande, M., 2021. Role of warm ocean conditions and the MJO in the genesis and intensification of extremely severe cyclone Fani. Sci. Rep. 11, 3607. https://doi.org/10.1038/s41598-021-82680-9

Venkatesan, R., Shamji, V.R., Latha, G., Mathew, S., Rao, R.R., Muthiah, A., Atmanand, M.A., 2013. In situ ocean subsurface time-series measurements from OMNI buoy network in the Bay of Bengal. Current Sci. 104 (9), 1166—1177.

Vinayachandran, P.N., 2013. Impact of Physical Processes on Chlorophyll Distribution in the Bay of Bengal, Indian Ocean Biogeochemical Processes and Ecological Variability. Geophys. Monogr. Ser. https://doi.org/10.1029/2008GM000705

Wang, C., Wu, L., 2018. Future Changes of the Monsoon Trough: Sensitivity to Sea Surface Temperature Gradient and Implications for Tropical Cyclone Activity. Earth's Futur. 6, 919—936. https://doi.org/10.1029/2018EF000858

Oceanologia 64 (2022) 457—472

Available online at www.sciencedirect.com

ScienceDirect

journal homepage: www.journals.elsevier.com/oceanologia

ORIGINAL RESEARCH ARTICLE

Numerical study of coastal wave profiles at the sandy beaches of Nowshahr (Southern Caspian Sea)

Seyed Masoud Mahmoudof*, Mohammadali Lotfi Takami

Iranian National Institute for Oceanography and Atmospheric Sciences (INIOAS), Tehran, Iran

Received 14 November 2021; accepted 9 March 2022
Available online 20 March 2022

KEYWORDS
SWASH Model;
Caspian Sea;
Wave evolution;
Infragravity waves;
Short wind-waves

Abstract This study aimed to investigate the capability of the one-dimensional (1D) mode of the Simulating WAves till SHore (SWASH), as a non-hydrostatic wave-flow model with six vertical layers, to reproduce the cross-shore wave evolution. For this purpose, the given model was initially calibrated for wave energy and the outputs were then verified with the field data measured at the Southern Caspian Sea. The calibration coefficients obtained for wave breaking are significantly less than the ones which have been mostly reported in previous studies for the two-dimensional (2D) mode of the SWASH. Although the reproduced wave height parameters are generally in good accordance with the field observations, the period parameters and the number of waves are overestimated and underestimated by the model, respectively. Moreover, the inaccuracies at the shallow stations are worse than at the transitional depths. The overestimation in both the reproduced energy of infragravity waves (IG) and their wavelength along with the underestimation in the wind-wave energy content are also among the factors responsible for the model deficiencies. The findings have revealed that the overestimation of the reproduced IG waves is the main reason for the underestimation of the breaking dissipation rate for irregular wave trains in the 1D mode. Therefore, more intensive breaking dissipation via selecting lower coefficient values is necessary to exhaust a certain energy content from longer waves in the 1D mode. This approach ultimately induces an over-dissipation of short wind-waves.

* Corresponding author at: Iranian National Institute for Oceanography and Atmospheric Sciences (INIOAS), Tehran, 1411813389, Iran.
E-mail address: m_mahmoudof@inio.ac.ir (S.M. Mahmoudof).
Peer review under the responsibility of the Institute of Oceanology of the Polish Academy of Sciences.

Production and hosting by Elsevier

https://doi.org/10.1016/j.oceano.2022.03.001

1. Introduction

Almost all nearshore hydrodynamic processes are controlled by wave transformations. Wind-waves, with periods lasting between 4 and 20 s, propagating toward shorelines also sense seabed disturbance, become skewed and asymmetric, and then break. The energy released from depth-induced wave breaking then drives nearshore currents, rips, and undertows and consequently causes sediment transport and morphological changes (Hoefel and Elgar, 2003; Longuet-Higgins and Stewart, 1964; Longuet-Higgins, 1970; MacMahan et al., 2006; Svendsen, 1984). Some energy content also transfers to low-frequency waves, known as infragravity (IG) waves or surf beat, having periods in the range of 20–200 s, and some other part transfers to higher harmonics through wave coupling or bore waves.

The IG waves, with small heights in deep water (Webb et al., 1991), may thus have the most energy contribution of the total wave train across inner surf and swash zones, especially under high-energy conditions (Gao, et al., 2019; Guza and Thornton, 1982). The domination of IG waves for stormy conditions in very shallow water also results in energy spectra with IG peaks, concurrent with flattening wind-wave peaks due to breaking dissipation. Numerous studies reported the stronger dependency of IG wave energy on swell than sea waves (e.g., Elgar et al., 1992; Mahmoudof, 2018a; Ruessink, 1998). Such waves can have significant impacts on dune erosion, sand bar, or mudflat formation (de Bakker et al., 2016a; de Vries et al., 2008; Roelvink et al., 2009), and may give rise to resonance and disorder in continuous dock operations in large harbors (Gao et al., 2020, 2021; González-Marco et al., 2008). The time-varying breakpoints of irregular waves during high-energy conditions and negative nonlinear wave-wave interactions under moderate conditions are known as two main generating sources of released and bound IG waves, respectively (Hasselmann, 1962; Longuet-Higgins and Stewart, 1962; Symonds et al., 1982). Battjes et al. (2004) realized the role of normalized bed slope parameter as $\beta_b = \frac{\alpha}{\omega}\sqrt{\frac{g}{d_b}}$ in the domination of each generating mechanism of IG waves. In this relationship, α is the bed slope, ω denotes the angular frequency, g, and d_b are the gravitational acceleration and the averaged breaking depth, respectively. In a mild-slope regime with $\beta_b < 0.3$, the generation of bound IG type as a result of nonlinear interactions is dominant. Larger values of β_b imply a steep-slope regime wherein the released type of IG due to moving breakpoints dominates in the surf zone. On very steep beaches or coastal cliffs, wherein IG waves are not fully dissipated, a significant proportion of their energy can thus reflect toward the sea, resulting in significant reflection coefficients close to or even greater than unity (Guza and Thornton, 1985; Mahmoudof et al., 2021; Sheremet et al., 2002). However, the energy of such waves is considerably dissipated until shorelines. The dissipation mechanisms of these waves have been thus far discussed in numerous studies (e.g., de Bakker et al. 2014; Ruju et al., 2012). On the other hand, positive triad wave-wave interaction is one of the processes that can transfer energy to higher harmonics in the shoaling zone. The primary swell waves can also decouple and decompose to several shorter and smaller secondary waves indicating a mild energy transfer to high-frequency harmonics especially on barred beaches (Masselink, 1998).

Considering the complexity of coastal hydrodynamic processes controlled by wave transformation, numerical models are useful tools to assess and predict these phenomena. Therefore, the models proposed for this purpose need to evaluate coastal wave evolution accurately. To meet this objective, wave characteristics and statistics (e.g., wave heights and period parameters) reproduced by such models must be verified with those observed in the field and laboratory measurements.

In this regard, phase-averaged or spectral wave models operate based on the energy-action equation, and solve the known source and sink terms (Komen et al., 1994; the Wave Model Development and Implementation Group [WAMDI], 1988). One of the important assumptions of these models is that the wave field is often founded on the near-Gaussian distribution, which is not valid in the shallow waters of nearshores due to the nonlinear effects of the wave field. The inaccuracy of phase-averaged models as a result of this discrepancy accordingly reveals the demand for models with the capability to capture high-order wave-wave interactions and reproduce wave nonlinearities near the shores.

Phase-resolving wave models can simulate the nonlinearities of shallow-water waves and reproduce nearshore hydrodynamic processes driven by wave transformations. Generally, the success of these models to represent coastal wave evolution has been thus far confirmed in several studies (e.g., Madsen et al., 2002; Torres-Freyermuth et al., 2007). The main concerning problem facing the application of these models is their high computational cost and time, even for small-scale domains. The Boussinesq and non-hydrostatic types of phase-resolving models are generally exploited to simulate coastal scale applications. The first type is a developed representation of weakly dispersive models (Gao, et al., 2017; Madsen et al., 2002; Nwogu, 1993; Wei et al., 1995). On the other hand, the non-hydrostatic models solve the basic conservation equations for mass and momentum (Ma et al., 2012; Stelling and Zijlema, 2003; Yamazaki et al., 2009). In the non-hydrostatic models, the free surface of the water is described using a single-valued function of the horizontal plane. However, these models often fail to accurately reproduce the details of wave-breaking processes such as air entrainment, wave-induced turbulence, and overturning.

The Simulating WAves till Shore (SWASH), as a non-hydrostatic wave-flow model based on nonlinear shallow water equations, is capable to explain complex changes in rapidly varying flows. The model assumes a hydrostatic pressure approximation in the frontline of breaking waves, ensuring that the waves develop a vertical face. The SWASH is also known as a valuable tool to investigate coastal wave processes controlled by wave breaking, such as frequency energy transfer, cease of wave-wave coupling, as well as IG wave generation and dissipation. Thus, an accurate evaluation of coastal wave breaking and evolution is a prerequisite to attain a proper estimation of other dependent processes. Although the model can simulate complex patterns in horizontally two-dimensional (2D) configurations, the horizontally one-dimensional (1D) mode is usually sufficient to study most wave evolution processes with efficient modeling time for engineering applications.

Coastal wave transformation reproduced by the SWASH has been thus far extensively validated against laboratory experiments. In this regard, Torres-Freyermuth et al. (2012) reported a good agreement between the model outcomes and the experimental measurements for wave transformation on a fringing reef. As well, Smit et al. (2013 and 2014) compared the model outputs with some experimental observations of random and unidirectional waves on a mild-slope beach, wherein the general success of the model to reproduce the surf zone wave characteristics was verified. Ruju et al. (2014) similarly confirmed the model reliability to simulate the run-up induced by irregular wave breaking on a gentle-slope beach by comparing the model results with laboratory experiment measurements. Moreover, de Bakker et al. (2016b) showed the appropriate capability of the SWASH to represent the IG waves generated by nonlinear triad interactions, using the experimental data recorded by Ruessink et al. (2013). In the same way, Mendes et al. (2018) assessed the impact of bars on energy transfer between IG and wind-waves on a dissipative beach utilizing the SWASH.

In contrast to laboratory validations, comparisons between the model results and field measurements are not very extensive. Moreover, some of these few studies incorporating field validations deduced the underestimation of wave-breaking dissipation and the overestimation of IG wave generation by the default 1D mode of the SWASH (e.g., de Bakker et al., 2014; Lerma et al., 2017). Therefore, the present study aimed to accurately investigate the capability of the 1D mode of SWASH to reproduce the profiles and characteristics of nearshore waves during storm periods. The model results were then compared with in-situ data measured on the Nowshahr beaches, located in the Southern Caspian Sea.

In this study, field measurements and conditions are explained in Section 2, and the numerical governing equations and model setup are reviewed in Section 3, as well as analysis methods are provided in Section 4. The results and their discussions, including the model calibration and the findings of time and frequency domain analyses, are then presented in Section 5, and the study is concluded in the last section.

2. Field study area

The Caspian Sea is the largest lake in the world, enclosed between Azerbaijan, Iran, Kazakhstan, Russia, and Turkmenistan. This inland water body has a 371,000 km^2 area and its freshwater is mostly provided by the Volga, the longest European river. The Caspian Sea is divided into three geographic regions, namely, the Northern, the Middle, and the Southern parts. The oceanic depths of more than 900 m can be found in the Southern Caspian Sea. The Northern and Middle parts are typically frozen within winter. This region is mostly encountering northwesterly strong winds, resulting in various hydrodynamic phenomena dependent on wave transformation on the southern beaches of the Caspian Sea. The negligible tidal range in the Southern part, commonly less than 10 cm, alongside the sandy beaches, provides a suitable environment to study shallow-water wave transformations.

The field data acquisition, including water level variations, was thus accomplished on a straight shore perpendicular transect located in the west of Nowshahr Port on the Southern Caspian Sea (Figure 1a). The study area has a sandy and single-barred beach. The measurement program was accordingly started on March 4, 6:00 p.m., and terminated on March 16, 9:00 a.m., 2014, lasting 13 days. Five pressure sensors and an Acoustic Doppler Current Profiler (ADCP) were deployed on the transect at the stations with depths varying between 4.8 m out of the surf zone till 0.8 m near the shore (Figure 1b). A buoy, installed at the depth of 22.5 m by the Iranian Ports and Maritime Organization, also measured the offshore spectral wave height. However, the data collected at this station were not applicable in the present study since the time series of the water level was not accessible. The water column pressure data were continuously recorded at ST1 and ST2 with a rate of four pieces of data per second. Moreover, the water-level and directional wave data were uninterruptedly measured for 17.07 min per hour by the ADCP at ST6. The pressure data were additionally gathered by pressure transducers at the other three stations with a sampling rate of 1 Hz. Data retrieval was mandatory after two days of measurement at these three stations due to the capacity of the data logger. Data recording was also conducted for three two-day cycles at ST3 and ST4 and one cycle at ST5. More details on instrumentation and measurement conditions are presented in Table 1.

The current profiles were measured using the ADCP at ST6 by averaging the velocity values within 20 minutes for each hour. The recoded current magnitude values were less than 0.1 m/s, indicating that no important event, dependent on current interactions, was expected.

The bathymetric data and beach profile were also gathered and recorded by a single-beam echo sounder at the beginning and end of the field measurement period. No significant bathymetric variation could be pointed out within the field measurement period. Moreover, the processed hydrographic data demonstrated no significant lateral variation and bathymetric event, parallel the shoreline. The recorded profile also has a mild bed with an averaged seaward slope of approximately 0.02. Some complementary details about field measurements can be realized in Mahmoudof et al. (2016).

3. Methods

3.1. Governing equations

Over the last decade, non-hydrostatic models have been increasingly implemented to simulate wave evolution under very different conditions, extended from long tsunami waves in oceanic scales to short wind-waves in coastal applications. The SWASH (Zijlema et al., 2011), as an open-source flow-wave model, is thus capable to simulate the free surface of waters, based on non-hydrostatic pressure distribution. The model can also describe nearshore wave transformations across surf and swash zones as results of nonlinear wave interactions, breaking, and runup at shorelines. The model can generally address the equations in the orthogonal and vertical multi-layered approach

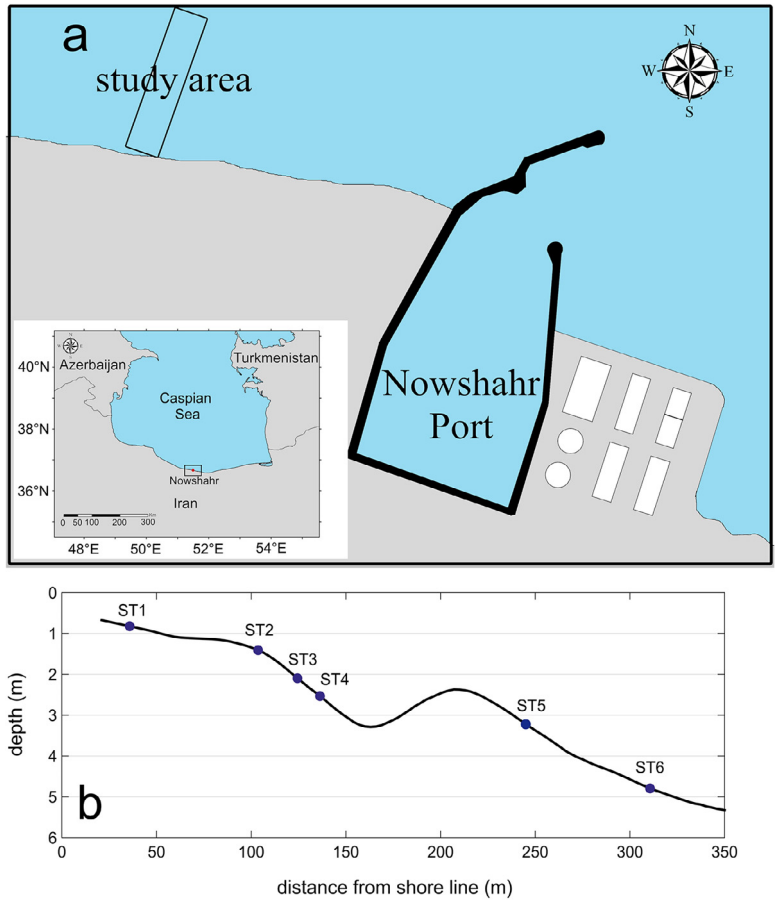

Figure 1 a) Location of the study area; b) bed profile variations of study area and measurement station positions.

Table 1 Characteristics of measurement stations.

Stations	Instrument name	Sampling rate (Hz)	Depth (m)	Distance from shore (m)	Duration
ST1	RBRvirtuoso	4	0.8	35	2014/03/04 – 2014/03/16 (continuously)
ST2	RBRvirtuoso	4	1.4	103	2014/03/04 – 2014/03/16 (continuously)
ST3	DST-centi Star-Oddi	1	2.2	120	2014/03/05 – 2014/03/07, 2014/03/09 – 2014/03/11, 2014/03/12 – 2014/03/14
ST4	DST-centi Star-Oddi	1	2.5	135	2014/03/05 – 2014/03/07, 2014/03/09 – 2014/03/11, 2014/03/12 – 2014/03/14
ST5	DST-centi Star-Oddi	1	3.2	245	2014/03/05 – 2014/03/07
ST6	ADCP	2	4.8	310	2014/03/03 – 2014/03/16 (continuously)

although they are typically introduced in the Cartesian system for simplicity purposes. These governing equations are the Reynolds-Averaged Navier-Stokes (RANS) types for an incompressible and constant-density fluid, which can explain nonlinear shallow-water events. However, the SWASH solves the transformed representation of the following equations in the sigma vertical-layer system:

$$\frac{\partial \eta}{\partial t} + \frac{\partial}{\partial x}\int_{-d}^{\eta} u dz = 0 \tag{1}$$

$$\frac{\partial u}{\partial t} + \frac{\partial uu}{\partial x} + \frac{\partial wu}{\partial z} = -\frac{1}{\rho}\frac{\partial (P_h + P_{nh})}{\partial x} + \frac{\partial \tau_{xz}}{\partial z} + \frac{\partial \tau_{xx}}{\partial x} \tag{2}$$

$$\frac{\partial w}{\partial t}+\frac{\partial uw}{\partial x}+\frac{\partial ww}{\partial z}=-\frac{1}{\rho}\frac{\partial P_{nh}}{\partial z}+\frac{\partial \tau_{zz}}{\partial z}+\frac{\partial \tau_{zx}}{\partial x} \quad (3)$$

$$\frac{\partial u}{\partial x}+\frac{\partial w}{\partial z}=0 \quad (4)$$

where η stands for the free water surface relative to still water level, t denotes the time, d is the still water depth, u and w indicate the depth-averaged flow velocities in the x and z directions, respectively, g shows the gravitational acceleration, ρ represents the fluid density, P_h and P_{nh} are the hydrostatic and non-hydrostatic pressure terms, respectively, and τ parameters are turbulent stresses evaluated based on a turbulent viscosity approximation and applying a standard κ-ε model (e.g., $\tau_{xz} = \nu\partial_z u$, where ν is the kinematic eddy-viscosity).

Near the shores, the main restricting and dissipating factor for wave energy is depth-induced wave breaking, which can exhaust considerable energy content within a few hundred meters. In the SWASH, energy dissipation due to wave breaking is applied by considering the similarity between breaking waves and moving hydraulic jumps along with controlling the vertical speed of the free surface. Accordingly, the wave breaking initiates once this value exceeds a breaking threshold ($\alpha < 1$) of the shallow water celerity as follows:

$$\frac{\partial \eta}{\partial t} > \alpha\sqrt{gh} \quad (5)$$

The wave breaking is also persistent while the fraction coefficient drops to β ($< \alpha$). The default values of α and β coefficients have been respectively set as 0.6 and 0.3 according to Smit et al. (2013), in agreement with Longuet-Higgins and Fox (1977). However, the values of these coefficients depend on the number of vertical layers for each simulation and can be set for a certain vertical layer number. For simulating mild nonlinear waves, propagating from deep to transitional depth, applying one to three layers is often sufficient for the model to capture the wave characteristics in an accurate manner (Smit et al., 2013). In shallow waters, wherein waves are highly nonlinear and close to break and flow velocity gradients increase, higher resolution is necessary for traditional non-hydrostatic models to accurately capture the vertical speed of the free surface. High vertical resolution also increases the time of simulation and reveals the importance of time and accuracy management for modeling purposes. However, the numerical approaches embedded in the SWASH can provide an opportunity to resolve nearshore wave evolution with relatively lower vertical layer numbers (see e.g., Rijnsdrop et al., 2015; Smit et al., 2014). In several studies, different vertical layers have been also applied to assess wave hydrodynamics in the presence of broken waves. In this line, de Bakker et al. (2014), Rijnsdrop et al. (2015), and Lerma et al. (2017) employed two vertical layers, and de Bakker et al. (2016b) and Mendes et al. (2018) set six layers in the vertical direction following Smit et al. (2014).

3.2. Model setup

The present simulation was performed in a non-stationary and 1D mode of the SWASH (version 7.01) using the Cartesian coordinate as the reference framework. It is usually recommended that the numerical spatial resolution should be typically set as 1/100 to 1/50 of the dominant wavelength for flow-wave models to accurately capture wave dynamics (Smit et al., 2013). In the present simulations, the computational grid size was thus selected to be equal to 0.4 m in the 1D mode match to less than 1/150 wavelength, corresponding to the stormy peak period. Therefore, the computational distance with a length of 380 m was divided into 950 separated meshes. This resolution could ensure that at least 30 points were appointed per wavelength for the waves up to $3f_p$ (as three times the main peak frequency) to accurately capture the characteristics of the dominant wavefield. The vertical resolution was additionally defined with six equidistant layers for the model to reproduce the wave evolution in an accurate manner. The time step was also set at $\Delta t = 0.005$ s. The simulation was then repeated for 300 measured bursts for 1200 s. As well, the open boundary was forced by 2048 water level data gathered by the ADCP at ST6 with the rate of 2 Hz. The water level data were also recorded at the locations corresponding to the other five measurement stations. The analyses were accomplished on the most energetic time series with a 1024-s duration for each station and burst. The breaker parameters were regarded as the calibration coefficients to tune the coastal wave energy in the surf zone. Other input parameter values were also set to the default values embedded in the SWASH.

4. Analysis method

In the present study, the SWASH performance to predict the wave transformation in the nearshore shallow water has been investigated qualitatively and quantitatively. Therefore, the time and frequency domain analyses have been accomplished to process the model results and field measurements. The field pressure data were thus converted into water-level ones, applying the depth attenuation-correction method considering the frequency of $f = 0.35$ Hz as the upper correction limit and wind-wave cutoff. The time-domain analysis is founded on zero-down/up crossing analysis. The significant wave height in the time domain analysis ($H_{1/3}$) is defined as the mean of the highest one-third of the waves as follows:

$$H_{1/3}=\frac{1}{N/3}\sum_{j=1}^{N/3}H_j \quad (6)$$

where j represents the rank number of the sorted waves according to their heights in the zero-crossing analysis. The corresponding period parameter to $H_{1/3}$ is also $T_{1/3}$ and calculated as follows:

$$T_{1/3}=\frac{1}{N/3}\sum_{j=1}^{N/3}T_j \quad (7)$$

wherein j is defined as the above and T_j shows the period of waves in the zero-crossing analysis. The parameters of mean height (H_{mean}) and mean period (T_{mean}) of the wave train are also expressed as the average height and period of total waves in a similar approach. It is clear that the number of total counted waves (hereafter referred to as *nw*) is a key factor in the time domain analysis.

For the spectral analysis, all 1024-s time series of water levels, resulting from the measurements and reproduced by the model, were divided into 128-s data blocks with 50% overlap. The coefficients developed from the fast Fourier transform (FFT) were then averaged for each frequency. Therefore, the degree of freedom and fundamental frequency of analysis were approximated as 32 and 0.0078 Hz, respectively.

The frequency of $f = 0.05$ Hz was also regarded as the separation threshold of IG and wind (sea-swell) waves following previous studies (e.g., Herbers et al., 1994, 1995; Thomson et al., 2006). In some researches, the frequency threshold of $f = 0.04$ had been similarly applied for longer oceanic IG waves (e.g., Elgar et al., 1992; Inch et al., 2017; Ruessink, 1998). The heights of IG (H_{ig}) and wind-waves (H_{ss}) were accordingly calculated using the following relationships, respectively:

$$H_{ig} = 4.004\sqrt{\int_0^{0.05\ Hz} E(f)\,df} \tag{8}$$

$$H_{ss} = 4.004\sqrt{\int_{0.05}^{0.35\ Hz} E(f)\,df} \tag{9}$$

where $E(f)$ shows the energy density of wave trains at the frequency of f. Three standard statistical indices of the scatter index (SI), the index of agreement (IA), and the normalized bias (NB) were also utilized to assess the performance and accuracy of the model to reproduce the wave energy content (spectral height; H_{m0}). The predicted and observed values of the wave height (H_{pre} and H_{obs}, respectively) were then placed in the following relationships to calculate the values of the above-mentioned statistical indices.

$$SI = \frac{\sqrt{\frac{1}{N}\sum_{i=1}^{N}\left(H_{pre}^{i} - H_{obs}^{i}\right)^2}}{\bar{H}_{obs}} \tag{10}$$

$$IA = 1.0 - \frac{\sum_{i=1}^{N}\left(H_{pre}^{i} - H_{obs}^{i}\right)^2}{\sum_{i=1}^{N}\left(\left|H_{pre}^{i} - \bar{H}_{obs}\right| + \left|H_{obs}^{i} - \bar{H}_{obs}\right|\right)^2} \tag{11}$$

$$NB = \frac{\sum_{i=1}^{N}\left(H_{pre}^{i} - H_{obs}^{i}\right)}{\sum_{i=1}^{N} H_{obs}^{i}} \tag{12}$$

5. Results and discussion

5.1. Field observations of wave regime

Two storms were the most important events recorded during the field measurements in this study. The wave heights within these two storms also reached approximately 1.3 m (Figure 2). The maximum peak period was more than 9 s and the maximum deviation of mean wave direction from the shore normal direction was 4°. The wave spectra for the storms were composed of one wave system with one single significant peak. As well, the offshore stormy waves had not broken before reaching ST6 according to the observational investigations at the coastal watchtower. The waves of both storms were modest swells, originated from the Middle Caspian Sea near 600 km away from the study area. During the storms, the local wind was also calm with velocities less than 6 m/s, recorded by a coastal synoptic station installed 10 km west of the study area.

Of note, very long-traveling and highly energetic swell waves can't be generally expected in the Caspian Sea due to the absence of a very long fetch, as well frozen body in the Northern part for more than half a year. In the present study, the bursts with the measured wave heights greater than 0.6 m at ST6 (including 19 and 30 bursts within the first and second storms, respectively) were thus supposed as high-energy conditions. The wave breaking was also the dominant shoreward phenomenon for such bursts. Therefore, they were utilized and investigated to tune the depth-induced wave breaking in the SWASH. The directional wave data gathered by the ADCP at ST6 also revealed minor wave reflections from the shoreline. The measured reflection coefficients calculated based on the method explained by Mahmoudof and Azizpour (2020) were less than 8% for the energetic wave conditions.

5.2. Wave energy content calibration

Most nearshore and coastal hydrodynamic processes are controlled by the energy content received from incident waves, directly or indirectly. Therefore, it is necessary to ensure the accuracy of numerical hydrodynamic models in the evaluation of significant spectral wave heights with an emphasis on wave energy. Accordingly, applying an accurate wave-breaking scheme is mandatory for numerical models to appropriately reproduce coastal phenomena.

As mentioned before, the SWASH regards the breaking dissipation for waves with the ratio of vertical speed of free surface to shallow water celerity, varying between β and α ($\beta < \alpha < 1$). The default values of α and β coefficients embedded in the SWASH are also respectively 0.6 and 0.3, according to the modeling results proposed by Smit et al. (2013) with two vertical layers. However, these values have resulted in a significant overestimation of spectral wave heights ($SI = 0.24$, $NB > 0.22$, and $IA < 0.38$) in the present study with the applied model setup within storm periods. This preliminary result indicates that the dissipation of default wave breaking setup is not sufficient for the present 1D mode of the SWASH, in agreement with the findings reported by Lerma et al. (2017). Therefore, considering the breaking parameters as the calibration coefficients was necessary to tune the energy of stormy waves within the studied surf zone. The numerical model was repeated 80 times with different values of α and β in the range of 0.2–0.6 and 0.05–0.30, respectively, with emphasis on pairs incorporating $\alpha < 0.4$ to compensate for the abovementioned overestimation. The statistical indices Eqs. (10)–(12) were then calculated for these 80 tests and three two-dimensional (2D) planes were developed via the Kriging technique (see https://worldwidescience.org/topicpages/k/kriging+interpolation+technique.html for more scientific details) for interpolation and extrapolation. The results are illustrated in Figure 3, wherein the data are shown as black dots in these diagrams. The hollow areas at upper left corners of the diagrams are indicating ranges with $\alpha < \beta$ conditions as theoretically unacceptable values of α and β. All the statistical indices confirm that the coefficients of $\alpha = 0.25$ and $\beta = 0.13$ have resulted in the most accurate reproduction of spectral significant wave height (H_{m0}) during high

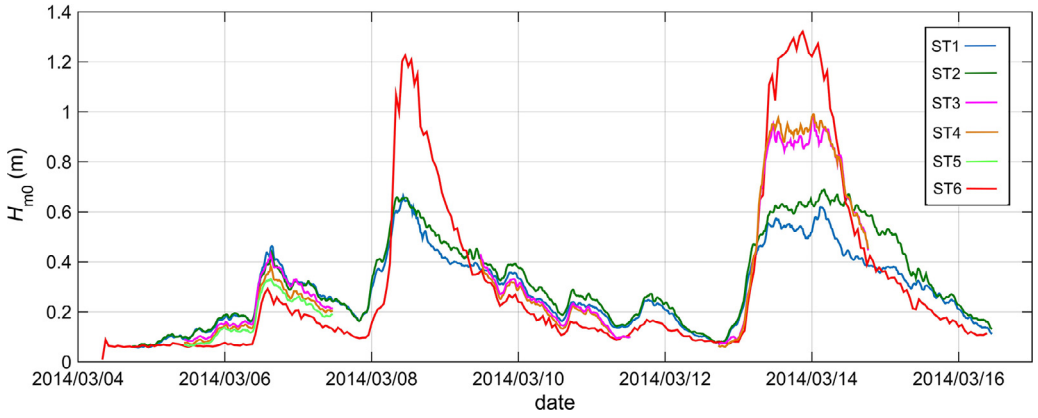

Figure 2 Variations of significant wave heights measured at the six stations within the measurement period.

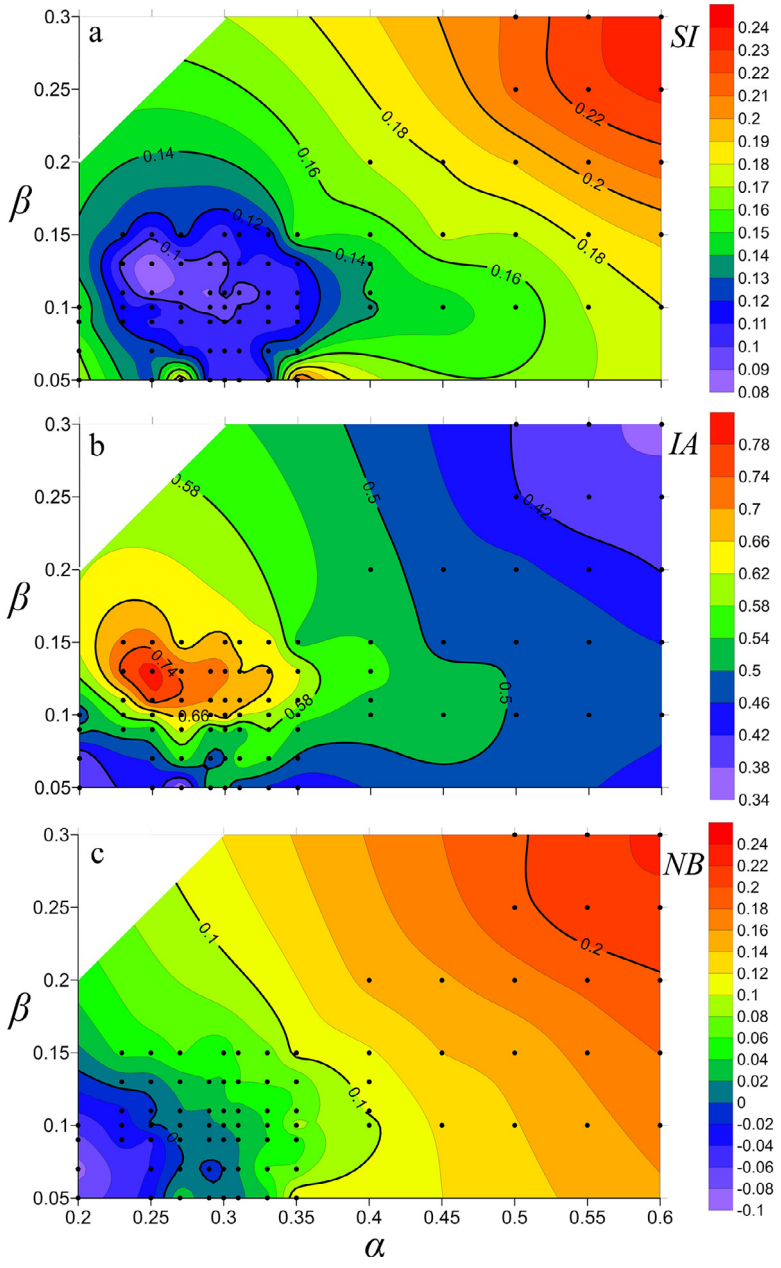

Figure 3 Distribution of statistical indices as functions of α and β; a) *SI*; b) *IA*; and c) *NB*.

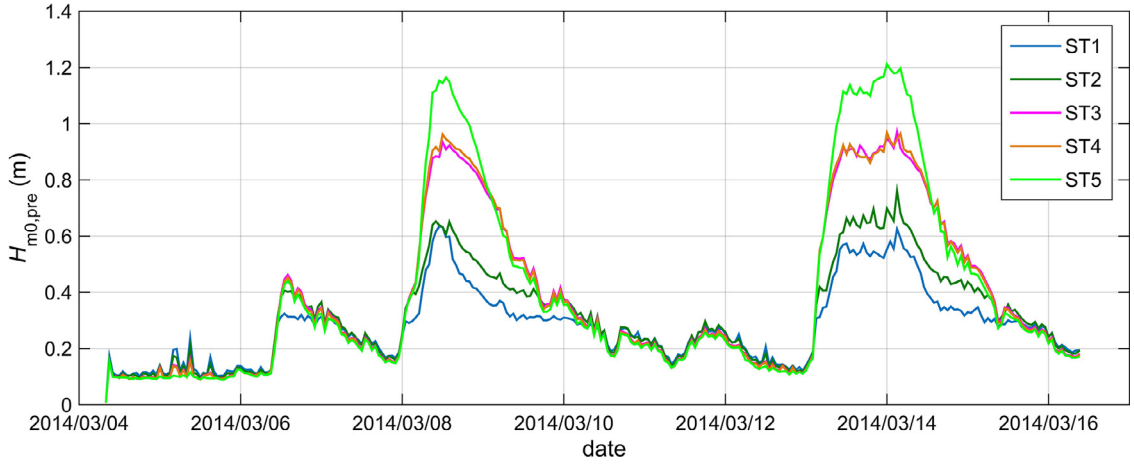

Figure 4 Time series of significant wave height at measurement stations reproduced by SWASH.

energy conditions. For the best result, the attained values of indices were less than 0.08 for the averaged *SI*, more than 0.80 for *IA*, and less than 0.01 for *NB*. The resulted values of breaking coefficients are also in good agreement with those attained in Lerma et al. (2017) for 1D mode and less than those in most of the values found in previous 2D-mode investigations. In this respect, Lerma et al. (2017) found that exerting $\alpha = 0.30$ and $\beta = 0.15$ could significantly improve their 1D model configuration results for very shallow waters. That SWASH calibration was for field-measured data at a complex and ripped bathymetry system. In another recalibration for 2D mode, according to laboratory experimental data, Smit et al. (2014) recommended the values of 1.0 and 0.6 for the coefficients of α and β when using six vertical layers, respectively. Mendes et al. (2018) and de Bakker et al. (2016b) correspondingly followed these suggested values for their laboratory experimental dataset measured by Ruessink et al. (2013). The default values of breaking coefficients were also applied in several 2D studies such as de Bakker et al. (2014), Liang et al. (2015), and Zhang and Stive (2019).

The time series of the spectral wave height (H_{m0}), reproduced by the calibrated model at ST1—ST5, are depicted in Figure 4. Comparing Figure 4 and Figure 2 also reveals a very good capability of the model to accurately predict the variations of energetic wave regime and significant wave heights across the shore. As well, the wave height variations evaluated by the model indicate that the depth-limited condition is dominant during two storm periods and saturated wave breaking decreases the wave height across the shore. Considering the wave setup calculated at the stations (but not shown here) by the model also resulted in relative wave height values (or spectral breaker index, $\gamma = H_{m0}/(d+\text{setup})$) varying in the range of 0.37 at ST5 to 0.66 at ST1. This value at ST1 is comparable to that of 0.73 proposed by Batjjes and Stive (1985) as the constant index for the spectral concept of depth-induced wave breaking.

5.3. Water-level profile assessment

The time-domain variables of $H_{1/3}$, H_{mean}, $T_{1/3}$, T_{mean}, and the *nw* were selected and calculated using the zero-down crossing method to verify the modeled wave profiles. These parameters, particularly period ones and *nw*, are strongly influenced by the variations of short and long waves as the results of wave breaking in the surf zone. The results reveal that the model has properly predicted the general spatial trends of these parameter variations during the storms. For example, the wave height parameters have been expectedly decreased from ST5 to ST1 as the result of depth-induced wave-breaking domination across the shore. On the other hand, the period parameters and *nw* show a shoreward rise and fall, respectively. These variations are the results of shoreward enhancement of IG waves due to water depth attenuation, as reported in several numerical and field studies on different beach environments (e.g., Mahmoudof and Siadatmousavi, 2020; Ruessink, 1998; Thomson et al., 2006).

Figures 5—7 compare the reproduced values of the above-mentioned wave parameters by the model and those observed in the field measurements. It can be generally seen that the *SI* values for height parameters are in the same order at all stations (Figure 5). Since the model has been calibrated for wave energy content, the values of reproduced wave height parameter are expectedly in acceptable accordance with the observed ones. However, the conditions for the period parameters and *nw* are different from the height ones. The resulted period parameters and *nw* by the model are somewhat acceptable at the transitional stations (viz. ST3 and ST4) and inaccurate at the shallow ones (namely, ST1 and ST2). Although the period parameters have been somewhat overestimated at ST3 and ST4, the model has exaggerated these parameters at ST1 and ST2 (Figure 6). While *SI* values for the period parameters are less than 0.15 for transitional stations, similar values have reached more than 1.00 at ST1. In other words, the model has overestimated the period parameters with an increasing trend toward the shore. The model approximately predicted the $T_{1/3}$ values more than two times of observed values at ST1 (the equation of the fitted line in Figure 6a). On the contrary, the model has underestimated *nw* with a shoreward increasing rate of inaccuracy (Figure 7). The predicted rising rate of *nw* values is also about one-quarter of the similar rate measured at the shallowest station (the slope of the fitted line in Figure 7a). All these results imply that a shoreward over-

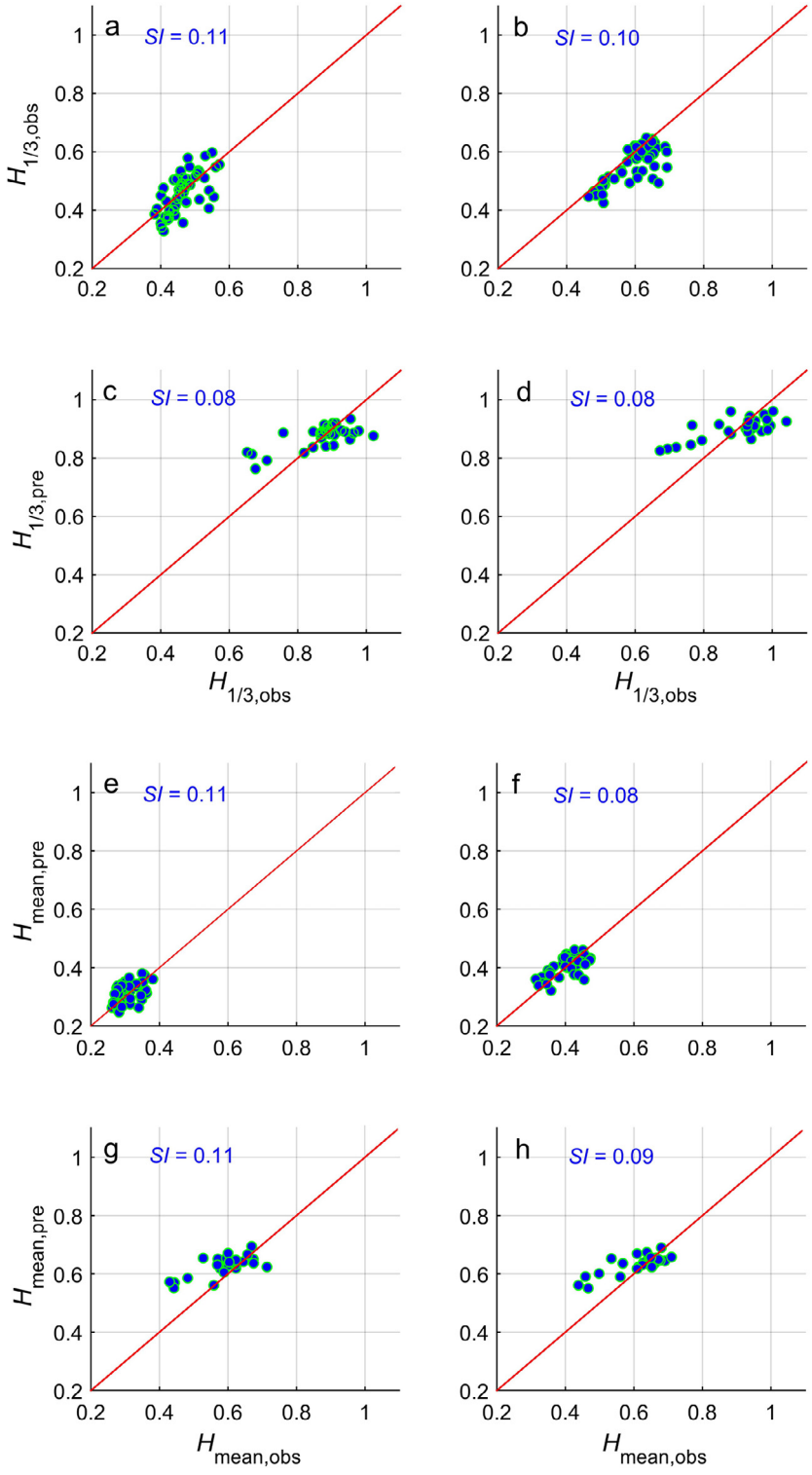

Figure 5 Comparison of height parameters reproduced by the model (pre) and those observed in the field measurements (obs); $H_{1/3}$ at a) ST1; b) ST2; c) ST3; d) ST4 and H_{mean} at e) ST1; f) ST2; g) ST3; h) ST4.

estimation in the generation of long IG waves, as a result of wave breaking or underestimation in short wind-waves can be probably responsible for these inaccurate estimations. High long waves can also make the zero-crossing analysis insensitive to short waves and decrease *nw*, consequently. Moreover, this can normally increase the period parameters.

5.4. Investigation of modeled long and short waves

Typically, the coastal wave regime is influenced by infragravity wave energy within high-energy conditions. These waves rarely break in the surf zone due to their long wavelength. However, breaking is one of their dissipating mech-

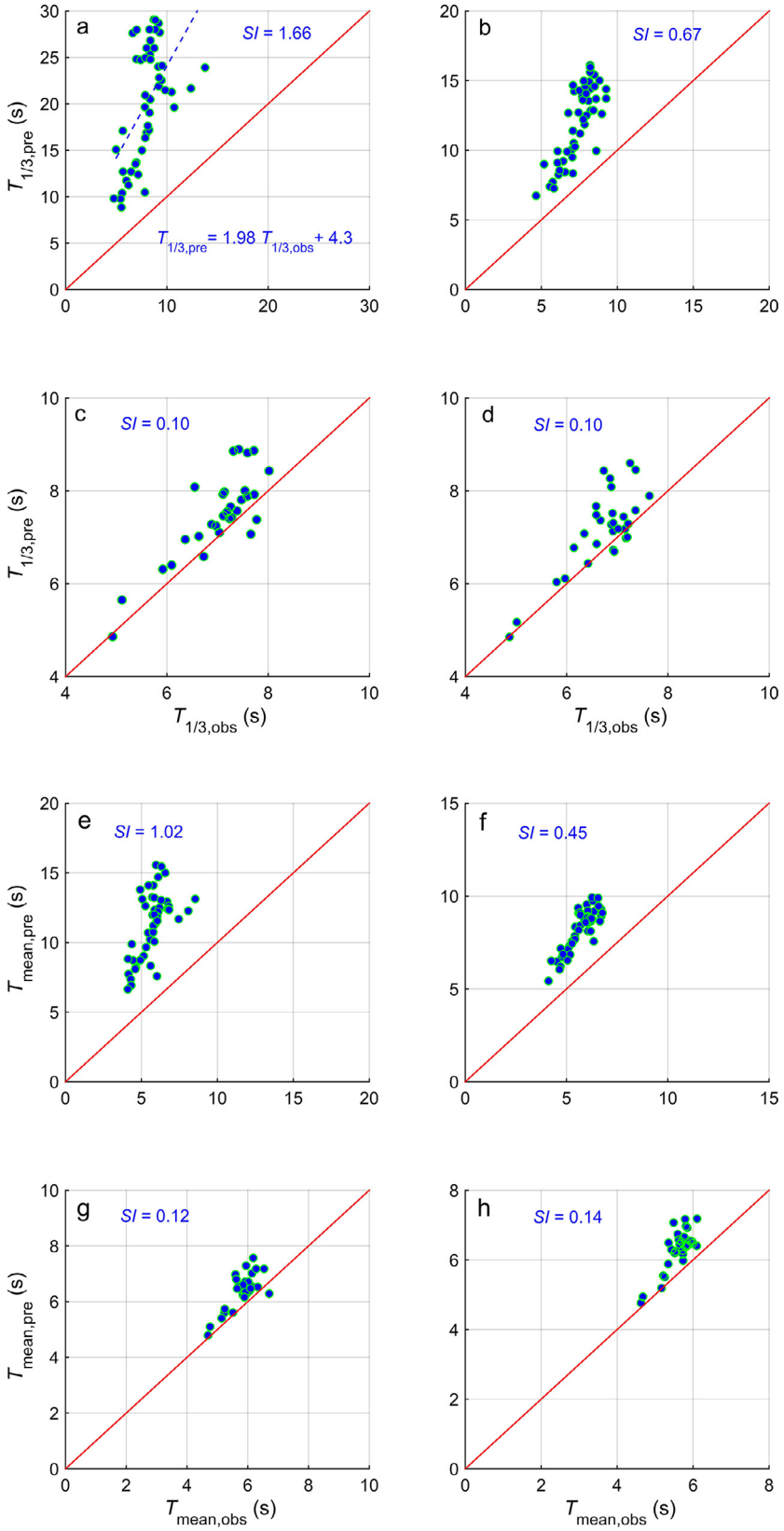

Figure 6 Comparison of period parameters reproduced by the model (pre) and those observed in the field measurements (obs); $T_{1/3}$ at a) ST1; b) ST2; c) ST3; d) ST4 and T_{mean} at e) ST1; f) ST2; g) ST3; h) ST4.

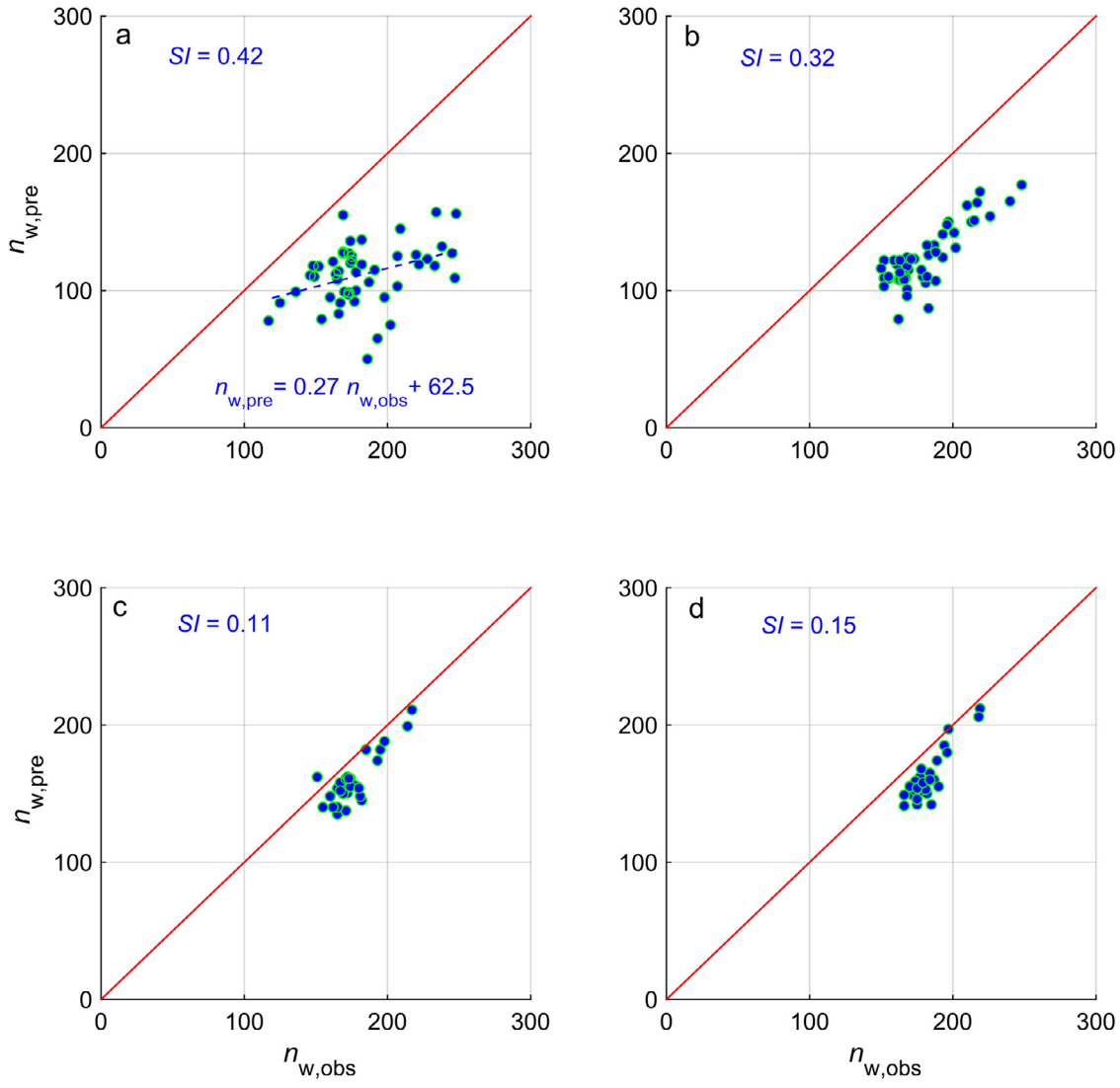

Figure 7 Comparison of the number of waves reproduced by the model (pre) and those observed in the field measurements (obs) at a) ST1; b) ST2; c) ST3; d) ST4.

anisms (de Bakker et al., 2014). Therefore, the increase in wave period parameters is expected at shallow waters within stormy durations. Moreover, wind-wave breaking and decomposition result in bore and short wave generation and some energy transfers to short waves (Mahmoudof, 2018b; Masselink, 1998).

Generally, bispectral analysis is necessary to determine the proportion of released and bound IG waves. However, the IG waves emerging in the present study can be regarded as the released type since they have been generated in the presence of severe breaking of wind-waves, as well all calculated values of β_b are greater than 0.3. The spectral analysis with similar conditions was also performed for model results and field measurements. The heights of IG waves were calculated for all time series using Eq. (8) to assess the accuracy of the model. Figure 8a—d compares the IG wave height values (H_{ig}) reproduced by the model against those observed at all measurement stations for stormy periods. Although the model can appropriately reproduce the saturation of IG waves in very shallow waters, it has considerably overestimated the heights of this type of wave at all stations. Comparing the resulted IG heights at the locations of stations reveals the general capability of the model to show the spatial enhancement of the IG waves. Nevertheless, the slopes of the fitted lines in Figure 8a—d indicates that the relative overestimation has been augmented from the deepest station toward the shore (from ST4 to ST1). Most similar previous studies confirmed the capability of the SWASH to consider the generation and development of released IG waves near shorelines (de Bakker et al., 2016b; Mendes et al., 2018; Rijnsdorp et al., 2015). In contrast, the earlier versions of phase-averaged spectral models such as the Simulating WAves Nearshore (SWAN) or WAVEWATCH III were unable to predict the generation of IG waves as a result of random breaking points of wind-waves. The absence of relevant source-term in those spectral models had made them impractical and fruitless for similar wave modeling in the very shallow water of beaches. Mahmoudof et al. (2018) accordingly tuned the breaking schemes embedded in the SWAN for the wind-waves for the present dataset and inevitably ig-

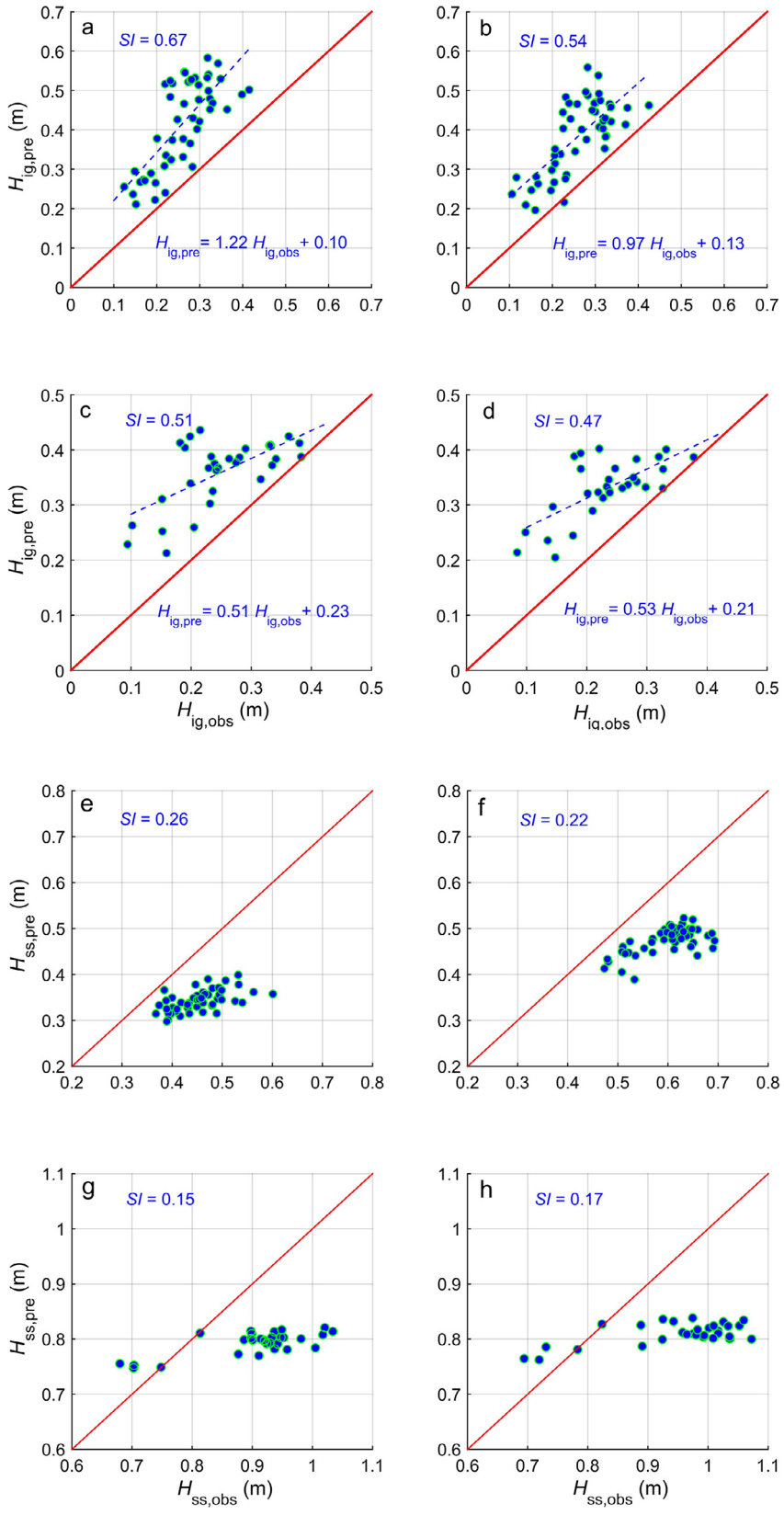

Figure 8 Comparison of infragravity and wind-waves heights reproduced by the model (pre) and those observed in the field measurements (obs); H_{ig} at a) ST1; b) ST2; c) ST3; d) ST4 and H_{ss} at e) ST1; f) ST2; g) ST3; h) ST4.

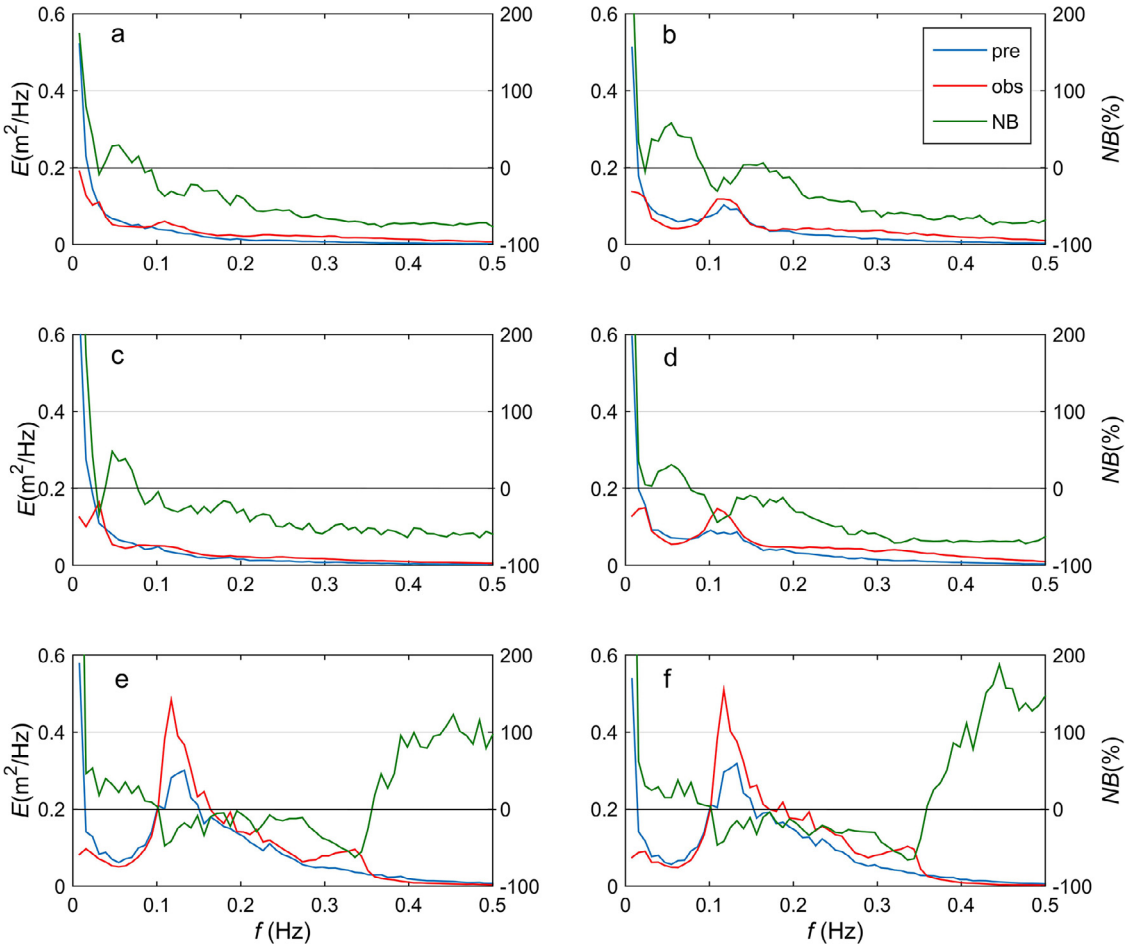

Figure 9 Wave energy and normalized bias spectra for the first storm at: a) ST1; b) ST2; and the second storm at: c) ST1; d) ST2; e) ST3, and f) ST4.

nored the low frequencies less than 0.05 Hz. However, some recent investigations have attempted to equip them with calculations of IG waves, but more verifications and validations are required (Reniers and Zijlema, 2022; Zheng et al., 2021). The study of Ardhuin et al. (2014) was one of the beginner investigations which incorporated the calculations of free IG waves in WAVEWWATCH III. The slope of the fitted curve at ST2 (in Figure 8b) is similar to the results of model run without bottom friction in Ardhuin et al. (2014) at sensor *I* deployed during the DUCK'94 experiment (see Figure 5 in Ardhuin et al., 2014). The slopes of fitted lines in Figure 8c and d are comparable with those of model runs with bottom friction applied only for wind sea and swell waves in that study. However, the comparisons of free IG waves in Ardhuin et al. (2014) pertained to offshore water depths.

A similar assessment was performed for wind-waves ($f > 0.05$ Hz) using Eq. (9) to calculate the relevant heights (H_{ss}). Figure 8e—h shows the results and compares the predicted and measured values of wind-wave heights. It is realized that the model has underestimated the wind-wave heights at all stations. The imperfection has also considerably increased for higher measured waves at ST3 and ST4 (see Figure 8g and h).

For more detailed investigations, the energy spectra were averaged in two groups of model outputs and measurements for the first and second storms with 19- and 30-hour durations, respectively. Also, the normalized bias spectra were evaluated deploying a formulation similar to Eq. (12). The results and comparisons are depicted in the six panels of Figure 9.

Generally, the calibrated model over-dissipated the main spectral peak of the wind-wave at all the stations within both storm durations. Moreover, the energy content of high and low harmonics has been respectively underestimated and overestimated by the model. The negative values of bias spectra are indicating that the wind-wave frequencies between 0.1 and 0.35 Hz have been generally underestimated by the model with a decreasing rate at all stations. On the other hand, the positive normalized bias of model estimation about the energy of low frequencies, $f < 0.1$ Hz, reaches values greater than +200% for $f < 0.02$ Hz. The overestimation in the narrow IG band ($f < 0.05$ Hz) is so important that the predicted energy at the first frequency is more than four times the observed value. Therefore, the first frequency is finally determined as the spectral peak by the model even for transitional depths (ST3 and ST4). Some ignored directional factors in 1D mode can be accordingly responsible for this overestimation. In this regard, de Bakker et al. (2014) pointed out that disregarding directional spreading in the 1D mode could be one of

the probable reasons for the overestimation of IG waves in the model results. Here, the opposite misevaluations of high and low harmonics are approximately balancing together and result in the same total energy content with the field data and equal significant wave heights (H_{m0}) to the measured values. The overestimation of IG and the underestimation of wind-waves have an indirect numerical consequence. These deficiencies result in a decrease in the breaking dissipation rate for the total irregular wave train by further resistance against breaking due to a reduction in wave steepness. Therefore, the lower values of breaking coefficients are necessary to dissipate a certain energy content from longer waves. Consequently, the calibration coefficients found in the present investigation for the 1D mode are less than those recommended in some previous studies for the 2D one. These decreased values of breaking coefficients can accordingly induce over-dissipation for and underestimation of short wind-wave heights. However, the ability of the model to present flattened, double-peaked, and IG-peaked spectra as the result of the frequency transmission of energy at nearshore shallow waters is admirable (Figure 9). However, this transferred energy from the main wind-wave frequencies to lower ones has been overestimated by the model.

In agreement with the measured data, a local peak at the frequency of $f = 0.23$ Hz as two times of the main spectral peak can be found in the model outputs at ST3 and ST4, indicating the probable capability of the model to evaluate and preserve the bound super harmonics (Figure 9e and f). However, these minor local peaks were eliminated after intensifying wave breaking at ST1 and ST2.

An accurate survey in Figure 9 also reveals that some minor challenges may face the model outputs. The minor observed wind-wave (at ~0.11 Hz) and local IG energy peaks (at ~0.03 Hz) are not also represented in the modeled spectrum at ST1 for the first storm (Figure 9a). Similarly, the observed peak frequency is $f = 0.0313$ Hz at ST1 for the second storm, but the model results show the first frequency (fundamental spectral frequency; $f = 0.0078$ Hz) as the calculated peak one (Fig.ure 9c). This means that the model has evaluated longer IG waves than real ones observed at this station. These findings have been similarly repeated at ST2 for both storms (Figure 9b and d).

The investigation of short and long waves reproduced by the model confirms that the calibrated SWASH model can appropriately predict the total energy content of the waves near the shorelines in the study area. However, the modeled water level profiles have some problems, which can be detected using zero-crossing analysis. Such deficiencies are the results of the overestimation of IG energy, the over-dissipation of short wind-waves, and representing lower IG peaks (that is, longer IG waves) by the model than those measured in the study area.

6. Conclusion

The capability of the 1D mode of the SWASH to reproduce the wave profile in very shallow waters was investigated in the present study, and then the results were compared with in-situ data measured at the Southern Caspian Sea during two storm events. The field data included water column pressure variations measured at six stations located on a perpendicular transect of the shoreline in the west of Nowshahr Port within ~two weeks. Two storms, including the modest swell waves with approximately 1.3 m heights, were also the most important recorded events occurring during the measurement period. The bursts with offshore wave heights greater than 0.6 m were then selected to assess the capability of the model to predict the wave evolution across the shore within high-energy conditions.

The model was run in the non-stationary and 1D mode with six vertical layers and spatial resolution less than 1/150 stormy wavelength. Two breaking parameters of the starting (α) and ending (β) wave break were also regarded as the calibration coefficients to tune the wave energy content in the study area. All the statistical indices implemented in the study (*SI, IA, and NB*) agree that the pair values of $\alpha = 0.25$ and $\beta = 0.13$ result in the most accurate values of H_{m0}. The attained values for the statistical parameters were $SI < 0.08$, $IA > 0.80$, and $NB < 0.01$ for the best results. The values of breaking coefficients found in this study are in good agreement with the reported values for the previous 1D mode simulations and less than those for previous similar 2D modeling studies.

The time-domain analysis has shown that although the calibrated model can appropriately predict the wave height parameters ($H_{1/3}$ and H_{mean}), the reproduced water level profiles by the model have some deficiencies. These problems are more significant for shallow stations than transitional water depths. The predicted period parameters ($T_{1/3}$ and T_{mean}) and the number of waves by the model are respectively greater and less than those observed in the field measurements.

Spectral analysis was also applied to investigate the details of the wave energy spectra reproduced by the model. Generally, the capability of the model to transfer energy from wind-waves to IG bands because of time-varying breaking points of wind-waves is satisfactory. However, the model overestimates the IG wave and underestimates the wind-wave energy content with a shoreward increasing rate of inaccuracy. These opposite inaccuracies are closely balanced together and the reproduced spectral wave heights are approximately equal to the observed values. Nevertheless, the modeled energy spectra are different from those observed in the field and then an exaggeration of IG wave heights is resulted from the model. The shoreward inaccuracy is increased in such a way that the fundamental frequency of analysis has been determined as the peak frequency of the nearshore waves by the model. The secondary effect of this inaccuracy is predicting longer IG waves than those determined in the field. Therefore, a more intensive breaking scheme (by exerting low values of breaking coefficients, found in the present study) is required to dissipate a certain energy content from longer waves reproduced by the model.

Finally, higher and longer IG waves and lower wind ones reproduced by the model can make the zero-crossing method insensitive to short wind-waves. Therefore, the time domain analysis represents a lower number of waves and greater values of period parameters for the model results compared with those found in the field measurements.

Acknowledgments

This study was supported by the Iranian National Institute for Oceanography and Atmospheric Science via project number INIOAS-399-021-01-038-01.

References

Ardhuin, F., Rawat, A., Aucan, J., 2014. A numerical model for free infragravity waves: Definition and validation at regional and global scales. Ocean Model. 77, 20—32. https://doi.org/10.1016/j.ocemod.2014.02.006

Battjes, J., Bakkenes, H., Janssen, T., Van Dongeren, A., 2004. Shoaling of subharmonic gravity waves. J. Geophys. Res. - Oceans 109. https://doi.org/10.1029/2003JC001863

Battjes, J., Stive, M., 1985. Calibration and verification of a dissipation model for random breaking waves. J. Geophys. Res. - Oceans (1978—2012) 90, 9159—9167. https://doi.org/10.1029/JC090iC05p09159

de Bakker, A., Brinkkemper, J., Van der Steen, F., Tissier, M., Ruessink, B., 2016a. Cross-shore sand transport by infragravity waves as a function of beach steepness. J. Geophys. Res. F: Earth Surf. 121, 1786—1799. https://doi.org/10.1002/2016JF003878

de Bakker, A., Tissier, M., Ruessink, B., 2014. Shoreline dissipation of infragravity waves. Cont. Shelf Res. 72, 73—82. https://doi.org/10.1016/j.csr.2013.11.013

de Bakker, A., Tissier, M., Ruessink, B., 2016b. Beach steepness effects on nonlinear infragravity-wave interactions: A numerical study. J. Geophys. Res. - Oceans 121, 554—570. https://doi.org/10.1002/2015JC011268

de Vries, J.v.T., Van Gent, M., Walstra, D., Reniers, A., 2008. Analysis of dune erosion processes in large-scale flume experiments. Coast. Eng. 55, 1028—1040. https://doi.org/10.1016/j.coastaleng.2008.04.004

Elgar, S., Herbers, T., Okihiro, M., Oltman-Shay, J., Guza, R., 1992. Observations of infragravity waves. J. Geophys. Res. 97, 15573—15577. https://doi.org/10.1029/92JC01316

Gao, J., Ji, C., Gaidai, O., Liu, Y., Ma, X., 2017. Numerical investigation of transient harbor oscillations induced by N-waves. Coast. Eng. 125, 119—131. https://doi.org/10.1016/j.coastaleng.2017.03.004

Gao, J., Ma, X., Dong, G., Chen, H., Liu, Q., Zang, J., 2021. Investigation on the effects of Bragg reflection on harbor oscillations. Coast. Eng. 170, 103977. https://doi.org/10.1016/j.coastaleng.2021.103977

Gao, J., Ma, X., Zang, J., Dong, G., Ma, X., Zhu, Y., Zhou, L., 2020. Numerical investigation of harbor oscillations induced by focused transient wave groups. Coast. Eng. 158, 103670. https://doi.org/10.1016/j.coastaleng.2020.103670

Gao, J., Zhou, X., Zhou, L., Zang, J., Chen, H., 2019. Numerical investigation on effects of fringing reefs on low-frequency oscillations within a harbor. Ocean Eng. 172, 86—95. https://doi.org/10.1016/j.oceaneng.2018.11.048

González-Marco, D., Sierra, J.P., de Ybarra, O.F., Sánchez-Arcilla, A., 2008. Implications of long waves in harbor management: the Gijón port case study. Ocean Coast. Manage. 51, 180—201. https://doi.org/10.1016/j.ocecoaman.2007.04.001

Guza, R., Thornton, E.B., 1985. Observations of surf beat. J. Geophys. Res. - Oceans 90, 3161—3172. https://doi.org/10.1029/JC090iC02p03161

Guza, R.T., Thornton, E.B., 1982. Swash oscillations on a natural beach. J. Geophys. Res. - Oceans 87, 483—491. https://doi.org/10.1029/JC087iC01p00483

Hasselmann, K., 1962. On the non-linear energy transfer in a gravity-wave spectrum Part 1. General theory. J. Fluid Mech. 12, 481—500. https://doi.org/10.1017/S0022112062000373

Herbers, T., Elgar, S., Guza, R., 1994. Infragravity-frequency (0.005—0.05 Hz) motions on the shelf. Part I: Forced Waves. J. Phys. Oceanogr. 24 (5), 917—927. https://doi.org/10.1175/1520-0485(1994)024<0917:IFHMOT>2.0.CO;2

Herbers, T., Elgar, S., Guza, R., O'Reilly, W., 1995. Infragravity-frequency (0.005—0.05 Hz) motions on the shelf. Part II: Free waves. J. Phys. Oceanogr. 25 (6), 1063—1079. https://doi.org/10.1175/1520-0485(1995)025<1063:IFHMOT>2.0.CO;2

Hoefel, F., Elgar, S., 2003. Wave-induced sediment transport and sandbar migration. Science 299, 1885—1887. https://doi.org/10.1126/science.1081448

Inch, K., Davidson, M., Masselink, G., Russell, P., 2017. Observations of nearshore infragravity wave dynamics under high energy swell and wind-wave conditions. Cont. Shelf Res. 138, 19—31. https://doi.org/10.1016/j.csr.2017.02.010

Komen, G., Cavaleri, L., Donelan, M., Hasselmann, K., Hasselmann, S., Janssen, P., 1994. Dynamics and Modelling of Ocean Waves Cambridge University Press, 532 pp. https://doi.org/10.1017/CBO9780511628955

Lerma, A.N., Pedreros, R., Robinet, A., Sénéchal, N., 2017. Simulating wave setup and runup during storm conditions on a complex barred beach. Coast. Eng. 123, 29—41. https://doi.org/10.1016/j.coastaleng.2017.01.011

Liang, B., Wu, G., Liu, F., Fan, H., Li, H., 2015. Numerical study of wave transmission over double submerged breakwaters using non-hydrostatic wave model. Oceanologia 57 (4), 308—317. https://doi.org/10.1016/j.oceano.2015.07.002

Longuet-Higgins, M., Fox, M., 1977. Theory of the almost-highest wave: the inner solution. J. Fluid Mech. 80, 721—741. https://doi.org/10.1017/S0022112077002444

Longuet-Higgins, M.S., Stewart, R., 1962. Radiation stress and mass transport in gravity waves, with application to 'surf beats. J. Fluid Mech. 13, 481—504. https://doi.org/10.1017/S0022112062000877

Longuet-Higgins, M.S., Stewart, R., 1964. Radiation stresses in water waves; a physical discussion, with applications. Deep Sea Res. Oceanogr. Abstr. Elsevier, 529—562. https://doi.org/10.1016/0011-7471(64)90001-4.

Longuet-Higgins, M.S., 1970. Longshore currents generated by obliquely incident sea waves: 1. J. Geophys. Res. 75, 6778—6789. https://doi.org/10.1029/JC075i033p06778

Ma, G., Shi, F., Kirby, J.T., 2012. Shock-capturing non-hydrostatic model for fully dispersive surface wave processes. Ocean Model. 43, 22—35. https://doi.org/10.1016/j.ocemod.2011.12.002

MacMahan, J.H., Thornton, E.B., Reniers, A.J., 2006. Rip current review. Coastal Eng. 53, 191—208. https://doi.org/10.1016/j.coastaleng.2005.10.009

Madsen, P.A., Bingham, H., Liu, H., 2002. A new Boussinesq method for fully nonlinear waves from shallow to deep water. J. Fluid Mech. 462, 1—30. https://doi.org/10.1017/S0022112002008467

Mahmoudof, S.M., 2018a. Investigation of Infragravity Waves Dependency on Wind Waves for Breaking and Nonbreaking Conditions in the Sandy Beaches of Southern Caspian Sea (Nowshahr Port). Int. J. Coastal Offsh. Eng. 1, 13—20. https://doi.org/10.29252/ijcoe.1.4.13

Mahmoudof, M., 2018b. Study of Low and High Harmonic Energy Amplification Due to Outer Surf-zone Wave Breaking. J. Oceanogr. 9, 1—9. https://doi.org/10.29252/joc.9.34.1

Mahmoudof, S.M., Azizpour, J., 2020. Field observation of wave reflection from plunging cliff coasts of Chabahar. App. Ocean Res. 95, 102029. https://doi.org/10.1016/j.apor.2019.102029

Mahmoudof, S.M., Azizpour, J., Eyhavand-Koohzadi, A., 2021. Observation of infragravity wave processes near the coastal cliffs

of Chabahar (Gulf of Oman). Estuarine Coast. Shelf Sci. 107226. https://doi.org/10.1016/j.ecss.2021.107226
Mahmoudof, S.M., Badiei, P., Siadatmousavi, S.M., Chegini, V., 2016. Observing and estimating of intensive triad interaction occurrence in very shallow water. Cont. Shelf Res. 122, 68—76. https://doi.org/10.1016/j.csr.2016.04.003
Mahmoudof, S.M., Badiei, P., Siadatmousavi, S.M., Chegini, V., 2018. Spectral Wave Modeling in Very Shallow Water at Southern Coast of Caspian Sea. J. Marine Sci. App. 17, 140—151. https://doi.org/10.1007/s11804-018-0011-y
Mahmoudof, S.M., Siadatmousavi, S.M., 2020. Bound infragravity wave observations at the Nowshahr beaches, southern Caspian Sea. App. Ocean Res. 98, 102122. https://doi.org/10.1016/j.apor.2020.102122
Masselink, G., 1998. Field investigation of wave propagation over a bar and the consequent generation of secondary waves. Coast. Eng. 33, 1—9. https://doi.org/10.1016/s0378-3839(97)00032-x
Mendes, D., Pinto, J.P., Pires-Silva, A.A., Fortunato, A.B., 2018. Infragravity wave energy changes on a dissipative barred beach: A numerical study. Coast. Eng. 140, 136—146. https://doi.org/10.1016/j.coastaleng.2018.07.005
Nwogu, O., 1993. Alternative form of Boussinesq equations for nearshore wave propagation. J. Waterw. Port C. 119, 618—638. https://doi.org/10.1061/(ASCE)0733-950X
Reniers, A., Zijlema, M., 2022. SWAN SurfBeat-1D. Coast. Eng. 172, 104068. https://doi.org/10.1016/j.coastaleng.2021.104068
Rijnsdorp, D.P., Ruessink, G., Zijlema, M., 2015. Infragravity-wave dynamics in a barred coastal region, a numerical study. J. Geophys. Res. - Oceans 120, 4068—4089. https://doi.org/10.1002/2014JC010450
Roelvink, D., Reniers, A., Van Dongeren, A., de Vries, J.v.T., McCall, R., Lescinski, J., 2009. Modelling storm impacts on beaches, dunes and barrier islands. Coast. Eng. 56, 1133—1152. https://doi.org/10.1016/j.coastaleng.2009.08.006
Ruessink, B., 1998. The temporal and spatial variability of infragravity energy in a barred nearshore zone. Cont. Shelf Res. 18, 585—605. https://doi.org/10.1016/S0278-4343(97)00055-1
Ruessink, B.G., Michallet, H., Bonneton, P., Mouazé, D., Lara, J., Silva, P.A., Wellens, P., 2013. Globex: wave dynamics on a gently sloping laboraty beach. Proc. Coast. Dyn. 2013, 1351—1362.
Ruju, A., Lara, J.L., Losada, I.J., 2012. Radiation stress and low-frequency energy balance within the surf zone: A numerical approach. Coast. Eng. 68, 44—55. https://doi.org/10.1016/j.coastaleng.2012.05.003
Ruju, A., Lara, J.L., Losada, I.J., 2014. Numerical analysis of run-up oscillations under dissipative conditions. Coast. Eng. 86, 45—56. https://doi.org/10.1016/j.coastaleng.2014.01.010
Sheremet, A., Guza, R., Elgar, S., Herbers, T., 2002. Observations of nearshore infragravity waves: Seaward and shoreward propagating components. J. Geophys. Res. - Oceans 107. https://doi.org/10.1029/2001JC000970
Smit, P., Janssen, T., Holthuijsen, L., Smith, J., 2014. Non-hydrostatic modeling of surf zone wave dynamics. Coastal Eng. 83, 36—48. https://doi.org/10.1016/j.coastaleng.2013.09.005
Smit, P., Zijlema, M., Stelling, G., 2013. Depth-induced wave breaking in a non-hydrostatic, near-shore wave model. Coastal Eng 76, 1—16. https://doi.org/10.1016/j.coastaleng.2013.01.008
Stelling, G., Zijlema, M., 2003. An accurate and efficient finite-difference algorithm for non-hydrostatic free-surface flow with application to wave propagation. Int. J. Numer. Methods Fluids 43, 1—23. https://doi.org/10.1002/fld.595
Svendsen, I.A., 1984. Mass flux and undertow in a surf zone. Coast. Eng. 8, 347—365. https://doi.org/10.1016/0378-3839(84)90030-9
Symonds, G., Huntley, D.A., Bowen, A.J., 1982. Two-dimensional surf beat: Long wave generation by a time-varying breakpoint. J. Geophys. Res. - Oceans 87, 492—498. https://doi.org/10.1029/JC087iC01p00492
The Wamdi Group, 1988. The WAM model-a third generation ocean wave prediction model. J. Phys. Oceanogr. 18, 1775—1810. https://doi.org/10.1175/1520-0485
Thomson, J., Elgar, S., Raubenheimer, B., Herbers, T., Guza, R., 2006. Tidal modulation of infragravity waves via nonlinear energy losses in the surfzone. Geophys. Res. Lett. 33. https://doi.org/10.1029/2005GL025514
Torres-Freyermuth, A., Mariño-Tapia, I., Coronado, C., Salles, P., Medellín, G., Pedrozo-Acuña, A., Silva, R., Candela, J., Iglesias-Prieto, R., 2012. Wave-induced extreme water levels in the Puerto Morelos fringing reef lagoon. Nat. Hazard. Earth Sys. 12, 3765—3773. https://doi.org/10.5194/nhess-12-3765-2012
Torres-Freyermuth, A., Losada, I.J., Lara, J.L., 2007. Modeling of surf zone processes on a natural beach using Reynolds-Averaged Navier-Stokes equations. J. Geophys. Res. - Oceans 112. https://doi.org/10.1029/2006JC004050
Webb, S.C., Zhang, X., Crawford, W., 1991. Infragravity waves in the deep ocean. J. Geophys. Res. - Oceans 96, 2723—2736. https://doi.org/10.1029/90JC02212
Wei, G., Kirby, J.T., Grilli, S.T., Subramanya, R., 1995. A fully nonlinear Boussinesq model for surface waves. Part 1. Highly nonlinear unsteady waves. J. Fluid Mech. 294, 71—92. https://doi.org/10.1017/S0022112095002813
Yamazaki, Y., Kowalik, Z., Cheung, K.F., 2009. Depth-integrated, non-hydrostatic model for wave breaking and run-up. Int. J. Numer. Method. Fluids 61, 473—497. https://doi.org/10.1002/fld.1952
Zhang, R., Stive, M.J., 2019. Numerical modelling of hydrodynamics of permeable pile groins using SWASH. Coast. Eng. 153, 103558. https://doi.org/10.1016/j.coastaleng.2019.103558
Zheng, Z., Ma, X., Ma, Y., Huang, X., Dong, G., 2021. Modeling of coastal infragravity waves using the spectral model WAVEWATCH III. Coast. Eng. 170, 104016. https://doi.org/10.1016/j.coastaleng.2021.104016
Zijlema, M., Stelling, G., Smit, P., 2011. SWASH: An operational public domain code for simulating wave fields and rapidly varied flows in coastal waters. Coast. Eng. 58, 992—1012. https://doi.org/10.1016/j.coastaleng.2011.05.015

Oceanologia 64 (2022) 473—488

Available online at www.sciencedirect.com

ScienceDirect

journal homepage: www.journals.elsevier.com/oceanologia

ORIGINAL RESEARCH ARTICLE

Hydrographic variation in a tropical coral reef system: The Veracruz Reef System, Gulf of Mexico

David Salas-Monreal[a,*], Rosalinda Monreal-Jimenez[b], Victor Kevin Contreras-Tereza[c], Maria Adela Monreal-Gomez[d], David Alberto Salas-de-Leon[d], Mayra Lorena Riveron-Enzastiga[e]

[a] *Institute of Marine Sciences and Fisheries, Universidad Veracruzana, Boca del Rio, Mexico*
[b] *Postgraduate in Earth Sciences, National Autonomous University of Mexico (UNAM), Ciudad Universitaria, Mexico City, Mexico*
[c] *Hydrometeorology Subcoordination, Mexican Institute of Water Technology, Jiutepec, Mexico*
[d] *Institute of Marine Sciences and Limnology, National Autonomous University of Mexico (UNAM), Ciudad Universitaria, Mexico City, Mexico*
[e] *Science Department, Noordwijk International College, Veracruz, Mexico*

Received 8 July 2021; accepted 9 March 2022
Available online 23 March 2022

KEYWORDS
Coral reefs;
Veracruz Reef System;
Reef corridor of the southwestern Gulf of Mexico;
Chlorophyll-*a* concentrations;
Hydrographic seasonal variability;
T-S diagrams

Abstract Three thousand forty-one profiles of temperature, salinity, density, dissolved oxygen, nitrogen and chlorophyll-*a* were used to study their seasonal variation on a tropical coral reef system, located in the central part, of the reef corridor of the southwestern Gulf of Mexico. The results revealed three seasons according to their hydrographic variations; the northerly wind season from September to April; the dry season from May to June; and the rainy season from July to August. The results of the density ratio during the dry season were ~1.25 on average, while during the rainy season it had an average value of ~0.62. Thus, the pycnocline was more influenced by the halocline during the rainy season and by the thermocline during the dry season. There was also an evident variation in chlorophyll-a concentration over the water column, which was not evident in the surface layer. During the summer (rainy season), dissolved oxygen was related to chlorophyll-a concentration; while, during the winter (northern wind season), these values were related to the vertical mixing of the water column due to wind stress. There was evidence of cooler ocean water intrusion into the Veracruz Reef System

* Corresponding author at: Instituto de Ciencias Marinas y Pesquerias, Universidad Veracruzana, Boca del Rio, Ver. 94290 Mexico.
E-mail address: davsalas@uv.mx (D. Salas-Monreal).
Peer review under the responsibility of the Institute of Oceanology of the Polish Academy of Sciences.

Production and hosting by Elsevier

https://doi.org/10.1016/j.oceano.2022.03.002

during the spring-summer season below ~10 m. Finally, a second halocline, pycnocline, and nitrocline were found near ~30 m depth during the rainy season.

1. Introduction

Coral reef systems cover only ~2% of total ocean areas, but their biodiversity per square meter is higher than those observed at most oceanic systems (Chacon-Gomez et al., 2013). Despite all negative impacts, most coral reef areas are still developing due to adaptation, evolution, and recruitment, i.e., coral larvae brought from other reef systems, owing to ocean circulation (Villegas-Sanchez et al., 2013). The variation of water temperature, salinity, density, nutrients, chlorophyll-*a*, and oxygen, among others, affects coral growth in tropical areas. Further, the hydrographic conditions are responsible for coral bleaching (Hughes et al., 2018). Most of these properties vary according to the velocity of the wind and currents. In addition, the interaction of tidal currents or synoptic oceanic currents with local bathymetry may also modify the hydrographic properties (Salas-Monreal et al., 2009). Therefore, it is important to know the variability of the hydrographic properties and its relationship to atmospheric and oceanic conditions, in order to predict the evolution of the coral reef systems around the world.

The continental shelf of the Gulf of Mexico (GoM) is an area composed of several coral reef systems (Carricart-Ganivet et al., 2011; Carricart-Ganivet and Merino, 2001; Moore and Bullis, 1960; Tunnell et al., 2007), which are well connected owing to ocean circulation (Atchison et al., 2008; Jordan-Dahlgren, 2002; Salas-Monreal et al., 2018; Sammarco et al., 2012; Sanvicente-Añorve et al., 2014; Schill et al., 2015). Current velocities within the southwestern GoM vary seasonally from ~0.10 to more than 0.30 m/s (Salas-Monreal et al., 2019). During winter, current velocities have a dominant southward direction, while during summer, they have a dominant northward direction (Riveron-Enzastiga et al., 2016). However, shifts in ocean currents occur from north to south and south to north throughout the year (Salas-Perez et al., 2012). Further, all coral reef areas within the western GoM are periodically covered by resuspended sediments, owing to winds and river discharges which may not favor their optimal development (Lugo-Fernandez et al., 2001). This phenomenon may be observed within the N_2 concentrations, indicative of nutrient resuspension (wind effect) or continental nutrient inputs (river discharges).

From all coral reef systems located in the western GoM, the Veracruz Reef System (VRS), located in front of one of the oldest cities in America (Veracruz, founded on April 22, 1519) (Figure 1), is considered among the largest and most resistant to seasonal variability (Salas-Perez and Granados-Barba, 2008). It is composed of 50 coral reefs (Liaño-Carrera et al., 2019) distributed over a shallow (~50 m) area of ~523 km^2 (Figure 1c). The VRS is located in the central part of the reef corridor of the southwestern GoM (Ortiz-Lozano et al., 2013), under the influence of river discharges, eddies, strong continuous winds, and upwelling conditions that modulate the hydrographic properties of the water column. Due to its proximity to the coast, satellites do not provide information about the surface conditions (e.g., salinity). Even though model outputs provide a first approximation of the hydrographic variability (Salas-Monreal et al., 2020), they still need in situ data for calibration purposes; thus, in situ data are the most accurate methods to describe the hydrological variability near the coast, under abrupt bathymetric changes.

On average, coral reefs developed in the upper 50 m within the continental shelf and are exposed to oceanic water conditions that favor coral development (Deslarzes, 1998; Rezak et al., 1985), as it is the case at the VRS (northern hemisphere), where the Gulf Common Water (GCW) irrigates the VRS during winter (Salas-Perez and Arenas-Fuentes, 2011). While during the rainy season, the water irrigating the VRS is a mixture between the GCW and the river discharges (Salas-Perez and Granados-Barba, 2008). The temporal and spatial variability of temperature and salinity fields in the VRS have previously been described using 24 h surveys (Chacon-Gomez et al., 2013; Salas-Monreal et al., 2009), annual in situ time series (Avendaño et al., 2019; Avendaño-Alvarez et al., 2017; Okolodkov et al., 2011; Salas-Monreal et al., 2019; Vera-Mendoza et al., 2017) or time series from moored sensors (Allende-Arandia et al., 2016; Mateos-Jasso et al., 2012). In general, three seasons were observed; cold atmospheric fronts (September to April), locally called northerly wind season, dry (May to June) and, rainy (July to August) seasons (Salas-Perez and Granados-Barba, 2008). During the northerly wind season, the water column seems to be well mixed, owing to strong wind speed (Riveron-Enzastiga et al., 2016), while during the dry and rainy seasons, there is a well-marked thermocline and halocline, respectively (Avendaño-Alvarez et al., 2017).

One of the interesting features of the VRS is the relatively high concentration and low variability of the chlorophyll-*a* values throughout the year, even under the presence of local hypoxic events (Avendaño et al., 2019; Avendaño-Alvarez et al., 2017). The hypoxic events result from bacterial activity due to high organic matter concentration, coming from the Jamapa River (Figure 1c) during the northerly wind and rainy seasons (Okolodkov et al., 2011; Salas-Monreal et al., 2020). During the rainy season, nutrients come from river inputs (Jamapa, La Antigua, and Papaloapan rivers), while during the northerly wind season, nutrients come from sediment resuspension, owing to strong wind speed (> 15 m/s) that reach the seafloor (Riveron-Enzastiga et al., 2016). Finally, during the dry season, the

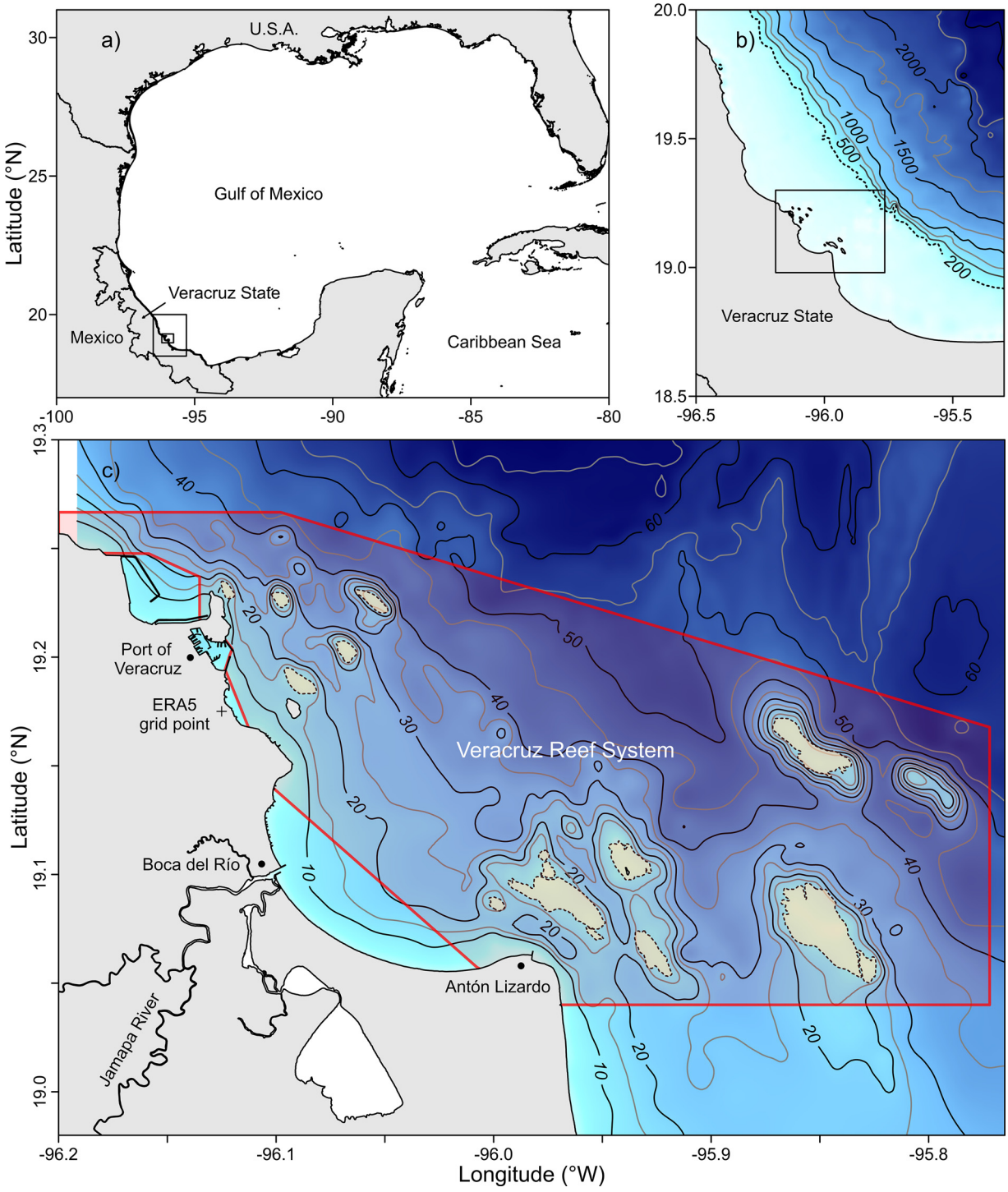

Figure 1 a) Location of the Veracruz Reef System (VRS), b) the continental shelf, and c) the bathymetry of the VRS. The 3,041 profiles of the water temperature (°C), salinity, density (kg/m^3), dissolved oxygen (ml/L), nitrogen (ml/L), and chlorophyll-*a* (μg/L) were recorded within the red area.

mechanisms by which the relatively high concentrations of nutrients are maintained at the VRS (Avendaño et al., 2019) have not been well described yet. They could be a combination of an eolic upwelling (Allende-Arandia et al., 2016; Mateos-Jasso et al., 2012) with a topographic upwelling (Riveron-Enzastiga et al., 2016), or the sporadic northerly winds interspersed with strong southerly winds, which mix the water column, increasing nutrient availability (Riveron-Enzastiga et al., 2016). Despite the mechanisms, there is evidence of high nutrient (N_2) concentrations throughout the

year at the VRS, confirmed with the relatively high values of chlorophyll-*a*, which had a low annual variability (Avendaño-Alvarez et al., 2017).

This study aims to increase our knowledge of the seasonal hydrographic variability in tropical coral reef systems. The VRS is used as an example since it is one of the largest coral reef systems in the southwestern GoM. This study is the first that includes more than 3,000 profiles over the entire VRS, analyzing the T-S diagram and the monthly hydrographic variability from two successive years (2011–2012); it is also the first study with N_2, O_2, and chlorophyll-*a* yearlong profiles covering the entire VRS. This is extremely useful to understand the hydrodynamics at which local organisms, such as corals, are subject and provide the first idea of the seasonal variability of the N_2, O_2, and chlorophyll-*a* over the entire VRS.

2. Data and methodology

Three thousand forty-one (3,041) profiles of water temperature, salinity, density, dissolved oxygen (DO), oxygen saturation, total nitrogen (N_2), and chlorophyll-*a* (chl-*a*) were recorded at the VRS during years 2011 and 2012. Even if there were profiles taken monthly at a fixed location, not all the profiles were recorded at the same place systematically. Nevertheless, all profiles were recorded over the VRS (Figure 1c). At least fifteen profiles were recorded weekly, not necessarily at the same location. Most of the CTD profiles lack specific coordinates (latitude and longitude), however, the general position where those data were obtained was known (southern, northern, central o seaward area). The specific date and time of the samplings, on the other hand, was known since the CTD provide us with this information. All data were recorded with a Sea-Bird Term19 Sea CAT profiler with added chlorophyll-*a*, nitrogen, and oxygen sensors. The CTD took one data every 0.25 s (4 Hz) to a maximum depth of 50 m (seafloor). The temperature was measured in ITS-90 degrees Celsius (°C) with an accuracy of 0.002°C. The salinity data were converted from the measured conductivity and temperature (Bennett, 1976). The salinity data have an accuracy of 0.003. The dissolved oxygen and the oxygen saturation data were obtained from an added optical dissolved oxygen sensor, with an accuracy of 0.015 ml/L. The Chlorophyll-*a* sensor, in turn, has an accuracy of 0.03 μg/L. Data processing was performed to obtain the T-S diagrams, as well as monthly charts of water temperature (°C), salinity, density (kg/m^3), dissolved oxygen (ml/L), oxygen saturation (%), total nitrogen (ml/L), and chlorophyll-*a* (μg/L) versus depth (m) from March 2011 to September 2012.

Since one of the main goals of this work is to study the hydrography and the T-S diagrams variability within the VRS, considering the VRS as one system, the 3,041 profiles were plotted regardless of their specific location within the VRS. Even if the Veracruz Reef System was shown to have spatial differences in salinity and temperature values from side to side of the system (Avendaño et al., 2019), a PCA-correlation and a dissimilarity analysis showed that the area was only divided into two groups, the near coastal areas, and the seaward reef areas (Avendaño-Alvarez et al., 2017) and that such dissimilarity was of less than 15%. There were other divisions in which the VRS was divided into northern and southern reef areas, including the Jamapa River, as the natural division among them (Salas-Monreal et al., 2009). However, in both cases, the division of the VRS implies that the shallow areas, either the coastal areas (< 10 m depth) or the northern reef areas (up to 25 m depth), could be distinguished from the deeper areas, either the seaward area (> 10 m depth) or the southern reef area (up to 50 m depth), due to the total depth of the CTD profile. Further, all CTD profiles where the salinity value was observed below 30 were not considered in this study since those profiles had a maximum depth below 6 m. Therefore, they were considered taken at the river mouth, an area not included in this study (Figure 1). In this way, it was possible to avoid misinterpretation of the results due to the direct influence of the river. However, the influence of the river was calculated using the ratio of curvature following Liaño-Carrera et al. (2019) as follows:

$$r = \frac{U}{f} \tag{1}$$

where U is the surface velocity of the river and f is the Coriolis frequency ($f = 2\Omega \sin \varphi$), which is a function of the latitude (φ). The latitude at the VRS was considered as 19.175°N. The river discharges of the Jamapa River were obtained from the Mexican national water commission (www.gob.mx/conagua), showing its maximum discharges from mid-June to mid-September (>100 m^3/s), and its lowest values from December to May (<20 m^3/s). The speed of the Jamapa River (Figure 1c) used in Equation (1) was calculated by dividing the river discharge by the area across the river mouth (~198 m^2).

Those were not the only assumptions taken in this study; it was also assumed that any profile taken with a total depth greater than 25 m was taken at the southern reef area (38%), and any profile taken at depths below 10 m and above 25 m depth were taken at the northern reef area (49%), while the remaining profiles (13%), were taken near the coast (<10 m depth) within the limits of the VRS (Figure 1c). This assumption was considered since none of the profiles were taken over any of the 50 reefs' crest or slope (Liaño-Carrera et al., 2019). The final assumption was that even if the VRS at a local scale has differences of salinity and temperature within the system, at mesoscale, it could be considered as part of the reef corridor of the southwestern GoM (Ortiz-Lozano et al., 2013), and therefore it could be considered as one reef system located in the western GoM.

The wind's dominant velocity was analyzed to elucidate if there is any atmospheric condition affecting its hydrographic properties, such as strong winds favoring vertical mixing or upwelling conditions. This analysis was also performed in order to explain if there is any dominant direction associated with one of the seasons (northerly wind season) and if such winds are strong enough to keep the water column well-mixed during the entire season. Eventually, the Ekman depth (D) was calculated to confirm if the water column of the VRS was affected by vertical mixing (if D > bathymetry) or if it could be affected by an eolic upwelling condition (if pycnocline depth ≤ D ≤ bathymetry) either at the VRS or at the external continental shelf adjacent to the VRS. The depth at which the winds may affect the water column (D) was calculated for the first time at the VRS as

follows:

$$D = \sqrt{\frac{2\pi A_z}{f}} U_{10} \quad (2)$$

where A_z is the dynamic viscosity considered as 1.759×10^{-4} kg/ms (Islade et al., 1972; Sharqawy et al., 2010), f is the Coriolis frequency, and U_{10} is the wind speed at 10 m high. The wind velocities were taken from Copernicus Marine Service (u and v-components at 10 m height) of ERA5-ECMWF (Hersbach et al., 2018). The hourly wind velocity data were obtained from 2011 to 2012 in the node located at 19.17°N, 96.13°W from which daily wind data components were obtained, then the wind depth influence was calculated. By simplifying Equation (2) to $\sqrt{\frac{7.6}{sin(\varphi)}} U_{10}$, it could be assumed that such depth (D) is a function of the speed of the wind multiplied by a constant. At the VRS, this constant was 4.81 s. Thus, D could be calculated as 4.81 U_{10} m.

Finally, the density ratio (R_ρ) was calculated to determine if the water column's stratification at the VRS depended more on salinity or temperature gradients. This was calculated as follows:

$$R_\rho = \frac{\alpha\left(\frac{\delta T}{\delta p}\right)}{\beta\left(\frac{\delta S}{\delta p}\right)} \quad (3)$$

where α is the thermal expansion coefficient (0.2), β is the haline contraction coefficient (0.8), p is the pressure, which increases with depth, and T and S are the temperature and salinity, respectively (Bidokhti and Ezam, 2009).

In addition to the monthly mean plots of each parameter, the standard deviation, or a fraction of it, was plotted, represented by the translucent shaded area around the mean. These monthly mean values were plotted versus depth to clarify if such properties could be divided into dry, rainy, and northerly wind seasons.

3. Results

The daily average wind velocity data at 10 m height (Figure 2a) showed the dominance of the northwesterly winds from September to April of both years (2011 and 2012), which reached up to 10 m/s; this is a common pattern observed during winter, as previously reported by Vera-Mendoza et al. (2017). According to Equation (2), during the passage of cold front events, the average depth of the wind influence over the water column was of ~25 m (Figure 2b). The strongest wind speeds were observed during the northerly wind season (Figure 2a), which induce a maximum depth of the wind influence of ~50 m, observed during three cold front events in January, March 2011, and December 2012.

While from May to August, the maximum depth influence of the wind was of ~15 m (Figure 2b). The maximum distance covered by the river discharge, which influences the strength of the stratification, was calculated using Equation (1). As mentioned, the speed of the Jamapa River (Figure 1c) used in Equation (1) was calculated by dividing the river discharge (Figure 2c) by the area across the river mouth (~198 m^2), which suggested a direct influence up to a ratio of ~15 km during the spring-summer season. This is the maximum distance from the center of the river mouth, at which the salinity, temperature, and density values related to the river discharge are expected to be found. Finally, from September to April, the direct influence of the river was observed up to a ratio of ~2 km, which did not reach the study area (red area in Figure 1c).

The strongest southeasterly winds were observed during tropical wave events, locally known as southerlies, on average, these events (southerlies) influence the water column up to a depth of ~7 m (Figure 2b). Thus, during the dry or rainy seasons (Figure 2), the water column is stratified, as observed in the temperature, salinity, nitrogen and density (σ_t) contour plots of 2011 and 2012 (Figure 3 a, b, c). The nitrogen distribution (Figure 3d) was inverse to temperature distribution (Figure 3a). The contour plots were obtained by performing a daily average of the hydrographic variables, with a vertical resolution of 0.25 m.

One interesting feature observed during May and June (dry season) of both years, in the temperature and salinity contour plots (Figure 3a, b), is the decrement of the near-bottom temperature to its minimum value (~20°C) and the increment of the salinity to its maximum value (~36.4). These features were observed from the bottom to 10 to 20 m depth. The lower temperatures observed during this season (Figure 3a) were not observed during winter; this was attributed to the fact that the strong winds (>10 m/s) were able to mix the entire water column from September to April (Figure 2b). The high nitrogen values (Figure 3d) observed during the northerly wind season (mainly during November–March) were related to vertical mixing of the water column, owing to strong wind speeds, which resuspended the seafloor nutrients. In contrast, the lower values observed during September 2011 and July 2012 were associated with an increment of the chlorophyll-a values (Figure 4a). This relation was corroborated with a linear correlation (with a confidence level of 90%; i.e. $z = 1.645$) between the nitrogen and the chlorophyll-a values ($r^2 > 0.7$) during September 2011 and July 2012. Finally, the dissolved oxygen (Figure 4b) and oxygen saturation (Figure 4c) were highly correlated to chlorophyll-a values from March to September ($r^2 > 0.7$), while from October to February, there was no correlation among them ($r^2 < 0.4$).

The monthly mean values of the temperature, salinity, sigma-t, nitrogen, chlorophyll-a, and dissolved oxygen for 2011 (Figure 5) and 2012 (Figure 6) were plotted versus depth. It was evident that from September to April (northerly wind season), the water column was more homogeneous than for the other months. However, the temperature, salinity, and density (sigma-t) profiles showed some vertical differences, contrary to the vertical homogeneous water column described before by Salas-Perez and Granados-Barba (2008). The surface layer was warmer (by ~1°C), with the exception of October 2011, less saline (by ~0.2), and less dense (by ~2 kg/m^3), with the exception of September 2012, when compared with the near-bottom water. In all cases, it has its highest vertical gradient between 10 to 20 m. Thus, even if the wind was able to mix the water column (Figure 2b), the hydrographic characteristics (Figures 5, 6) still showed some differences between the surface and bottom waters.

During June and July, a well-marked thermocline was presented at ~30 m (−0.6°C/m) associated with oceanic

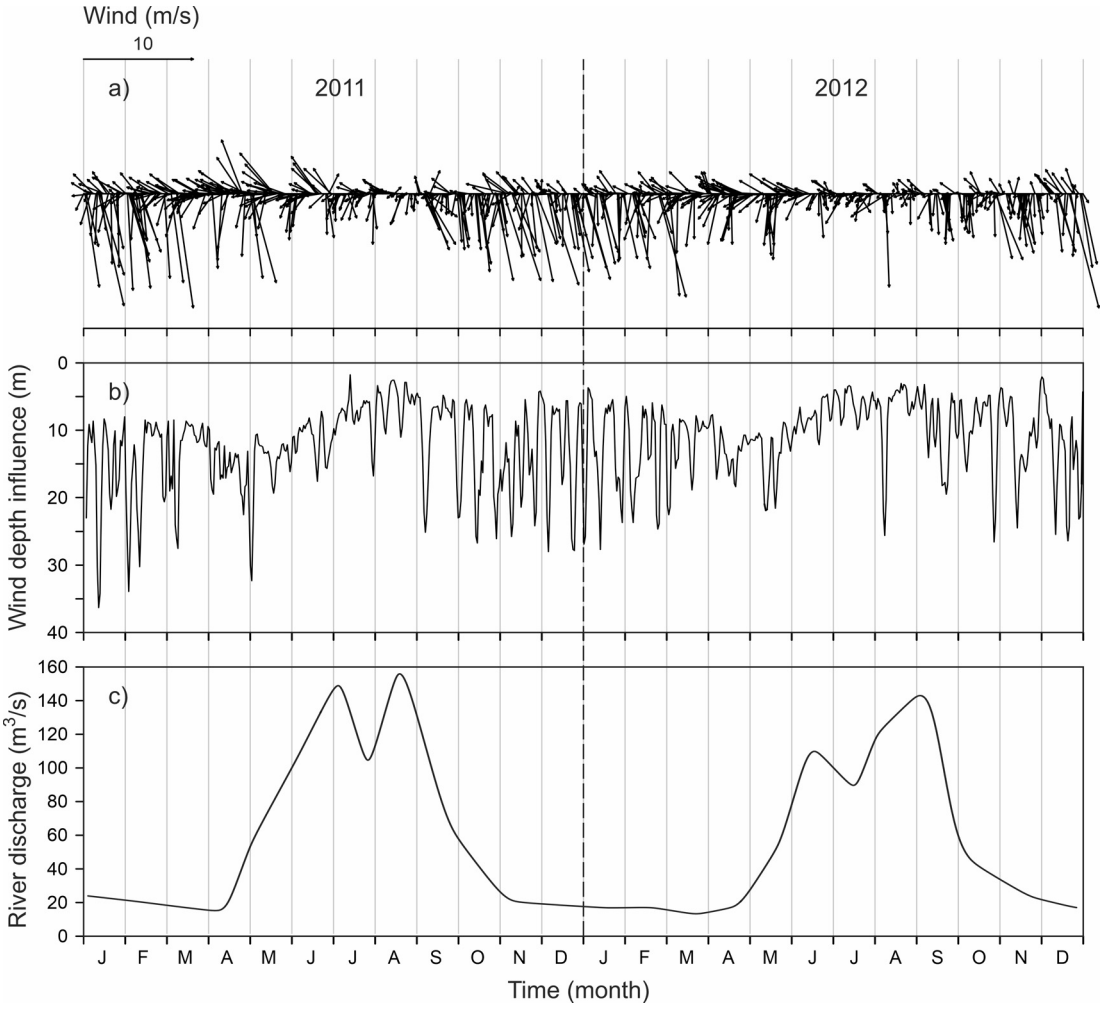

Figure 2 a) Stick plot of the wind velocity (m/s), b) the depth of influence of the wind ($D = 4.81\ U_{10}$), and c) the river discharges of the Jamapa River during 2011 and 2012.

water intrusion during summer (Allende-Arandía et al., 2016; Mateos-Jasso et al., 2012; Riveron-Enzastiga et al., 2016; Salas-Monreal et al., 2009), this idea was reinforced with the vertical profiles of the monthly mean nitrogen, which showed an increment of ~0.085 $\frac{ml}{L\ m}$ at the pycnocline depth. From May to August (dry and rainy seasons) of both years, the halocline was always present over the first 10 m (Figures 5, 6), owing to additional precipitation during the rainy season (Figure 2c) and extra solar irradiation during the dry season. An interesting feature observed during July 2012 was the presence of a second thermocline, pycnocline and nitrocline near 35 m (Figure 6), it is the first time that this condition has been reported at the VRS.

From March 2011 to September 2012, the chlorophyll-*a* profiles (Figures 5e, 6e) had their highest values below ~25 m (>3 μg/L), with the exception of April 2012, consistent with the maximum subsurface values found at the VRS (Avendaño-Alvarez et al., 2017), and in the western Pacific Ocean (Furuya, 1990), among others. The lowest values were always found at the surface due to photoinhibition (Falkowski et al., 1993). Finally, the oxygen profiles of 2011 (1,764 profiles) have higher standard deviation (σ) values than those of 2012 (1,277 profiles), implying that year 2012 was more homogeneous than 2011. This was depicted with the shadow area of Figures 5 and 6, surrounding the mean monthly profile (solid color lines). The shadow area represents the standard deviation (σ), which in some cases it was divided by 2 or 5 ($\sigma/2$; $\sigma/5$) in order to better appreciate the profile. However, some of the standard deviation value differences could be associated with sampling frequency. There were ~16% more profiles in 2011 than in 2012.

According to temperature and salinity profiles (Figures 5a, b, and 6a, b), the dry season was depicted from May to June, when the pycnocline was related to the thermocline. While during the rainy season (July—August), the pycnocline was more related to the halocline. This was confirmed with the density ratio obtained from Equation (3). During the dry season, the density ratio calculated every 0.25 m was of ~1.25 on average, while during the rainy season, it had an average value of ~0.62. Thus, the pycnocline was more influenced by the halocline during the rainy season and by the thermocline during the dry season. Finally, the northerly wind season was considered from September to April, when the strongest wind speed was able to mix the water column (Figures 5a, b, c, and 6a, b, c).

The hydrographic properties were then divided into dry, rainy, and northerly wind seasons. This division was performed to observe the characteristic seasonal behavior of

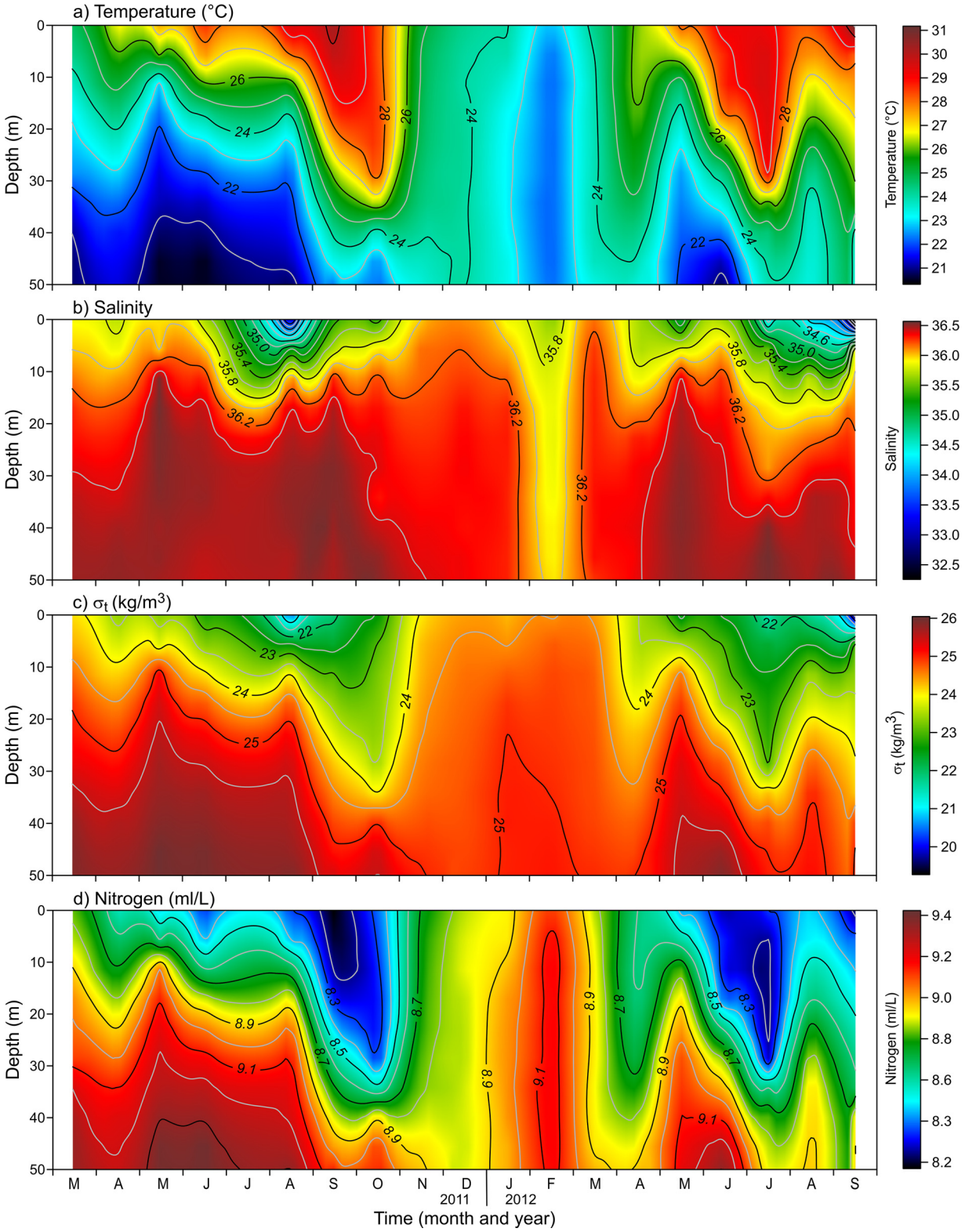

Figure 3 Time series contour plots of a) temperature (°C), b) salinity, c) sigma-*t* (kg/m^3), and d) nitrogen (ml/L) from March 2011 to September 2012.

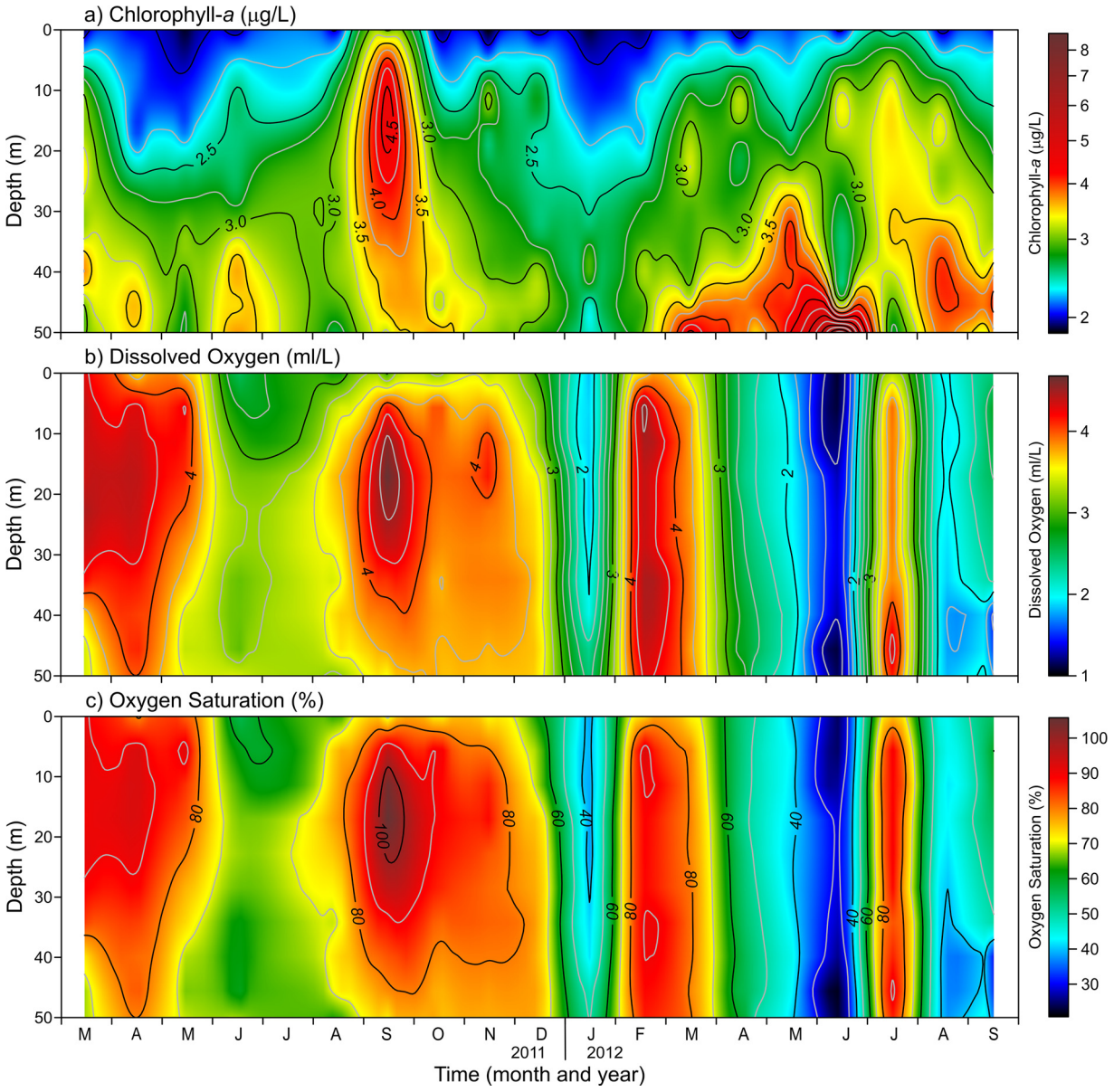

Figure 4 Time series of the contour plots of a) chlorophyll-*a* (μg/L), b) dissolved oxygen (ml/L), and c) oxygen saturation (%) from March 2011 to September 2012.

the hydrographic properties for 2011 (Figure 7) and 2012 (Figure 8). In Figures 7 and 8, the yellow profiles represent the dry season from May to June; the blue profiles the rainy season from July to August; and the purple profiles the northerly wind season from September to April. The time-integrated seasonal average values of the temperature, salinity, and density (σ_t) profiles during the rainy season, have a marked first gradient at ~10 m, and a second gradient, although weaker, at ~30 m (Figures 7a, b, c and 8a, b, c). The halocline and pycnocline observed at 10 m, has previously been reported at the VRS (Allende-Arandía et al., 2016; Avendaño-Alvarez et al., 2017; Mateos-Jasso et al., 2012; Riveron-Enzastiga et al., 2016; Salas-Monreal et al., 2009; Salas-Perez et al., 2020). In 2011 and 2012, the 10 m nitrocline (Figures 7d, and 8d) was evident during the dry and rainy seasons; during the rainy season, a stronger nitrocline was also present at ~30 m. The ~30 m halocline, pycnocline, and nitrocline are reported in this study for the first time during the rainy season of 2011 and 2012. The deepest pycnocline was more evident during 2012, even when this year was relatively dryer than 2011 (Figure 2c). The pycnocline was attributed to near-bottom water intrusion of oceanic water during this season (Figures 3, 5, 6). During the rainy season, the predominant southeasterly winds were not strong enough to induce an eolic upwelling (Allende-Arandía et al., 2016; Mateos-Jasso et al., 2012). However, there is evidence of bottom water intrusion into the VRS as depicted with the temperature, salinity, density (σ_t), and nitrogen profiles (Figures 3, 5, 6). Therefore, the mechanism by which the oceanic water is intruded into the VRS still needs to be clarified. The seasonal profiles of dissolved oxygen and oxygen saturation (Figures 7f, g, and 8f, g) showed similar patterns among them as expected; however, in order to separate the rainy season from the dry and northerly wind seasons using this hydrographic property, it would be recommended to use the oxygen satura-

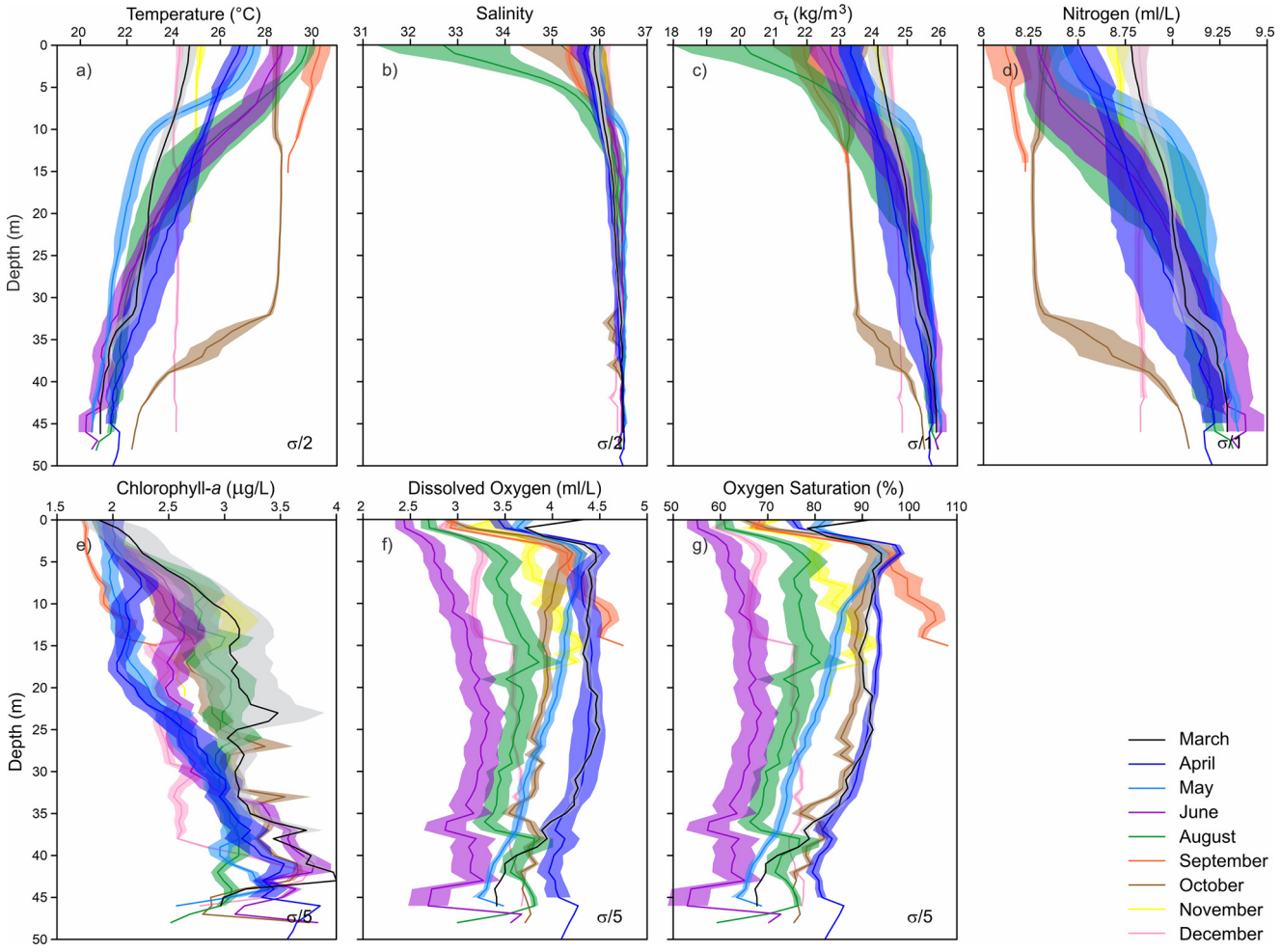

Figure 5 Monthly mean profiles of a) temperature (°C), b) salinity, c) sigma-*t* (kg/m^3), d) nitrogen (ml/L), e) chlorophyll-*a* (µg/L), f) dissolved oxygen (ml/L), and g) oxygen saturation (%) from March to December 2011. The shadow area shows the standard deviation (σ). The standard deviation was divided by 2 ($\sigma/2$) or 5 ($\sigma/5$) in order to better appreciate the profiles.

tion values, rather than the dissolved oxygen values due to the separation of the values among seasons (Figures 7f, g, and 8f, g).

The depth variation of the hydrographic properties within the VRS of 2011 and 2012 was also depicted with the T-S diagrams (Figure 9). 2011 had a higher range of temperature and salinity when compared to 2012. This was attributed to the difference in river discharges for both years (Figure 2c), which mainly affects the near-surface values (Figures 5, 6, 7 and 8). Below sigma-*t* of 23 kg/m^3, both years were similar, except for the relatively low salinity values observed between the sigma-*t* values of 24 to 25 kg/m^3 (Figure 9b), during February 2012 (purple dots with a temperature range of 22 to 22.5°C and a salinity of 35) (Figure 6a, b, c). This could be a common feature in every February, which was not confirmed in this study since the time series started in March 2011. During the dry (Figure 9c) and rainy (Figure 9e) seasons of 2011, the density values (sigma-*t*) were higher than those observed during 2012 (Figure 9d, f); this agrees with the bottom water intrusion described before (Figure 3). One of the differences between the T-S diagrams shown in this study and those previously reported at the VRS (Salas-Perez and Arena-Fuentes, 2011) is the dispersion of the temperature values observed during the northerly wind season (Figure 9a, b). The northerly wind season of 2012 shows more agglomerated values (between 22 to 26°C) than 2011, which is more consistent with what has previously been reported at the VRS (Riveron-Enzastiga et al., 2016; Salas-Perez and Arenas-Fuentes, 2011). The discrepancy occurred during 2011, where the temperature values were more dispersed (between 20 to 31°C), crossing the isopycnals (from 21 to 26 kg/m^3). The discrepancy between the T-S diagrams observed between 2011 and 2012 could be attributed to the length of the series, which starts in March 2011 and ends in September 2012, during the northerly wind season. Therefore, further investigations are needed during the northerly wind season over the deepest ($>$ 40 m) areas of the VRS to confirm if this is a common pattern of the season. One of the apparent discrepancies regarding the T-S diagrams observed here with those previously reported (Riveron-Enzastiga et al., 2016; Salas-Perez and Arenas-Fuentes, 2011) could be related to the total depth of the profiles. The previous T-S diagrams were obtained using profiles above 25 m (Riveron-Enzastiga et al., 2016; Salas-Perez and Arenas-Fuentes, 2011), while the diagrams

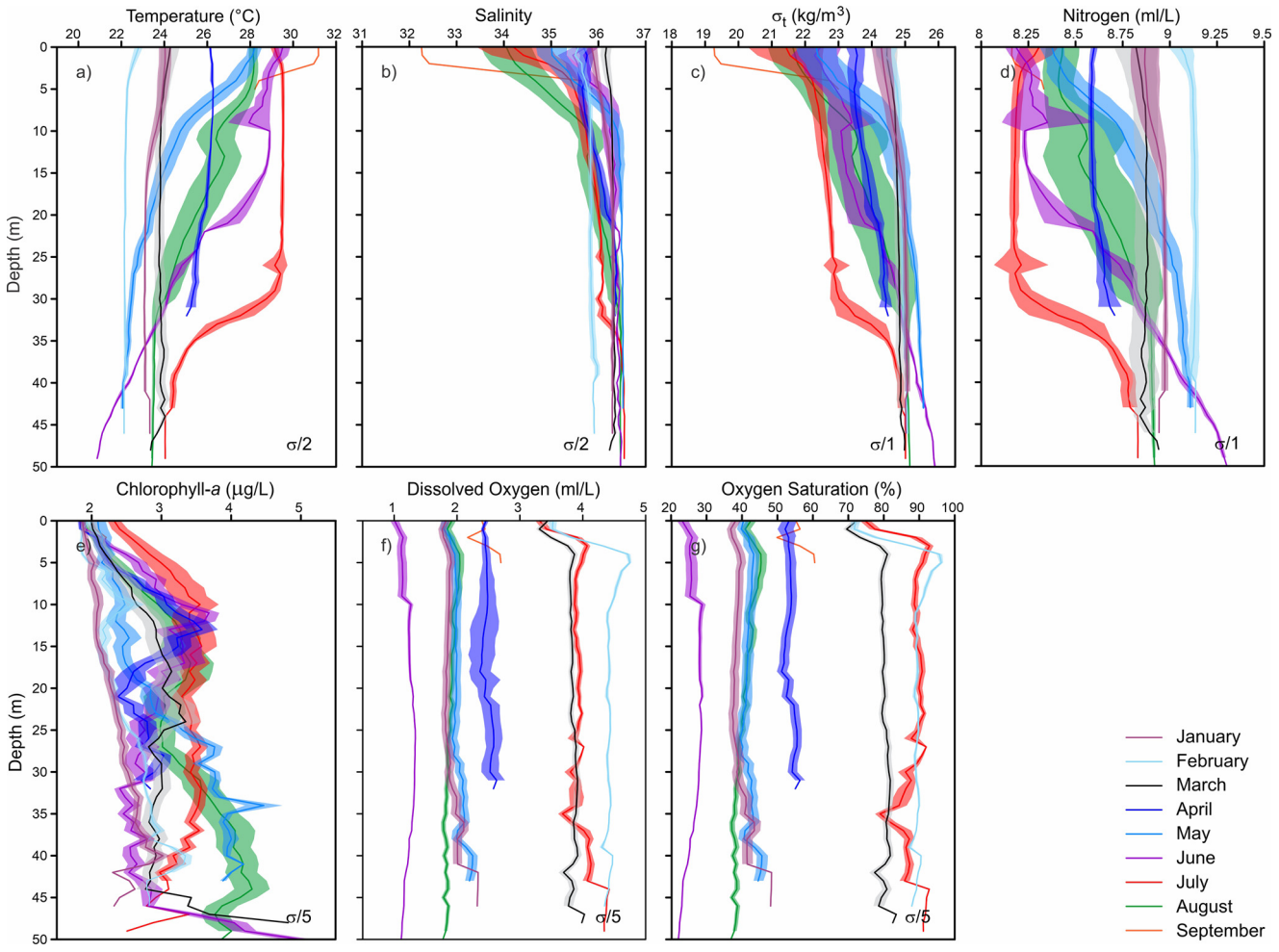

Figure 6 Monthly mean profiles of a) temperature (°C), b) salinity, c) sigma-*t* (kg/m^3), d) nitrogen (ml/L), e) chlorophyll-*a* (µg/L), f) dissolved oxygen (ml/L), and g) oxygen saturation (%) from January to September 2012. The shadow area shows the standard deviation (σ). The standard deviation was divided by 2 ($\sigma/2$) or 5 ($\sigma/5$) in order to better appreciate the profiles.

showed in this study (Figure 9) were made with profiles above 50 m. According to Figures 3 and 9, the GCW could be observed around sigma-*t* of 25 kg/m^3, consistent with the water intrusion observed from ∼10 m depth to the bottom, during the dry and rainy seasons (Figure 3c). The GCW has a temperature and salinity range of 22 to 28°C and 36.2 to 36.4, respectively (Aldeco et al., 2009). However, the lower temperatures ($<$ 22°C) observed at sigma-*t* greater than 25.5 kg/m^3 (Figure 9) are also in agreement with the oceanic water located in the region of the Campeche Canyon reported by Aldeco et al. (2009). Thus, confirming a near-bottom water intrusion.

4. Discussion

According to the meteorological data (Figure 2), the VRS could be divided into dominant northerly wind season from September to April and dominant southerly wind season from May to August. During the dominant northerly wind season, the wind speed was strong enough to mix almost the entire water column, as observed in the contour plots of temperature, salinity, density (σ_t), nitrogen (Figure 3), chlorophyll-*a*, dissolved oxygen, and oxygen saturation (Figure 4). However, the water column was only homogeneous above ∼25 m as previously reported at the VRS (Allende-Arandía et al., 2016; Avendaño-Alvarez et al., 2017; Mateos-Jasso et al., 2012; Riveron-Enzastiga et al., 2016; Salas-Monreal et al., 2009; Salas-Perez and Arenas-Fuentes, 2011; Salas-Perez et al., 2020), below this depth, the near-bottom water showed some differences with the near-surface values. This has not been observed before, due to the total depth of the previous study areas within the VRS ($<$ 25 m). On the other hand, from May to August of both years (2011 and 2012), the dominant southeasterly wind was interspersed with northwesterly winds (Figure 2a). However, the wind speed was not strong enough to reach the pycnocline depth (below 10 m: Figure 3c), i.e. it was not strong enough to break the pycnocline, since the presence of the pycnocline depends on the strength of the stratification and the wind speed. However, there is still evidence of near-bottom water intruding from 10 m depth to the bottom. The water intrusion was observed from May to August during dominant southerly winds. During this

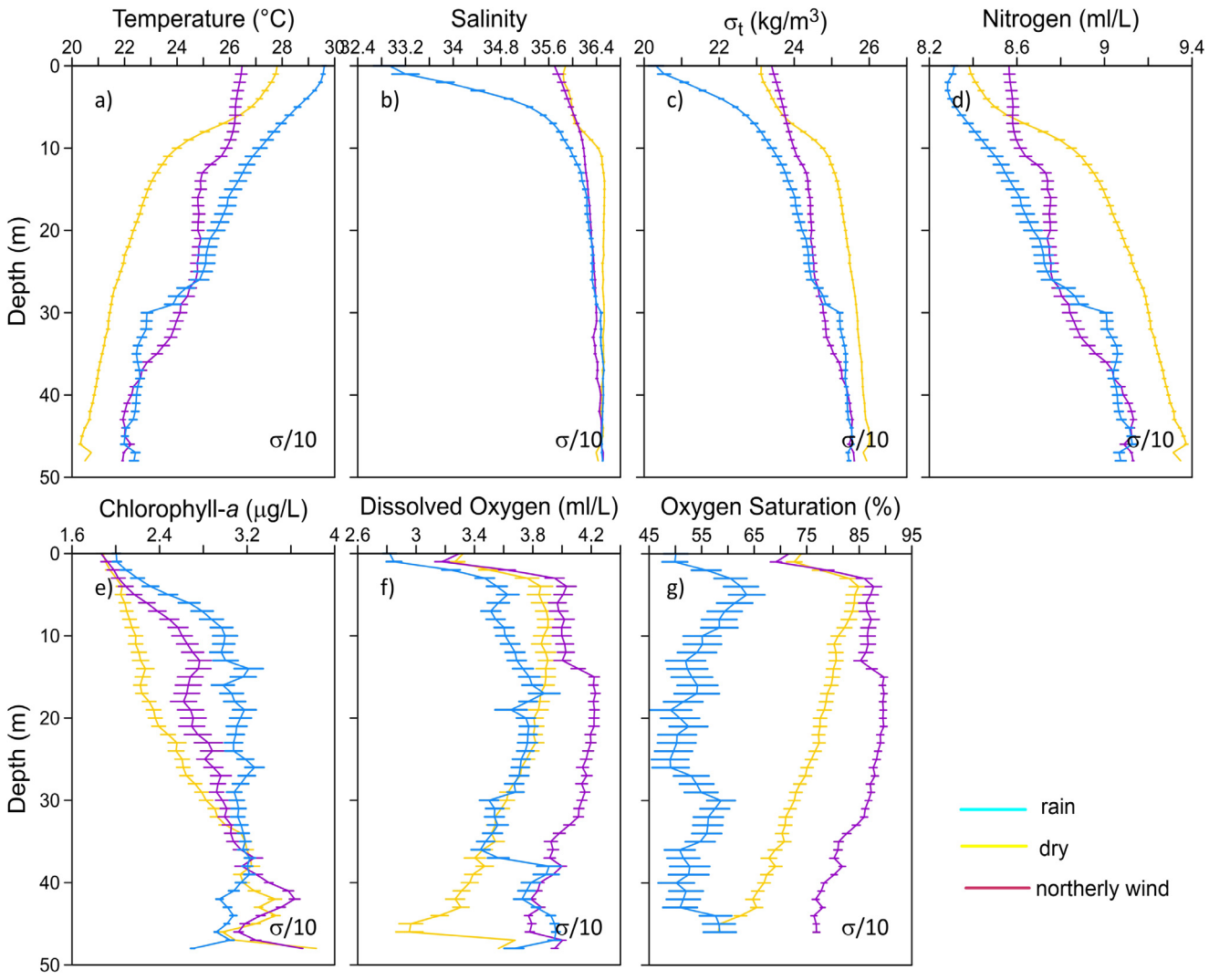

Figure 7 Seasonal mean profiles of a) temperature (°C), b) salinity, c) sigma-*t* (kg/m^3), d) nitrogen (ml/L), e) chlorophyll-*a* (μg/L), f) dissolved oxygen (ml/L), and g) oxygen saturation (%) from March to December 2011. The horizontal bars show the standard deviation (σ). The standard deviation was divided by 10 (σ/10) to appreciate the profiles better. The blue, yellow and purple profiles represent rainy (August), dry (May–June), northerly wind (March–April and September–December) seasons, respectively.

time, we could also divide the season (dominant southerly winds) into dry (May to June) and rainy season (July to August), modifying the previously division suggested by Salas-Perez and Granados-Barba (2008). During the dry season, the pycnocline was more related to the thermocline, while during the rainy season, it was more related to the halocline due to an increment in the rain. During those seasons, the strong southeasterly wind was not able to reach the thermocline or the halocline (Figure 3). Further, the southeasterly events (passage of tropical waves) were followed by northerly winds (Figure 2a). This shift in wind direction did not allow the necessary conditions to develop an eolic upwelling event. Thus, continuous eolic upwelling events (Allende-Arandía et al., 2016; Mateos-Jasso et al., 2012) seem unlikely to occur at the VRS.

Another mechanism should be responsible for the near-bottom water intrusion, as observed with the temperature, salinity, density (Figure 3a, b, c), and nitrogen values (Figure 3d). One of the possible explanations for the near-bottom water intrusion could be the intensification of the cyclonic Gyre of Campeche, as suggested by Guerrero et al. (2020). During the spring-summer season, the Gyre of Campeche gets close to the continental shelf near the 21°N (Salas-Perez et al., 2012), intensifying the along-shelf currents (southward). Thus, a topographic upwelling condition seems unlikely under such circumstances (Riveron-Enzastiga et al., 2016). On the other hand, the collision of Loop Current anticyclones against the western continental shelf slope of the GoM constitutes probably the main mechanism that converts the Subtropical Under Water (SUW) to GCW in the GoM, this water mass intrudes the Veracruz continental shelf (Vidal et al., 1992). The intrusion of the near-bottom water could then be associated to the interaction between the along-shelf current (southward) with the continental shelf at ~21°N (Guerrero et al., 2020), since this mechanism will provide a continuous supply of oceanic water toward the VRS, as observed in this study during the spring-summer season. The continuous injection of oceanic

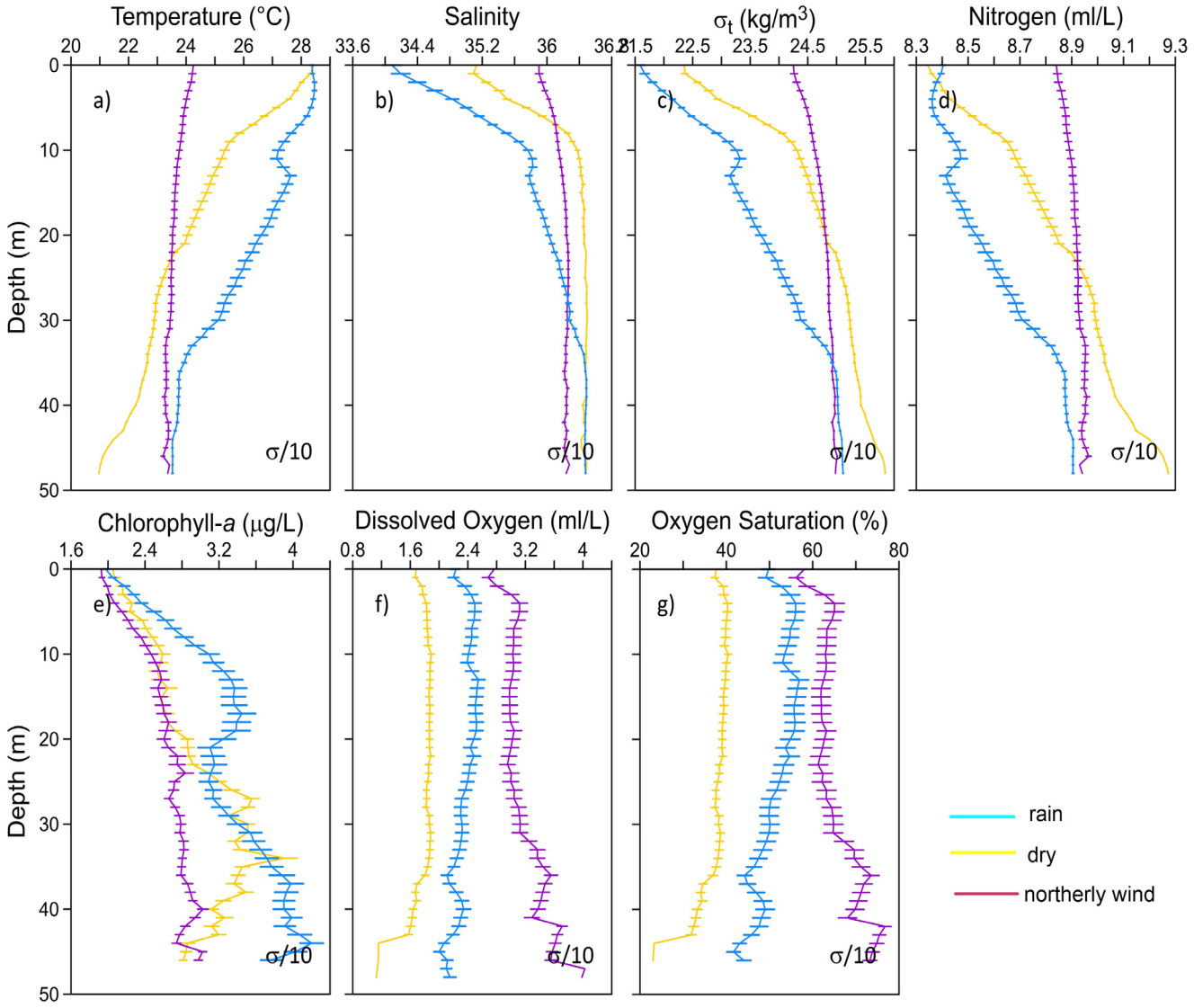

Figure 8 Seasonal mean profiles of a) temperature (°C), b) salinity, c) sigma-*t* (kg/m^3), d) nitrogen (ml/L), e) chlorophyll-*a* (μg/L), f) dissolved oxygen (ml/L), and g) oxygen saturation (%) from January to September 2012. The horizontal bars show the standard deviation (σ). The standard deviation was divided by 10 ($\sigma/10$) to appreciate the profiles better. The blue, yellow and purple profiles represent rainy (July—August), dry (May—June), northerly wind (January-April and September) seasons, respectively.

water should intensify during July and August, when a second pycnocline was present (Figures 7, 8), bringing a colder water mass (Figure 9).

Regardless of the mechanisms that introduce near bottom oceanic water to the VRS, during the summer season, the VRS has temperature and salinity values within the range of the GCW, as previously reported by Salas-Perez and Arenas-Fuentes (2011). The decrement of the temperature ($<$ 22°C) and the high values of nitrogen ($\sim$9.1 ml/L) favor coral development, providing nutrients and inhibiting coral bleaching, making the VRS and an ideal area for coral development. In coral reef areas under the influence of upwelling events such as in Panama (D'Croz and Mate, 2004), the Colombian Caribbean (Diaz-Pulido and Garzon-Ferreira, 2002), the eastern Pacific (Glynn and Morales, 1997), Taiwan (Mayfield et al., 2013), Polynesia (Wolanski and Delesalle, 1995), among others, the intrusion of cold rich-nutrient waters helps corals to grow and develop properly. In contrast, the nitrogen values suggested a high concentration of suspended particles during the northerly wind season (Figures 7, 8). This condition was also observed over the entire western GoM with satellite data (Kineke et al., 2006; Walker and Rouse, 1993), this is vital for the development of coral reefs since the attenuation of light may limit their growth rate (Kleypas et al., 1999; Perry and Macdonald, 2002). As a general balance, the harm done by light limitation and coral coverage with resuspended sediments (Chacon-Gomez et al., 2013) during the northerly wind season is surpassed by the benefits of the mechanisms that brings cold rich-nutrient waters to the system, during the dry and rainy seasons.

Finally, the phytoplankton may consume the nitrogen (Figure 3d) and increase the amount of dissolved oxygen (Figure 4b), as observed during September and October 2011. During February, the increment of the dissolved oxygen has a different mechanism, an increment of the north-

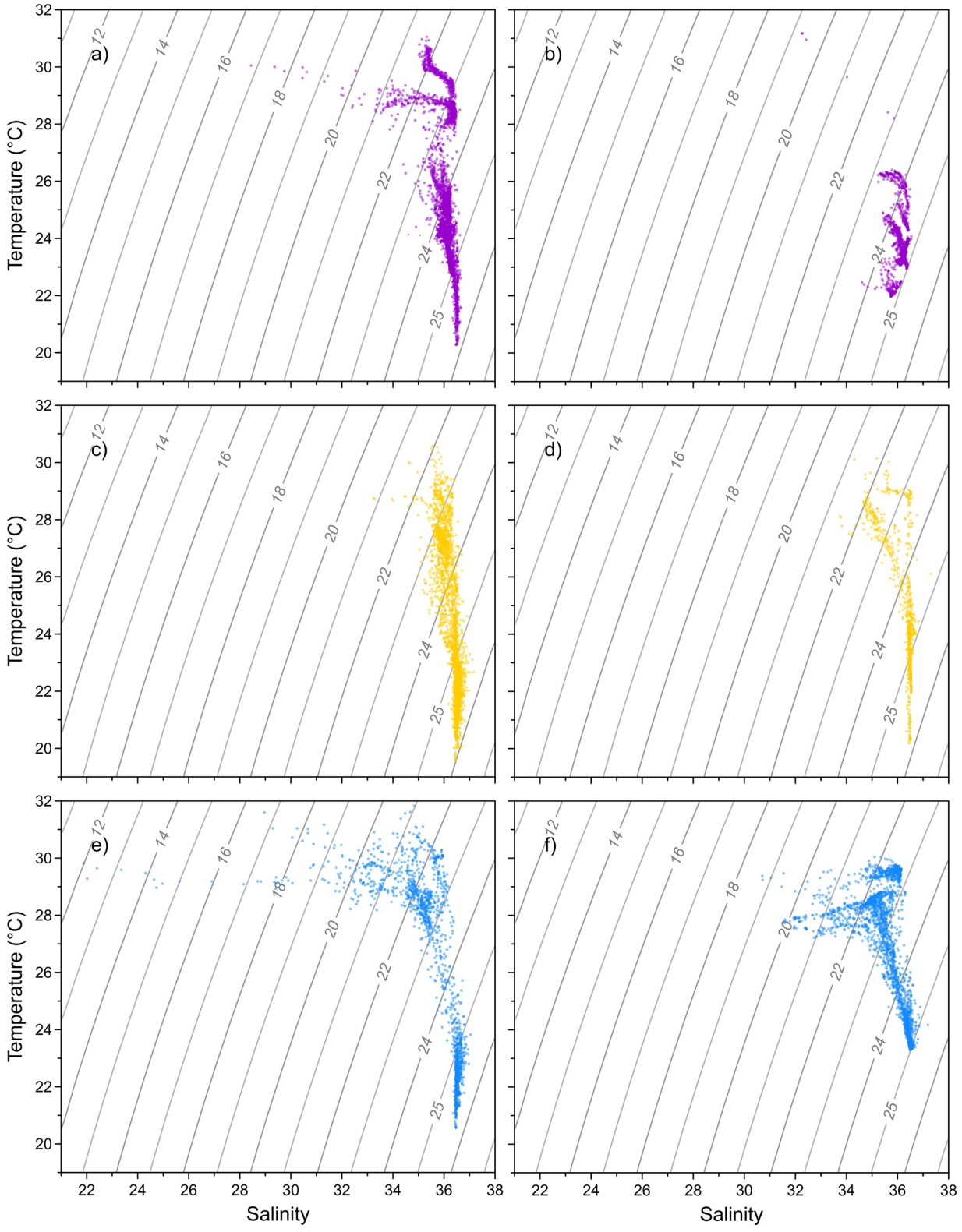

Figure 9 Seasonal T-S diagrams. The purple dots represent the northerly wind season a) 2011 March—April and September—December, and b) 2012 January—April and September. The yellow dots represent the dry season c) 2011 May—June, and d) 2012 May—June. The blue dots represent the rainy season e) 2011 August, and f) 2012 July—August.

westerly winds (Figure 2a) mix the entire water column, increasing the nitrogen (Figure 3d) and oxygen concentrations (Figure 4b, c) along the water column, which was not related to an increment of the chlorophyll-*a* concentration (Figure 4a). The wind-driven mixing was also evident with the temperature and salinity values along the water column (Figure 3a, b). During January, the decrement of the dissolved oxygen (<2 ml/L) (Figure 4b) was directly related to the low concentration of chlorophyll-*a* (<2.5 ml/L) (Figure 4a). Thus, there is a water column seasonal variation of the chlorophyll-*a* below 10 m, in contrast to the constant concentration values reported near the surface by Avendaño et al. (2019).

5. Conclusions

The vertical profiles of the temperature, salinity, density, dissolved oxygen, nitrogen, and chlorophyll-*a* over the entire Veracruz Reef System, were analyzed to study the seasonal hydrographic variation of the reef area, from March 2011 to September 2012. The results showed three seasons; the northerly wind season from September to April; the dry season from May to June, and the rainy season from July to August. The three thousand forty-one profiles showed the influence of the halocline and the thermocline over the pycnocline during the rainy and dry seasons, respectively. There is a direct correlation between the concentration of chlorophyll-*a* and the dissolved oxygen during August–September 2011 and July 2012. This correlation was not observed during March, April 2011 and February 2012, when the increment of the dissolved oxygen in the water column was related to vertical mixing and not to chlorophyll-*a* concentration. During the northerly wind season, the wind was able to mix almost the entire water column during cold front events. Even under the absence of cold front events, the lack of heavy rain periods and relatively lower solar irradiation (winter) combined with the sustained local winds did not allow the presence of the pycnocline. While during summer, the wind was not able to mix the water column, even when the atmospheric tropical waves may, under some circumstances, reach the pycnocline depth. Thus, from September to April (northerly wind season), atmospheric forcing had a greater influence on hydrographic parameters than river discharges, while form July to August (rainy season), river discharges had a greater influence on hydrographic parameters than atmospheric forcing. Finally, there was evidence of oceanic water intrusion into the VRS below ~10 m, which favors coral growth during the spring-summer (dry-rainy) season. During the rainy season the presence of a second halocline, pycnocline, and nitrocline, at ~30 m depth was related to the intrusion of a colder oceanic water into the VRS.

Acknowledgments

The authors would like to acknowledge the work of all students, crew members, and researchers that help during the different stages of data collection, to Jorge Castro for figure improvement.

References

Aldeco, J., Monreal-Gómez, M.A., Signoret, M., Salas-de-León, D.A., Hernández-Becerril, D.U., 2009. Occurrence of a subsurface anticyclonic eddy, fronts, and *Trichodesmium spp*. Cien. Mar. 35 (4), 333–344. https://doi.org/10.7773/cm.v35i4.1551

Allende-Arandía, M.E., Zavala-Hidalgo, J., Romero-Centeno, R., Mateos-Jasso, A., Vargas-Hernández, J.M., Zamudio, L., 2016. Analysis of ocean current observations in the northern Veracruz Coral Reef System. Mexico. J. Coast. Res. 32 (1), 46–55. https://doi.org/10.2112/JCOASTRES-D-14-00148.1

Atchison, A.D., Sammarco, P.W., Brazeau, D.A., 2008. Genetic connectivity in corals on the Flower Garden Banks and surrounding oil/gas platforms, Gulf of Mexico. J. Exp. Mar. Biol. Ecol. 365 (1), 1–12. https://doi.org/10.1016/j.jembe.2008.07.002

Avendaño-Alvarez, O., Salas-Monreal, D., Marin-Hernandez, M., Salas-de-Leon, D.A., Monreal-Gomez, M.A., 2017. Annual hydrological variation and hypoxic zone in a tropical coral reef system. Reg. Stud. Mar. Sci. 9, 145–155. https://doi.org/10.1016/j.rsma.2016.12.007

Avendaño, O., Salas-Monreal, D., Anis, A., Salas-de-Leon, D.A., Monreal-Gomez, M.A., 2019. Monthly surface hydrographical variability in a coral reef system under the influence of river discharges. Estuar. Coast. Shelf Sci. 222, 53–65. https://doi.org/10.1016/j.ecss.2019.04.012

Bennett, A.S., 1976. Conversion of in situ measurements of conductivity to salinity. Deep Sea Research and Oceanographic Abstracts 23 (2), 157–165. https://doi.org/10.1016/S0011-7471(76)80024-1

Bidokhti, A.A., Ezam, M., 2009. The structure of the Persian Gulf outflow is subjected to density variations. Ocean Sci. 5 (1), 1–12. https://doi.org/10.5194/os-5-1-2009

Carricart-Ganivet, J.P., Merino, M., 2001. Growth responses of the reef-building coral Montastraea annularis along a gradient of continental influence in the southern Gulf of Mexico. Bull. Mar. Sci. 68 (1), 133–146. https://doi.org/10.1007/s00338-010-0604-7

Carricart-Ganivet, J.P., Beltrán-Torres, A.U., Horta-Puga, G., 2011. Distribution and prevalence of coral diseases in the Veracruz Reef System, Southern Gulf of Mexico. Dis. Aquat. Organ. 95 (3), 181–187. https://doi.org/10.3354/dao02359

Chacon-Gomez, I.C., Salas-Monreal, D., Riveron-Enzastiga, M.L., 2013. Current pattern and coral larval dispersion in a tropical coral reef system. Cont. Shelf Res. 68, 23–32. https://doi.org/10.1016/j.csr.2013.08.014

Diaz-Pulido, G., Garzón-Ferreira, J., 2002. Seasonality in algal assemblages on upwelling-influenced coral reefs in the Colombian Caribbean. Bot. Mar. 45 (3), 284–292. https://doi.org/10.1515/BOT.2002.028

D'Croz, L., Maté, J.L., 2004. Experimental responses to elevated water temperature in genotypes of the reef coral *Pocillopora damicornis* from upwelling and non-upwelling environments in Panama. Coral Reefs 23 (4), 473–483. https://doi.org/10.1007/s00338-004-0397-7

Deslarzes, K.J.P., 1998. The Flower Garden Banks (Northwest Gulf of Mexico): Environmental Characteristics and Human Interaction. OCS Report MMS 98-0010. US Department of the Interior, Minerals Management Service, Gulf of Mexico OCS Region, New Orleans, LA (US), 100 pp.

Falkowski, P.G., Greene, R., Kolber, Z., 1993. Light utilization and photoinhibition of photosynthesis in marine phytoplankton (No. BNL-49821; CONF-9309312-1). Brookhaven National Lab, Upton, NY (United States).

Furuya, K., 1990. Subsurface chlorophyll maximum in the tropical and subtropical western Pacific Ocean: vertical profiles of phytoplankton biomass and its relationship with chlorophyll-*a*

and particulate organic carbon. Mar. Biol. 107 (3), 529—539. https://doi.org/10.1007/BF01313438

Glynn, P.W., Morales, G.E.L., 1997. Coral reefs of Huatulco, West Mexico: reef development in upwelling Gulf of Tehuantepec. Rev. Biol. Trop. 45 (3), 1033—1047. https://revistas.ucr.ac.cr/index.php/rbt/article/view/21114.

Guerrero, L., Sheinbaum, J., Mariño-Tapia, I., González-Rejón, J.J., Pérez-Brunius, P., 2020. Influence of mesoscale eddies on cross-shelf Exchange in the western Gulf of Mexico. Cont. Shelf Res. 209. https://doi.org/10.1016/j.csr.2020.104243

Hersbach, H., Bell, B., Berrisford, P., Biavati, G., Horányi, A., Muñoz Sabater, J., Nicolas, J., Peubey, C., Radu, R., Rozum, I., Schepers, D., Simmons, A., Soci, C., Dee, D., Thépaut, J-N., 2018. ERA5 hourly data on single levels from 1979 to present. Copernicus Climate Change Service (C3S) Climate Data Store (CDS). (Accessed on 01-12-2021). https://doi.org/10.24381/cds.adbb2d47

Hughes, T.P., Kerry, J.T., Simpson, T., 2018. Large-scale bleaching of corals on the Great Barrier Reef. Ecology 99 (2), 501. https://doi.org/10.1007/s003380050154

Isdale, J.D., Spence, C.M., Tudhope, J.S., 1972. Physical properties of sea water solutions: viscosity. Desalination 10 (4), 319—328.

Jordan-Dahlgren, E., 2002. Gorgonian distribution patterns in coral reef environments of the Gulf of Mexico: evidence of sporadic ecological connectivity? Coral Reefs 21 (2), 205—215. https://doi.org/10.1007/s00338-002-0226-9

Kineke, G.C., Higgins, E.E., Hart, K., Velasco, D., 2006. Fine-sediment transport associated with cold-front passages on the shallow shelf. Gulf of Mexico. Cont. Shelf Res. 26 (17—18), 2073—2091. https://doi.org/10.1016/j.csr.2006.07.023

Kleypas, J.A., McManus, J.W., Meñez, L.A.B., 1999. Environmental limits to coral reef development: where do we draw the line? Am. Zool. 39 (1), 146—159. https://doi.org/10.1093/icb/39.1.146

Liaño-Carrera, F., Camarena-Luhrs, T., Gómez-Barrero, A., Martos-Fernández, F.J., Ramírez-Macias, J.I., Salas-Monreal, D., 2019. New coral reef structures in a tropical coral reef system. Lat. Am. J. Aquat. Res. 47 (2), 270—281. https://doi.org/10.3856/vol47-issue2-fulltext-7

Lugo-Fernandez, A., Deslarzes, K.J.P., Price, J.M., Boland, G.S., Morin, M.V., 2001. Inferring probable dispersal of Flower Garden Banks coral larvae (Gulf of Mexico) using observed and simulated drifter trajectories. Cont. Shelf Res. 21 (1), 47—67. https://doi.org/10.1016/S0278-4343(00)00072-8

Mateos-Jasso, A., Zavala-Hidalgo, J., Romero-Centeno, R., Allende-Arandía, M.E., 2012. Variability of the thermohaline structure in the northern Veracruz Coral Reef System. Mexico. Cont. Shelf Res. 50, 30—40. https://doi.org/10.1016/j.csr.2012.10.001

Mayfield, A.B., Fan, T.Y., Chen, C.S., 2013. Physiological acclimation to elevated temperature in a reef-building coral from an upwelling environment. Coral Reefs 32 (4), 909—921. https://doi.org/10.1016/j.csr.2012.10.001

Moore, D.R., Bullis Jr, H.R., 1960. A deep-water coral reef in the Gulf of Mexico. Bull. Mar. Sci. 10 (1), 125—128.

Okolodkov, Y.B., Aké-Castillo, J.A., Gutiérrez-Quevedo, M.G., Pérez-España, H., Salas-Monreal, D., 2011. Annual cycle of the plankton biomass in the National Park Sistema Arrecifal Veracruzano, southwestern Gulf of Mexico. In: Katell, G. (Ed.), Zooplankton and phytoplankton: Types, Characteristics and Ecology. Nova Science Publishers, 63—88.

Ortiz-Lozano, L., Pérez-España, H., Granados-Barba, A., González-Gándara, C., Gutiérrez-Velázquez, A., Martos, J., 2013. The Reef Corridor of the Southwest Gulf of Mexico: Challenges for its management and conservation. Ocean Coast. Manag. 86, 22—32. https://doi.org/10.1016/j.ocecoaman.2013.10.006

Perry, C.T., Macdonald, I.A., 2002. Impacts of light penetration on the bathymetry of reef microboring communities: implications for the development of microendolithic trace assemblages. Palaeogeogr. Palaeoclimatol. Palaeoecol. 186 (1—2), 101—113. https://doi.org/10.1016/S0031-0182(02)00446-7

Rezak, R., Bright, T.J., McGrail, D.W., 1985. Reefs and Banks of the Northwestern Gulf of Mexico: their Geological, Biological, and Physical Dynamics. John Wiley & Son, New York, 259 pp.

Riveron-Enzastiga, M.L., Carbajal, N., Salas-Monreal, D., 2016. Tropical coral reef system hydrodynamics in the western Gulf of Mexico. Sci. Mar. 80 (2), 237—246.

Salas-Monreal, D., Marin-Hernandez, M., Salas-Perez, J.J., Salas-de-Leon, D.A., Monreal-Gomez, M.A., Perez-España, H., 2018. Coral reef connectivity within the Western Gulf of Mexico. J. Mar. Syst. 179, 88—99. https://doi.org/10.1016/j.jmarsys.2017.12.001

Salas-Monreal, D., Riveron-Enzastiga, M.L., Salas-Perez, J.J., Bernal-Ramirez, R., Marin-Hernandez, M., Granados-Barba, A., 2020. Bathymetric flow rectification in a tropical micro-tidal estuary. Estuar. Coast. Shelf Sci. 235, 106562. https://doi.org/10.1016/j.ecss.2019.106562

Salas-Monreal, D., Salas-de-León, D.A., Monreal-Gómez, M.A., Riverón-Enzástiga, M.L., 2009. Current rectification in a tropical coral reef system. Coral Reefs 28 (4), 871—879. https://doi.org/10.1007/s00338-009-0521-9

Salas-Monreal, D., Valle-Levinson, A., Athie, G., 2019. Flow modifications over a tropical coral reef system. Estuar. Coast. Shelf Sci. 217, 271—280. https://doi.org/10.1016/j.ecss.2018.11.029

Salas-Perez, J.J., Arenas-Fuentes, V., 2011. Winter water mass of the Veracruz Reef System. Atmósfera 24 (2), 221—231.

Salas-Perez, J.J., Granados-Barba, A., 2008. Oceanographic characterization of the Veracruz reef system. Atmósfera 21, 281—301. http://www.scielo.org.mx/scielo.php?script=sci_arttext&pid=S0187-62362008000300005&nrm=iso

Salas-Perez, J.J., Jordan-Garza, A.G., Salas-Monreal, D., 2020. Climate variability over the reef corridor of the southwestern Gulf of Mexico. Atmósfera 33 (2), 143—157. https://doi.org/10.20937/atm.52730

Salas-Perez, J.J., Salas-Monreal, D., Monreal-Gómez, M.A., Riveron-Enzastiga, M.L., Llasat, C., 2012. Seasonal absolute acoustic intensity, atmospheric forcing and currents in a tropical coral reef system. Estuar. Coast. Shelf Sci. 100, 102—112. https://doi.org/10.1016/j.ecss.2012.01.002

Sammarco, P.W., Brazeau, D.A., Sinclair, J., 2012. Genetic connectivity in scleractinian corals across the Northern Gulf of Mexico: oil/gas platforms, and relationship to the Flower Garden Banks. PLoS One 7 (4). https://doi.org/10.1371/journal.pone.0030144

Sanvicente-Añorve, L., Zavala-Hidalgo, J., Allende-Arandía, M.E., Hermoso-Salazar, M., 2014. Connectivity patterns among coral reef systems in the southern Gulf of Mexico. Mar. Ecol. Prog. Ser. 498, 27—41. https://doi.org/10.3354/meps10631

Schill, S.R., Raber, G.T., Roberts, J.J., Treml, E.A., Brenner, J., Halpin, P.N., 2015. No reef is an island: integrating coral reef connectivity data into the design of regional-scale marine protected area networks. PLoS One 10 (12). https://doi.org/10.1371/journal.pone.00144199

Sharqawy, M.H., Lienhard, J.H., Zubair, S.M., 2010. Thermophysical properties of seawater: a review of existing correlations and data. Desalination Water Treat 16 (1—3), 354—380. https://doi.org/10.5004/dwt.2010.1079

Tunnell, J.W., Chavez, E.A., Withers, K., 2007. Coral reefs of the southern Gulf of Mexico. Texas A&M University Press, Corpus Christi, Texas, 194 pp.

Vera-Mendoza, R.R., Salas-de-León, D.A., Salas-Monreal, D., Ortiz-Figueroa, M., 2017. Wind forcing of sea level variability in a tropical coral reef area in the western Gulf of Mexico. Lat. Am. J. Aquat. Res. 45 (4), 797—806. https://doi.org/10.3856/vol45-issue4-fulltext-15

Vidal, M.V.V., Vidal, F.V., Pérez-Molero, J.M., 1992. Collision of a loop current anticyclonic ring against the continental shelf

slope of the western Gulf of Mexico. J. Geophys. Res. 97 (02), 2155—2172.

Villegas-Sánchez, C.A., Pérez-España, H., Rivera-Madrid, R., Salas-Monreal, D., Arias-González, J.E., 2013. Subtle genetic connectivity between Mexican Caribbean and south-western Gulf of Mexico reefs: the case of the bicolor damselfish, *Stegastes partitus*. Coral Reefs 33 (1), 241—251. https://doi.org/10.1007/s00338-013-1083-4

Walker, N.D., Rouse Jr, L.J., 1993. Satellite assessment of Mississippi River discharge plume variability. OCS Study MMS 93 —0044, US Department of the Interior, Minerals Management Service, Gulf of Mexico OCS Region, New Orleans, L.A, 50 pp.

Wolanski, E., Delesalle, B., 1995. Upwelling by internal waves, Tahiti, French Polynesia. Cont. Shelf Res. 15 (2—3), 357—368. https://doi.org/10.1016/0278-4343(93)E0004-R

Oceanologia 64 (2022) 489—502

Available online at www.sciencedirect.com

ScienceDirect

journal homepage: www.journals.elsevier.com/oceanologia

ORIGINAL RESEARCH ARTICLE

Distribution of anisakid nematodes in the muscle tissue of cod (*Gadus morhua*) from the Norwegian Sea

Katarzyna Nadolna-Ałtyn[a,*], **Magdalena Podolska**[a], **Joanna Pawlak**[a], **Beata Szostakowska**[b]

[a] *National Marine Fisheries Research Institute, Gdynia, Poland*
[b] *Medical University of Gdańsk, Gdynia, Poland*

Received 10 January 2022; accepted 18 March 2022
Available online 31 March 2022

KEYWORDS
Anisakis;
Pseudoterranova;
Atlantic cod;
Gadus morhua;
North Atlantic

Abstract Atlantic cod (*Gadus morhua*) is an important commercial fish species on the world market. The aim of our studies was to explore the presence, intensity of infection and distribution of the zoonotic nematodes of the different genera of Anisakidae in the muscle tissue of *G. morhua* from the Norwegian Sea. Cod from fishing areas FAO IIa1 (n = 50) and FAO IIa2 (n = 56) were sampled in March 2017. The unskinned flesh of each fish was examined using a white-light transilluminator. Collected parasites were identified to the genus level, and a subsample was identified using molecular methods. We found a higher prevalence of infection with *Anisakis* than with *Pseudoterranova* in the musculature of cod from both fishing areas. In FAO IIa1, a lower prevalence of infection with *Pseudoterranova* was recorded (14%) than in FAO IIa2 (~39%). However, the intensity of infection was higher (53) in FAO IIa2 than in FAO IIa1 (8 parasites per fish). The opposite was found with *Anisakis* (prevalence 88% in FAO IIa1 and ~55% in FAO IIa2, intensity up to 30 and up to 25 parasites per fish respectively). Most *Anisakis* larvae were present in the belly flaps (predominantly the left side), while *Pseudoterranova* spp. were dispersed with descending frequency in belly flaps, dorsal fillet and caudal fillet.

* Corresponding author at: National Marine Fisheries Research Institute, Kołłątaja 1, 81-332 Gdynia, Poland.
E-mail address: knadolna@mir.gdynia.pl (K. Nadolna-Ałtyn).
Peer review under the responsibility of the Institute of Oceanology of the Polish Academy of Sciences.

Production and hosting by Elsevier

https://doi.org/10.1016/j.oceano.2022.03.003

Molecular identification revealed the presence of *A. simplex* (s.s.), *P. decipiens* (s.s.) and *P. krabbei* in both areas, and a hybrid of *P. decipiens* and *P. krabbei* in FAO IIa2.

1. Introduction

Atlantic cod (*Gadus morhua*) occurs in shelf waters throughout the North Atlantic Ocean and its adjacent seas (Cohen et al., 1990). In Europe, it has been recorded from the northwestern Iberian Peninsula to the Barents Sea, including British and Icelandic waters, as well as some brackish water localities in the Baltic Sea (Bañon et al., 2010; ICES, 2005). Atlantic cod is one of the most important commercial fish species on the world market. According to a report from the Food and Agriculture Organization of the United Nations (FAO) in 2012, it was among the 10 most-fished species in the world in 2010 and 2011, with about 200 000 tonnes landed per year, and was one of the most important species in European commercial fisheries (Cardinale et al., 2013). In 2016, landings of cod in the EU reached more than 91 000 tonnes and had a value of EUR 226 million (EUMOFA, 2018). The top three EU players in the cod fishery were Denmark, the UK and Spain. Most cod landings in Spain are frozen, while those in Denmark and UK are almost entirely fresh products. Fresh cod landed in the UK reached a 10-year peak at more than 15 000 tonnes (EUMOFA, 2018). The reason for such great interest in fisheries of this species is the popularity of cod with consumers, because of its mild flavour and dense, flaky white flesh.

The European Food Safety Authority (EFSA) has stated that all wild-caught fish (particularly if intended to be eaten raw or nearly raw) must be considered at risk of containing viable parasites of concern to human health (EFSA, 2010). The most dangerous parasites for human health that can be found in cod fillets are Anisakidae nematodes: *Anisakis simplex* and *A. pegreffii* (Audicana and Kennedy, 2008; Ishikura et al., 1993; Mattiucci et al., 2013), as well as *Pseudoterranova* spp. (Mattiucci et al., 2013; Mehrdana et al., 2014; Shamsi and Suthar, 2016; Torres et al., 2007). Viable, invasive anisakid larvae accidentally ingested by humans may cause anisakidosis. Symptoms of acute anisakidosis include nausea, diarrhea, vomiting, and intense abdominal pain (Hochberg et al., 2010; Ishikura et al., 1993). There are no published case studies of acute anisakidosis caused by eating infected cod. Nevertheless, two cases of allergy related to anisakidosis following consumption of raw cod have been reported (Alonso-Gómez et al., 2004). Although adequate treatment kills the parasite (Wharton and Aalders, 2002), some of the allergenic proteins of anisakid nematodes are thermostable (Audicana et al., 2002; Moneo et al., 2005). Brunet et al. (2017) demonstrated two cases of infection with *Pseudoterranova decipiens s.s.* in French patients after consumption of a baked cod.

The presence of Anisakidae nematodes in North Atlantic cod muscle tissue has been known for many years: they were recorded in cod fillets from the southern Canadian mainland between 1946 and 1956 (Scott and Martin, 1957), and from different areas adjacent to Newfoundland in the periods 1947–1953 (Templeman et al., 1957) and 1984–1985 (Chandra and Khan, 1988). Parasites, including nematodes, were considered to be biological indicators of stocks of Atlantic cod sampled between 1981 and 1983 off Newfoundland, Canada (Khan and Tuck, 1995). The presence and abundance of *A. simplex* larvae in the flesh of Atlantic cod was examined between 1985 and 1987 in the western Atlantic Ocean around Newfoundland and Labrador: their presence and abundance of parasites varied geographically and increased with cod size (Brattey and Bishop, 1992). Cod from the Gulf of St. Lawrence were examined for the presence of nematodes between 1990 and 1992 (Boily and Marcogliese, 1995), while the occurrence of anisakid nematodes in Atlantic cod was investigated in west Greenland in 2005 (Mouritsen et al., 2010). Cod from Iceland, the Norway coast, the Barents Sea and Arctic waters were examined for the presence of *Pseudoterranova decipiens* (former name *Terranova decipiens*) and *Anisakis* sp. between 1971 and 1973, with different levels of infection being observed in various stocks (Platt, 1975). Fillets of Norwegian Arctic cod from the Barents Sea in 1989 showed a 96% infection rate with *A. simplex*, with a significant difference in mean intensity of infection between oceanic and coastal fish (Aspholm, 1995). Anisakidae larvae were found in 34.7% of cod fillets from fish caught in the northeastern Atlantic ocean (Piccolo et al., 1999). Nematodes were recorded in cod from the Barents Sea in 2002 (Sobecka et al., 2011) and 2011 (Najda et al., 2018). Research conducted during 2013–2014 in the Barents Sea confirmed the high prevalence of cod infection with *A. simplex* (~90% of fillets), although infection with *Pseudoterranova* was lower (less than 10%) (Gay et al., 2018). Most research on cod from the Norwegian Sea was conducted in the coastal waters of Balsfjord and Ullsfjord (Hemmingsen et al., 1991), Balsfjord (Hemmingsen et al., 1992, 1995), Oslofjord (Aspholm et al., 1995; Jensen and Idås, 1992), Altafjord (Hemmingsen et al., 1993), near the island of Vega (Strømnes and Andersen, 1998, 2000) and in Trondheimsfjord (Perdiguero-Alonso et al., 2008). Nematode parasites in cod have also been noted in Icelandic waters (Hauksson, 2011; Perdiguero-Alonso et al., 2008), the Irish and Celtic Seas (Perdiguero-Alonso et al., 2008), and the Central and Northern North Sea (Gay et al., 2018; Perdiguero-Alonso et al., 2008). Nematode parasites were even recorded in cod larvae from the North Sea (Skovgaard et al., 2011). Despite the above research, there is currently a lack of knowledge about the level of cod infection in offshore waters of the Norwegian Sea. Because the level of infection with nematode parasites may differ significantly even between neighboring areas (Molina-Fernandez et al., 2015; Platt, 1975), we decided to focus

on the spatial distribution of cod infection with Anisakidae nematodes in the North East Atlantic.

The Norwegian Sea has been an important and intensively exploited cod fishing ground for many years (Bertheussen and Dreyer, 2019). Norwegian cod products are offered in various forms (whole fresh or frozen fish, fresh fillets, dried, dried salted or wet salted) and are exported to destinations over almost the whole world: Europe, Africa, South America and Asia (Asche et al., 2018).

There are a variety of methods of detecting the presence of nematodes in the fillets of fish. Some of them are not suitable for use during fish processing, because the tissues of the fish are destroyed. For example, both the compression technique (Karl and Leinemann, 1993) and digestion in artificial gastric juice (Llarena-Reino et al., 2013) allow the quantitative determination of nematodes, but lead to the destruction of fish tissue. Moreover, the UV-compression technique (Gomez-Morales et al., 2018), considered today to be the most sensitive among non-destructive methods that assess the risk of human infection by zoonotic nematodes, is limited to frozen products, because it relies on the ability of dead anisakid larvae to show fluorescence under UV light, and is not applicable in the case of fresh fillets. Emerging technologies such as imaging spectroscopy (Heia et al., 2007), multispectral imaging (Stormo et al., 2007; Wold et al., 2001), hyperspectral imaging (Sivertsen et al., 2011), X-ray (Heia et al., 1997) or magnetic resonance imaging (Bao et al., 2017) are used less frequently in the fish processing industry.

Our investigation was conducted using candling, which detects parasites by visual inspection of fish tissues over a light source. Although routine screening of fillets by candling is not 100% effective (Bao et al., 2019; Gomez-Morales et al., 2018; González et al., 2018; Levsen et al., 2005; Mercken et al., 2020a), it is the most widely adopted method in industry, where more accurate laboratory methods of detection are not routinely used. The main advantages of candling are its relatively low cost and simplicity and that it allows detection and immediate removal of visible parasites with minimal damage to the fillet's muscle tissue. In addition, many previous studies have been carried out using candling, allowing better comparison of the results obtained. Thus, the aim of our studies was to explore the level of infection with anisakids and the distribution of the different genera of Anisakidae nematodes in the muscle tissue of *G. morhua* using the detection method routinely applied in fish processing plants.

2. Material and methods

2.1. Sampling and detection of parasites

Cod was caught during a commercial survey in March 2017 in two areas of the North Atlantic, FAO IIa1 (n = 50) and FAO IIa2 (n = 56), as shown on the map (Figure 1). This sampling period was chosen because data (2007—2016) from the Norwegian Directorate of Fisheries showed the monthly average cod catch in this area to be highest in March (Bertheussen and Dreyer, 2019). Randomly chosen whole fish with undercut throats were kept on ice and frozen for further analysis. Subsequently, in the laboratory, after thawing for 24 h, standard ichthyological analysis was performed.

The presence of nematode parasites in different parts of the cod muscle tissue was evaluated. The unskinned flesh from both the right and left side of each animal was divided into three parts: anterior ventral (belly flaps), dorsal fillet and caudal fillet. Each part was examined for the presence of parasites in the muscle tissue using a transilluminator. All parasites detected were collected for further parasitological identification.

2.2. Identification of parasites

All detected parasites were collected and identified to the genus level on the basis of anatomo-morphological features as described by Fagerholm (1982) and Berland (1989). A subsample of parasites (16 *Anisakis* sp. and 34 *Pseudoterranova* sp.) of different origins was molecularly identified. Representative examples of each nematode species were selected from both regions in proportion to the number of nematodes of each species collected for that region. The target of molecular analysis in all cases was internal transcribed spacer 1 of the ribosomal DNA (ITS-1 rDNA). DNA was isolated using a Genomic Mini Kit (A&A Biotechnology, Gdynia, Poland) according to the instructions. The analysis of ITS-1: the amplification was performed using NC5 (forward) 5′ GTA GGT GAA CCT GCG GAA GGA TCA TT 3′ and NC13R (reverse) 5′ GCT GCG TTC TTC ATC GAT 3′ primers (Zhu et al., 2000,2002). The reaction mixture consisted of 25 μl PCR Master Mix Plus High GC (ready-to-use PCR mixture containing Taq DNA polymerase, PCR buffer, $MgCl_2$ and dNTPs; A&A Biotechnology), 2 μl each primer (concentration 10 μM) and 5 μl DNA template, supplemented with deionized water up to 50 μl. The PCR conditions were as follows: 3 min at 94°C (initial denaturation) followed by 30 cycles of denaturation at 94°C for 30 s, annealing of primers at 55°C for 30 s, strand elongation at 72°C for 30 s and a final extension step of 5 min at 72°C. If the amplification was weak, the reaction was repeated, increasing the number of cycles to 40. Polymerase chain reaction (PCR) products were sequenced directly using standard procedures and amplification primers. Sequences were analysed using GeneStudio™ Professional (GeneStudio, Inc., USA) and confirmed by a BLAST search of GenBank. The sequences obtained have been deposited in GenBank with the accession numbers given in the Results.

2.3. Parasitological descriptors

The descriptors of parasite distribution used in the present study followed the definitions given by Bush et al. (1997). Prevalence is "the number of hosts infected with one or more individuals of a parasite species (or of a taxonomic group) divided by the number of hosts examined for that parasite species". The abundance is "the number of individuals of a particular parasite in/on a single host regardless of whether or not the host is infected". The intensity (of infection) is "the number of individuals of a particular parasite species in a single infected host". Both abundance and intensity of infection were calculated, to make it easier to compare the results obtained with the information presented in previous research.

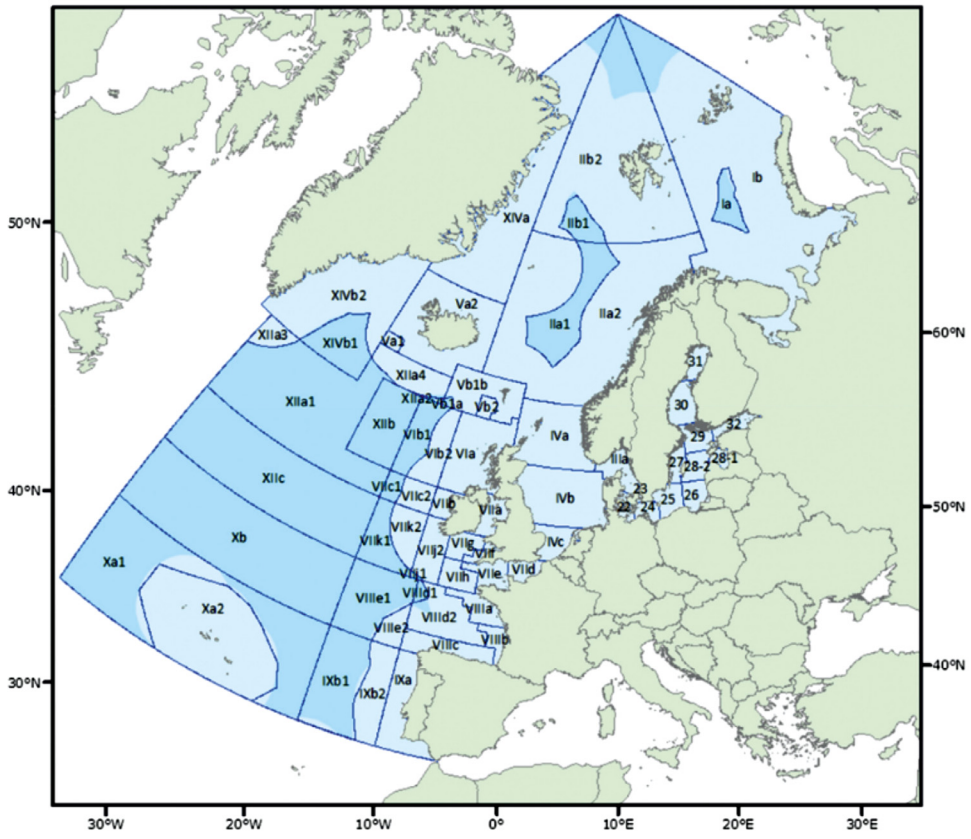

Figure 1 Map of the FAO 27 area (Cardinale et al., 2013).

2.4. Data analysis

Generalized linear models (GLMs) (McCullagh and Nelder, 1989) were applied to analyse the prevalence of cod infection in representatives of the genera *Anisakis* and *Pseudoterranova* in whole cod musculature (gutted fish) with respect to various biological and spatial parameters. The following model was fitted:

$$G(\text{inf}) = \text{area} + \text{sex} + \text{gonad developmental stage} + \text{TL} + \text{error};$$

where G is a link function and inf represents the prevalence of infection with *Anisakis* spp. or *Pseudoterranova* spp. The total body length (TL) was taken as the covariate, whereas the area, sex and gonad developmental stage were treated as factors. The error distribution was assumed to be binomial, and the logit link function was used. Corner point parameterization was imposed, i.e. factor effects for level one were assumed to be zero for all factors. Thus, the factor effects for the other levels may be regarded as the difference between the effect at any given level and the effect at level one. First, the initial model (which included all considered variables and factors) was fitted. The significance of the factors and covariates was then tested, and only significant terms were left in the final model. Tests were performed by deletion and those terms whose deletion did not result in a significant increase in deviance (i.e. the GLM measure of discrepancy between the modelled and observed values) were excluded from the model.

Due to the fact that the presence of parasites in the caudal part of the fillet was very low, for the purposes of the Wilcoxon matched-pairs test, the results obtained from counting the parasites in dorsal and caudal parts of the fillet were combined and compared with results obtained from counting the parasites in the belly flap. The Wilcoxon matched-pairs test was employed to assess the significance of the differences in the distribution of parasites in the various parts of the fish musculature (fillets *vs* belly flaps; left *vs* right fillets; left *vs* right belly flaps).

3. Results

3.1. Biological parameters of the fish

Cod sampled in the FAO IIa1 area were 63—92 cm in length, while fish caught in the FAO IIa2 area were smaller (52—70 cm in length). In both areas, the majority of the catch were males (88% in FAO IIa1 and 78.57% in FAO IIa2) (Table 1). On the basis of anatomo-morphological features, in total in FAO IIa1, 22 specimens of the *Pseudoterranova* genus and 223 individuals *Anisakis* genus larvae were recorded in the muscle tissue of cod, while in FAO IIa2 these numbers were 243 and 130, respectively.

Table 1 Total body length, prevalence (P), intensity (I) and abundance (A) of infection of cod with anisakid larvae. N = number of fish examined.

Area	Sex	N	Length of fish (cm)			*Anisakis*			*Pseudoterranova*			Total		
			Mean	Min	Max	P (%)	I	A	P (%)	I	A	P (%)	I	A
FAO IIa1	males	44	80.43	63	92	86.36	4.74	4.09	13.64	3.33	0.45	86.36	5.26	4.55
	females	6	82.83	68	90	100.00	7.17	7.17	16.67	2.00	0.33	100.00	7.50	7.50
	sum	**50**	**80.72**	**63**	**92**	**88.00**	**5.07**	**4.46**	**14.00**	**3.14**	**0.44**	**88.00**	**5.57**	**4.90**
FAO IIa2	males	44	65.27	46	74	47.73	5.05	2.41	40.91	10.83	4.43	70.45	9.71	6.84
	females	12	66.08	52	70	83.33	2.40	2.00	33.33	12.00	4.00	91.67	6.55	6.00
	sum	**56**	**65.45**	**46**	**74**	**55.36**	**4.19**	**2.32**	**39.29**	**11.05**	**4.34**	**75.00**	**8.88**	**6.66**
Sum		**106**	**72.65**	**46**	**92**	**70.75**	**4.71**	**3.33**	**27.36**	**9.14**	**2.50**	**81.13**	**7.19**	**5.83**

Table 2 Molecular identification of subsample of parasites found in the musculature of the cod (*Gadus morhua*) from the North Atlantic.

Area	*Anisakis simplex* s.s.	*Pseudoterranova krabbei*	*Pseudoterranova decipiens*	*Pseudoterranova decipiens / Pseudoterranova krabbei*
FAO IIa1	10	6	5	
FAO IIa2	6	17	5	1
Sum	**16**	**23**	**10**	**1**

3.2. Molecular identification of Anisakidae parasites

A subsample of parasites was selected for molecular identification, taking into account the number of parasites representing each species found in each fishing area. Accordingly, 21 and 29 Anisakidae larvae were collected from the musculature of cod from FAO IIa1 and FAO IIa2, respectively, and were identified using molecular genetics tools. For FAO IIa1, larvae were identified as *A. simplex* (s.s.), *P. decipiens* (s.s.) and *P. krabbei*. For FAO IIa2, the same species were identified together with one hybrid of *P. decipiens* and *P. krabbei* (Table 2). In the case of hybrid form, a heterozygote pattern was detected in all four nucleotide positions located in ITS-1 rDNA, differentiating *P. krabbei* and *P. decipiens* (Table 3). Examples of DNA sequences (deposited in GenBank) of parasites found in cod caught in FAO IIa1 are *A. simplex* (accession no. MW367082), *P. decipiens* (MW367084) and *P. krabbei* (MW367086); and of those caught in FAO IIa2: *A. simplex* (MW367083), *P. decipiens* (MW367085), *P. krabbei* (MW367087), and a hybrid of *P. decipiens* and *P. krabbei* (MW367088).

3.3. Parasitological descriptor: prevalence of infection

The prevalence of infection with Anisakidae nematodes in both sampling areas was high, at 88% in FAO IIa1 and 75% in FAO IIa2, but the parasite fauna composition was different. In FAO IIa1, a lower prevalence of infection with *Pseudoterranova* of 14% was observed, while in FAO IIa2 this was 39%; the opposite trend was observed for prevalence of infection with *Anisakis*, which was higher in FAO IIa1 (88%) than in FAO IIa2 (55%).

3.4. Data analysis: GLM models of the prevalence of infection

The sampling area had a significant effect in the GLM models of the prevalence of infection with *Anisakis* spp. and *Pseudoterranova* spp. The modeled prevalence of *Anisakis* spp. was higher in FAO IIa1 than in FAO IIa2 ($p<0.001$). In contrast, the prevalence of *Pseudoterranova* spp. was higher in FAO IIa2 than in FAO IIa1 ($p=0.005$). The sex of the host was significant only for *Anisakis* spp., where modeled infection was higher in females than in males ($p=0.026$). The prevalence of cod infection with Anisakidae species and the effect of area on the prevalence model (with standard errors, S.E.) are presented in Figure 2. Parameter estimates are given in Table 4.

3.5. Parasitological descriptors: intensity and abundance of infection

Intensity of infection with Anisakidae parasites differed in both areas: for *Pseudoterranova* spp. up to 8 parasites per infected fish were found in FAO IIa1 (abundance 0.44) and up to 53 parasites per fish in FAO IIa2 (abundance 4.34); for *Anisakis* spp. there were, respectively, up to 30 parasites per fish (abundance 4.46) and up to 25 parasites per fish (abundance 2.32).

3.6. Distribution of parasites in cod fillets

The distribution of parasites in the various parts of the flesh (right *vs* left, anterior ventral *vs* dorsal *vs* caudal) was recorded for all larvae belonging to the genera *Anisakis* and *Pseudoterranova*. The presence of Anisakidae nematodes in different parts of the cod musculature was analysed. In cod caught in FAO IIa1, *Pseudoterranova* spp. were found in the

Table 3 Comparison of ITS-1 nucleotide sequences with a graphical presentation of diagnostic nucleotide positions differentiating *Pseudoterranova krabbei*, *P. decipiens* and hybrid specimen *P. krabbei* x *P. decipiens* obtained in this study.

		Alignment position according to *P. krabbei* MW367086			
Parasite species	Accession number	45	208	234	260
P. krabbei	MW367086	G	A	C	T
P. decipiens	MW367085	A	G	A	C
Hybrid specimen	MW367088	A/G	A/G	A/C	T/C
Graphical presentation of diagnostic nucleotide positions		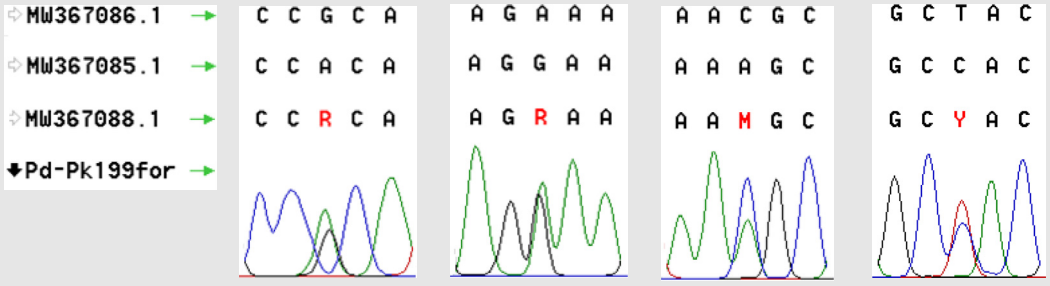			

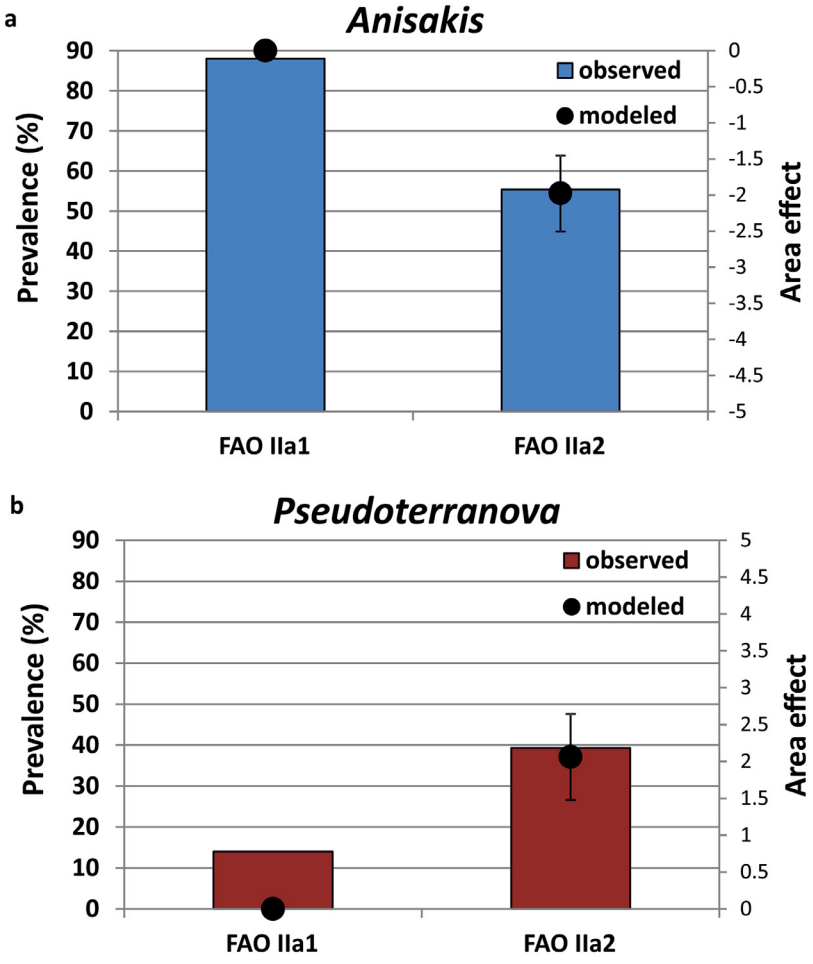

Figure 2 The prevalence of larval infections of *Anisakis* (a) and *Pseudoterranova* (b) genera in cod, relative to the effect of area included in the GLM model (with S.E.).

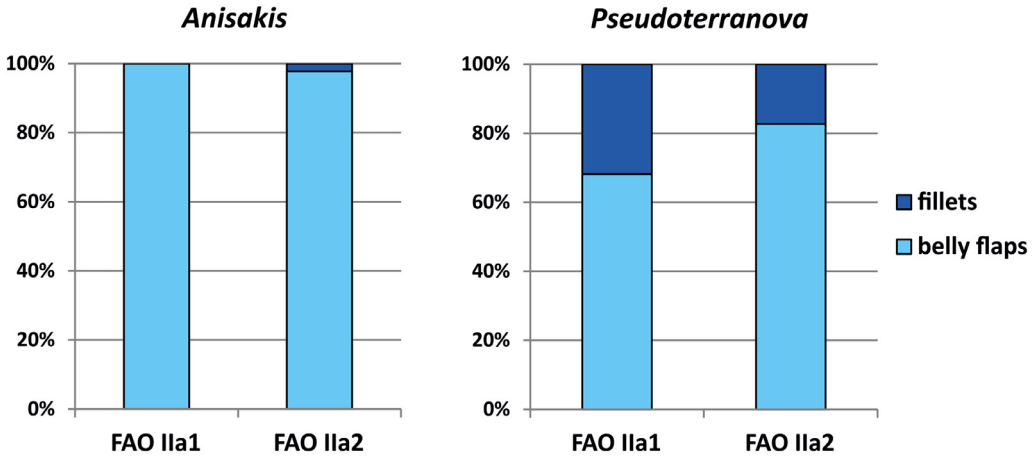

Figure 3 The distribution of *Anisakis* and *Pseudoterranova* in the flesh of cod.

Table 4 Parameter estimates (with s.e.) for models of the prevalence of infection with *Anisakis* and *Pseudoterranova* genera in cod (*Gadus morhua*) from the North Atlantic.

Anisakis				
Parameter		Estimate	S.E.	P
Intercept		1.88	0.44	<.001
Area	FAO IIa1	0.00	Aliased	
	FAO IIa2	−1.98	0.53	<.001
Sex	males	0.00	Aliased	
	females	1.81	0.81	0.026
Pseudoterranova				
Parameter		Estimate	S.E.	P
Intercept		−1.82	0.41	<.001
Area	FAO IIa1	0.00	Aliased	
	FAO IIa2	1.38	0.49	0.005

belly flaps of 5 fish and in 3 of these fish the parasite was also found in the dorsal fillet; we also recorded 2 fish with this parasite only in the dorsal fillet. Caudal fillet musculature was free of *Pseudoterranova* in these fish. In cod caught in FAO IIa2, *Pseudoterranova* spp. were observed in all tissues analysed with the following frequency: belly flaps, 17 fish; dorsal fillets, 11 fish; and caudal fillets, 7 fish. *Anisakis* spp. larvae were observed mainly in the belly flaps (in 44 fish from FAO IIa1 and in 31 fish from FAO IIa2) and only occasionally in caudal fillet (in two fish from FAO IIa2). Detailed information on the distribution of nematodes in each part of the cod musculature is presented in Table 6 and Figure 3.

The presence of nematodes with respect to the side of the musculature was also analysed. *Pseudoterranova* spp. were found in both left and right fillets with similar frequency in both sampling areas, while *Anisakis* spp. larvae were more often observed in the left belly flaps in both areas (Tables 5 and 6).

Wilcoxon matched-pairs tests revealed that the number of larvae representing both *Anisakis* and *Pseudoterranova* genera was significantly higher in belly flaps compared to fillets ($p < 0.001$ and $p=0.025$, respectively). *Anisakis* spp. larvae were found in significantly higher numbers ($p=0.047$) in left than right belly flaps. There were no significant differences in the lateral distribution of *Pseudoterranova* spp.

The intensity of infection differed depending on the location of the fish musculature. *Pseudoterranova* spp. mostly occurred in the belly flaps (15 parasites in fish from FAO IIa1 and 201 in cod from FAO IIa2), with fewer in the dorsal part (7 and 35, respectively) and only occasionally in caudal fillet (only 7 parasites in FAO IIa2 samples). *Anisakis* larvae were present almost exclusively in the belly flaps (223 parasites in FAO IIa1 and 127 in FAO IIa2), but occasionally in the caudal fillet (just 3 parasites in cod from FAO IIa2).

Coinfection with *Pseudoterranova* and *Anisakis* larvae was observed in the case of 18 fish (17%): 7 fish (14%) from FAO IIa1 and 11 fish (almost 20%) from FAO IIa2. Because most *Anisakis* specimens were present in the belly flaps, any coinfection was observed in that part of the fillet.

4. Discussion

Catches of Atlantic cod (*Gadus morhua*) from known spawning grounds are often heavily skewed towards males (Dean et al., 2014), which is also reflected in our sampling results. This might be explained by sex-specific behavior during spawning (Nordeide and Folstad, 2000): mature males aggregate on spawning grounds whereas females seem to be distributed peripherally or above the male aggregations (Morgan and Trippel, 1996; Nordeide, 1998).

Atlantic cod has an exceptionally rich and varied parasite fauna compared with most other species of marine fish (Hemmingsen and MacKenzie, 2001). It is one of the fish species that is most heavily infected with anisakid nematodes in the North Atlantic and its adjacent seas (Nadolna and Podolska, 2014; Mercken et al., 2020b,c).

Molecular identification revealed the presence of *Anisakis simplex* s.s., *Pseudoterranova decipiens* and *Pseudoterranova krabbei* in the muscle tissue of cod from the Norwegian Sea. These species were previously identified in cod by numerous authors (Boily and Marcogliese, 1995; Brattey and Bishop, 1992; Mattiucci and Nascetti, 2008; Mattiucci et al., 1997; McClelland and Marcogliese, 1994;

Table 5 Percentage of total *Anisakis* and *Pseudoterranova* genera detected in the various parts of the fillets of cod in the present study.

Genus/Area	Number of anisakids	Belly flaps		Fillets			
		Left	Right	Left dorsal	Right dorsal	Left caudal	Right caudal
Anisakis							
FAO IIa1	223	61.0	39.0	0.0	0.0	0.0	0.0
FAO IIa2	130	63.8	33.8	0.0	0.0	2.3	0.0
Sum	353	62.0	37.1	0.0	0.0	0.8	0.0
Pseudoterranova							
FAO IIa1	22	18.2	50.0	22.7	9.1	0.0	0.0
FAO IIa2	243	48.6	34.2	6.6	7.8	1.2	1.6
Sum	265	46.0	35.5	7.9	7.9	1.1	1.5

Table 6 Number of anisakids in relation to part of fillets.

Sample	Number of fish	Number of anisakids			Variance	S. D.	S. E.	P**
		Total	Min-Max*	Mean				
Anisakis								
Fillets	106	3	0—2	0.03	0.05	0.22	0.02	< 0.001
Flaps	106	350	0—30	3.30	27.13	5.21	0.51	
Left fillets	106	3	0—2	0.03	0.05	0.22	0.02	0.500
Right fillets	106	0	0—0	0	0	0	0	
Left flaps	106	219	0—22	2.07	14.84	3.85	0.37	0.037
Right flaps	106	131	0—8	1.24	3.36	1.83	0.18	
Pseudoterranova								
Fillets	106	49	0—6	0.46	1.47	1.21	0.12	0.025
Flaps	106	216	0—50	2.04	51.14	7.15	0.69	
Left fillets	106	24	0—3	0.23	0.39	0.62	0.06	1.000
Right fillets	106	25	0—3	0.24	0.51	0.71	0.07	
Left flaps	106	122	0—37	1.15	19.01	4.36	0.42	0.477
Right flaps	106	94	0—32	0.89	12.81	3.58	0.35	

* per fish
** Wilcoxon Matched Pairs Test

Strømnes and Andersen, 1998). Gay et al. (2018) revealed the presence of *A. pegreffii* in fillets of cod from the northern North Sea, but this species occurs rarely and was not detected during our studies. However, we did uncover one example of a hybrid of *P. decipiens* and *P. krabbei* in cod muscle from FAO IIa2. Although such a hybrid has previously been reported from this area, the host was not specified (Paggi et al., 1991).

We found a high prevalence of infection with Anisakidae nematodes in cod fillets in both study areas of the offshore waters of the Norwegian Sea. However, the parasite fauna composition was different in each area. In FAO IIa1, there was a lower prevalence of infection with *Pseudoterranova* spp. than in FAO IIa2, while in contrast the prevalence of infection with *Anisakis* spp. larvae was higher in FAO IIa1. The abundance and intensity of infection with Anisakidae parasites also differed in both areas: for *Pseudoterranova* the number of infected fish caught in FAO IIa2 was higher than in FAO IIa1, while for *Anisakis* the reverse was true.

Previous studies that focused on the presence, intensity and distribution of the different genera of ascaridoid nematodes in *G. morhua* from different regions of the Atlantic Ocean also showed that parasitological descriptors varied depending on the sampling area, for example, for various cod stocks in the North Atlantic in the 1970s (Platt, 1975) or more recently in the Barents Sea *vs* North Sea (Gay et al., 2018). The prevalence of cod infection with *Anisakis* spp. in fillets was only ~10% in the central North Sea (ICES area IVb) and ~85% in the northern North Sea (ICES area IVa), while in the Barents Sea (ICES area I) the prevalence was ~90% (Gay et al., 2018). Our sampling areas were situated between the northern North Sea and the Barents Sea, and therefore it might be expected that the level of infection would be similar, with a high value in the range 85-90%. Nevertheless, our results show differences between the two study areas, FAO IIa1 and FAO IIa2, where the prevalence of *Anisakis* spp. infection in cod fillet was 88% and 55%, respectively. In contrast, the prevalence of infection with *Pseudoterranova* spp. in cod fillets was 20—30% in the northern North Sea and less than 10% in the Barents Sea (Gay et al., 2018) using the UV-compression method, while in our studies the equivalent figures were 14% in FAO IIa1 and 39.29%

in FAO IIa2 using candling. The less-sensitive method used in our studies showed a higher infection than described by Gay et al. (2018) in neighboring areas and indicates that cod from FAO IIa2 generally harbor more *Pseudoterranova* in the musculature than those from other areas studied. Taking into account that candling generally underestimates infection levels compared with UV-compression, which is considered to be more effective (Levsen, 2005), the level of cod fillet infection might be even higher.

According to Gay et al. (2018) the abundance of *Anisakis* in fillet of cod from the northern North Sea was 6.12 ± 6.32 (intensity 7.17 ± 6.27; max 29) and from the Barents Sea 4.84 ± 6.56 (intensity 5.36 ± 6.69, max 65), while for *Pseudoterranova* the abundance values were 0.88 ± 4.41 (intensity 3.29 ± 8.09; max 46) and 0.03 ± 0.18 (intensity 1.00 ± 0.00, max 1), respectively. In our studies, the abundance of *Anisakis* in fillets was lower than recorded previously in the northern North Sea and Barents Sea: 4.46 in FAO IIa1 (maximum intensity 30 parasites per fish) and 2.32 in FAO IIa2 (maximum intensity 25 parasites per fish). In the case of *Pseudoterranova*, the abundance of 0.44 (max intensity 8 parasites per fish) in FAO IIa1 was lower than in the northern North Sea and higher than in the Barents Sea, but in FAO IIa2 the abundance was higher at 4.34 (max intensity 53 parasites per fish) than reported in neighboring regions by Gay et al. (2018). Again, our results might be an underestimated due to the method used (candling *vs* UV-compression).

The differences in the levels of infection between the areas analyzed in our studies and the neighboring regions studied previously (Gay et al., 2018) might be driven by several factors: as mentioned above, different methods were used; sampling was conducted in other areas of North Atlantic, and at a different time (year and season: spring in our study *vs* summer for Gay et al., 2018); the length distribution of the fish might differ between the analyzed samples. Fish length, sampling area, and sampling month or year are all known to influence the distribution of *Anisakis* in fish (Gay et al., 2018). Hemmingsen et al. (1995) reported maximum mean intensity and abundance of *A. simplex* in cod in a subarctic fjord, Balsfjord, in Norway in the autumn, while Strømnes and Andersen (2000) noticed a 'spring rise' of *A. simplex* third-stage larvae in some fish species in Norwegian waters. Natural changes in host and parasite populations should be also taken into account as an explanation of the observed differences.

There are several cod stocks in the eastern North Atlantic, and while all of them exhibit a common life history pattern, considerable regional variations exist in their recruitment, growth rate, age of maturity, migration patterns, food and spawning time (Rätz and Lloret, 2003). Living in different habitats results in different exposure to parasitic infection and each habitat brings unique possibilities for closing the parasite life cycle. The life cycles of nematodes of genera *Anisakis* and *Pseudoterranova* are broadly similar and involve crustaceans and many species of fish that serve as intermediate or paratenic hosts, with marine mammals as the final hosts (McClelland et al., 1990). Important cetacean hosts for *A. simplex* are the harbor porpoise, *Phocoena phocoena* (Herreras et al., 2004), the white-beaked dolphin, *Lagenorhynchus albirostris*, and the common bottlenose dolphin, *Tursiops truncatus* (Smith and Wootten, 1978). The common seal (harbour seal), *Phoca vitulina*, is considered to be the most important final host for *P. decipiens* (Aspholm et al., 1995). The mature parasites produce eggs, which are released with the faeces of the final host and lead to free swimming ensheathed larvae in the marine environment. The larvae undergo one or two moults before being ingested by invertebrates, mostly small crustaceans. Depending on the fishing area, suitable intermediate hosts may occur more or less abundantly and may still be unknown (Klimpel et al., 2004). Wootten and Waddell (1977) revealed that *Phocanema* (current name: *Pseudoterranova*) larvae were common in the musculature of cod from the west coast of Scotland and rare in fish from the central northern North Sea, while *Anisakis* larvae were abundant in cod and whiting from the offshore northern North Sea and less common in other areas. The reason for such variations was explained by differences in the geographical distribution of the invertebrate and vertebrate hosts of the parasites. Studies conducted by Wootten and Bron (2008) revealed that only *Anisakis* was found in fish feeding on planktonic crustaceans, while *Pseudoterranova* has a more benthic and inshore habitat, and is thus more likely to be found in bottom-feeding fish (e.g. cod). This might explain why during our studies more cod infected with *Anisakis* were found in sampling area FAO IIa1, which is located offshore.

However, experimental studies revealed that, in the eggs of *A. simplex* and *P. decipiens*, two moults occur during larval development (Køie et al., 1995); therefore, invasive L3 larvae are likely to be present in seawater and are available for invertebrates, fish and mammals. In this case, an intermediate host is not always needed in the life cycle of the parasite. If they are present, the intermediate hosts are eaten by a wide variety of transport or paratenic hosts, including fish. At this stage, many different life-cycle patterns may be observed (EFSA, 2010), but ultimately infected fish are eaten by the definitive host and the life cycle of the parasite is completed. Fish that live in a habitat where: 1) final hosts are numerous (and consequently there is large-scale transmission of parasite eggs into the environment); 2) the water conditions are favorable to parasite egg dispersion and survival; 3) appropriate intermediate hosts are present and numerous or not needed, are more exposed to parasitic infection. Factors that drive the behavior of the larvae in the paratenic host are not fully known. Most parasites remain in the visceral cavity of the fish or within the visceral organs, whereas in other cases parasites migrate to the musculature of the fish (Cipriani et al., 2016).

Our studies reveal that the distribution of parasites is not uniform in cod muscle tissue. Comparing the distribution of parasites in the flesh of cod using the Wilcoxon matched-pairs test revealed that significantly more *Anisakis* larvae ($p=0.037$) were localized in the left than the right belly flaps. These results are in accordance with the findings of Petrie et al. (2009), but these authors detected significantly more parasites ($p < 0.000001$) of both genera (*Anisakis* and *Pseudoterranova*) in the left than the right side of the body.

The dominance of *A. simplex* larvae (~58%) in the left-sided musculature was demonstrated during research conducted in the 1980s on Atlantic cod from Newfoundland and Labrador (Brattey and Bishop, 1992). An asymmetric distribution of *Anisakis* and *Pseudoterranova* (more larvae

in the left body musculature) was also reported for Atlantic cod by Smith and Hemmingsen (2003). Similarly in all species of fish examined by Petrie et al. (2009), except mackerel, there were significantly greater numbers of larval anisakids in flesh from the left side of the fish. Petrie et al. (2009) speculated that this was because the disposition of organs within the body cavity might to some extent obstruct the path of migrating worms into the right-sided musculature. Smith and Hemmingsen (2003) also proposed that the asymmetrical arrangement of internal organs in the cod (including the digestive tract) might result in asymmetrical distribution of *Anisakis* larvae in the musculature of the fish. However, for fish sampled in the northern North Sea, the right-sided fillets were slightly more infected with Anisakidae parasites than the left, whereas the opposite was observed for fish sampled in the Barents Sea (Gay et al., 2018).

In our studies the majority of larvae were located in the belly flaps (99% of *Anisakis* larvae and 82% of *Pseudoterranova*); indeed, the number of *Anisakis* and *Pseudoterranova* individuals was significantly higher in belly flaps than in fillets ($p < 0.001$ and $p = 0.025$, respectively). Similar results were obtained by Petrie et al. (2009) for *Anisakis*: significantly more larvae ($p < 0.000001$) were detected in the belly flaps compared to the fillets; however, for *Pseudoterranova,* there was no significant difference in the distribution between belly flaps and fillets ($p = 0.396$). In our studies, in the dorsal parts of the cod musculature, only *Pseudoterranova* larvae were present. Similarly the majority of *A. simplex* larvae (~95%) occurred in the flesh surrounding the body cavity (Brattey and Bishop, 1992). The prevalence and abundance of the parasites in the anterior part of the fillet were always greater than those for the posterior part (Gay et al., 2018; Novotny and Uzmann, 1960). According to Petrie et al. (2009) significantly more *A. simplex* were found in the belly flaps than in the fillets in all fish species. *P. decipiens* was significantly more abundant in the fillets of monkfish, but there was no difference between the numbers of this parasite in belly flaps and fillets in cod. The presence of the majority of larvae in the belly flaps might be explained by the short distance that larvae need to migrate from the digestive tract.

We observed differences in distribution between genera: *Anisakis* were present mainly in the belly flaps, while *Pseudoterranova* were present (with descending frequency) in belly flaps, dorsal fillet and caudal fillet. An important factor influencing the migratory distance and encapsulation site of *A. simplex* L3 larvae might be the special attributes of the particular microhabitats encountered by infecting larvae within their hosts, such as the availability of exploitable nutrients (Strømnes and Andersen, 1998). This suggests that the distribution of larvae might be driven by the diversity of the biochemical environment within the host. One of the most important drivers of parasitic migration seems to be lipids, which are very important for parasite survival (Jordanova et al., 2005). Nematodes must acquire lipids, mainly fatty acids and sterols, because they are not biosynthesized from scratch (Chitwood and Lusby, 1991; Köhler and Voigt, 1988). This hypothesis has been confirmed by the identification of lipids in the cuticle of the parasitic nematode *A. simplex* and the somatic tissues of the Atlantic cod (Mika et al., 2010). *A. simplex* L3 larvae have a preference for host tissue with high lipid content (Strømnes and Andersen, 1998, 2003). In experimental studies, it was shown that in a microhabitat containing few or no lipids, the L3 larvae were apparently stimulated to increase their mobility and actively seek new and possibly better microhabitats (Strømnes, 2014).

Parasitic infections affect almost all fish species and pose a serious problem for the fishing industry in many countries. Therefore, updated knowledge about the level of infection with zoonotic parasites is important, particularly in the case of fish species intended for human consumption. It is helpful to avoid catches in areas where the level of parasitic infection is high, which minimizes the risk to consumers health (Rahmati et al., 2021a,b) and delivers the safest raw material for fish processing. The Norwegian Sea is an important cod fishing ground and Norway is a key player in the European export of cod (as a wide range of products) worldwide; therefore our results may be of commercial as well as scientific value. Recently, the northeast Atlantic has been identified as a high-risk hot spot for the presence of *Anisakis* spp. in Gadidae fish, posing a potential hazard of anisakiosis (Rahmati et al., 2021a). It is worth emphasizing that levels of fish infection vary both temporally and spatially and should be regularly monitored.

Some research suggests that populations of anisakids are shifting over time. Thus, Molina-Fernández et al. (2015) and Rahmati et al. (2021a) demonstrated that the prevalence of *Anisakis* infection in fish may vary even between geographically close locations. Fiorenza et al. (2020) estimated that on average *Anisakis* spp. abundance increased more than 100 times from 1978 to 2015, with the most affected area being the northeastern Atlantic. The elimination of zoonotic nematodes from fish is essential in the context of ensuring the safety and quality of fish products. The phenomenon of accumulation of anisakids in certain parts of the fillet (belly flaps) allows for the elimination of most parasites by cutting off the abdominal parts of the fillet. This simple procedure minimizes the risk of human infection by accidental consumption of nematode larvae and improves the aesthetic value of the product. However, further treatment should be used to at least kill the larvae that may remain in the other parts of the fillet.

Financial support

This work was supported by the National Centre for Research and Development under the Strategic Program Biostrateg (grant number BIOSTRATEG2/296211/4/NCBR/2016).

Acknowledgements

Authors thank the Reviewers for their positive comments and careful review, which helped to improve the manuscript.

References

Alonso-Gómez, A., Moreno-Ancillo, A., López-Serrano, M.C., Suarez-de-Parga, J.M., Daschner, A., Caballero, M.T., Bar-

ranco, P., Cabañas, R., 2004. *Anisakis simplex* only provokes allergic symptoms when the worm parasitises the gastrointestinal tract. Parasitol. Res. 93 (5), 378—384. https://doi.org/10.1007/s00436-004-1085-9

Asche, F., Cojocaru, A.L., Gaasland, I., Straume, H.-M., 2018. Cod stories: Trade dynamics and duration for Norwegian cod exports. J. Commod. Mark. 12, 71—79. https://doi.org/10.1016/j.jcomm.2017.12.002

Aspholm, P.E., 1995. *Anisakis simplex* Rudolphi, 1809, infection in fillets of Barents Sea cod *Gadus morhua* L. Fish. Res. 23, 375—379. https://doi.org/10.1016/0165-7836(94)00348-Z

Aspholm, P.E., Ugland, K.I., Jødestøl, K.A., Berland, B., 1995. Sealworm (*Pseudoterranova decipiens*) infection in common seals (*Phoca vitulina*) and potential intermediate fish hosts from the outer Oslofjord. Int. J. Parasitol. 25, 367—373. https://doi.org/10.1016/0020-7519(94)00133-9

Audicana, M.T., Kennedy, M.W., 2008. *Anisakis simplex*: from obscure infectious worm to inducer of immune hypersensitivity. Clin. Microbiol. 21 (2), 360—379. https://doi.org/10.1128/CMR.00012-07

Audicana, M.T., Ansotegui, I.J., de Corres, L.F., Kennedy, M.W., 2002. *Anisakis simplex*: dangerous — dead and alive? Trends Parasitol. 18 (1), 20—25. https://doi.org/10.1016/S1471-4922(01)02152-3

Bañon, R., Villegas-Ríos, D., Serrano, A., Mucientes, G., Arronte, J.C., 2010. Marine fishes from Galicia (NW Spain): an updated checklist. Zootaxa 2667, 1—27.

Bao, M., Strachan, N.J.C., Hastie, L.C., Mac Kenzie, K., Seton, H.C., Pierce, G.J., 2017. Employing visual inspection and Magnetic Resonance Imaging to investigate *Anisakis simplex* s.l. infection in herring viscera. Food Control 75, 40—47. https://doi.org/10.1016/j.foodcont.2016.12.030

Bao, M., Pierce, G.J., Strachan, N.J.C., Pascual, S., Gonzalez—Munoz, M., Levsen, A., 2019. Human health, legislative and socioeconomic issues caused by the fish-borne zoonotic parasite *Anisakis*: Challenges in risk assessment. Trends Food Sci. Technol. 86, 298—310.

Berland, B., 1989 Identification of larval nematodes from fish. In H. Möller (Eds.), Nematode problems in North Atlantic fish (pp. 16-22). Report from a workshop in Kiel, 3—4 April 1989. ICES, C.M./F6.

Bertheussen, B.A., Dreyer, B.M., 2019. Is the Norwegian cod industry locked into a value-destructive volume logic? Mar. Policy 103, 113—120. https://doi.org/10.1016/j.marpol.2019.02.023

Boily, F., Marcogliese, D.J., 1995. Geographical variations in abundance of larval anisakine nematodes in Atlantic cod (*Gadus morhua*) and American plaice (*Hippoglossoides platessoides*) from the Gulf of St. Lawrence. Can. J. Fish. Aquat. 52 (S1), 105—115. https://doi.org/10.1139/f95-516

Brattey, J., Bishop, C.A., 1992. Larval *Anisakis simplex* (Nematoda: Ascaridoidea) Infection in the musculature of Atlantic Cod, *Gadus morhua*, from Newfoundland and Labrador. Can. J. Fish. Aquat. 49 (12), 2635—2647. https://doi.org/10.1139/f92-292

Brunet, J., Pesson, B., Royant, M., Lemoine, J.-F., Pfaff, A.W., Abou-Bacar, A., Year, H., Fréalle, E., Dupouy-Camet, J., Merino-Espinosa, G., Gómez-Mateos, M., Martin-Sanchez, J., Candolfi, E., 2017. Molecular diagnosis of Pseudoterranova decipiens s.s. in human, France. BMC Infect. Dis. 17. https://doi.org/10.1186/s12879-017-2493-7, Art. No. 397

Bush, A.O., Lafferty, K.D., Lotz, J.M., Shostak, A.W., 1997. Parasitology meets ecology on its own terms: Margolis et al. Revisited. J. Parasitol. 83 (4), 575—583. https://doi.org/10.2307/3284227

Cardinale, M., Dörner, H., Abella, A., Andersen, J.L., Casey, J., Döring, R., Kirkegaard, E., Motova, A., Anderson, J., Simmonds, E.J., Stransky, C., 2013. Rebuilding EU fish stocks and fisheries, a process under way? Mar. Policy 39, 43—52. https://doi.org/10.1016/j.marpol.2012.10.002

Chandra, C.V., Khan, R.A., 1988. Nematode Infestation of Fillets from Atlantic Cod, *Gadus morhua*, off Eastern Canada. The J. Parasitol. 74 (6), 1038—1040. https://doi.org/10.2307/3282229

Chitwood, D.J., Lusby, W.R., 1991. Metabolism of plant sterols by nematodes. Lipids 26, 619—627. https://doi.org/10.1007/BF02536426

Cipriani, P., Acerra, V., Bellisario, B., Sbaraglia, G.L., Cheleschi, R., Nascetti, G., Mattiucci, S., 2016. Larval migration of the zoonotic parasite *Anisakis pegreffii* (Nematoda: Anisakidae) in European anchovy, *Engraulis encrasicolus*: implications to seafood safety. Food Control 59, 148—157. https://doi.org/10.1016/j.foodcont.2015.04.043

Cohen, D.M., Inada, T., Iwamoto, T., Scialabba, N., 1990. Gadiform fishes of the world. FAO Fisheries Synopsis 10, 125.

Dean, M.J., Hoffman, W., Zemeckis, D., Armstrong, M.P., Cadrin, S.X., 2014. Cod Spawning Behavior and Observed Sex Ratios: A Liability and an Asset. American Fisheries Society 144th Annual Meeting. Conference Paper.

EFSA, 2010. Scientific opinion on risk assessment of parasites in fishery products. Panel on Biological Hazards (BIOHAZ). EFSA J. 8, 1543.

EUMOFA, 2018. The EU fish market 2018.

Fagerholm, H.P., 1982. Parasites of fish in Finland. VI. Nematodes. Acta Academiae Aboensis B 40, 128.

Fiorenza, E.A., Wendt, C.A., Dobkowski, K.A., King, T.L., Pappaionou, M., Rabinowitz, P., Samhouri, J.F., Wood, C.L., 2020. It's a wormy world: Meta-analysis reveals several decades of change in the global abundance of the parasitic nematodes *Anisakis* spp. and *Pseudoterranova* spp. in marine fishes and invertebrates. Glob. Change Biol. 26(5), 2854—2866. https://doi.org/10.1111/gcb.15048

Gay, M., Bao, M., MacKenzie, K., Pascual, S., Buchmann, K., Bourgau, O., Couvreur, C., Mattiucci, S., Paoletti, M., Hastie, L.C., Levsen, A., Pierce, G.J., 2018. Infection levels and species diversity of ascaridoid nematodes in Atlantic cod, *Gadus morhua*, are correlated with geographic area and fish size. Fish. Res. 202, 90—102. https://doi.org/10.1016/j.fishres.2017.06.006

Gómez-Morales, M.A., Martínez Castro, C., Lalle, M., Fernández, R., Pezzotti, P., Abollo, E., Pozio, E., 2018. UV-press method versus artificial digestion method to detect Anisakidae L3 in fish fillets: Comparative study and suitability for the industry. Fish. Res. 202, 22—28.

Gonzalez, A.F., Gracia, J., Minino, I., Romon, J., Larsson, C., Maroto, J., Regueira, M., Pascual S., 2018. Approach to reduce the zoonotic parasite load in fish stocks: When science meets technology. Fish. Res. 202, 140—148. https://doi.org/10.1016/J.FISHRES.2017.08.016

Hauksson, E., 2011. The prevalence, abundance, and density of *Pseudoterranova* sp. (p) larvae in the flesh of cod (*Gadus morhua*) relative to proximity of grey seal (*Halichoerus grypus*) colonies on the coast off Drangar, Northwest Iceland. J. Mar. Biol. Article ID 235832. https://doi.org/10.1155/2011/235832

Heia, K., Lauritzen, K., Nilsen, H., Wold, J.P., Wedberg, T., 1997. Studies of methods for detection and removal of nematodes in whitefish: x-ray, CT, NMR, time-gating and optical measurements. Report no. 11. Norwegian Institute of Fisheries and Aquaculture Research Ltd., Tromsø.

Heia, K., Sivertsen, A.H., Stormo, S.K., Elvevoll, E., Wold, J.P., Nilsen, H., 2007. Detection of nematodes in cod (*Gadus morhua*) fillets by imaging spectroscopy. Int. J. Food Sci. 72 (1), article id. E011-5. https://doi.org/10.1111/j.1750-3841.2006.00212.x

Hemmingsen, W., MacKenzie, K., 2001. The parasite fauna of the atlantic cod, *Gadus morhua* L. Adv. Mar. Biol. 40, 1-80. https://doi.org/10.1016/S0065-2881(01)40002-2

Hemmingsen, W., Lombardo, I., MacKenzie, K., 1991. Parasites as biological tags for cod, *Gadus morhua* L., in northern Norway: a pilot study. Fish. Res. 12 (40), 365—373. https://doi.org/10.1016/0165-7836(91)90019-C

Hemmingsen, W., Lile, N., Halvorsen, O., 1992. The parasite fauna of cod *(Gadus morhua* L.) in North Norway. Polar Biol. 12, 739–742. https://doi.org/10.1007/BF00238876

Hemmingsen, W., Lile, N., Halvorsen, O., 1995. Search for seasonality in occurrence of parasites of cod, *Gadus morhua* L. in a fjord at 70°N. Polar Biol. 15, 517–522. https://doi.org/10.1007/BF00237466

Hemmingsen, W., Lysne, D.A., Eidnes, T., Skorping, A., 1993. The occurrence of larval ascaridoid nematodes in wild-caught and in caged and artificially fed Atlantic cod, *Gadus morhua* L., in Norwegian waters. Fish. Res. 15 (4), 379–386. https://doi.org/10.1016/0165-7836(93)90088-O

Herreras, M.V., Balbuena, J.A., Aznar, F.J., Kaarstad, S.E., Fernández, M., Raga, J.A., 2004. Population structure of *Anisakis simplex* (Nematoda) in harbor porpoises *Phocoena phocoena* off Denmark. J. Parasitol. 90, 933–938. https://doi.org/10.1645/GE-188R

Hochberg, N.S., Hamer, D.H., Hughes, J.M., Wilson, M.E., 2010. Anisakidosis: Perils of the Deep. Clin. Infect. Dis. 51 (7), 806–812. https://doi.org/10.1086/656238

ICES, 2005. Spawning and life history information for North Atlantic cod stocks. ICES Cooperative Res. Rep. 274, 152.

Ishikura, H., Kikuchi, K., Nagasawa, K., Ooiwa, T., Takamiya, H., Sato, N., Sugane, K., 1993. Anisakidae and anisakidosis. In: Sun, T. (Ed.), Progress in Clinical Parasitology. Springer, New York, 43–102. https://doi.org/10.1007/978-1-4612-2732-8_3

Jensen, T., Idås, K., 1992. Infection with *Pseudoterranova decipiens* (Krabbe, 1878) larvae in cod (*Gadus morhua*) relative to proximity of seal colonies. Sarsia 76 (4), 227–230. https://doi.org/10.1080/00364827.1992.10413478

Jordanova, R., Radoslavov, G., Fischer, P., Torda, A., Lottspeich, F., Boteva, R., Walter, R.D., Bankov, I., Liebau, E., 2005. The highly abundant protein Ag-lbp55 from *Ascaridia galli* represents a novel type of lipid-binding proteins. J. Biol. Chem. 280 (50), 41429–41438. https://doi.org/10.1074/jbc.M504474200

Karl, H., Leinemann, M., 1993. A fast and quantitative detection method for nematodes in fish fillets and fishery products. Arch. Lebensm. Hyg. 44, 124–125.

Khan, R.A., Tuck, C., 1995. Parasites as biological indicators of stocks of Atlantic cod (*Gadus morhua*) off Newfoundland. Canada. Can. J. Fish. Aquat. 52 (S1), 195–201. https://doi.org/10.1139/f95-527

Klimpel, S., Palm, H.W., Ruckert, S., Piatkowski, U., 2004. The life cycle of *Anisakis simplex* in the Norwegian Deep (northern North sea). Parasitol. Res. 94 (1), 1–9. https://doi.org/10.1007/s00436-004-1154-0

Køie, M., Björn, B., Burt, M.D.B., 1995. Development to third-stage larvae occurs in the eggs of *Anisakis simplex* and *Pseudoterranova decipiens* (Nematoda, Ascaridoidea, Anisakidae) Can. J. Fish. Aquat. Sci. 52 (1), 134–139. https://doi.org/10.1139/f95-519

Köhler, P., Voigt, W., 1988. Nutrition and metabolism. In: Melhorn, H. (Ed.), Parasitology in Focus. Springer, Heidelberg, Germany, 412–453.

Levsen, A., Lunestad, B.T., Berland, B., 2005. Low Detection Efficiency of Candling as a Commonly Recommended Inspection Method for Nematode Larvae in the Flesh of Pelagic Fish. J. Food Prot. 68 (4), 828–832.

Llarena-Reino, M., Piñeiro, C., Antonio, J., Outeriño, L., Vello, C., González, A.F., Pascual, S., 2013. Optimization of the pepsin digestion method for anisakids inspection in the fishing industry. Vet. Parasitol. 191 (3–4), 276–283. https://doi.org/10.1016/j.vetpar.2012.09.015

Mattiucci, S., Nascetti, G., 2008. Advances and trends in the molecular systematics of anisakid nematodes, with implications for their evolutionary ecology and host-parasite co-evolutionary processes. Adv. Parasitol. 66, 47–148. https://doi.org/10.1016/S0065-308X(08)00202-9

Mattiucci, S., Nascetti, G., Clanchi, R., Paggi, L., Arduino, P., Margolis, L., Brattey, J., Webb, S., D'Amelio, S., Orecchia, P., Bullini, L., 1997. Genetic and ecological data on the *Anisakis simplex* complex, with evidence for a new species (Nematoda, Ascaridoidea, Anisakidae). J. Parasitol. 83 (3), 401–416. https://doi.org/10.2307/3284402

Mattiucci, S., Fazii, P., De Rosa, A., Paoletti, M., Megna, A.S., Glielmo, A., De Angelis, M., Costa, A., Meucci, C., Calvaruso, V., Sorrentini, I., Palma, G., Bruschi, F., Nascetti, G., 2013. Anisakiasis and Gastroallergic Reactions Associated with *Anisakis pegreffii* Infection. Italy. Emerg. Infect. Dis. 19 (3), 496–499. https://doi.org/10.3201/eid1903.121017

McClelland, G., Marcogliese, D.J., 1994. Larval anisakine nematodes as biological indicator of cod (*Gadus morhua*) populations in the southern Gulf of St. Lawrence and on the Breton Shelf. Canada. Bull. Scandinavian Soc. Parasitology 4 (2), 97–116.

McClelland, G., Misra, R.K., Martell, D.J., 1990. Larval anisakine nematodes in various fish species from Sable Island Bank and vicinity. Can. Bull. Fish Aquat. Sci. 222, 83–118.

McCullagh, P., Nelder, J.A., 1989. Generalized Linear Models, 2nd ed. Chapman and Hall, London.

Mehrdana, F., Bahlool, Q.Z.M., Skov, J., Marana, M.H., Sindberg, D., Mundeling, M., Overgaard, B.C., Korbut, R., Strøm, S.B., Kania, P.W., Buchmann, K., 2014. Occurrence of zoonotic nematodes *Pseudoterranova decipiens*, *Contracaecum osculatum* and *Anisakis simplex* in cod (*Gadus morhua*) from the Baltic Sea. Vet. Parasitol. 205, 581–587. https://doi.org/10.1016/j.vetpar.2014.08.027

Mercken, E., Van Damme, I., Šoba, B., Vangeenberghe, S., Serradell, A., Lumain, J.P.L., De Sterck, T., Lalle, M., Gabriël, S., 2020a. High occurrence of Anisakidae at retail level in cod (*Gadus morhua*) belly flaps and the impact of extensive candling. Food Waterborne Parasitol. 22. https://doi.org/10.1016/j.fawpar.2020.e00108

Mercken, E., Van Damme, I., Serradell, A., Gabriël, S., 2020b. Presence of Anisakidae in commercial fish species imported into the Belgian food markets: A systematic review and meta-analyses. Int. J. Food Microbiol. 218 (108456), 1–11. https://doi.org/10.1016/j.ijfoodmicro.2019.108456

Mercken, E., Van Damme, I., Vangeenberghe, S., Serradell, A., De Sterck, T., Lumain, J.P.L., Gabriël, S., 2020c. Ascaridoids in commercial fish: Occurrence, intensity and localization in whole fish and fillets destined for the Belgian market. Int. J. Food Microbiol. 327, 108657. https://doi.org/10.1016/j.ijfoodmicro.2020.108657

Mika, A., Gołębiowski, M., Szafranek, J., Rokicki, J., Stepnowski, P., 2010. Identification of lipids in the cuticle of the parasitic nematode *Anisakis simplex* and the somatic tissues of the Atlantic cod *Gadus morhua*. Exp. Parasitol. 124 (3), 334–340. https://doi.org/10.1016/j.exppara.2009.11.013

Molina-Fernández, D., Malagón, D., Gómez-Mateos, M., Benítez, R., Martín-Sánchez, J., Adroher, F.J., 2015. Fishing area and fish size as risk factors of Anisakis infection in sardines (*Sardina pilchardus*) from Iberian waters, southwestern Europe. Int. J. Food Microbiol. 203, 27–34. https://doi.org/10.1016/j.ijfoodmicro.2015.02.024

Moneo, I., Caballero, M.L., González-Muñoz, M., Rodríguez-Mahillo, A.I., Rodríguez-Perez, R., Silva, A., 2005. Isolation of a heat-resistant allergen from the fish parasite *Anisakis simplex*. Parasitol. Res. 96 (5), 285–289. https://doi.org/10.1007/s00436-005-1362-2

Morgan, M.J., Trippel, E.A., 1996. Skewed sex ratios in spawning shoals of Atlantic cod (*Gadus morhua*). ICES J. Mar. Sci. 53 (Suppl. 1), 820–826. https://doi.org/10.1006/jmsc.1996.0103

Mouritsen, K., Hedeholm, R., Schack, H., Møller, L., Storr-Paulsen, M., Dzido, J., Rokicki, J., 2010. Occurrence of anisakid nematodes in Atlantic cod (*Gadus morhua*) and Greenland cod (*Gadus ogac*), West Greenland. Acta Parasitol. 55 (1), 81–89. https://doi.org/10.2478/s11686-010-0009-3

Najda, K., Kijewska, A., Kijewski, T., Plauška, K., Rokicki, J., 2018. Distribution of ascaroidoid nematodes (Nematoda: Chromadorea: Ascaridoidea) in fish from the Barents Sea. Oceanol. Hydrobiol. Stud. 47 (2), 128—139. https://doi.org/10.1515/ohs-2018-0014

Nadolna, K., Podolska, M., 2014. Anisakid larvae in the liver of cod (*Gadus morhua*) L. from the southern Baltic Sea. J. Helminthol. 88 (2), 237—246. https://doi.org/10.1017/S0022149X13000096

Nordeide, J.T., 1998. Coastal and North-east Arctic cod (*Gadus morhua* L.)—do they mingle at the spawning grounds in Lofoten? Sarsia 83, 373—379. https://doi.org/10.1080/00364827.1998.10413696

Nordeide, J.T., Folstad, I., 2000. Is cod lekking or a promiscuous group spawner? Fish Fish. 1, 90—93. https://doi.org/10.1046/j.1467-2979.2000.00005.x

Novotny, A.J., Uzmann, J.R., 1960. A statistical analysis of the distribution of a larval nematode (*Anisakis* sp.) in the musculature of chum salmon (*Oncorhynchus keta*-Walbaum). Exp. Parasitol. 10, 245—262. https://doi.org/10.1016/0014-4894(60)90062-x

Paggi, L., Nascetti, G., Cianchi, R., Orecchia, P., Mattiucci, S., D'Amelio, S., Berland, B., Brattey, J., Smith, J.W., Bullini, L., 1991. Genetic evidence for three species within *Pseudoterranova decipiens* (Nematoda, Ascaridida, Ascaridoidea) in the North Atlantic and Norwegian and Barents Seas. Int. J. Parasitol. 21 (2), 195—212. https://doi.org/10.1016/0020-7519(91)90010-5

Perdiguero-Alonso, D., Montero, F.E., Raga, J.A., Kostadinova, A., 2008. Composition and structure of the parasite faunas of cod, Gadus morhua L. (Teleostei: Gadidae), in the North East Atlantic. Parasit. Vectors 1, 23. https://doi.org/10.1186/1756-3305-1-23

Petrie, A., Wooten, R., Bruno, D., MacKenzie, K., Bron, J., 2009. A survey of Anisakis and Pseudoterranova in Scottish fisheries and the efficacy of current detection methods. Report of Food Standard Agency — Project S14008.

Piccolo, G., Manfredi, M.T., Hoste, L., Vercruysse, J., 1999. Anisakidae larval infection in fish fillets sold in Belgium. Vet. Quart. 21 (2), 66—67. https://doi.org/10.1080/01652176.1999.9694995

Platt, N.E., 1975. Infestation of cod (*Gadus morhua* L.) with larvae of codworm (*Terranova decipiens* Krabbe) and herringworm, *Anisakis* sp. (Nematoda Ascaridata), in North Atlantic and Arctic Waters. J. Appl. Ecol. 12 (2), 437—450. https://doi.org/10.2307/2402166

Rahmati, A.R., Kiani, B., Afshari, A., Moghaddas, E., Williams, M., Shamsi, S., 2021a. World-wide prevalence of Anisakis larvae in fish and its relationship to human allergic anisakiasis: a systematic review. Parasitol. Res. 119, 3585—3594. https://doi.org/10.1007/s00436-020-06892-0

Rahmati, A.R., Moghaddas, E., Kiani, B., Afshari, A., Williams, M., Shamsi, S., 2021b. Anisakis allergy: unjustified social alarm versus healthy diet; commentary to the "Letter to the Editor" of Drs Daschner, Levsen, Cipriani, and del Hoyo, referencing to "Worldwide prevalence of Anisakis larvae in fish and its relationship to human allergic anisakiasis: a systematic review. Parasitol. Res. 120, 1921—1923. https://doi.org/10.1007/s00436-021-07083-1

Rätz, H.J., Lloret, J., 2003. Variation in fish condition between Atlantic cod (*Gadus morhua*) stocks, the effect on their productivity and management implications. Fish. Res. 60 (2—3), 369—380. https://doi.org/10.1016/S0165-7836(02)00132-7

Scott, D.M., Martin, W.R., 1957. Variation in the incidence of larval Nematodes in Atlantic cod fillets along the Southern Canadian Mainland. J. Fish. Res. 14 (6), 975—996. https://doi.org/10.1139/f57-043

Shamsi, S., Suthar, J., 2016. Occurrence of *Terranova* larval types (Nematoda: Anisakidae) in Australian marine fish with comments on their specific identities. PeerJ. 4, e1722. https://doi.org/10.7717/peerj.1722

Sivertsen, A.H., Heia, K., Stormo, S.K., Elvevoll, E., Nilsen, H., 2011. Automatic nematode detection in cod fillets (*Gadus morhua*) by transillumination hyperspectral imaging. J. Food Sci. 76, 77—83.

Skovgaard, A., Bahlool, Q.Z.M., Munk, P., Berge, T., Buchmann, K., 2011. Infection of North Sea cod, *Gadus morhua* L., larvae with the parasitic nematode *Hysterothylacium aduncum* Rudolphi. J. Plankton Res. 33 (8), 1311—1316. https://doi.org/10.1093/plankt/fbr027

Smith, J.W., Hemmingsen, W., 2003. Atlantic cod *Gadus morhua* L.: Visceral organ topography and the asymetrical distribution of larval ascaridoid nematodes in the musculature. Ophelia 57 (3), 137—144. https://doi.org/10.1080/00785236.2003.10409510

Smith, J.W., Wootten, R., 1978. Anisakis and Anisakiasis. Adv. Parasitol. 16, 93—148. https://doi.org/10.1016/s0065-308x(08)60573-4

Sobecka, E., Łuczak, E., Więcaszek, B., Antoszek, A., 2011. Parasite community structure of cod from Bear Island (Barents Sea) and Pomeranian Bay (Baltic Sea). Pol. Polar Res. 32 (3), 253—262. https://doi.org/10.2478/V10183-011-0016-6

Stormo, S.K., Sivertsen, A.H., Heia, K., Nilsen, H., Elvevoll, E., 2007. Effects of single wavelength selection for Anisakid roundworm larvae detection through multispectral imaging. J. Food Prot. 70 (8), 1890—1895. https://doi.org/10.4315/0362-028x-70.8.1890

Strømnes, E., 2014. An in vitro study of lipid preference in whaleworm (*Anisakis simplex*, Nematoda, Ascaridoidea, Anisakidae) third-stage larvae. Parasitol. Res. 113, 1113—1118. https://doi.org/10.1007/s00436-013-3748-x

Strømnes, E., Andersen, K., 1998. Distribution of whaleworm (*Anisakis simplex*, Nematoda, Ascaridoidea) L3 larvae in three species of marine fish; saithe (*Pollachius virens* (L.)),cod (*Gadus morhua* L.) and redfish (*Sebastes marinus* (L.)) from Norwegian waters. Parasitol. Res. 84, 281—285. https://doi.org/10.1007/s004360050396

Strømnes, E., Andersen, K., 2000. Spring rise'' of whaleworm (*Anisakis simplex*; Nematoda, Ascaridoidea) third-stage larvae in some fish species from Norwegian waters. Parasitol. Res. 86, 619—624. https://doi.org/10.1007/PL00008541

Strømnes, E., Andersen, K., 2003. Growth of whaleworm (*Anisakis simplex*, Nematodes, Ascaridoidea, Anisakidae) third-stage larvae in paratenic fish hosts. Parasitol. Res. 89, 335—341. https://doi.org/10.1007/s00436-002-0756-7

Templeman, W., Squires, H.J., Fleming, A.M., 1957. Nematodes in the fillets of cod and other fishes in Newfoundland and neighbor in areas. J. Fish. Res. 14, 831—897. https://doi.org/10.1139/f57-037

Torres, P., Jercic, M.I., Weitz, J.C., Dobrew, E.K., Mercado, R.A., 2007. Human pseudoterranovosis, an emerging infection in Chile. J. Parasitol. 93, 440—443. https://doi.org/10.1645/GE-946R.1

Wharton, D.A., Aalders, O., 2002. The response of *Anisakis* larvae to freezing. J. Helminthol. 76, 363—368. https://doi.org/10.1079/JOH2002149

Wootten, R., Waddell, I.F., 1977. Studies on the biology of larval nematodes from the musculature of cod and whiting in Scottish waters. ICES J. Mar. Scie 37 (3), 266—273. https://doi.org/10.1093/icesjms/37.3.266

Wold, J., Westad, F., Heia, K., 2001. Detection of parasites in cod fillets by using SIMCA classification in multispectral images in the visible and NIR region. Appl. Spectrosc. 55 (8), 1025—1034.

Wootten, R., Bron, J., 2008. Worms in fish. Aquaculture news 34, 20—21.

Zhu, X., D'Amelio, S., Paggi, L., Gasser, R.B., 2000. Assessing sequence variation in the internal transcribed spacers of ribosomal DNA within and among members of the *Contracaecum osculatum*

complex (Nematoda: Ascaridoidea: Anisakidae). Parasitol. Res. 86 (8), 677—683.

Zhu, X., D'Amelio, S., Palm, H.W., Paggi, L., George-Nascimento, M., Gasser, R.B., 2002. SSCP-based identification of members within the *Pseudoterranova decipiens* complex (Nematoda: Ascaridoidea: Anisakidae) using genetic markers in the internal transcribed spacers of ribosomal DNA. Parasitology 124, 615—623. https://doi.org/10.1017/s0031182002001579

Oceanologia 64 (2022) 503—513

Available online at www.sciencedirect.com

ScienceDirect

journal homepage: www.journals.elsevier.com/oceanologia

ORIGINAL RESEARCH ARTICLE

Mud volcano as a feature of emergence in Caspian Sea

Danial Ghaderi, Maryam Rahbani*

Faculty of Marine Science and Technology, University of Hormozgan, Bandar Abbas, Iran

Received 2 September 2021; accepted 18 March 2022
Available online 1 April 2022

KEYWORDS
Dashli Island;
Daşlı ada;
Mud volcano;
Eruption;
Emergence;
Sentinel-1;
Sentinel-2

Abstract An eruption occurred on Dashli Island, 75 km from Baku, on 4th of July 2021, at 21:51 local time. The island is known as the mud volcano and has a history of eruption. We suspected that mud volcano eruption causes emergence on this island. Thus, the effect of this 2021 eruption is investigated using a remote sensing technique. Processed Sentinel-1 and 2 images are employed for this aim. We considered pre- and post-eruption scenarios to evaluate the effect of this eruption on the island. Satellite image classification is used to calculate shoreline changes. Results show that Dashli Island with an area of about 8.55 ha before eruption is now expanded to about 21.8 ha (about 155% increase). The DInSAR method is used to estimate the ground displacement of the island. According to the results, a two-year-displacement before the eruption was between 0.18 and 0.2 m, while a five-month-displacement after the eruption is estimated to be between 0.32 and 0.4 m. Considering ground displacement pre- and post-eruption we estimated 62000 m^3 land gaining, due to emergence. We concluded that mud volcano can be counted as a feature of emergence in Dashli Island.

* Corresponding author at: Faculty of Marine Science and Technology, University of Hormozgan, Bandar Abbas, Iran, Tel: +989373683087.
E-mail addresses: m_rahbani@hormozgan.ac.ir, maryamrahbani@yahoo.com (M. Rahbani).
Peer review under the responsibility of the Institute of Oceanology of the Polish Academy of Sciences.

Production and hosting by Elsevier

https://doi.org/10.1016/j.oceano.2022.03.006

1. Introduction

Mud volcano is a geological phenomenon, in which their activities are controlled by a combination of the gravitational instability of the rapidly buried sediment and the overpressure of deep hydrocarbon production (Mazzini et al., 2021; Mazzini and Etiope, 2017). This geological phenomenon forms in sedimentary onshore and offshore basins, where the eruption causes the subsurface muds to be uplifted (Odonne et al., 2020). Natural gases' underground reservoirs, tectonic activities and groundwaters are primary factors for a mud volcano (Müller, 2019). Various reasons have been proposed for the eruption of mud volcanoes including earthquakes (Manga et al., 2009; Manga and Brodsky, 2006) or pressure of gas hydrate (Dimitrov, 2002).

More than 2500 mud volcanoes are identified around the world, of which 353 are in Azerbaijan (the largest number of mud volcanoes in a country). About half of these mud volcanoes in Azerbaijan are located in the Caspian Sea (Baloglanov et al., 2018; Müller, 2019). The entire Caspian region has long been known as a mud volcano-rich region (Kopf, 2002). Thus, the appearance of small islands is reported in this area due to the eruption of submarine mud volcanoes (Schweder, 1893). Mud volcanoes can be divided into different categories depending on their morphology and activity. The most active region with the largest number of mud volcanoes in the world is located in the Baku region of the Caspian coast, eastern Azerbaijan, which is mostly cone-shaped (Dimitrov, 2002). Also, the largest mud volcano in the world is located in Azerbaijan with a height of about 400 m and a diameter of up to 3 km (Müller, 2019). These volcanos may be dormant for decades, but mostly are continuously blubbering and/or erupting continually. A large amount of mud could be discharged through the atmosphere and/or huge fireballs burst into the sky with any eruption (Müller, 2019); like the one that occurred in the Dashli Island, on 4th of July 2021 at 21:51 local time (GMT +4); 75 km from Baku in the Caspian Sea. The flame of this eruption was about 500 m (Baker, 2021; BBC News, 2021; Browne, 2021; The Guardian, 2021). The degassing process during eruption has the potential to extrude enormous volumes of rock material and sediment (Rapoport et al., 1986) and in the case of Dashli Island eruption, Sentinel-2 satellite collected data via an image taken on the 4th of July 2021, which revealed a significant amount of sediment outcrop.

A method to trace a mud volcano/volcano is to analyze remote sensing images, which is a popular and trustable method for such a phenomenon. Novellino et al. (2020) examined shoreline changes for volcanic activity in 2018–2019 at Anak Krakatau, Indonesia using satellite imagery. They used Sentinel-2 multispectral imagery, NDWI index, and Otsu thresholding to extract coastline changes. Patrick et al. (2004) monitored the thermal activity of mud volcano in the Copper River Basin, Alaska, using Landsat 7 ETM + thermal band data and a new Aster sensor. Using The Differential Interferometry Synthetic Aperture Radar (DInSAR) technique, Antonielli et al. (2014) estimated the ground deformation due to the activity of mud volcanoes of Azerbaijan. The pattern of ground displacement they observed for different date intervals was a cumulative value of up to 20 cm and 10 cm at the Ayaz – Akhtarma and Khara – Zira Islandmud volcanoes, respectively.

InSAR satellites were launched in the early 90s in order to approach interferometric techniques. InSAR is commonly used to monitor and estimate ground deformation related to earthquakes and volcanic activities (Bouchra et al., 2020). We likewise applied these methods to survey the shoreline changes and ground displacement that occurred on July 2021 in Dashli Island, to verify whether such a phenomenon could cause emergence. For this purpose, Sentinel-2 satellite images with a spatial resolution of 10 m and Sentinel-1 satellite SAR images have been employed.

2. Study area

Dashli Island (Azerbaijani: Daşlı ada, also called Dashly Island), in the Baku Archipelago (Aliyev et al., 2015; Guliev and Panahi, 2004) with the geographical location of 39.620278°N and 49.711944°E, in the southern Caspian Sea (Figure 1A–B), is located 75 km from Baku, 30 km from the coast of Azerbaijan, 10 km from Umid Gas field, and near the island of Cigil Adasi (Figure 1C). The island is known as an active mud volcano, which is continuously blubbering. According to the recorded reports, two previous eruptions on this island return back to the years 1920 and 1945 (Baloglanov et al., 2018). The latest eruption on this island occurred on the 4th of July 2021. Figure 1C shows the satellite image (Sentinel-2) of the island on the 4th of July 2021 at 07:26 (UTC), before the eruption, and Figure 1D-E shows the images of the Sentinel-1 on the 8th of July and Sentinel-2 on the 24th of July, after the eruption, respectively.

In order to evaluate the significance of hydrodynamic factors in this phenomenon, we overviewed the average annual pattern of current and wind in the area Baku Archipelago (Figure 2A–B). The average annual current velocity and direction in the area adjacent to Dashli Island is 6 cm/s and northeast respectively (Figure 2A) (Dyakonov, 2020; Dyakonov and Ibrayev, 2020). Wind pattern is presented as annual means with the resolution of 0.125° × 0.125° using ERA-Interim (Berrisford et al., 2011). The maximum wind speed and direction adjacent to Dashli Island is about 4 m/s and north/northeast respectively (Figure 2B). The hydrodynamics of the area expresses the south and southwest direction of the current and wind. This pattern is evident in Figure 1E, where we can see parts of erupted matter being departed and transported as suspended matters away from the island, along the current direction, on the 24th of July.

3. Material and methods

3.1. Data collection

To trace the effect of eruption, images of the island were collected from Sentinel satellites, before and after the eruption; referred to afterward as scenario "A" and "B" respectively. In scenario "A" data from July 2018, 2019, 2020, and 2021 were considered to evaluate shoreline changes, and data from 8th of February 2021 and 2nd of July 2021 were used to estimate ground displacement. In scenario "B" data on the 14th, 19th, and 24th of July and 13th of August 2021 were considered for evaluation of shoreline changes,

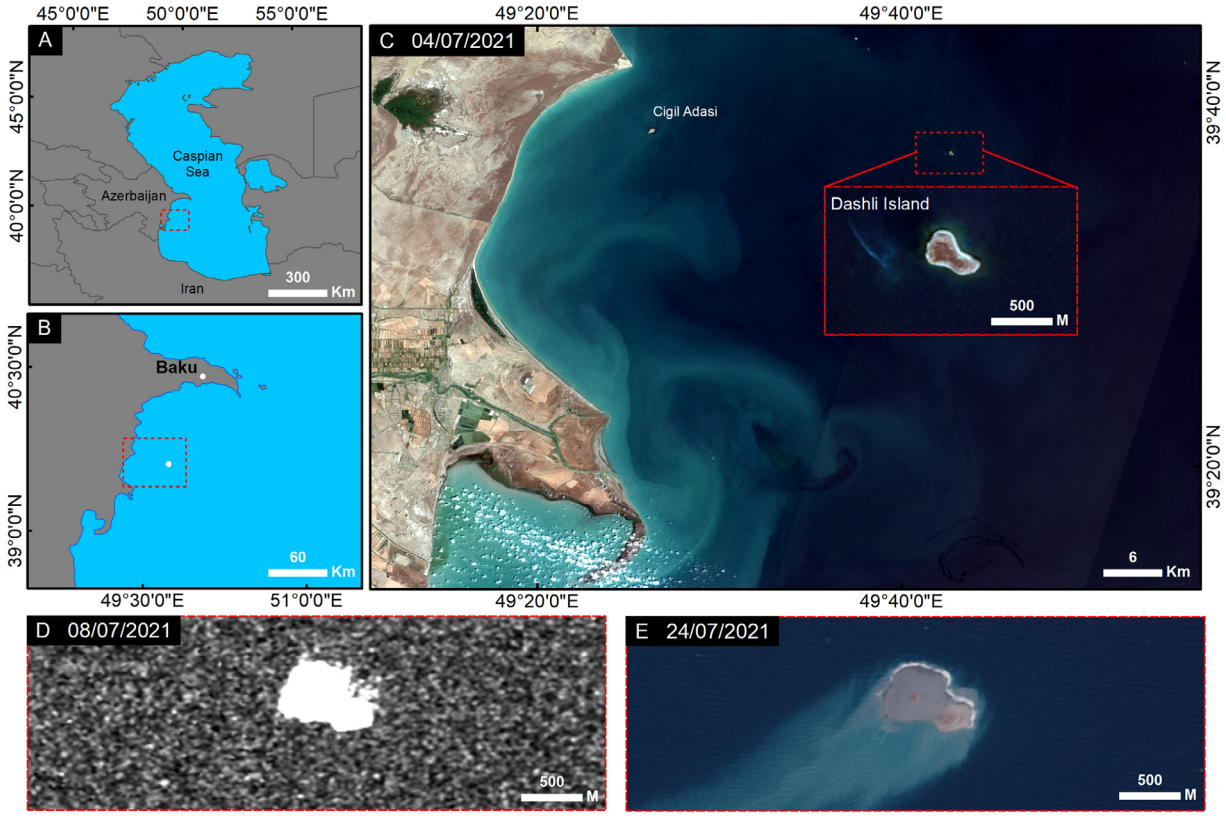

Figure 1 A—B) Location of Dashli Island in the Caspian Sea, C) Sentinel-2 image before the eruption (4th of July), D) Sentinel-1 image after the eruption (8th of July), and E) Sentinel-2 image after the eruption (24th of July).

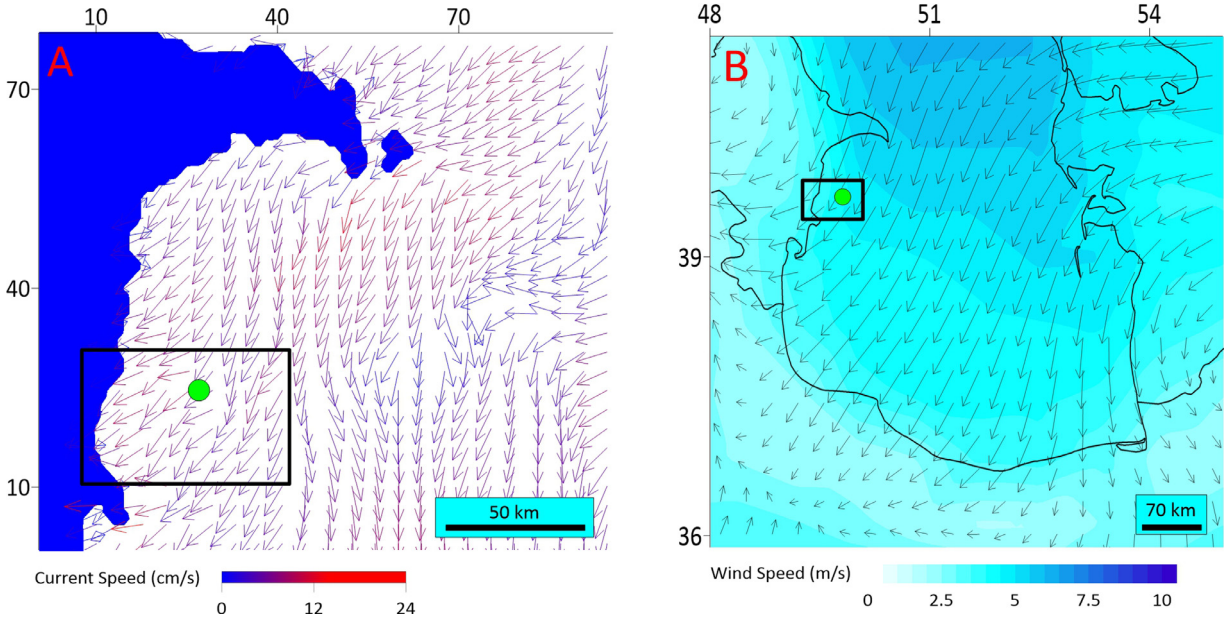

Figure 2 Annually averaged (A) current pattern around Baku Archipelago region (Dyakonov and Ibrayev, 2020) and (B) wind pattern (ECMWF) in the South Caspian Sea. Note: The green circle shows the location of Dashli Island.

Table 1 Bands information and date used from Sentinel-1 and 2 satellites.

Satellite	Date	Instrument	Band used	Central wavelength (nm)	Bandwidth (nm)	Scenario
Sentinel-2 A	25/07/2019	MSI	B3, B8	559.8, 832.8	36, 106	A
	19/07/2020					A
	04/07/2021					A
	14/07/2021					B
	24/07/2021					B
	13/08/2021					B
Sentinel-2 B	25/07/2018	MSI	B3, B8	559.0, 832.9	36, 106	A
	19/07/2021					B
Satellite	**Date**	**Product**		**Polarization used**		**Scenario**
Sentinel-1 A	02/07/2021	IW_GRD		VH		A
	08/07/2021					B
	14/07/2021					B
	01/08/2021					B
	08/02/2021	IW_SLC		VV		A
	02/07/2021					
	02/07/2021					B
	17/12/2021					

and data from the 2nd of July 2021 and the 17th of December 2021 were used for estimating ground displacement. All data is collected from the *Earth Explorer Database* of the *U.S. Geological Survey* and *Copernicus Open Access Hub* of the *ESA* (ESA, 2020; United States Geological Survey, 2020). Table 1 summarizes detailed information about the satellites in use. *Product Level-1C (L1C)* of Sentinel-2 A & B, product *IW_GRD*, and *IW_SLC* of Sentinel-1 A were the data we used in this research. The spatial resolution of Sentinel-2 A & B data is 10 m, and they subsets into frames of 100 km $\times$ 100 km, and product *IW_GRD* subsets into frames of 250 km $\times$ 250 km (Gascon et al., 2017; Spinosa et al., 2021). Sentinel-2 is designed to provide optimized images for studying vegetation, urban planning, terrestrial ecosystems, and inland waters (Soria et al., 2017). Sentinel-1 has a C-band (part of the electromagnetic spectrum in the microwave range of frequencies between 4.0 GHz and 8.0 GHz.), and a *Synthetic Aperture Radar (SAR)* instrument, which enables it to operate in any weather conditions, regardless of light availability (Elhag and Bahrawi, 2019; Spinosa et al., 2021).

3.2. Satellite image classification for shoreline evaluation

L1C product is radiometrically and geometrically corrected as standard (Barsi et al., 2018), and is georeferenced to *UTM/WGS84* projection. They however should be atmospherically corrected before analyzing. Several methods are available for atmospheric correction including *ACOLITE, Sen2Cor, iCOR, Polymer processor,* and *C2RCC*[1] which should be selected according to the type of the study area. *C2RCC* processor is the method used for coastal environments, thus we applied this method in our research which was also employed in other works of literature such as Ghaderi and Rahbani (2020) and Pereira-Sandoval et al. (2019).

Product *IW_GRD* of Sentinel-1 requires pre-processing suggested in Taha and Elbeih (2010), Yen and Kim (2020), and Zollini et al. (2019). They carried out the data processing in four steps: A) refining with the *orbit files*, B) radiometrically correction (for converting digital pixel values into radar backscatter values), C) lee filtering to reduce the speckle noise, and D) repairing geometrically using *terrain-corrected* by *SRTM (1 sec) digital surface model* to avoid repair distortion. Following this method, we carried out all processes for both Sentinel-1 and 2 products, using SNAP version 7.0.

To separate land from water in Sentinel-2 data, band spectral properties were considered. Different band ratio methods are available for this separation, among them *Normalized Difference Water Index (NDWI)* (McFeeters, 1996), which is used in this research (Eq. (1)). The *NDWI* index uses bands 3 and 8, with high reflection of green wavelength and NIR (respectively) to specify between land and water features, and to convert pixels into positive for water features and negative for vegetation and/or soil features respectively (Do et al., 2019).

$$NDWI = \frac{B_{GREEN} - B_{NIR}}{B_{GREEN} + B_{NIR}} \quad (1)$$

To identify land from water features in product *IW_GRD*, VH polarization data were considered as in Zollini et al. (2019). We used unsupervised classification *Expectation–maximization algorithm (EM)* to divide the features into two clusters of land and water (Moser, 2002; Pôssa et al., 2018). This algorithm is efficient specifically for small areas (ESA, 2021), which is the case in our research and is

[1] Case 2 Regional CoastColour

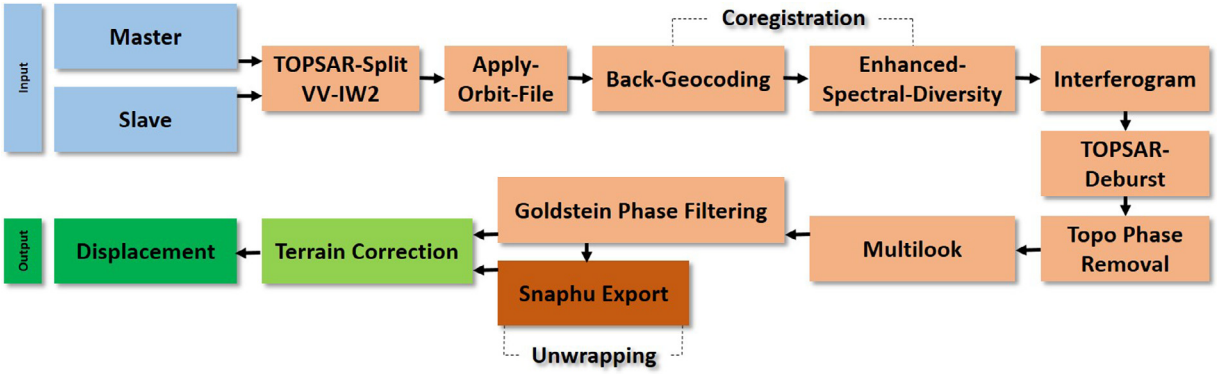

Figure 3 Schematic steps of DInSAR method (Bouchra et al., 2020; Edalat et al., 2020).

also applied in previous studies including but not limited to Baselice and Ferraioli (2013), Long et al. (2014) and Su et al. (2014).

3.3. Data processing to estimate ground displacement

To estimate the ground displacement due to the 2021 eruption in Dashli Island, we employed two SAR data before (Master) and after (Slave) the eruption. DInSAR methods and SNAPHU application are used for this purpose (Antonielli et al., 2014). DInSAR is a scientific approach for monitoring land deformation (Edalat et al., 2020), using DEM data and phase information of the two spatial similar area of SAR data (Edalat et al., 2020). The total phase ($\emptyset_{int}$) is the sum of several components represented in Eq. (2). Hanssen (2001) suggested $\emptyset_{int}$ could be representative of ground displacement ($\emptyset_{Movement}$), since in comparative scales other parameters of the equation cancels each other relatively.

$$\emptyset_{int} = \emptyset_{Topography} + \emptyset_{Change} + \emptyset_{Movement} + \emptyset_{Atmosphere} + \emptyset_{Noise} \quad (2)$$

Differential Radar Interferometry of SNAP toolbox software used to generate *differential interferograms*, which were filtered afterwards by *Goldstein Phase Filtering*. Before *unwrapped interferogram* generates displacement, unpacking phase should be done by SNAPHU. Then, the results were georeferenced by *Doppler Terrain Correction SRTM* (1 sec) (Bouchra et al., 2020; Edalat et al., 2020). Figure 3 shows the flowchart of the DInSAR method in the SNAP toolbox software.

4. Results and discussion

4.1. Accuracy assessment for shoreline detection

The acceptability of unsupervised classification of the EM algorithm depends on the level of accuracy assessment (Islam et al., 2021). Here we used Cohen's kappa coefficient (Rosenfield and Fitzpatrick-Lins, 1986) and confusion matrix (applying User Accuracy) to calculate the accuracy and efficiency of the EM algorithm and to detect the two land and water features (Figure 4). The overall accuracy of the confusion matrix (AC) and the kappa coefficient (Kappa) are presented in Figure 4. The efficiency of the EM algorithm in Sentinel-2 and Sentinel-1 images are fairly good (~0.98 and 0.95 respectively); which is also evident in the provided classified images (Figures 6 and 7). Calculating accuracy values for the 14th of July for both Sentinel-2 and 1, we reached 97.84 and 0.95 values for AC and Kappa for Sentinel-1, and 99.13 and 0.98 values for AC and Kappa Sentinel-2 respectively. Figure 5 shows the images derived from Sentinel-1 and Sentinel-2 before and after the eruption; it also shows the differences between SAR images and multi-spectral images. SAR images are more confident than the multi-spectral image, since they are available even during unsuitable weather conditions. For instance, the first multi-spectral satellite image after the eruption could not be used due to the heavy cloud cover (58.8%), while the SAR image on the 8th of July was the first qualified image, well captured the effect of the eruption (Figure 1C). According to classification performance (Figure 4) Sentinel-2 multi-spectral data are more reliable, thus we used these data to define the borders of the island before and after the eruption.

4.2. Effect of eruption

4.2.1. Shoreline change

To evaluate the shoreline changes of the island before the eruption (Scenario "A") images of Sentinel-2 of July, 2018, 2019, 2020 and 2021 were employed (Figure 6). Our evaluation demonstrates small changes in the area of the island since 2018, with about 0.7 ha increase till the 4th of July 2021, just before the eruption. The largest percentage of the change was about 10% (between 19/07/2020 and 25/07/2019). Besides, the perimeter of the island during these years varied between 1.1 km and 1.3 km (Table 2).

To survey the shoreline changes due to the eruption 2021 (Scenario "B") three images of July and one image of August were employed, and compared with those of scenario "A", which clarifies significant increase in the islands mass area, and increment of the island's borders. This means huge release of erupted mud arising from the mud volcano causes

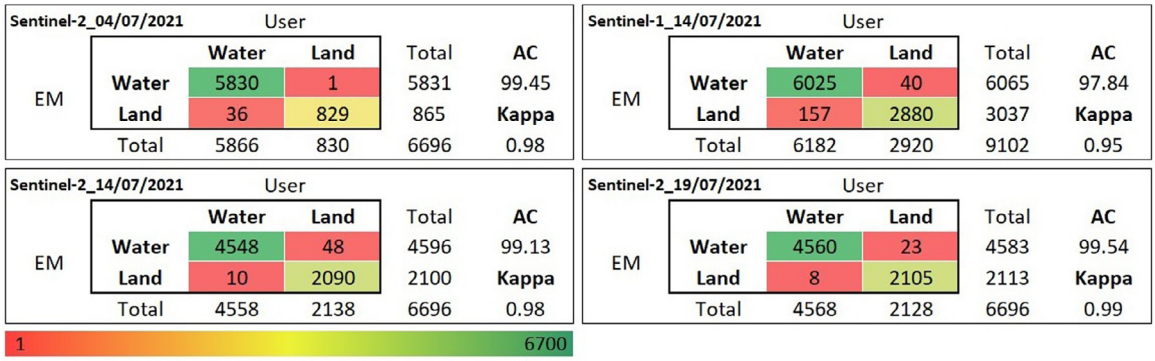

Figure 4 Confusion matrix and Cohen's kappa coefficient of EM algorithm classification.

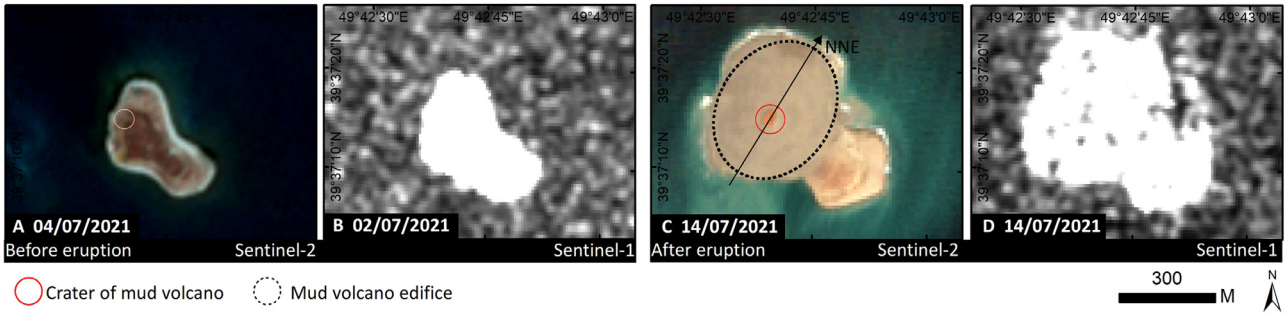

Figure 5 Dashli Island's SAR Images (Sentinel-1) and Sentinel-2, A and B represent the island before the eruption (Scenario "A"), and C and D after the eruption (Scenario "B"). The red circle and black ellipse represent the crater of the mud volcano and mud volcano edifice, respectively.

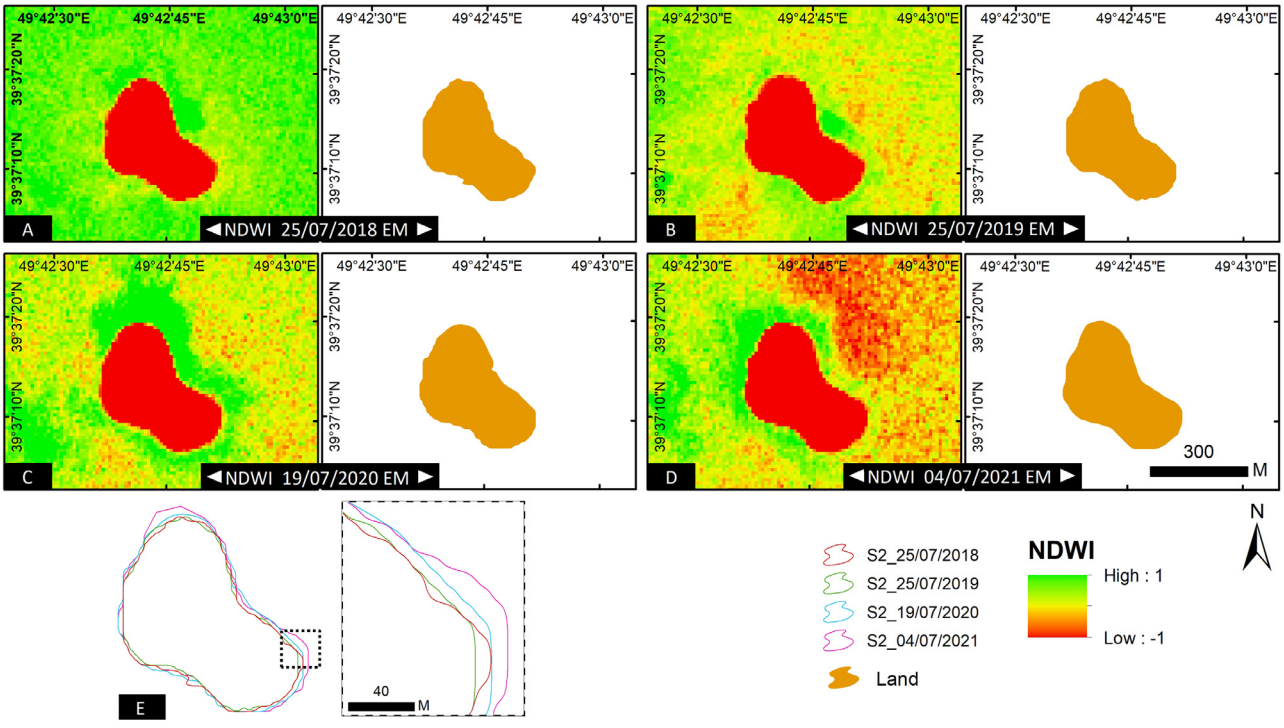

Figure 6 Dashli Island condition before the eruption (Scenario "A"). A–D) NDWI (Normalized Difference Water Index) results of Sentinel-2 products (left), and EM classification results (right). E) Borders of the island between 2018–2021.

Table 2 Details about the shoreline changes in Scenario "A" and "B".

Product		Date	Area (ha)	Percent change ha (up to the date)	Perimeter (m)	Diameter (m)	
						small (SD)	large (LD)
Scenario A							
	S2B_MSI-L1C	25/07/2018	7.8	—	1162.6	171.8	405.5
	S2A_MSI-L1C	25/07/2019	7.6	−2.43 (to 25/07/2018)	1137.3	166.2	411.1
	S2A_MSI-L1C	19/07/2020	8.4	10.12 (to 25/07/2019)	1177.9	187.4	417.3
	S2A_MSI-L1C	**04/07/2021**	**8.6**	**1.97 (to 19/07/2020)**	**1194.7**	**177.1**	**430.4**
Scenario B							
	S2A_MSI-L1C	14/07/2021	20.2	136.34 (to 04/07/2021)	1932.1	280.4	615.9
	S2B_MSI-L1C	19/07/2021	21.1	146.99 (to 04/07/2021)	1945.7	287.2	617.8
	S2A_MSI-L1C	24/07/2021	26.4	208.62 (to 04/07/2021)	2394.0	322.0	652.6
	S2A_MSI-L1C	**13/08/2021**	**21.8**	**154.98 (to 04/07/2021)**	**1902.1**	**296.0**	**618.6**

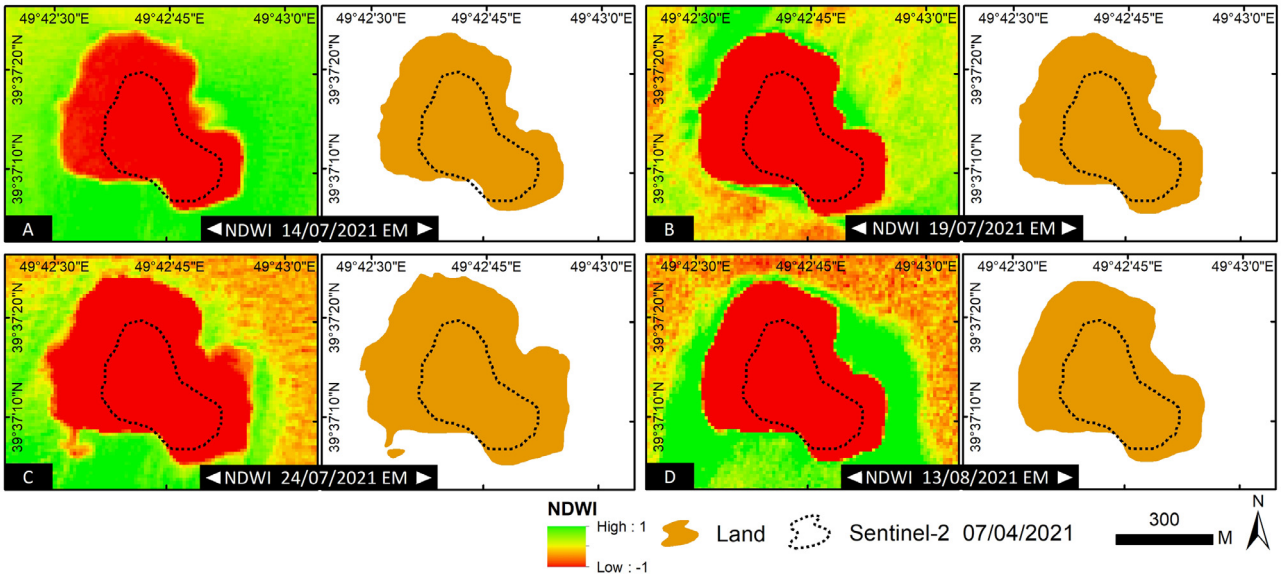

Figure 7 Dashli Island condition after the eruption (Scenario "B"), A—D) NDWI (Normalized Difference Water Index) results of Sentinel-2 products (left), and EM classification results (right). The dashed-black-curves show the border of the island before the eruption (4th of July).

expansion of the island (Figure 7). Results indicate that the island's area is increased till 13th of August by up to 21.8 ha (Figure 7) and 155% (Table 2). The new feature of the island is owed by the geometry and position of the feeder dike which extrude the mud during eruptive activity. The crater of the mud volcano is located in the western part of the island (see Figure 5C), probably sourced by a roughly NNE-trending feeder. Thus, we suggest that the orientation of the feeder dike corresponds to the long axis of the mud volcano edifice.

The smallest and largest diameters of the island (SD and LD respectively) before and after eruption were calculated to verify the most exposed area to the island expansion (Table 2). Results indicate 119.0 and 188.2 m increase along SD and LD, respectively; meaning the main expansion occurred along the LD (See Figure 7).

4.2.2. Ground displacement

Calculating ground displacement is a way to estimate the emergence of the island due to the eruption, and could be achieved using DInSAR method to generate differential interferograms and SNAPHU to produce actual displacement of the island. Again, we considered two scenarios for ground displacement; one for 5 months pre-eruption as scenario "A", and another for 5 months post-eruption as scenario "B" (Figure 8).

We are aware that DInSAR method is very sensitive to atmospheric conditions, thus we selected cloud-free data to estimate the differential interferograms. According to Figure 8A displacement due to the eruption is obvious (complex pattern of fringes in differential interferogram). For more clarity, the phase changes are prepared along the two diameters of the island (LD and SD in Figure 8C) to illustrate

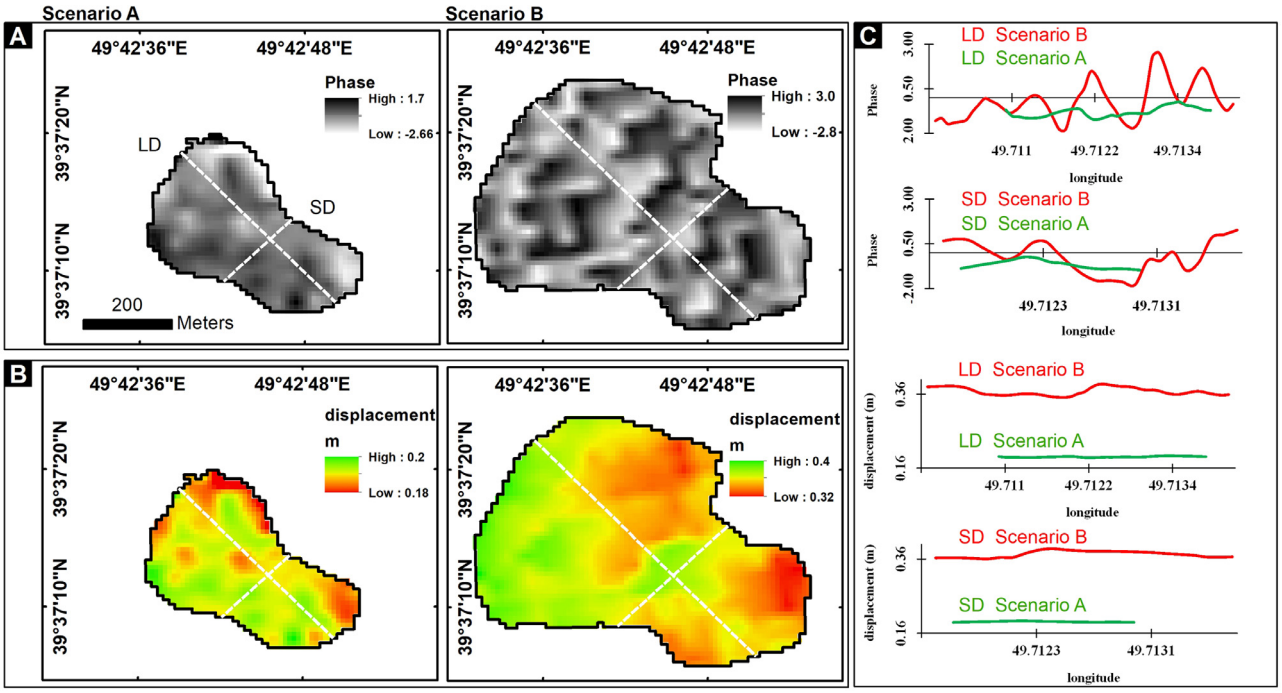

Figure 8 A) Differential interferograms after filtering, B) actual ground displacement, and C) phase changes of differential interferogram and actual ground displacement along SD (small diameter) and LD (long diameter).

the phase changes for two scenarios. The phase change in scenario "B" (red line) is more visible than in scenario "A" (Green line). To represent ground displacement, we used Eq. 2 as suggested by Hanssen (2001), since the actual displacement would be well justified subtracting the two data with time interval (Figure 8B). Displacement in scenario "A" is between 0.18 and 0.2 m, while in scenario "B" is between 0.32 and 0.4 m. Figure 8C also shows the clear increase of the diameters SD and LD after the eruption. It should be mentioned that for more reliability we considered a wider range of two years (30/07/2018—02/07/2021) to produce differential interferograms and actual displacement of the island (Appendix A, Figure 9D and E) before the eruption, and we achieved a range of displacement between 0.17 and 0.23, which is fairly similar with the results derived as pre-eruption for 5 months.

According to the results, the largest ground displacement is observed in the western part of the island (about 0.4 m), which can be counted as the main emergence of the island (Figures 7 and 8C). Besides, the central part of the island also shows ground displacement of the order of 0.4 m, which in this case can be counted as land uplift. After the western part, North and Southeast of the island are the area where emergence is evident. Comparing these results with the pattern of current and wind (see Figure 2) we concluded geometry of the island and the location of the mud volcano is the main concern for the island expansion and the hydrodynamic condition plays no or minor role in this phenomenon.

In general, on the basis of shoreline change (horizontal) and ground displacement (vertical) we calculated a rough volume of land emergence of about 62000 m^3, and the total uplift of the island as about 103500 m^3.

5. Conclusions

In this research, using remote sensing technique, we surveyed the impact of a mud volcano's eruption on Dashli Island located in the south of the Caspian Sea (75 km from Baku). We observed considerable shoreline change in the released images of the island due to the eruption. Thus we used processed Sentinel-1 and 2 satellite images of pre- and post-eruption to evaluate possible emergence in this island due to this phenomenon. Two methods were employed including satellite image classification to detect the shoreline change, and DInSAR to estimate ground displacement. According to satellite image classification of pre- and post-eruption, the small and large diameters of the island are increased 119.0 m, 188.2 m respectively, and the main expansion of the island is at the western side. It is more likely that the geometry and position of the volcano, located on the western part of the island, is responsible for this expansion. Particularly, hydrodynamic activities around the island are of minor or no concern. We also analyzed the DInSAR results to estimate the uplift of the island. These results revealed that the ground displacement of the island was between 0.17 and 0.23 m during the two years before the eruption, while this displacement increases between 0.32 and 0.4 m in just 5 months after the eruption. This means about 62000 m^3 of the island emerged from the sea due to this eruption. We suggest that mud volcano in this island caused sustained emergence.

Appendix A

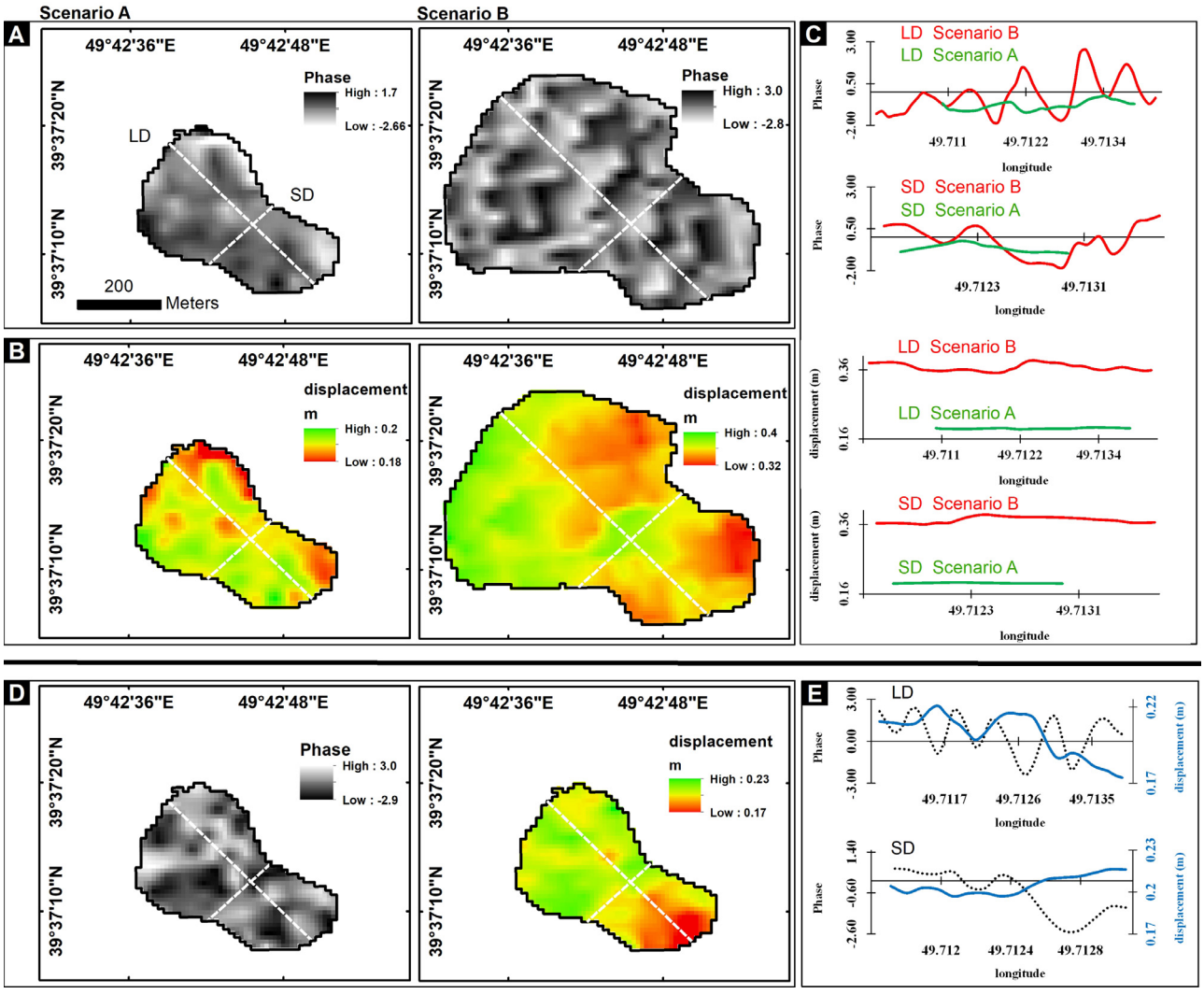

Figure 9 A) Differential interferograms after filtering, B) actual ground displacement, and C) phase changes of differential interferogram and actual ground displacement along SD (small diameter) and LD (long diameter). D) Differential interferograms after filtering and actual ground displacement of 30/07/2018 (Master) and 02/07/2021 (Slave). E) Phase changes and ground displacement along SD and LD of 30/07/2018 and 02/07/2021.

References

Antonielli, B., Monserrat, O., Bonini, M., Righini, G., Sani, F., Luzi, G., Feyzullayev, A.A., Aliyev, C.S., 2014. Pre-eruptive ground deformation of Azerbaijan mud volcanoes detected through satellite radar interferometry (DInSAR). Tectonophysics 637, 163—177. https://doi.org/10.1016/j.tecto.2014.10.005

Aliyev, A.A., Guliyev, I.S., Dadashov, F.H., Rakhmanov, R.R., 2015. Atlas of the world mud volcanoes. Nafta-Press Publ.

Baker, H., 2021. Rare mud volcano explodes into towering inferno in Caspian Sea [WWW Document]. https://www.livescience.com/caspian-sea-explosion-mud-volcano.html (accessed 7.28.21).

Baloglanov, E.E., Abbasov, O.R., Akhundov, R.V, 2018. Mud volcanoes of the world: Classifications, activities and environmental hazard (informational-analytical review). Eur. J. Nat. Hist. 12—26.

Barsi, J.A., Alhammoud, B., Czapla-Myers, J., Gascon, F., Haque, M.O., Kaewmanee, M., Leigh, L., Markham, B.L., 2018. Sentinel-2A MSI and Landsat-8 OLI radiometric cross comparison over desert sites. Eur. J. Remote Sens. https://doi.org/10.1080/22797254.2018.1507613

Baselice, F., Ferraioli, G., 2013. Unsupervised Coastal Line Extraction From SAR Images. IEEE Geosci. Remote Sens. Lett. 10, 1350—1354. https://doi.org/10.1109/LGRS.2013.2241013

BBC News", 2021. Azerbaijan mud volcano triggers huge blast in Caspian oil and gas fields [WWW Document]. https://www.bbc.com/news/world-europe-57722236 (accessed 7.28.21).

Berrisford, P., Dee, D.P., Poli, P., Brugge, R., Fielding, M., Fuentes, M., Kr allberg, P.W., Kobayashi, S., Uppala, S., Simmons, A., 2011. The ERA-Interim archive Version 2.0. Reading, Shinfield Park.

Bouchra, A., Mustapha, H., Mohammed, R., 2020. D-InSAR Analysis of Sentinel-1 Data for Landslide Detection in Northern Morocco, Case Study: Chefchaouen. J. Geosci. Environ. Protect. 08, 84—103. https://doi.org/10.4236/gep.2020.87005

Browne, E., 2021. What Is a Mud Volcano? Huge Explosion Rocks Oil-Rich Caspian Sea [WWW Document]. https://www.

newsweek.com/what-mud-volcano-explained-huge-explosion-fire-caspian-sea-oil-1606877 (accessed 7.28.21).
Dimitrov, L.I., 2002. Mud volcanoes—the most important pathway for degassing deeply buried sediments. Earth Sci. Rev. 59, 49—76. https://doi.org/10.1016/S0012-8252(02)00069-7
Do, A.T.K., Vries, S.de, Stive, M.J.F., 2019. The Estimation and Evaluation of Shoreline Locations, Shoreline-Change Rates, and Coastal Volume Changes Derived from Landsat Images. J. Coastal Res. 35, 56. https://doi.org/10.2112/JCOASTRES-D-18-00021.1
Dyakonov, G., 2020. High-resolution data on mesoscale dynamics of the Caspian Sea upper layer, obtained in a numerical reconstruction [WWW Document]. *Mendeley Data*. https://doi.org/10.17632/st2grwnhmv.1
Dyakonov, G.S., Ibrayev, R.A., 2020. High-resolution data on mesoscale dynamics of the Caspian Sea upper layer, obtained in a numerical reconstruction. *Data Brief*. 30, 105368. https://doi.org/10.1016/j.dib.2020.105368
Edalat, A., Khodaparast, M., Rajabi, A.M., 2020. Detecting Land Subsidence Due to Groundwater Withdrawal in Aliabad Plain, Iran, Using ESA Sentinel-1 Satellite Data. Nat. Resour. Res. 29, 1935—1950. https://doi.org/10.1007/s11053-019-09546-w
Elhag, M., Bahrawi, J.A., 2019. Sedimentation mapping in shallow shoreline of arid environments using active remote sensing data. Nat. Hazard. 99, 879—894. https://doi.org/10.1007/s11069-019-03780-4
ESA, 2021. Expectation maximization (em) cluster analysis. [WWW Document]. ESA. https://www.brockmann-consult.de/beam/doc/help/clusteranalysis/EM.html
ESA, 2020. Copernicus Open Access Hub of the ESA [WWW Document]. https://scihub.copernicus.eu/ (accessed 8.2.20).
Gascon, F., Bouzinac, C., Thépaut, O., Jung, M., Francesconi, B., Louis, J., Lonjou, V., Lafrance, B., Massera, S., Gaudel-Vacaresse, A., Languille, F., Alhammoud, B., Viallefont, F., Pflug, B., Bieniarz, J., Clerc, S., Pessiot, L., Trémas, T., Cadau, E., De Bonis, R., Isola, C., Martimort, P., Fernandez, V., 2017. Copernicus Sentinel-2A calibration and products validation status. Remote Sens https://doi.org/10.3390/rs9060584
Ghaderi, D., Rahbani, M., 2020. Shoreline change analysis along the coast of Bandar Abbas city, Iran using remote sensing images. Int. J. Coastal Offshore Eng. 4, 51—64.
Guliev, I., Panahi, B., 2004. Geodynamics of the deep sedimentary basin of the Caspian Sea region: paragenetic correlation of seismicity and mud volcanism. Geo-Mar. Lett. 24, 169—176. https://doi.org/10.1007/s00367-004-0174-1
Hanssen, R.F., 2001. Radar Interferometry, Remote Sensing and Digital Image Processing. Dordrecht, Springer Netherlands, 308 pp. https://doi.org/10.1007/0-306-47633-9
Islam, M.S., Uddin, M.A., Hossain, M.A., 2021. Assessing the dynamics of land cover and shoreline changes of Nijhum Dwip (Island) of Bangladesh using remote sensing and GIS techniques. Reg. Stud. Mar. Sci. 41, 101578. https://doi.org/10.1016/j.rsma.2020.101578
Kopf, A.J. , 2002. SIGNIFICANCE OF MUD VOLCANISM. Rev. Geophys.. 40, 2-1-2—52. https://doi.org/10.1029/2000RG000093
Long, T., Jiao, W., He, G., Wang, W., 2014. Automatic Line Segment Registration Using Gaussian Mixture Model and Expectation-Maximization Algorithm. IEEE J. Sel. Top. Appl. Earth Obs. Remote Sens. 7, 1688—1699. https://doi.org/10.1109/JSTARS.2013.2273871
Manga, M., Brodsky, E., 2006. SEISMIC TRIGGERING OF ERUPTIONS IN THE FAR FIELD: Volcanoes and Geysers. Annu. Rev. Earth Planet. Sci. 34, 263—291. https://doi.org/10.1146/annurev.earth.34.031405.125125
Manga, M., Brumm, M., Rudolph, M.L., 2009. Earthquake triggering of mud volcanoes. Mar. Pet. Geol. 26, 1785—1798. https://doi.org/10.1016/j.marpetgeo.2009.01.019
Mazzini, A., Akhmanov, G., Manga, M., Sciarra, A., Huseynova, A., Huseynov, A., Guliyev, I., 2021. Explosive mud volcano eruptions and rafting of mud breccia blocks. Earth Planet. Sci. Lett. 555, 116699.
Mazzini, A., Etiope, G., 2017. Mud volcanism: An updated review. Earth Sci. Rev. 168, 81—112.
McFEETERS, S.K., 1996. The use of the Normalized Difference Water Index (NDWI) in the delineation of open water features. Int. J. Remote Sens. 17, 1425—1432. https://doi.org/10.1080/01431169608948714
Moser, G., 2002. Unsupervised change-detection methods for remote-sensing images. Opt. Eng. 41, 3288. https://doi.org/10.1117/1.1518995
Müller, H.E.J., 2019. The Mud Volcanoes of Azerbaijan—a Potential UNESCO World Heritage Site. World Heritage Watch Report 28.
Novellino, A., Engwell, S.L., Grebby, S., Day, S., Cassidy, M., Madden-Nadeau, A., Watt, S., Pyle, D., Abdurrachman, M., Edo Marshal Nurshal, M., Tappin, D.R., Andri Kurniawan, I., Hunt, J., 2020. Mapping Recent Shoreline Changes Spanning the Lateral Collapse of Anak Krakatau Volcano, Indonesia. Appl. Sci. 10, 536. https://doi.org/10.3390/app10020536
Odonne, F., Imbert, P., Dupuis, M., Aliyev, A.A., Abbasov, O.R., Baloglanov, E.E., Vendeville, B.C., Gabalda, G., Remy, D., Bichaud, V., Juste, R., Pain, M., Blouin, A., Dofal, A., Gertauda, M., 2020. Mud volcano growth by radial expansion: Examples from onshore Azerbaijan. Mar. Pet. Geol. 112, 104051. https://doi.org/10.1016/j.marpetgeo.2019.104051
Patrick, M., Dean, K., Dehn, J., 2004. Active mud volcanism observed with Landsat 7 ETM+. J. Volcanol. Geotherm. Res. 131, 307—320. https://doi.org/10.1016/S0377-0273(03)00383-4
Pereira-Sandoval, M., Ruescas, A., Urrego, P., Ruiz-Verdú, A., Delegido, J., Tenjo, C., Soria-Perpinyà, X., Vicente, E., Soria, J., Moreno, J., 2019. Evaluation of Atmospheric Correction Algorithms over Spanish Inland Waters for Sentinel-2 Multi Spectral Imagery Data. Remote Sens. 11, 1469. https://doi.org/10.3390/rs11121469
Pôssa, É.M., Maillard, P., Gomes, M.F., Silva, I., Leão, G., 2018. On water surface delineation in rivers using Landsat-8, Sentinel-1 and Sentinel-2 data. In: Neale, C.M., Maltese, A. (Eds.), Proc. SPIE Oct. SPIE, 45. https://doi.org/10.1117/12.2325725
Rapoport, A.J., Tjokrosapoetro, S., Charlton, T.R., 1986. Mud Volcanoes, Shale Diapirs, Wrench Faults, and Melanges in Accretionary Complexes, Eastern Indonesia. Am. Assoc. Pet. Geol. Bull. 70. https://doi.org/10.1306/94886CA9-1704-11D7-8645000102C1865D
Rosenfield, G.H., Fitzpatrick-Lins, K., 1986. A coefficient of agreement as a measure of thematic classification accuracy. Photogramm. Eng. Remote Sens. 52, 223—227.
Schweder, G., 1893. Über Schlammvulkane und Inselbildung im Kaukasus und Kaspisee. Korr. Blatt. Nat. Ver. Riga, XXXVI 41—42.
Soria, X., Delegido, J., Urrego, E.P., Pereira-Sandoval, M., Vicente, E., Ruiz-Verdu, A., Soria, J.M., Peña, R., Tenjo, C., Moreno, J., 2017. Validación de algoritmos para la estimación de la clorofila-a con Sentinel-2 en la Albufera de València. In: Proceedings of the XVII. Congreso de La Asociación Española de Teledetección, 289—292.
Spinosa, A., Ziemba, A., Saponieri, A., Damiani, L., El Serafy, G., 2021. Remote Sensing-Based Automatic Detection of Shoreline Position: A Case Study in Apulia Region. J. Mar. Sci. Eng. 9, 575. https://doi.org/10.3390/jmse9060575
Su, L., Gong, M., Sun, B., Jiao, L., 2014. Unsupervised change detection in SAR images based on locally fitting model and semi-EM algorithm. Int. J. Remote Sens. 35, 621—650. https://doi.org/10.1080/01431161.2013.871596
Taha, L.G.E., Elbeih, S.F., 2010. Investigation of fusion of SAR and Landsat data for shoreline super resolution mapping: the northeastern Mediterranean Sea coast in Egypt. Appl. Geomatics. 2, 177—186. https://doi.org/10.1007/s12518-010-0033-x

The Guardian, 2021. Azerbaijan says 'mud volcano' caused Caspian Sea explosion [WWW Document]. https://www.theguardian.com/world/2021/jul/05/explosion-rocks-caspian-sea-near-azerbaijan-gas-field (accessed 7.28.21).

United States Geological Survey, 2020. EarthExplorer [WWW Document]. https://earthexplorer.usgs.gov/ (accessed 8.2.20).

Yen, N.H., Kim, T.L.T., 2020. Coastline changes detection from Sentinel—1 satellite imagery using spatial fuzzy clustering and interactive thresholding method in Phan Thiet, Binh Thuan. Vietnam J. Hydrometeorology 1—10.

Zollini, S., Alicandro, M., Cuevas-González, M., Baiocchi, V., Dominici, D., Buscema, P.M., 2019. Shoreline Extraction Based on an Active Connection Matrix (ACM) Image Enhancement Strategy. J. Mar. Sci. Eng. 8, 9. https://doi.org/10.3390/jmse8010009

Oceanologia 64 (2022) 514—534

Available online at www.sciencedirect.com

ScienceDirect

journal homepage: www.journals.elsevier.com/oceanologia

ORIGINAL RESEARCH ARTICLE

A coupled model for sediment transport dynamics and prediction of seabed morphology with application to 1DH/2DH coastal engineering problems

Vasileios Afentoulis[a,*], **Andreas Papadimitriou**[a], **Kostas Belibassakis**[b], **Vasiliki Tsoukala**[a]

[a] *Laboratory of Harbour Works, Department of Water Resources and Environmental Engineering, School of Civil Engineering, National Technical University of Athens, Greece*
[b] *School of Naval Architecture and Marine Engineering, National Technical University of Athens, Athens, Greece*

Received 12 August 2021; accepted 18 March 2022
Available online 4 April 2022

KEYWORDS
Sediment transport;
Coastal dynamics;
Boussinesq Wave Model;
Numerical modeling;
Coastal structures

Abstract Coastline retreat poses a threat to nearshore environment and the assessment of erosion phenomena is required to plan the coastal engineering works. The hydromorphodynamic response of a beach to natural and artificial forcing factors differ considerably, as the nearshore processes are especially complex and depended on a multitude of parameters, including prevailing wave and hydrodynamic conditions, beach topography, sediment characteristics and the presence of coastal protection works. The present study serves the purpose of numerically evaluating nearshore morphological processes and ultimately assessing the capacity of coastal defence structures to control beach erosion. For this reason, a new sediment transport model including unsteady effects and swash zone morphodynamics, was coupled to the highly nonlinear Boussinesq wave model FUNWAVE-TVD, providing integrated predictions of bed level evolution, across various timescales of interest. The compound model was vali-

* Corresponding author at: Laboratory of Harbour Works, Department of Water Resources and Environmental Engineering, School of Civil Engineering, National Technical University of Athens, Greece. Tel.: 0033 (0)767943773.
E-mail address: af.vasilis@gmail.com (V. Afentoulis).
Peer review under the responsibility of the Institute of Oceanology of the Polish Academy of Sciences.

Production and hosting by Elsevier

https://doi.org/10.1016/j.oceano.2022.03.007

dated thoroughly against laboratory data and other numerical investigations. Overall, a good agreement between experimental and numerical results was achieved for a number of test cases, investigating the effects of different types of shore protection structures. The proposed integrated model can be a valuable tool for engineers and scientists desiring to obtain accurate bed level predictions, over complex mildly and steeply sloping sea bottoms composed of non-cohesive sediment particles.

List of parameters

Parameter	Description, units
A	Wave amplitude, m
C_d	Bottom friction coefficient
c	Sediment concentration by mass or volume, m^3/m^3
c_a	Reference sediment concentration, m^3/m^3
c_x, c_y	Wave propagation velocities, m/s
d	Diameter of bed material, mm
d_{50}	Median size of sediment, mm
D	Volumetric deposition rate, m^3/s
D_*	Dimensionless particle size
E	Volumetric erosion rate, m^3/s
f_c	Current friction coefficient
f_w	Wave friction coefficient
g	Gravitational acceleration, m/s^2
h	Water depth, m
H	Wave height, m
H_S	Significant wave height, m
H_{m0}	spectral significant wave height, m
K_c, K_l	Cross-shore and long-shore swash coefficients
M	Horizontal flux term
n_p	Sand porosity
k_s	Roughness height, m
q	volumetric net transport rate, m^2/s
R^b	Eddy-viscosity-type breaking term
R^s	Subgrid turbulent mixing term
R	Bottom friction term
Re_*	Shear Reynolds number
T	Wave period, s
T_p,	Peak wave period, s
u	Instantaneous velocity in x direction, m/s
$\bar{u}$	Mean horizontal velocity in x direction, m/s
u_w	Oscillatory horizontal velocity, m/s
$U_{\delta w}$	Near-bottom wave velocity, m/s
u_a	horizontal velocity at adaptive reference level, m/s
U_C	Mean current velocity, m/s
u_*	Shear velocity, m/s^2
u_o	Scaling velocity, m/s
v	Velocity in y direction, m/s
v_o	Scaling velocity in y direction, m/s
w_s	Settling velocity, m/s
z	Vertical distance above the bottom, m
z_a	Reference height, m
β	Parameter of sediment diffusivity
ε	Empirical sediment coefficient
ε_s	Sediment diffusivity, m^2/s
$\varepsilon_{s,c}$	Current-related sediment diffusivity coefficient, m^2/s
$\varepsilon_{s,w}$	Wave-related sediment diffusivity coefficient, m^2/s
Δ_r	Ripple height
δ_w	Thickness of near-bed sediment mixing layer, m
ζ	Water level, m
η	Surface elevation, m
κ	Karman number
θ	Shields number
θ_c	Critical Shields number
ρ	Water density, kg/m^3
ρ_s	Sediment density, kg/m^3
τ	Shear stress, N/m^2
τ_c	Dimensionless critical shear stress
ν_t	Eddy viscosity, m^2/s
ω	Wave frequency, Hz
μ	Dimensionless measure of dispersion
φ_m	Internal friction angle, deg

1. Introduction

Sandy coasts have been constantly modified as a result of natural processes involving wind waves or swell, currents, sea level variability and aeolian sediment transport (Divinsky et al., 2021; Divinsky and Kosyan, 2020; Roelvink and Costas, 2019). Erosion of the coastal seabed and ultimately a retreat of shoreline position is caused by a combination of the abovementioned processes and has strong implications to the economy, environment and community safety since a multitude of activities are concentrated at the coastal zones. Additionally, anthropogenic unplanned infrastructures in the coastal zone, along with jetties and other obstacles to longshore transport, reflective vertical walls that accelerate offshore sand bar migration (Seabergh and Kraus, 2003), as well as devegetation along

coasts are key causes intensifying beach erosion in the long term (Ruiz-Martínez et al., 2016).

The most widely applied engineering technique to control beach erosion is the construction of coastal defense structures, which can also provide sufficient protection against flooding phenomena to the inland (Charlier and De Meyer, 1989; Nordstrom, 2014; Pranzini et al., 2015; Servold et al., 2017; van Rijn, 2013). A variety of coastal defenses can be encountered in the literature of coastal engineering, such as detached emerged and submerged breakwaters, groynes, seawalls, riprap and wave attenuators. Emerged breakwaters, the presence of which leads to reduced wave agitation alters the patterns of the nearshore breaking wave-induced current field and creates the appropriate conditions for sediment deposition, thus enabling shoreline advance. It should be noted that emerged breakwaters have been used at a lesser extent in the recent decades as a protection solution, due to their negative impact on the aesthetic characteristics of coastal landscape. Hence, submerged structures provide a good compromise between the need to reduce the wave energy close to the shore and the aim to ensure landscape preservation and a good water quality though the exchange of water between offshore and inshore areas. Moreover, in case the longshore sediment transport dominates the sediment transport regime, groynes are employed to retain the beach and maintain the stability of the littoral system.

The investigation of nearshore hydrodynamic and morphodynamic patterns, associated with the presence of coastal structures, has been carried out through laboratory experiments during the last decades. In the studies of Ming and Chiew (2000) and Birben et al. (2007) a series of experiments were used to analyze the effect of offshore breakwaters on beach morphology and sediment accumulation ratio. Cáceres et al. (2008) carried out an experimental research to assess wave overtopping and wave-induced current field in the breaker zone around low-crested structures. A new dimensionless parameter (β) was proposed by Mahmoudof and Hajivalie (2021), through experimental investigations in order to describe wave transmission and reflection phenomena over submerged breakwaters. However, scaling effects inherently linked to the experimental conditions and the sediment transport processes (Gorrick and Rodríguez, 2014) render the long-term prediction of coastal bed evolution through experimental procedures a difficult task. As a consequence, process-based models that can advance understanding of the dominant process response (and feedbacks) of littoral systems to a wide range of coastal defense structures, have been extensively used in coastal engineering (Afentoulis et al., 2017; Kobayashi, 2016; Lesser et al., 2004; Nam et al., 2011; Postacchini et al., 2016; Tang et al., 2017; Zyserman and Johnson, 2002).

These composite nearshore models are usually comprised of wave propagation, hydrodynamic, and sediment transport/morphology models. A variety of sophisticated numerical tools have been utilized for the simulation of wave transformation processes, taking into consideration that for most coastal configurations waves are the dominant driving factor, inducing morphological changes. Two distinct approaches have been highlighted (Hotlhiujsen, 2003) for the numerical investigation of the dominant processes governing wave transformation:

1) The phase-averaged approach that describes wave propagation in the spatial and time domain using the variance-density spectrum, which is the Fourier transformation of the auto-covariance function of free-surface elevation. The most notoriously used models following this approach are 3rd generation spectral wave models (Benoit et al., 1997).
2) The phase resolving deterministic approach describing details of the wave field in the spatial and temporal domain at a resolution that is a small fraction of the wavelength / period. In this category, models solving the mild slope, shallow water (SWE), or Boussinesq equations have been employed.

It should be noted that despite the plethora of modeling tools available, each one is associated with flaws, which have to be taken into serious consideration for the purpose of predicting the morphological evolution of coastal areas. Models based on the phase averaging approach are computationally efficient but omit a large number of dominant wave processes in the nearshore, especially considering that wave diffraction, reflection and run-up are not usually accounted for. In addition, coherencies observed in the wave field and caused by abrupt bottom variations and strong current gradients are unable to be simulated in these models (Smit et al., 2015). Phase resolving models are able to resolve many of the aforementioned important wave transformation processes but are often associated with major constraints, i.e. mildly sloping bottoms (for models based on the mild slope wave equations) and satisfaction of the shallow water approximation (for the SWE wave models). From deep to shallow water, dispersive nonlinear wave effects can be simulated satisfactorily using Boussinesq models (Kennedy et al., 2001; Madsen et al., 1997) since they are sufficiently accurate in resolving nearshore wave phenomena, such as refraction and diffraction (Do et al., 2020). However, until recent decades, their application to hydrodynamic modeling in engineering projects was limited due to high computational cost (Klonaris et al., 2018, 2020) rendering their use in practical applications almost impossible.

Nowadays, several Boussinesq-type models coupled with a sediment transport module, suitable for coastal engineering applications, can be encountered in the literature of coastal engineering (Gallerano et al. 2016; Karambas and Koutitas, 2002; Karambas, 2012; Klonaris et al., 2016; Kobayashi et al., 2000; Malej et al., 2019). Moreover, different researches have successfully predicted the shoreline evolution and beach morphology in the vicinity of detached breakwaters, groynes, or vertical quay walls (Bouvier et al., 2019; Ding and Wang, 2008; Hieu et al., 2020; Karambas and Samaras, 2017). Tsiaras et al. (2020) used a nonlinear breaking wave and morphodynamic model, including unsteady aspects of the sand transport for evaluating the potential influence of the transmission coefficient and of the net mass influx over structure in the design process of submerged breakwaters. Moreover, Klonaris et al. (2020) provided a detailed experimental and numerical investigation about the effects of rubble-mound submerged breakwaters on beach morphology, using a compound Boussinesq-type model. Although up to present, numerical predictions of wave-current interactions and morphological responses, with and without the presence of coastal structures, are

still associated with considerable uncertainty related to the highly non-linear nature of these physical processes. In the above-mentioned studies, either the wave and hydrodynamic module does not consider the reflection and transmission (e.g. permeability) characteristics of emerged breakwaters and vertical obstacles, or the utilized sediment transport approximations are not suitable to capture the wave non-linear effects on sand transport and simulate the 3D characteristics of the suspended sediment transport loads.

In the present study, a fully nonlinear Boussinesq model (Shi et al., 2012), FUNWAVE — Total Variation Diminishing (TVD), tasked with the simulation of wave propagation and hydrodynamic circulation was directly coupled to a quasi-3-D sediment transport and morphology model, which was developed by the authors of this study. Thus, taking advantage of FUNWAVE model's capacity to provide information on coastal structure's reflection and transmission behavior and employing advanced sediment transport approximations, including unsteady sand transport aspects, this study seeks to reduce the uncertainty in hydro-morphodynamic predictions. Special attention was given to the role of sediment transport dynamics across the swash zone, incorporating them in the morphodynamic model, while advanced techniques were utilized to model the three-dimensional patterns of suspended load fluxes and consider wave nonlinear and unsteady effects on bed load transport rates. Our scope is to introduce an integrated model that can be utilized to a wide range of maritime engineering applications, both for soft engineering (beach replenishment, sand dune management, drainage) and hard engineering techniques (design of groynes, breakwaters, seawalls, revetments). A particular effort was made to keep the computational complexity at a reasonable level by utilizing morphological acceleration techniques and exploiting the efficient parallel scheme of the wave model. Moreover, in order to ensure the reliability of our numerical modelling approach, the compound model was extensively validated for five distinctive test cases, covering a wide range of coastal engineering applications in both experimental and field scales and providing significant insights into the morphological response of sandy beaches to the combined action of waves and currents.

2. Description of models and formulations

A fully coupled method for simulation of wave-current-seabed interaction was developed within the context of our research. The numerical output of FUNWAVE-TVD model is used as forcing for a two-dimensional sediment transport model in an interactive mode, while the computation of sediment fluxes and morphological changes provides the feedback of bathymetry updates on wave computations. Particularly, the seabed morphology is updated over a morphological time step (Δt_{mor}) and for every bed level update, simulations by three numerical tools are performed: FUNWAVE-TVD model, followed by a sediment transport model and a bathymetry updating module. This process is repeated until a preset duration, coinciding with the simulation end time is reached. The relevant flow chart outlining the model interaction and feedback is illustrated in Figure 1. The implementation of a morphological acceleration factor (Morfac) serves to multiply bed level changes by a nonunity integer quantity and therefore alters the morphology time scale. In this research, three different time scales and steps were utilized in order to simulate nearshore processes of a different nature, the time step (Δt) of the wave model (FUNWAVE-TVD), the time interval of wave action which is necessary to obtain the time averaged (mean) velocities that are referred here as currents (Δt_{cur}) and the morphological time step (Δt_{mor}) which is required to calculate bathymetry updates.

2.1. Hydrodynamics

Wave propagation and hydrodynamic circulation can be simulated by FUNWAVE-TVD model from deep to shallow water, including the surf and swash zone. The governing equations of the above model were based on the fully nonlinear Boussinesq equations (Nwogu et al., 1992), modified by Chen et al. (2003) and Chen (2006) and extended to incorporate a moving reference level (Kennedy et al., 2001). FUNWAVE-TVD is a nonlinear wave model that operates with a hybrid finite-volume and finite-difference TVD-type scheme developed by Shi et al. (2012). The shock-capturing wave-breaking scheme, chosen for this study, was based on the work of Tonelli and Petti (2009). This method takes advantage of the shock-capturing ability of non-linear shallow water equations (NSWE) and can simulate the moving hydraulic jumps. Following the Courant-Friedrichs-Lewy (CFL) criterion, an adaptive time step was implemented, based on a third-order Runge-Kutta scheme for nonlinear spatial discretization. The model includes wetting-drying moving boundary conditions with the incorporation of Harten-Lax-van Leer (HLL) construction method into the scheme. The sponge layer technique introduced by Larsen and Dancy (1983) is used by FUNWAVE-TVD model to deal with internal wave reflection problems. The governing equations of the wave model are presented below:

$$\eta_t + \nabla \cdot \boldsymbol{M} = 0, \tag{1}$$

$$\boldsymbol{u}_{a,t} + (\boldsymbol{u}_a \cdot \nabla)u_a + g\nabla\eta + \boldsymbol{V}_1 + \boldsymbol{V}_2 + \boldsymbol{V}_3 + \boldsymbol{R} + \boldsymbol{R}^b + \boldsymbol{R}^s = 0. \tag{2}$$

Equation (1) represents the depth-integrated mass conservation, while Equation (2) denotes the depth-averaged horizontal momentum. The symbol $\boldsymbol{M}$ of Equation (1) is the horizontal flux and can be further expressed as:

$$\boldsymbol{M} = (h+\eta)\left[\boldsymbol{u}_a + \mu^2\left\{\left(\frac{{z_a}^2}{2} - \frac{1}{6}\left(h^2 - \eta h + \eta^2\right)\right)\nabla(\nabla\cdot\boldsymbol{u}_a)\right) + \right.$$
$$\left. + \left(z_a + \frac{1}{2}(h-\eta)\right)\nabla(\nabla\cdot(h\boldsymbol{u}_a))\right\}\Bigg], \tag{3}$$

where η is the sea-surface elevation, h is the water depth, $\boldsymbol{u}_a$ the horizontal velocity at the adaptive reference elevation, z_a and μ denotes a dimensionless measure of dispersion. In addition, $\boldsymbol{V}_1$ and $\boldsymbol{V}_2$ are the dispersive Boussinesq terms, $\boldsymbol{V}_3$ accounts for the second-order effect of vertical vorticity, $\boldsymbol{R}$ represents the quadratic form of the bottom friction modeled by $C_d\boldsymbol{u}_a|\boldsymbol{u}_a|$, where C_d is the bottom friction coefficient. The term $\boldsymbol{R}^b$ in Equation (2) can be used optionally, to model the eddy-viscosity-type breaking terms

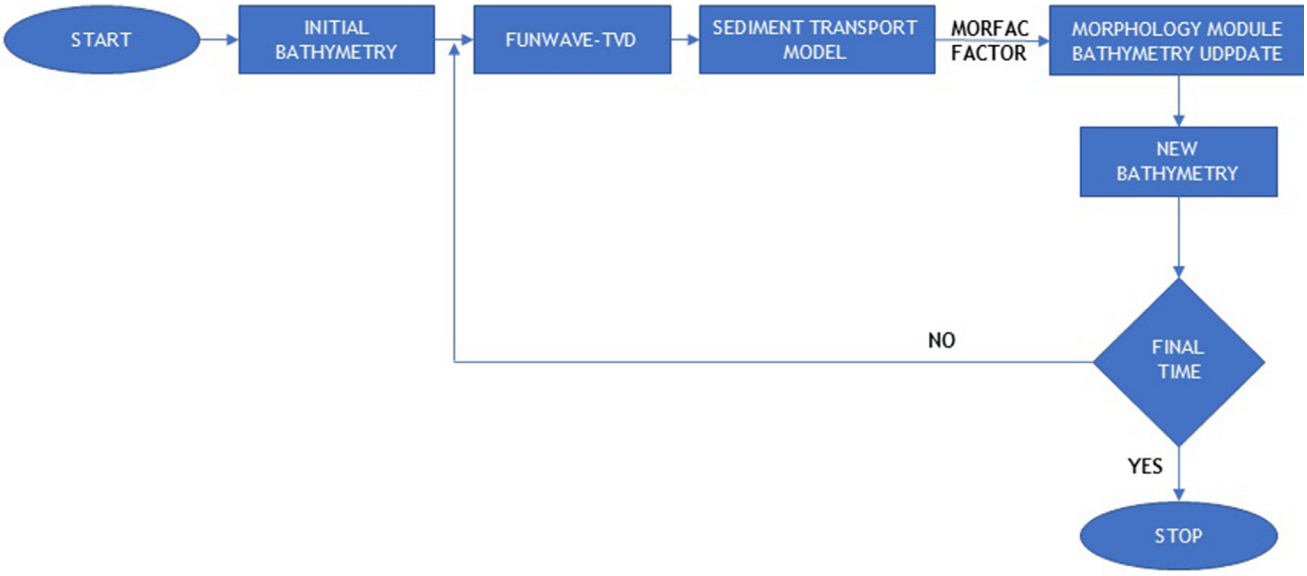

Figure 1 Flow chart of wave-current, sediment transport and morphology models.

(in this study the shock-capturing scheme of Tonelli and Petti (2009) was activated), while the term $\boldsymbol{R}^s$ accounts for the subgrid turbulent mixing (Chen et al., 2003). A Smagorinsky-type (1963) subgrid turbulent mixing algorithm is employed and the eddy viscosity associated with the subgrid mixing is determined by breaking-induced current field (Chen et al., 1999).

FUNWAVE-TVD model can simulate wave-generated nearshore currents, such as rip current or alongshore currents, and eddies due to shear instabilities, estimated via the $\boldsymbol{R}$, $\boldsymbol{R}^b$, $\boldsymbol{R}^s$ dissipative and diffusive terms. In recent studies, Boussinesq models have been utilized to model rip currents (Geiman et al., 2011; Johnson and Pattiaratchi, 2006) and alongshore currents (Chen et al., 2003; Feddersen et al., 2011) in the nearshore zone. Geiman et al. (2011) presented a numerical study on wave averaging effects on estimates of the surf zone mixing. Their study revealed that FUNWAVE-TVD model is able to reproduce 1-h time-averaged mean Eulerian velocities consistent with field measurements and numerical findings.

2.2. Morphodynamics

In the present study, a new numerical model developed by the authors of this paper was applied to assess nearshore morphodynamics. The mode of suspended sediment movement is investigated using Van Rijn's (1993) formula, while a formula for unsteady oscillatory flows, suggested by Ribberink (1998) for the estimation of bed load transport, was implemented. The usage of Van Rijn's approximation serves to distinguish suspended load transport that is computed above a reference height α and bed-load transport, which was estimated using the near-bottom hydrodynamic parameters. It is also suited to assess sediment transport rates in combined breaking or non-breaking wave and current conditions. In the following subsections, the governing equations will be presented. Moreover, it has to be mentioned that the Boussinesq-type 2DH model provided depth-averaged hydrodynamic parameters, that were exploited to extract near-bed flow characteristics and nonlinear time-varying near-bottom wave velocities using the parameterization suggested by Karambas and Samaras (2017), initially proposed by Isobe and Horikawa (1982) and modified by Grasmeijer (2002). This technique is based on the energy flux method, in which the fifth-order Stokes and the third-order cnoidal wave theories were implemented appropriately, according to the applicable range. Two parameters were utilized by Isobe and Horikawa (1982) to represent the asymmetry of the velocity profile, based on laboratory and field experimental results. Thus, wave properties such as the wave profile and water particle velocities can be extracted at an arbitrary depth, based on the offshore wave height and period, local water depth and bed slope without explicitly quantifying skewness. Grasmeijer (2002) modified this approximation to calculate time-varying near-bed orbital velocities using local wave characteristics.

2.2.1. Suspended load transport

Van Rijn (1993) suggested a multi-layer model, describing the time-averaged sediment concentration profile. This profile can be obtained by the integration of the time-averaged convection-diffusion under equilibrium (stationary) conditions. The three-dimensional convection-diffusion (mass-balance) equation for the suspended sediment can be written, as follows:

$$\frac{\partial(c)}{\partial t}+\frac{\partial(uc)}{\partial x}+\frac{\partial(vc)}{\partial y}+\frac{\partial[(w-w_s)c]}{\partial z}-\frac{\partial}{\partial x}\left[\varepsilon_{s,x}\frac{\partial(c)}{\partial x}\right]-\frac{\partial}{\partial y}\left[\varepsilon_{s,y}\frac{\partial(c)}{\partial y}\right]-\frac{\partial}{\partial z}\left[\varepsilon_{s,z}\frac{\partial(c)}{\partial z}\right]=0, \quad (4)$$

in which (u,v,w) = local flow velocities, $(\varepsilon_{s,x}, \varepsilon_{s,y}, \varepsilon_{s,z})$ = local turbulent sediment mixing, w_s = particle fall velocity, and c = sediment concentration.

Integration of Equation (4) with respect to z leads to:

$$\frac{\partial(c_{ave})h}{\partial t}+\frac{\partial(Uc_{ave})h}{\partial x}+\frac{\partial(Vc_{ave})h}{\partial y}-\frac{\partial}{\partial x}\left[\varepsilon_{s,x}h\frac{\partial(c_{ave})}{\partial x}\right]-\frac{\partial}{\partial y}\left[\varepsilon_{s,y}h\frac{\partial(c_{ave})}{\partial y}\right]=S, \quad (5)$$

where c_{ave} is the depth-averaged concentration and (U, V, W) the depth-averaged velocities, and S represents the source term of the convection-diffusion equation that is based on the mismatch between a current and an equilibrium concentration (Galappatti and Vreugdenhil, 1985; Galappatti, 1983). In order to estimate the equilibrium concentration, we need to prescribe the boundary conditions of the problem. Considering that the concentration presents variability in a time-scale much larger than the representative wave period stationary conditions in the surface and in the bed boundary are assumed. Thus, the longitudinal diffusion terms can be neglected in relation to the vertical diffusion term, whilst the unsteady concentration term $(\partial(c_{ave})/\partial t)$ is relatively small with respect to the other terms. Moreover, at the water surface, the vertical diffusive flux through the free surface is equal to zero:

$$-w_s c - \varepsilon_{s,cw}\frac{dc}{dz} = 0, \text{ at } z = \eta. \tag{6}$$

At bed-boundary surface, the vertical mixing or the exchange of sediment fluxes, according to Galappati (1983), can be described as:

$$-w_s c - \varepsilon_{s,cw}\frac{dc}{dz} = D - E, \text{ at } z = z_b, \tag{7}$$

where D is the sediment deposition rate and E being the sediment erosion rate.

The sediment erosion rate was evaluated explicitly, while the deposition rate was included in the transport equation implicitly (Lesser et al., 2004), as follows:

$$\text{Erosion rate}: c_\alpha \frac{\varepsilon_s}{\Delta z}, \text{ Deposition rate}: c_k\left(\frac{\varepsilon_s}{\Delta z} + w_s\right), \tag{10}$$

in which, c_α = sediment concentration at the reference level α, ε_s = sediment vertical diffusion coefficient, Δz = vertical distance from the reference level α to the center of reference cell, and c_k = sediment concentration in the reference cell. The vertical distribution coefficient due to currents can be calculated using a parabolic approximation as proposed by Van Rijn (1993).

Erosion and deposition rates are responsible for the vertical readjustment of the concentration distribution and they were used, herein, in order to estimate sediment source and sink terms throughout the vertical. It should be noted that source and sink terms are not normally time-invariant over depth. However, in this study, we consider the existence of an equilibrium concentration profile, which is adjusted to current conditions within a specific time interval. The adjustment of the depth-averaged concentration to its equilibrium value, for specific time and space scales, was described by Katopodi and Ribberink (1992).

For oscillatory flows, the concentration at the reference level α is expressed as:

$$c_a = 0.015\rho_s \frac{D_{50}}{\alpha}\frac{\left(\frac{\theta-\theta_{cr}}{\theta_{cr}}\right)^{1.5}}{D_*^{0.3}}, \tag{8}$$

where ρ_s = sediment density, α = reference level, D_{50} = median particle diameter of bed material, θ = Shields parameter, θ_{cr} = critical Shields parameter, D_* = non-dimensional particle diameter. The reference level (α) herein, was considered equal to $0.5*\Delta_r$ (wave-induced ripple height), while its maximum value cannot be greater than the 20% of the water column.

The vertical distribution coefficient due to the total wave and current mixing was calculated following Lesser et al. (2004) and Van Rijn (1993). This method provides detailed information of distribution coefficient variations over the water depth and leads to similar turbulent mixing values to those generated by the standard algebraic turbulence (Lesser et al., 2004).

Thus, the vertical distribution coefficient due to currents can be calculated as:

$$\varepsilon_{s,c} = k\beta u_{*,c} z\left(1 - \frac{z}{h}\right) \text{for } z < 0.5h,$$
$$\varepsilon_{s,c} = 0.25k\beta u_{*,c} z(1 - z/h) \text{ for } z \geq 0.5h, \tag{9}$$

where, $\varepsilon_{s,c}$ = vertical diffusion coefficient due to currents, k = von Kármán constant (0.4), $u_{*,c}$ = current related bed shear velocity, β van Rijn's factor (used to describe the difference between fluid and granular diffusion).

The vertical distribution coefficient due to waves is calculated as:

$$\varepsilon_{s,w} = \varepsilon_{s,bed} = 0.004 D_* \delta_s U_{\delta w}, \text{ for } z \leq \delta_s,$$
$$\varepsilon_{s,w} = \varepsilon_{s,max} = 0.035 h H_s / T_P, \text{ for } z \geq 0.5h,$$
$$\varepsilon_{s,w} = \varepsilon_{s,bed} + (\varepsilon_{s,max} - \varepsilon_{s,bed})\left(\frac{z - \delta_s}{0.5h - \delta_s}\right), \text{ for } \delta_s < z < 0.5h, \tag{10}$$

where $\varepsilon_{s,w}$ = vertical distribution coefficient due to waves, δ_s = thickness of the near-bed sediment mixing layer, which was equal to three times the ripple height ($\delta_s = 3 * \Delta_r$), $U_{\delta w}$ = near-bottom wave velocity, D_* = non-dimensional particle diameter. The total vertical diffusion coefficient can be expressed as:

$$\varepsilon_{s,Tot} = \sqrt{{\varepsilon_{s,w}}^2 + {\varepsilon_{s,c}}^2}. \tag{11}$$

Ultimately, after integration of the convection diffusion equation over the time the net suspended sediment fluxes can be expresses as follows:

$$\boldsymbol{q_s} = \left(\overline{c_{ave} h U_c - \varepsilon_{s,x} h \frac{\partial c_{ave}}{\partial x}}, \overline{c_{ave} h V_c - \varepsilon_{s,y} h \frac{\partial c_{ave}}{\partial y}}\right), \tag{12}$$

where, U_c and V_c mean over the depth current velocities.

2.2.2. Bed-load transport

Following the approach suggested by Ribberink (1998), bed-load sediment transport can be calculated using a formula for unsteady oscillatory flows where the instantaneous solid flux is assumed to be proportional to a function of the difference between the actual time-dependent bed shear stress and the critical bed shear stress (Figure 4). Therefore, the nonlinear effects of wave asymmetry on bedload transport rates can be satisfactory predicted using the proposed approach. Ribberink's (1998) formulation has been calibrated towards several flume data sets including wave-current interaction in a plane regime (suspended load negligible) and field data (unidirectional flows in rivers). In total, more than 75 bed-load transport measurements in oscillating water tunnels were utilized to corroborate the validity of this approach (Ribberink, 1998). The solid fluxes can be calculated, as follows:

$$\boldsymbol{q_{SB}} = m_{Rib}\sqrt{(s-1)gd^3}\langle\left(\left|\overrightarrow{\theta(t)}\right| - \theta_{cr}\right)^{n_{Rib}}\frac{\overrightarrow{\theta(t)}}{|\theta(t)|}\rangle, \tag{13}$$

where, $\overrightarrow{\theta(t)} = 0.5 f_{cw}|u(t)|\overrightarrow{u(t)}/[(s-1)gd]$ is the time-dependent Shields parameter with the instantaneous velocity $\overrightarrow{u(t)} = \overrightarrow{U_c} + \overrightarrow{u_w(t)}$, s is the relative density of sediment and f_{cw} the wave-current friction factor. $\langle\ \rangle$: Time-averaged over wave period, and $m_{Rib} = 11$, $n_{Rib} = 1.65$: adjusted coefficients.

2.2.3. Swash zone

The swash zone is the area of the coastal environment where the waves run up and down, dissipating or reflecting their energy after moving towards the shore. The sediment fluxes are often large close to the shoreline because of swash uprush and backwash phases. Sediment transport generated from bed evolution at a swash time scale can be several orders of magnitude larger than those derived from the most of available sediment transport formulas, applied in the surf zone. Thus, numerical models often underestimate this sediment migration and tend to yield sediment transport that decreases too rapidly from the swash zone towards the offshore (Klonaris, 2016; Masselink et al., 2009; Nam et al., 2009). For the estimation of longshore and cross-shore sediment transport in the swash zone, the approximation proposed by Larson and Wamsley (2007) has been used. The net transport rates can be expressed as follows:

$$q_{tc,net} = K_c \frac{\tan\varphi_m}{\tan^2\varphi_m - \left(\frac{dh}{dx}\right)^2} \frac{u_0^3}{g}\left(\frac{dh}{dx} - \tan\beta_e\right)\frac{t_0}{T}, \tag{14}$$

$$q_{tl,net} = K_l \frac{\tan\varphi_m}{\tan^2\varphi_m - \left(\frac{dh}{dx}\right)^2} \frac{u_0^2 v_0}{g}\frac{t_0}{T}, \tag{15}$$

where K_c, K_l are cross-shore and long-shore empirical coefficients, respectively, φ_m is the internal friction angle ($\approx 30°$). v_0, u_0 and t_0 are scaling velocities and time, T is the swash duration (considered equal to the incidence wave period), $\tan\beta_e$ is the foreshore equilibrium slope. The calculation of scale velocities was based on the ballistic theory, while the wave front velocities at the still-water shoreline obtained by FUNWAVE-TVD model were used as initial conditions, for more details see Larson et al. (2004). Equation (15) implies that the cross-shore sediment transport rate is zero if foreshore slope is in equilibrium, while longshore transport still occurs if the transporting velocity v_0 is not zero during the uprush and backwash phase. In order to define the foreshore equilibrium, slope the methodology suggested by Larson and Wamsley (2007) and Larson et al. (2004) was applied herein. Thus, the equilibrium slope can be expressed as:

$$\tan\beta_e = \frac{I_U - I_B}{I_U + I_B}\tan\varphi_m, \tag{16}$$

where

$$I_U = \frac{1}{T}\int_{t_s}^{t_m} (|\theta(t)|)^{3/2}\mathrm{d}t,$$

$$I_B = \frac{1}{T}\int_{t_m}^{t_e} (|\theta(t)|)^{3/2}\mathrm{d}t, \tag{17}$$

in which T is the wave period, t_s and t_e the start and end time of the swash oscillation, and t_m the moment at which uprush changes to backwash.

Klonaris et al. (2018) proved that the application of the latter quasi-empirical formulation is especially efficient in predicting swash morphodynamics, in conjunction with a phase resolving Boussinesq-type model, ensuring the continuity of sediment fluxes throughout the surf and swash zones and providing a smooth transition between them. The main advantage of this approximation is that the computed sediment transport rates do not decrease too rapidly from the swash to offshore zones, guaranteeing the stability of the solution throughout the entire coastal zone.

The investigation of sediment dynamics in this zone is of high interest for engineering applications. Swash dynamics determine the shoreline position, thus the precise evaluation of the natural processes in this zone contributes to the performance evaluation of coastal defense structures in terms of their capacity to maintain or advance the shoreline seaward. Hence, it is considered that combining a highly nonlinear Boussinesq wave model with a sophisticated representation of wetting-drying conditions, along with a quasi-3D sediment transport formula incorporating sediment fluxes in the swash zone is crucial in obtaining accurate bed level predictions in the presence of coastal engineering structures, therefore improving engineering design.

2.3. Morphology

Total sediment transport rates are computed as the sum of the bed and suspended loads in the intermediate depths and surf zone. In the swash zone, the sediment rates, estimated using Larson and Wamsley's (2007) approximation, are also added to the total sum of sediment fluxes in cross-shore and alongshore direction. The variables of FUNWAVE-TVD model have been used to estimate these rates following the time scale of hydrodynamic circulation. However, morphological changes vary at a different and slower rate compared to the short-term variations of hydrodynamics. Thus, the estimation of bathymetry update requires maintaining a budget of the sediment fluxes that have been derived by averaging the instantaneous flow parameters. Thus, these sediment transport fluxes were integrated over a number of time steps, which correspond to several wave periods. The bathymetry update was calculated by solving the sediment mass conservation equation which reads:

$$\frac{\partial z_b}{\partial t} = -\frac{\mathrm{Morfac}}{1-n_p}\nabla\cdot\boldsymbol{q}_{tot}, \tag{18}$$

where n_p is the sediment porosity, $\boldsymbol{q}_{tot} = (q_{tot,x}, q_{tot,y})$ denotes the total volumetric sediment transport rate equal to the sum of suspended and bed-load transport rate, z_b is the local bottom elevation and Morfac is a morphological acceleration factor (Lesser, 2004). This nonunity factor (Morfac) applies a scalar multiplier to the sediment continuity equation and speeds up the depth change rates, multiplying them by a constant value. In this study, Morfac values (ranging from 1 to 30) were systematically adapted to be compared with a baseline condition of no acceleration. Care must be taken not to exaggerate with extreme Morfac values, in order to describe realistically the interaction of the wave, hydrodynamic and morphology modules.

The effect of the bed slope on sediment transport has been included following Watanabe (1988). Following Leont'yev (1996) and Karambas et al. (2002) the sediment mass conservation equation can be obtained from

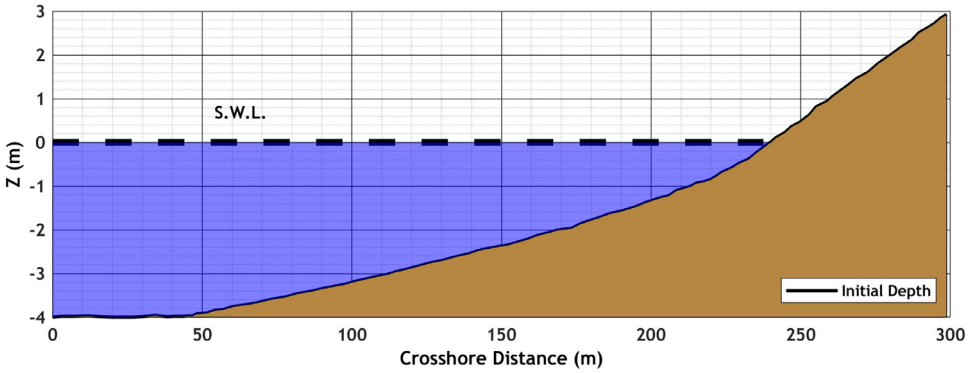

Figure 2 Initial beach profile setup in the Dette et al. (2002) experiments.

Equation (18) as follows:

$$\frac{\partial z_b}{\partial t} = -\frac{\partial}{\partial x}\left(q_{tot,x} - \varepsilon|q_{tot,x}|\frac{\partial z}{\partial x}\right) - \frac{\partial}{\partial y}\left(q_{tot,y} - \varepsilon|q_{tot,y}|\frac{\partial z}{\partial y}\right), \quad (19)$$

in which, ε is an empirical coefficient that varies within the range of 2.0 to 5.0. The second term in each of the parentheses in the right part of Equation (19) describes the diffusion term, as well as additional gravitational term reflects the effect of local bed slope on sediment transport.

3. Model validation

For the validation of the presented composite model, four different test cases were evaluated, both in 1DH and 2DH configurations. Our results were compared to experimental and numerical findings involving hydrodynamic, sediment transport loads and short and medium-term bathymetry changes. Taking advantage of FUNWAVE-TVD model's capacity to employ rapidly varying terrains and steep slopes in the surf zone, this study provides significant insights into the sediment transport dynamics in a variety of coastal engineering applications. Sediment transport and morphology evolution were analyzed for the case of large-scale wave flumes using the experimental findings of Alsina et al. (2012) and Dette et al. (2002). These test cases were also utilized for the calibration of several empirical factors and formulas, as the required computational cost for the performed simulations was significantly lower than that of the 2DH cases. Our numerical model was applied afterwards, in the case of the physical experiments of Badiei et al. (1995), concerning the effect of a groyne on the shore morphology. Ultimately, the effect of shore parallel emerged and submerged breakwaters on the hydrodynamics and morphology was evaluated. For this purpose, our numerical results were quantitatively compared to the empirical models from previous related studies (Bos et al., 1997; Cáceres et al., 2005; Deltares/Delft Hydraulics, 1997). Thus, the efficiency of the proposed coupled model was tested under real field dimensions and for a total duration of 50 days, providing significant conclusions about the time scale of the achieved morphological equilibrium.

Table 1 Summary of the retrieved experimental wave and bathymetry data from the study of Dette et al. (2002).

H_s (m)	1.20
T_p (s)	5.5
Water depth at wavemaker (m)	5.0
D_{50} (mm)	0.30
Total duration (h)	23
Bed slope	Varying

3.1. 1DH Surf and swash zone morphological processes in cross-shore direction

3.1.1. Large Wave Flume experiment

The first set of comparisons refers to the experimental campaign carried out at the Grosser Wellenkanal in Hannover within the context of the EU SAFE project. The results of this work were presented in the study of Dette et al. (2002). The main objective of that study was to investigate the effectiveness of beach nourishment as a soft protection technique to combat coastline erosion. The experiments were performed in a wave flume 324 m long, while the width and the depth of the flume were 5 m and 7 m, respectively. Figure 2 depicts a layout of the flume bathymetry. Herein, the test B2 of the experimental campaign was reproduced in order to evaluate the results of our numerical coupled model. Irregular waves were applied ($H_s = 1.20$ m and $T_p = 5.5$ s) using a TMA spectrum internal wavemaker (Wei and Kirby, 1999), for a total duration of 23 hours. The initial bathymetry was characterized by a horizontal bed of 5 m depth followed by the theoretical Bruun equilibrium profile (Bruun, 1954; Dean, 1977) below the water level. The sea bottom was represented by well-sorted sand with a median sediment size of $D_{50} = 0.30$ mm. A summary of the retrieved experimental wave and bathymetry data that were used as input for the numerical simulation is given in Table 1.

The bathymetry data were discretized on an equispaced grid with a spatial step of $\Delta\chi = 0.5$ m and a fixed bottom friction coefficient was utilized and set equal to $C_d = 0.008$, as it was found that it leads to the best agreement with the experimental data. The minimum water depth used to represent wetting-drying conditions was set equal to 0.01 m.

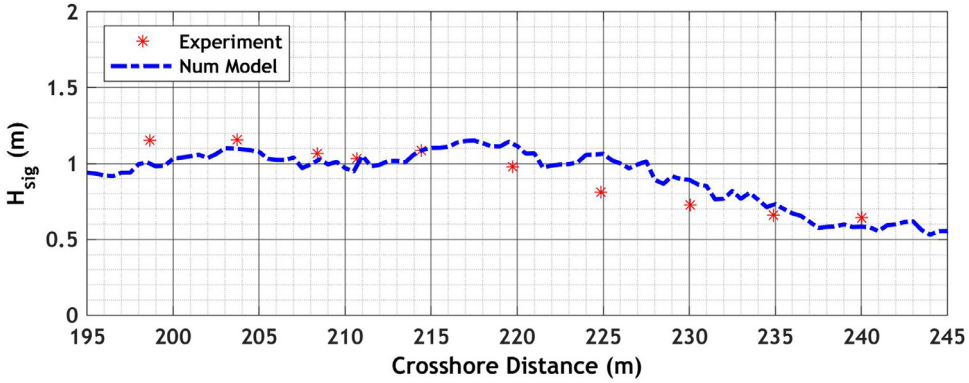

Figure 3 Computed and measured significant wave height after 19 h 45 min. of wave action for the test case B2 in Dette et al. (2002).

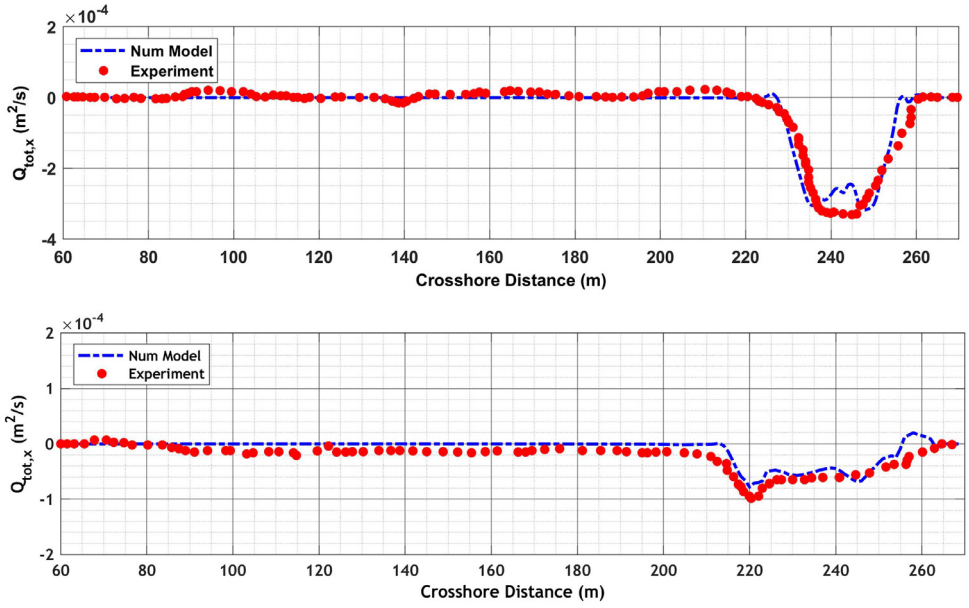

Figure 4 Computed and measured total sediment transport rate after 1.5 h (up) and after 19 h 45 min. (down) for the test case B2 in Dette et al. (2002).

The selected Courant number in the time-stepping scheme of the FUNWAVE-TVD model was relatively low (CFL = 0.3) to achieve numerical stability. A low morphological factor was utilized (Morfac = 2) to ensure the stability of the numerical simulation and calibrate the sediment transport model. The empirical coefficient ε of Equation (19) was set equal to 5, in order to represent the effect of the bed slope on seabed morphology. The applied settling velocity w_s was equal to 0.0267 m/s, with sand porosity $n_{p=}$ 0.4.

Figure 3 shows the distribution of significant wave height along the flume profile and the comparison between the computed and measured data for the test B2 of Dette et al. (2002). Computed and measured values of sediment transport rates and seabed geometry are depicted in Figures 4 and 5, respectively. The wave height distribution was accurately computed using FUNWAVE-TVD model taking advantage of its high order nonlinearity. Moreover, the sediment transport model reproduced adequately the peaks of the sediment load distribution along the cross-shore profile. The bar formation is well predicted, although the model overestimates the shoreline erosion in the swash zone.

3.1.2. SANDS experiment

This test case refers to the Hydralab III SANDS project (Scaling and Analysis and New instrumentation for Dynamic bed testS). The experiment was carried out in the Canal de Investigacion y Experimentacion Maritima (CIEM) at the Universidad Politecnica de Cataluña (UPC), Barcelona. The dimensions of the large-scale wave flume were: 100m long, 3m wide and 4.5 m deep. Figure 6 shows a snapshot of the initial bathymetry in the laboratory flume. The experimental findings were presented in the study of Alsina et al. (2012). The main purpose of this physical experiment was to investigate the link between swash zone dynamics and surf zone morphodynamics and how dissipative beaches with mild-sloping beach face tend to decrease the rate of sand bar migration towards the sea, while more reflective swash conditions intensify sediment transport erosive rates.

During the experiment, moderately energetic random waves were applied (H_s = 0.53 m and T_p = 4.14 s) and the same wave conditions were repeated for a series of 47 tests. Each test was comprised of 500 waves with a to-

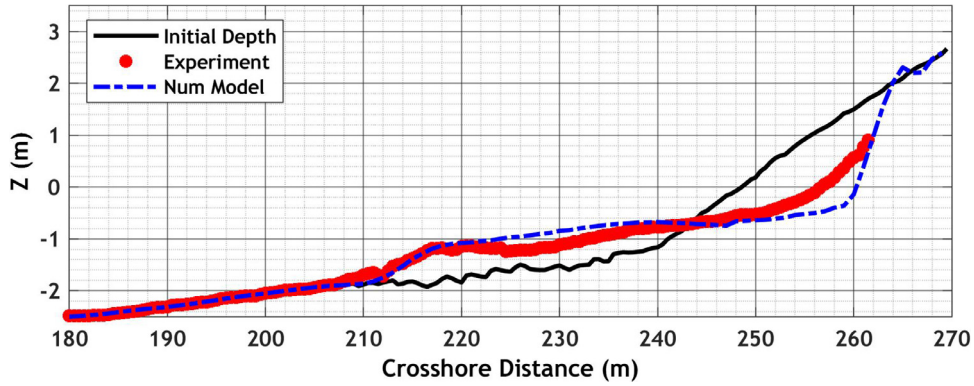

Figure 5 Computed and measured bottom elevation after 19 h 45 min. of wave action for the test case B2 in Dette et al. (2002).

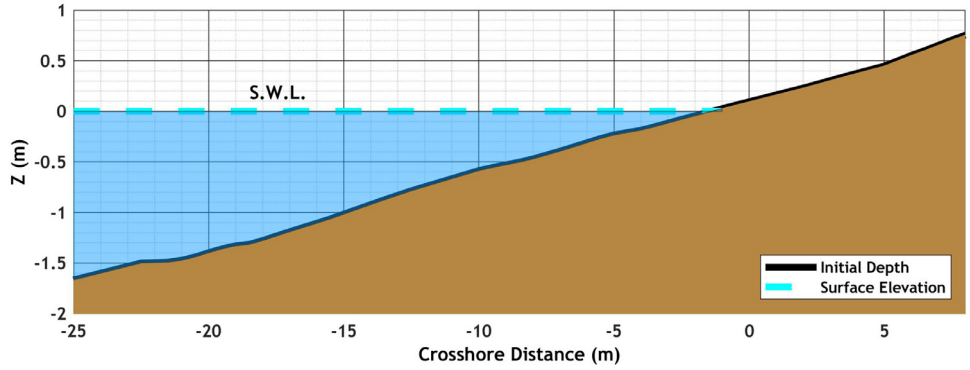

Figure 6 Initial beach profile used for SANDS experiment (Alsina et al. 2012).

Table 2 Summary of the retrieved experimental wave and bathymetry data from the study of Alsina et al. (2012).

H_s (m)	0.53
T_p (s)	4.14
Total duration (h)	21.15
Water depth at wavemaker (m)	2.47
D_{50} (mm)	0.25
Bed slope	1:10

tal duration equal to 27 min. The random wave time series corresponded to a JONSWAP spectrum with a peak factor of $\gamma = 3.3$. The initial bathymetry was characterized by a constant sloping beach with a gradient of 1:10. The sea bottom was represented by well-sorted sand with a median sediment size $D_{50} = 0.25$ mm. A summary of the retrieved experimental wave and bathymetry data that were used as input for the numerical simulation is given in Table 2.

In order to reproduce the experimental procedure numerically, the bathymetric data were interpolated on a fine grid with a spatial step of $\Delta x = 0.2$ m. The initial bathymetry consisted of a horizontal bottom of 2.47 m depth followed by a uniform slope of 1:10. A fixed bottom friction coefficient (C_d) was utilized and set at 0.009 and the minimum water depth for wetting-drying conditions was considered equal to 0.01 m. Once again, the Courant number used in the time-stepping scheme of the FUNWAVE-TVD model was relatively low ($CFL = 0.3$) in order to achieve numerical stability. No morphological acceleration factor (Morfac = 1) was employed, as the total simulation time was relatively low (Duration= 21.15h). Similar wave conditions to that of the experiment were generated ($H_s = 0.53$ m and $T_p = 4.14$ s) by an irregular wavemaker in a water depth of 2.47 m, producing a JONSWAP spectrum. The empirical coefficient ε of Equation (19) was set equal to 5. in order to consider the impact of the bed slope on seabed morphology. The applied settling velocity w_s was equal to 0.0267 m/s, with sand porosity $n_p = 0.4$.

The initial computed and measured cross-shore distribution of significant wave height after 21.15 hours of wave action are both depicted in Figure 7. The initial beach profile, as well as the computed and measured final beach profiles at 21.15 hours, are also shown in Figure 7. The present test case corresponds to erosive conditions close to the swash zone due to the initial reflective beach profile that, in turn, force significant sediment quantities into deeper water. FUNWAVE-TVD model estimated accurately the cross-shore wave height distribution due to its higher order of nonlinearity. However, it should be noted that some discrepancies between measurements and numerical results appear in the area where water depth is less than 0.5 m. A breaking event takes place just after $x = -20$ m leading to the formation of the inner bar.

The numerical outputs of the sediment transport model are in good agreement with experimental results, as an accurate prediction of the sandbar formation was achieved. Overall, the evolution of the bed shape over time follows

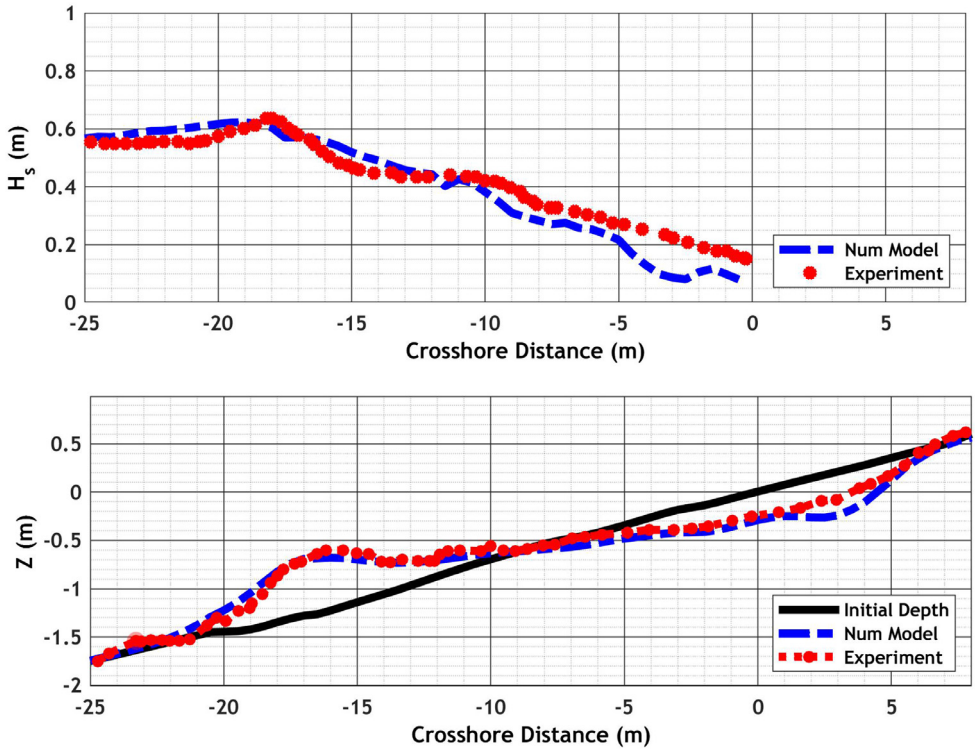

Figure 7 Computed and measured cross-shore distribution of significant wave height after 21.15 hours (top panel). Computed and measured final beach profile after 21.15 hours (bottom panel).

the same sequence as that of the experiment, since a seaward sandbar migration was observed. However, a bed-change over-estimation of $\pm$ 0.10 cm can be detected in the swash and surf zone.

3.2. 2DH numerical simulations for the effect of a single groyne structure on the shore

The impact of a groyne structure, which acts as an artificial obstacle to the longshore sediment transport and affects the subsequent shoreline evolution, was numerically investigated in our study and compared with the experimental findings of Badiei et al. (1995). Single groynes are referred to as the structures that are usually placed normal to the shoreline and block the littoral drift partially or completely (Kristensen et al., 2016). Groynes are employed to produce sediment cells in which the shore can turn against the locally predominant wave direction. These structures can also be situated close to a river mouth to aid the canalization of the flow into the sea (Valsamidis et al., 2017), or as terminal structures (jetties) which limit the amount of sediment, deposited in the harbor basin. An accretive or erosive trend is expected to occur in the vicinity of a groyne due to the presence of a source or sink, respectively. Moreover, in coastal management, a system of multiple groynes is typically used to advance the shore seaward and trap large amounts of sediments by blocking alongshore sediment fluxes. Thorough research of groyne system functionality was conducted by French (2001).

The physical model presented by Badiei et al. (1995) concerns nearshore sediment transport dynamics and morphological effects of groynes on a mobile bed with an initial straight beach, which was exposed to obliquely incident irregular waves at an angle of 11.6 degrees (with respect to the shore-normal). The test NT2 of the experimental study was reproduced numerically in the scope of the present work. The median particle diameter of bed material (D_{50}) was 0.12 mm and the initial cross-shore constant beach slope was 1:10.

The integrated coupled model was applied to reproduce the hydrodynamic and morphodynamic conditions of the experiment. The spatial domain has been discretized with a spatial step of $\Delta x = 0.2$ m and $\Delta y = 0.5$ m in cross-shore and alongshore direction, respectively. Irregular waves (characterized by a JONSWAP spectrum at the wave-maker), were generated with $H_s = 0.8$ m and $T_p = 1.15$ s, whilst the angle between the normal to the coast and the main direction of wave propagation was set at 11.6°. For the absorption of the wave energy propagating out of the model area, a sponge layer of about 5 m was applied at the offshore boundary of FUNWAVE-TVD model and periodic lateral boundary conditions were employed. In Figure 8, the initial bathymetry with a constant slope of 10:100 is illustrated. The wave-maker was placed at X = 7 m and in the deepwater region a flat bottom of 2 m was considered. The total duration of the simulation was 12 hours, equal to that of the experiment and a morphological acceleration factor in the order of 5 was employed. The applied settling velocity w_s was equal to 0.0084 m/s, with sand porosity $n_p = 0.39$.

Figure 9 depicts the wave-induced current field after 1 hour of wave action. The groyne structure alters the longshore currents' direction in its vicinity, as decreased velocities can be seen in the lee side of the structure.

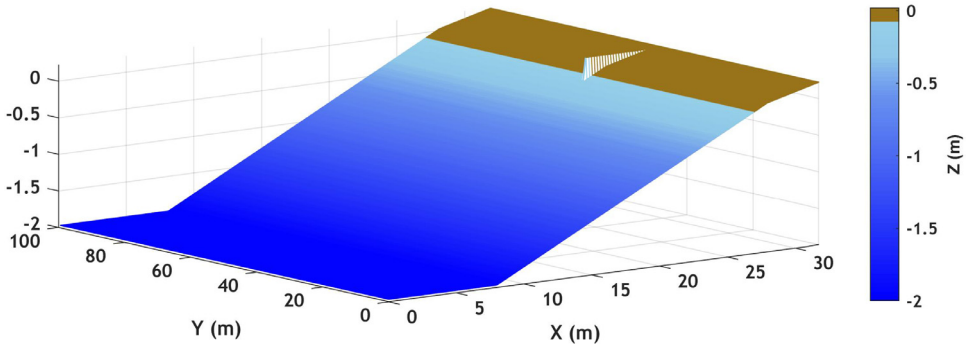

Figure 8 3D view of model's initial bathymetry.

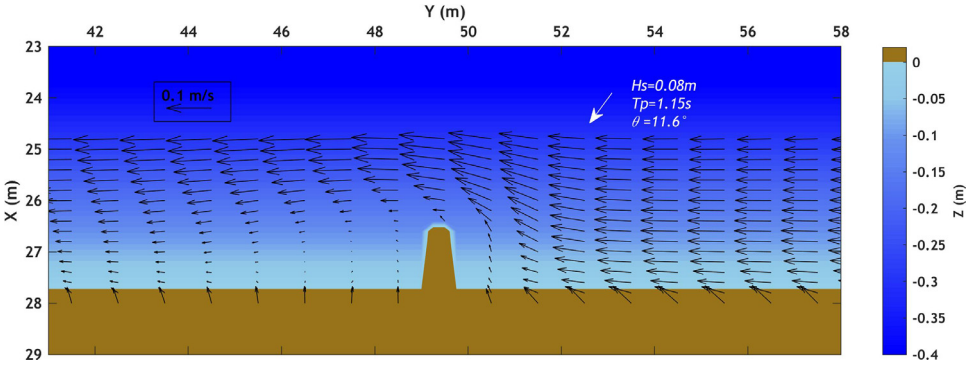

Figure 9 Simulated hydrodynamic circulation after 1 hour of wave action for a groyne field subject to waves with a 11.6° angle of incidence. Color map corresponds to the initial bathymetry.

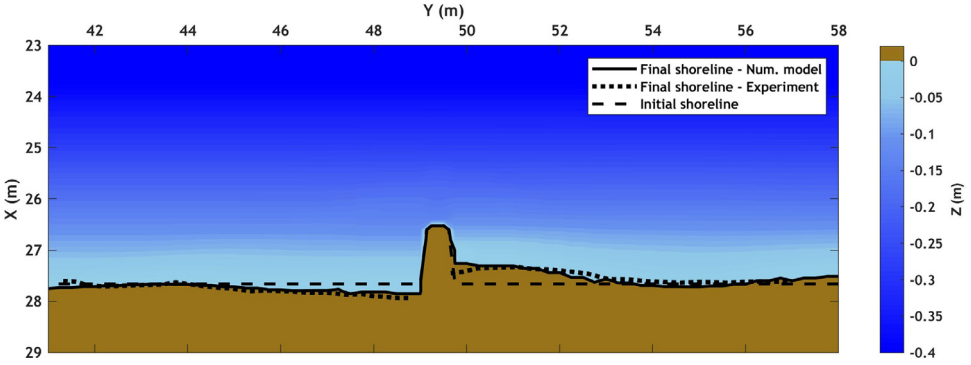

Figure 10 Simulated bathymetry for a groyne field subject to waves with a 11.6° angle of incidence depicting the measured (dotted line) and computed (solid line) final shoreline position. Color map indicates the final bathymetry.

The nearshore currents reach a maximum velocity of about 0.1 m/s. Moreover, offshore-oriented velocities are observed in the swash zone, reflected from the beach face, with a maximum velocity of 0.06 m/s. The direction and order of magnitude of computed currents are in line with the numerical findings of the study of Karambas and Samaras (2017), in which the present experimental test case was also reproduced. However, reflection phenomena in the vicinity of groyne are less intense in our study, due to the application of inner sponge layers that represent flow friction and energy dissipation within the structure.

Figure 10 shows the final bottom evolution after 12 hours of wave action. The sediment accretion updrift of the structure contributes to an advance of the shoreline seaward, whilst the lack of sediments at the lee side of the structure results in a shoreline retreat. Overall, the numerical findings are in very good agreement with the experimental results, as is evident in Figure 10. The computed final shoreline position is almost identical to that of the experiment, with some small discrepancies encountered close to the lateral boundaries.

3.3. 2DH numerical simulations for the effect of a detached breakwater on the shore

3.3.1. Single emerged breakwater

To provide significant protection against erosion phenomena in the littoral environment, layout optimization of a breakwater is necessary. Previous studies have revealed that breakwater geometry affects hydrodynamic processes and evolution of bottom topography, resulting in a plan form

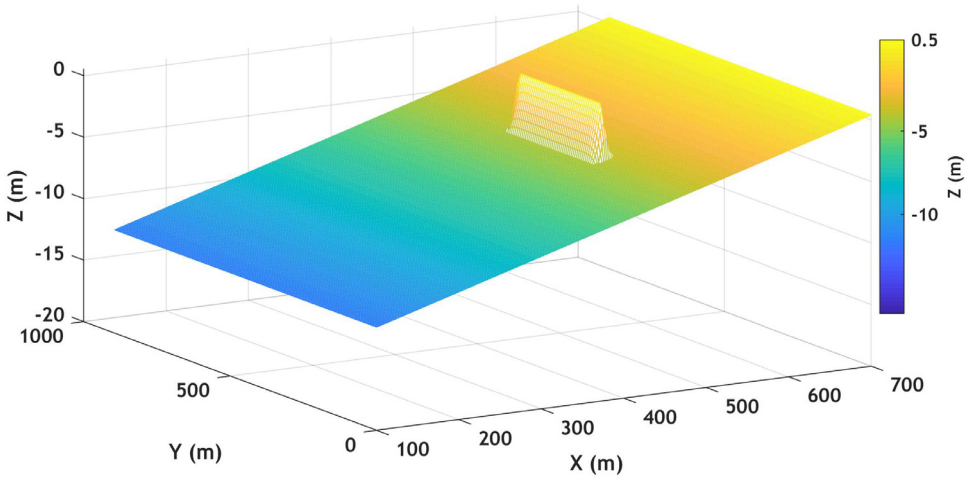

Figure 11 3D illustration of the initial bathymetry (breakwater at 200 m from shore).

development (formation of tombolo or salient) in the lee of the breakwater (Bos et al., 1997; Cáceras et al., 2005; Deltares/Delft Hydraulics, 1997; Zyserman et al., 2002). The type of beach plan form strongly depends on the dimensions and location of the structure. In the case of emerged detached breakwaters, the beach can extend and come in contact with the structure (formation of tombolo). Permanent tombolo is expected for L/D $>$ 1 and salient for L/D $<$ 1 according to Van Rijn (2011) with L being the breakwater length, and D being the offshore distance to the original shoreline. However, the morphological evolution in the lee of breakwaters is a complex physical process that cannot be analyzed in terms of only two parameters (L, D). The beach response relies on several environmental factors, such as three-dimensional bathymetry characteristics, prevailing hydrodynamic conditions and sediment supply. Additionally, geometric properties of the structure, including freeboard, structure slopes, crest width, length of the gap between segments of the breakwater system, and breakwater porosity are known to be influential in beach morphology (Afentoulis et al., 2019).

Deltares/Delft Hydraulics (1997) and Bos et al. (1997) carried out a study about the effect of a detached emerged breakwater on coastal hydro-morphodynamics, using numerical modeling approaches. Herein, this work is used as a benchmark test for the validation of our numerical model in field conditions. This application is of high interest, as the model's behavior may vary from laboratory to field dimensions. It has been revealed that the achievement of moveable bed equilibrium is slower in the field than in the laboratory's controlled conditions, where the use of lightweight sediment can introduce additional scale effects (Gorrick and Rodríguez, 2014). Hence, the present test case corresponds to a total duration of 50 days, which is deemed a sufficient period to explore the model's capacity to capture fluid-seabed interactions over a relatively larger time scale.

The examined test case consisted of 300 m long breakwater with a crest height of $+0.5$ m, located on an initially along-shore uniform sloping bottom, with a slope of 1:50 and placed at 200 m offshore the shore. In order to reproduce this test case numerically, the bathymetric data were interpolated over a rectangular grid with a spatial step of $\Delta x = 2$ m and $\Delta y = 5$ m in cross-shore and alongshore direction, respectively. Irregular waves were generated with $H_{rms} = 2.0$ m and $T_p = 8.0$ s. Fine sand was considered with median sediment size $D_{50} = 0.25$ mm. The applied settling velocity w_s was equal to 0.0267 m/s, with sand porosity $n_p = 0.41$ and the selected Courant number in the time-stepping scheme of the FUNWAVE-TVD model was CFL $=$ 0.45. A sponge layer 100 m wide was applied at the offshore side to absorb the reflected waves from the breakwater. The dissipation of wave energy at the breakwater location was achieved using large bottom friction locally (a high drag coefficient of $C_d = 10$ was considered) and periodic lateral boundary conditions were applied. A morphological acceleration factor (Morfac $=$ 30) was employed to reduce the relatively high computational cost. The morphological acceleration option was activated after 7 days of wave action when quasi-steady flow conditions prevailed. In Figure 11 the initial bathymetry along with the breakwater configuration is illustrated.

Figure 12 shows a snapshot of the computed instantaneous free surface elevation. The nearshore processes that can be identified in this Figure are the wave shoaling, diffraction into the sheltered area as well as run-up and run-down. The wave breaking over the breakwater can be observed at X $=$ 400 m. Subsequently, Figure 13 depicts the mean sea level during the 1st hour of wave action. Wave set-up of about 0.08m can be observed in the lee part of the breakwater and in the illuminated area due to the wave-induced flux nearshore.

The initial wave-induced current field after 1 hour of wave action, superimposed with bathymetry contours, is depicted in Figure 14. A formation of two eddies can be observed in the lee of the breakwater. The generation of eddies is due to the current circulation towards the sheltered area, parallel to the shoreline and across both sides. This formation is generated due to the gradient of the mean sea level between the illuminated area and the sheltered area, which leads to diffraction effects with a consequent forcing of currents towards the down-wave of the structure (Karambas, 2012). Additionally, weak rip currents with a velocity of about 0.2 m/s can be identified between the

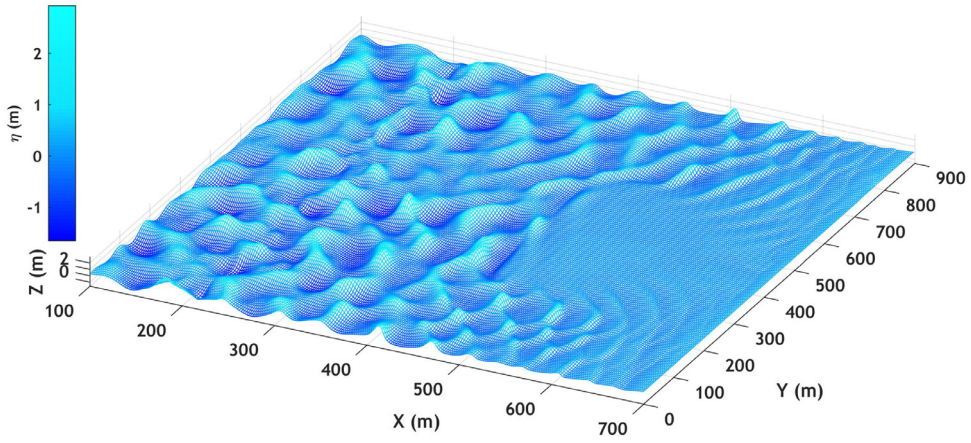

Figure 12 Snapshot of the instantaneous computed free surface elevation.

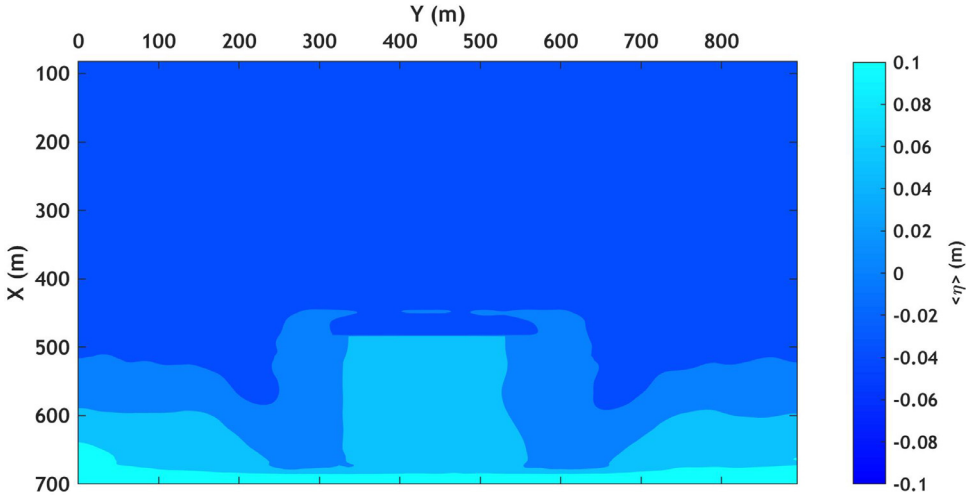

Figure 13 Mean surface elevation during the 1st hour of wave action.

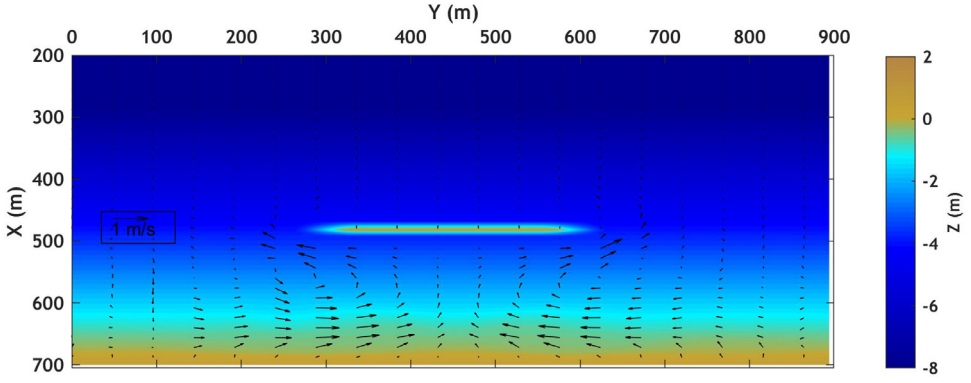

Figure 14 Simulated hydrodynamics after 1 hour of wave action. Colors: initial Bathymetry, vectors: calculated wave induced current intensity and direction.

lateral boundaries of the model and the structure, while offshore-oriented velocities are detected close to the shore, reflected from the beachface with a maximum velocity of 0.75 m/s.

Figure 15 shows the wave-induced current field after 1 day of wave action, superimposed with seabed changes during this time. The seabed evolution is more intense in the zones where significant spatial velocity gradients occur. The developed plan form results in a shortening in the shore-normal direction of the two eddies, which are shifted towards the two gaps, with a slight decrease of the relevant velocities compared to the initial current field. Close to the shore, the seaward oriented currents resulted in the altering of the uniformity of the beach in the alongshore direc-

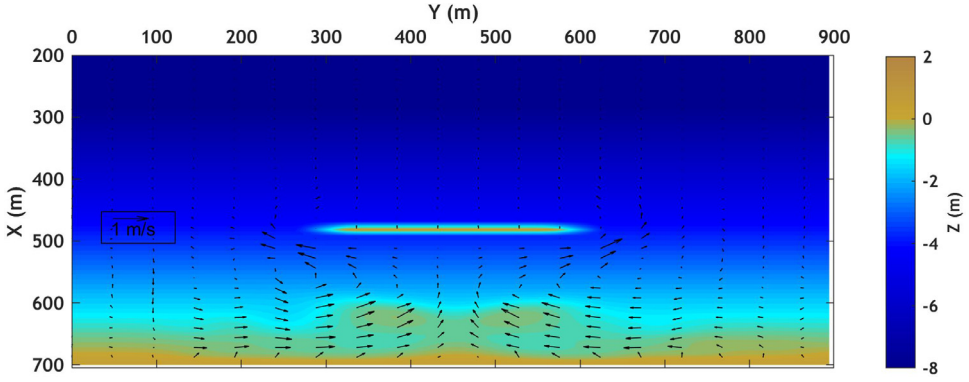

Figure 15 Simulated morphodynamics after 1 day of wave action. Colors: sea bed elevation, vectors: calculated mean wave induced current intensity and direction.

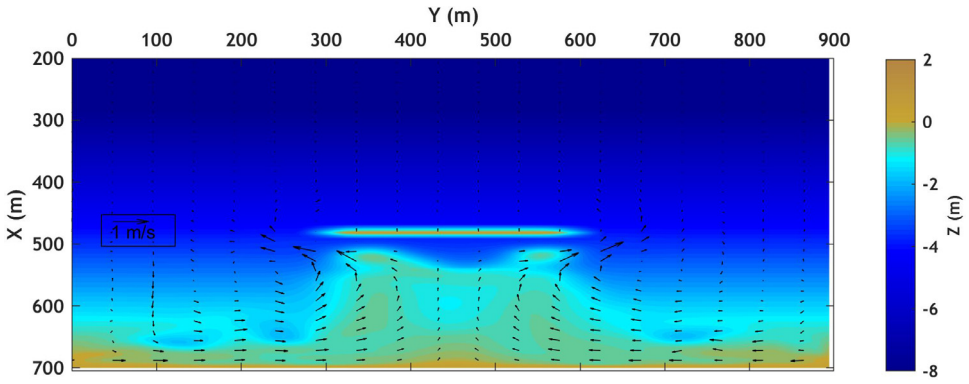

Figure 16 Simulated morphodynamics after 10 days of wave action. Colors: sea bed elevation, vectors: calculated mean wave induced current intensity and direction.

tion, with associated erosion conditions. Figure 16 shows the seabed elevation after 10 days of wave action and the associated wave-induced currents. Behind the structure, the shoreline extends out and a tombolo starts to be formed. It should be mentioned that the initial geometry with a cross-shore constant slope is not realistic, thus the wave-current-seabed system tends to find equilibrium by altering the beach slopes near the shoreline. Therefore, dissipative conditions are observed in the foreshore beach morphology after 10 days and the computed erosion of the beach face at both sides is about 1m. This three-dimensional beach form forces alongshore nearshore currents with a magnitude of 0.3 m/s. In addition, strong rip currents with a magnitude of about 0.9 m/s are detected in the vicinity of the breakwater.

The bathymetry obtained after 50 days of wave action is illustrated in Figure 17. It can be observed that no significant differences in sea bottom geometry take place between 10 and 50 days. It is concluded that the rate of bottom level change was high initially and slowed down as equilibrium approached. Close to the equilibrium stage, relatively weak velocities of about 0.3 m/s characterize the wave-induced current field. During this phase, the waves break out of the shadow zone due to the presence of the tombolo, resulting in a less energetic current field in the protected area. Consequently, since the current velocities are relatively weak, the sediment fluxes are insignificant and there is no noticeable change of the seabed geometry.

The agreement between the obtained results and the corresponding retrieved data of the study of Deltares/Delft Hydraulics (1997) seems quite satisfactory, concerning the accretion close to the center-line of the wave tank and the observed erosion of the beach face at both sides. Overall, a formation of tombolo was achieved for $L/D > 1$, which is in line with the available field data used in the study of Deltares/Delft Hydraulics (1997). Furthermore, the outcome of our numerical investigation is consistent with the computed bottom evolution and hydrodynamics revealed in the study of Razak et al. (2018), concerning a similar test case. Razak et al. (2018) used XBeach model to assess beach response in the lee part of breakwater under the same wave conditions as that used in our study. Once again, a single tombolo was formed after 50 days of wave action whilst the computed currents followed flow patterns (discrete vortices) close to our estimates.

3.3.2. Single submerged breakwater

The proposed coupled model was utilized to investigate the hydrodynamic and morphodynamic patterns as well as the beach morphology in the vicinity of a submerged offshore breakwater. These structures lead in wave energy reduction through depth-induced wave breaking and the shoreline response to submerged breakwater is gov-

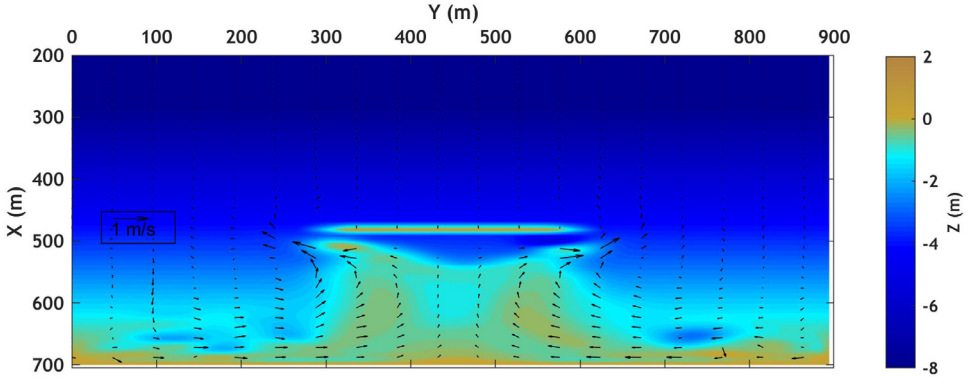

Figure 17 Simulated morphodynamics after 50 days of wave action. Colors: sea bed elevation, vectors: calculated mean wave induced current intensity and direction.

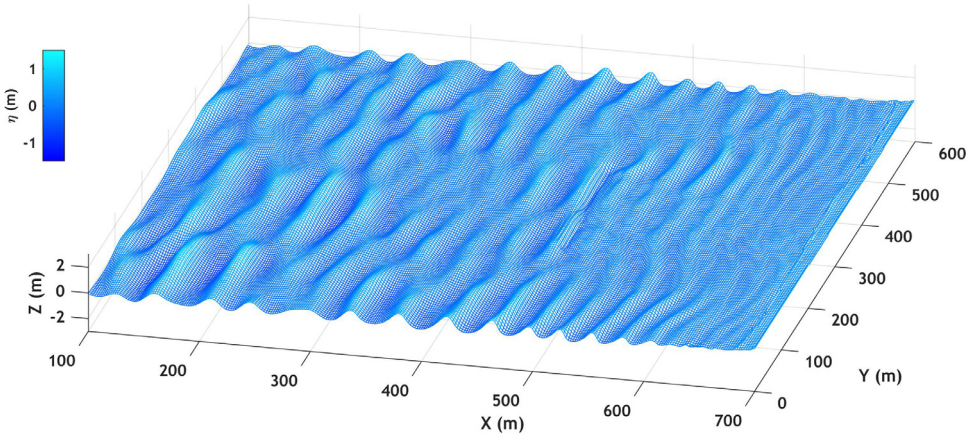

Figure 18 Snapshot of the instantaneous computed free surface elevation.

erned by hydrodynamic processes such as wave setup, wave set-down, onshore mass flux, and nearshore currents (Ranasinghe et al., 2010). The effect of structure freeboard is also dominant in shaping hydrodynamic patterns shoreward of the breakwaters. When a submerged breakwater is located close to the beach, strong erosion behind the structure appears and high turbulence levels occur due to wave breaking associated with high sediment suspension, which can be driven outwards the sheltered area by diverging fluxes (Tsiaras et al., 2020). Thus, potential erosion could occur in the case of short structure distances relative to the shore. Cáceres et al. (2005) used numerical modeling approaches, based on a phase averaged wave driver, to investigate the bed evolution behind low-crested structures. The effect of structure freeboard and significant wave height were thoroughly analyzed.

In order to evaluate the effect of submerged structures on beach morphology, the study of Cáceres et al. (2005) was utilized as a benchmark case. A smooth cross-shore slope, around 2:100, characterized the seabed and the bathymetric data were interpolated over a rectangular grid with a spatial step of $\Delta\chi = 2$ m and $\Delta y = 4$ m in cross-shore and alongshore direction, respectively. Irregular waves were generated with $H_{rms} = 1.0$ m and $T_p = 4.0$ s with a shore-normal direction. The breakwater crest height was set at -0.5 m (freeboard $= 0.5$ m) and the structure was placed in a distance of 230 m to the shore. The bottom evolution was computed for a duration of 200 hours and a morphological acceleration factor (Morfac $= 15$) was employed to reduce the computational cost. No sponge layers were employed in the location of the structure to simulate the depth-induced wave breaking and discharge flux over the submerged breakwater. Fine sand was considered with median sediment size $D_{50} = 0.25$ mm. The applied settling velocity w_s was equal to 0.0267 m/s, with sand porosity $n_p = 0.41$ and the selected Courant number in the time-stepping scheme of the FUNWAVE-TVD model was CFL $= 0.45$.

In Figure 18, a snapshot of the free surface elevation is illustrated. It can be observed that some wave breaking is initiated on the breakwater crest at X $= 470$ m while a portion of incident wave energy is reflected from the front breakwater face. The transmission of waves from the downstream side of the breakwaters is highly nonlinear, where free and bound transmitted waves travel into the shore (Christou et al., 2008). Nearshore phenomena such as wave shoaling, diffraction, run-up and run-down can also be identified in Figure 18. In contrast to emerged structures, submerged breakwater leads to wave transmission and overtopping. These processes can be reproduced more accurately through the highly nonlinear phase-resolving wave driver proposed in this study in contrast to the phase-averaged one utilized in Cáceres et al. (2005). Thus, the net mass transport that occurs above the structure increases wave-setup in the lee zone, which in turn forces outward rip currents around the heads of the structures and through the gaps.

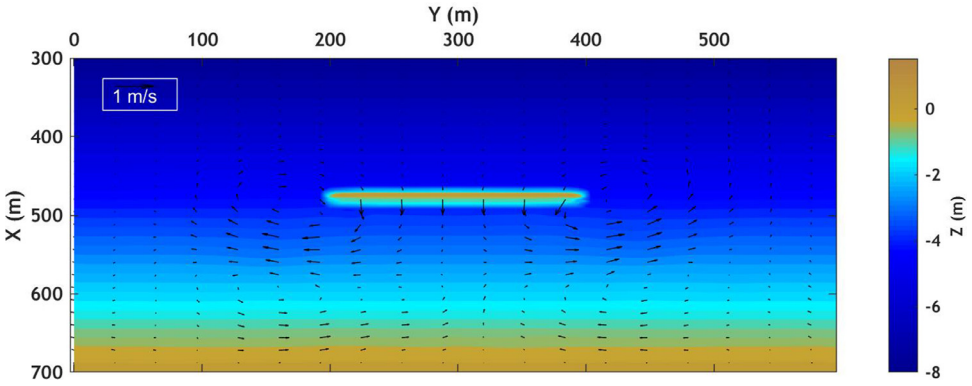

Figure 19 Simulated hydrodynamics after 1 hour of wave action. Colors: initial bathymetry, vectors: calculated wave induced current intensity and direction.

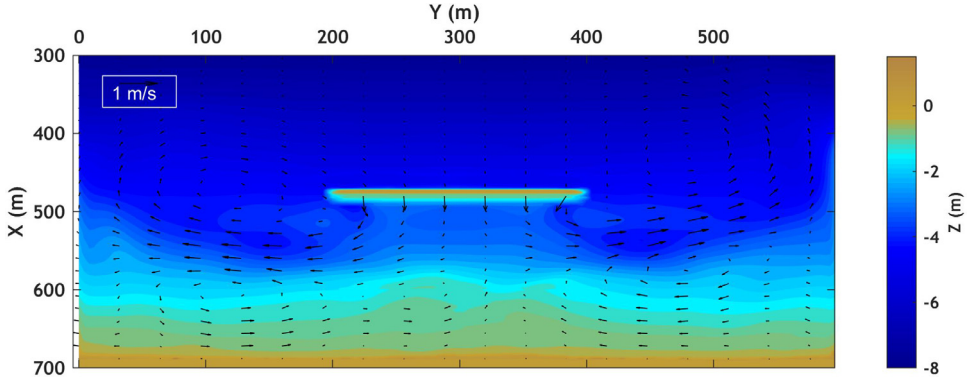

Figure 20 Simulated hydrodynamics after 200 hours of wave action. Colors: final bathymetry, vectors: calculated wave induced current intensity and direction.

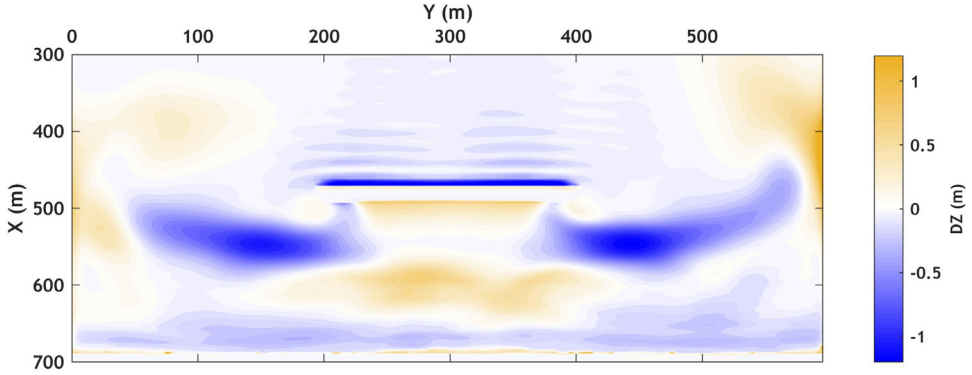

Figure 21 Simulated seabed changes after 200 hours of wave action. Colors: Seabed level changes (Dz).

Figure 19 presents seabed geometry and the wave-induced current field after one hour of wave action. Two symmetric eddies can be identified associated with strong currents of about 0.8 m/s. This is in line with the other studies, which have revealed that the dominant source of vorticity, in the case of submerged breakwaters, is located around the edges of the structure (Bouvier et al., 2019). In contrast to the case of the emerged breakwater, the nearshore vortex is hindered, and the order magnitude of nearshore velocities is relatively low, of about 0.3 m/s. This is due to the fact that the overtopping flux extends in a limited area around the structure and governs the circulation, suppressing the nearshore currents.

The computed bathymetry and the associated wave-induced current field after 200 hours of wave action are presented in Figure 20. The model results are in good agreement with the findings of Cáceres et al. (2005), as the integrated model succeeded in reproducing all morphological and hydrodynamic patterns behind the breakwater and up to the shore. Once again two symmetric eddies can be identified outside of the sheltered area, while strong diverging erosive currents, with a velocity of 0.8 m/s, prevail through the gaps. The overall bottom evolution reveals erosion close to the structure, while the shoreline is accreting, and the formation of salient can be observed. Figure 21 illustrates computed bottom elevation changes after 200 hours of wave

action. The predicted bed-level accretion in the sheltered area is about 1 m, whilst intense erosion of 1.2 m can be identified in the zone where erosive diverging currents appear. Furthermore, slight bed level erosion of 0.3 m can be observed close to the swash zone.

4. Conclusions

In the present paper, a newly developed sediment transport model was introduced and coupled to a highly nonlinear Boussinesq wave model in order to assess the combined effect of waves and currents and ultimately the bed level evolution of coastal areas. Special attention was given to the swash zone dynamics which are considered dominant in shaping the morphological bed level changes, as well as to the unsteady wave effects on the bed load sediment transport rates. The combination of the sophisticated Boussinesq model along with a quasi-3D sediment transport model incorporating swash zone dynamics is considered to be extremely valuable in obtaining accurate bed level predictions in complex coastal areas. Of particular interest was the investigation of the interaction between hydrodynamics, seabed and coastal structures, with the obtained results having strong implications on the improvement of the structures' design and performance in protecting the shoreline.

The model was validated against the experimental data of Alsina et al. (2012) and Dette et al. (2002) in order to assess seabed morphology in the inner and swash zone. The prediction of erosion or accretion close to the shoreline is crucial for engineering applications and can affect the solution throughout the whole computational domain. The effect of swash zone dynamics was embedded, and the good agreement between model results and laboratory measurements enhance the robustness of our numerical approach. For the evaluation of the morphological influence of groyne structures, the physical experiment of Badiei et al. (1995) was reproduced. The numerical model results are in very good agreement with the experimental findings in the context of an accurate prediction of the measured bed evolution and shoreline position. Moreover, the performance of the composite model was evaluated in terms of its capacity to estimate the effects of detached emerged and submerged breakwaters on morphological features under real field conditions. The computational results were quantitatively compared to those of other studies (Cáceres et al., 2005; Deltares/Delft Hydraulics, 1997) and a good agreement was achieved. The formation of tombolo/salient was reproduced accurately and was found to be in agreement with the limits defined in the literature.

Regarding the several parameters/coefficients that utilized in this research, special attention should be given to the choice of the empirical coefficient of Equation (19), where values up to 3 should be employed for intermediate beaches and up to 5 for reflective beach profiles, in order to represent avalanching phenomena associated with steep slopes. This element was proven particularly important in order to guarantee the stability of the numerical simulations and the accuracy of the final solution, in combination with a properly selected time step of the continuity equation (Exner), which was set equal or slightly higher than the corresponding one, used in hydrodynamic simulations. Furthermore, the application of periodic boundary conditions allowed us to obtain a realistic wave-induced current field and minimize boundary effects in 2DH simulations. In addition, the acceleration techniques utilized in this research were significantly effective to reduce the computational burden, although a sensitivity analysis that was carried out herein, revealed that the values of the nonunity factor (Morfac) greater than 30 affects unrealistically the hydrodynamic solution. In the absence of clearly defined limits in the literature, Morfac values were adopted with particular caution in this work by performing trial and error simulations of a few hours, to define the upper allowable values of Morfac. This analysis served to consider non-linear morphological responses to wave forcing, and obtain a good compromise between simulation speed and accurate results.

In this study, swash and nearshore morphodynamics were investigated over dissipative and reflective beaches, as well as in transition profiles between the two states, where the formation of wave-breaking induced sandbars under the shoreface was accurately predicted, especially in the case of 1DH applications that allow us to assess small-scale physical processes. Although, further investigations are needed to model sand ripple morphology using finer grids and accretive wave sequences during the transition from reflective to dissipative beach states, knowing that the simulation of nearshore accretion phenomena is generally a more demanding task that requires the implementation of groundwater processes. Moreover, in order to extend the limitation of the present numerical approach, the role of aeolian sediment transport has to be considered in case of dune erosion and further benchmark test cases need to be evaluated, including estuary dynamics and gravel beaches.

Considering all the above, it is believed that the presented integrated model can be a valuable asset for engineers and scientists desiring to obtain accurate bed level evolution predictions in complex bathymetries with the presence of a variety of coastal protection structures, both in experimental and in field cases thus improving their design and configuration.

Declaration of competing interest

The authors declare that they have no known competing financial interests or personal relationships that could have appeared to influence the work reported in this paper.

References

Afentoulis, V., Eleftheria, K., Eleni, S., Evangelos, M., Archontia, L., Christos, M., Vasiliki, T., 2017. Coastal Processes Assessment Under Extreme Storm Events Using Numerical Modelling Approaches. Environ. Process. 4 (3), 731—747. https://doi.org/10.1007/s40710-017-0253-8

Afentoulis, V., Chini, N., Bardey, P., Raffourt, C., 2019. Sea bed evolution in the vicinity of longitudinal submerged discontinuous breakwaters — Acripelagos. International Scientific Conference on Design and Management of Harbor, Coastal and Offshore Works Athens, Greece.

Alsina, J.M., Cáceres, I., Brocchini, M., Baldock, T.E., 2012. An experimental study on sediment transport and bed evolution under different swash zone morphological conditions. Coast. Eng. 68, 31—43. https://doi.org/10.1016/j.coastaleng.2012.04.008

Badiei, P., Kamphuis, J.W., Hamilton, D.G., 1995. Physical experiments on the effects of groins on shore morphology. In: Proceedings of the Coastal Engineering Conference. https://doi.org/10.1061/9780784400890.129

Benoit, M., Marcos, F., Becq, F., 1997. Development of a third generation shallow-water wave model with unstructured spatial meshing. In: Proceedings of the Coastal Engineering Conference, 465—478. https://doi.org/10.1061/9780784402429.037

Birben, A.R., Özölçer, I.H., Karasu, S., Kömürcü, M.I., 2007. Investigation of the effects of offshore breakwater parameters on sediment accumulation. Ocean Eng. 34 (2), 284—302. https://doi.org/10.1016/j.oceaneng.2005.12.006

Bos, K.J., Roelvink, J.A., Dingemans, M.W., 1997. Modelling the impact of detached breakwaters on the coast. In: Proceedings of the Coastal Engineering Conference. https://doi.org/10.1061/9780784402429.157

Bouvier, C., Castelle, B., Balouin, Y., 2019. Modeling the impact of the implementation of a submerged structure on surf zone sandbar dynamics. J. Mar. Sci. Eng. 117 (4). https://doi.org/10.3390/jmse7040117

Bruun, P., 1954. Coast Erosion and the Development of Beach Profiles, US Army Corps of Engineers, 44. US Beach Erosion Board.

Cáceres, I., Sánchez-Arcilla, A., Zanuttigh, B., Lamberti, A., Franco, L., 2005. Wave overtopping and induced currents at emergent low crested structures. Coast. Eng. 52 (10—11), 931—947. https://doi.org/10.1016/j.coastaleng.2005.09.004

Cáceres, I., Stive, M.J.F., Sánchez-Arcilla, A., Trung, L.H., 2008. Quantification of changes in current intensities induced by wave overtopping around low-crested structures. Coast. Eng. 55 (2), 113—124. https://doi.org/10.1016/j.coastaleng.2007.09.003

Charlier, R.H., de Meyer, C.P., 1989. Coastal defense and beach renovation. Ocean and Shoreline Management 12 (5—6), 525—543. https://doi.org/10.1016/0951-8312(89)90029-5

Chen, Q., 2006. Fully Nonlinear Boussinesq-Type Equations for Waves and Currents over Porous Beds. J. Eng. Mech. 132 (2), 220—230. https://doi.org/10.1061/(asce)0733-9399(2006)132:2(220)

Chen, Q., Dalrymple, R.A., Kirby, J.T., Kennedy, A.B., Haller, M.C., 1999. Boussinesq modeling of a rip current system. J. Geophys. Res. Oceans 104 (C9), 20617—20637. https://doi.org/10.1029/1999jc900154

Chen, Q., Kirby, J.T., Dalrymple, R.A., Shi, F., Thornton, E.B., 2003. Boussinesq modeling of longshore currents. J. Geophys. Res. Oceans 108 (C11). https://doi.org/10.1029/2002jc001308

Christou, M., Swan, C., Gudmestad, O.T., 2008. The interaction of surface water waves with submerged breakwaters. Coast. Eng. 55 (12), 945—958. https://doi.org/10.1016/j.coastaleng.2008.02.014

Dean, R., G., 1977. Equilibrium beach profiles: US Atlantic and Gulf coasts. Department of Civil Engineering and College of Marine Studies., University of Delaware.

Deltares Delft Hydraulics, 1997. Two-dimensional and one-dimensional model simulations for the effect of a single detached breakwater on the shore. Deltares (WL), Delft, Netherlands.

Dette, H.H., Larson, M., Murphy, J., Newe, J., Peters, K., Reniers, A., Steetzel, H., 2002. Application of prototype flume tests for beach nourishment assessment. Coast. Eng. 47 (2), 137—177. https://doi.org/10.1016/S0378-3839(02)00124-2

Divinsky, B.V., Kosyan, R.D., 2020. Influence of the climatic variations in the wind waves parameters on the alongshore sediment transport. Oceanologia 62 (2), 190—199. https://doi.org/10.1016/j.oceano.2019.11.002

Divinsky, B.V., Ryabchuk, D.V., Kosyan, R.D., Sergeev, A.Y., 2021. Development of the sandy coast: Hydrodynamic and morphodynamic conditions (on the example of the Eastern Gulf of Finland). Oceanologia 63 (2), 214—226. https://doi.org/10.1016/j.oceano.2020.12.002

Ding, Y., Wang, S.S.Y., 2008. Development and Application of a Coastal and Estuarine Morphological Process Modeling System. J. Coastal Res. 10052, 127—140. https://doi.org/10.2112/1551-5036-52.sp1.127

Do, J.D., Jin, J.Y., Hyun, S.K., Jeong, W.M., Chang, Y.S., 2020. Numerical investigation of the effect of wave diffraction on beach erosion/accretion at the Gangneung Harbor. Korea. J. Hydro-Environ. Res. 29, 31—44. https://doi.org/10.1016/j.jher.2019.11.003

Feddersen, F., Clark, D.B., Guza, R.T., 2011. Modeling surf zone tracer plumes: 1. Waves, mean currents, and low-frequency eddies. J. Geophys. Res. Oceans, 116(C11). https://doi.org/10.1029/2011JC007210

French, P., 2001. Coastal Defences Processes, Problems and Solution. Taylor & Francis Group. https://doi.org/10.4324/9780203187630

Galappatti, G., Vreugdenhil, C.B., 1985. A depth-integrated model for suspended sediment transport. J. Hydraulic Res. 23. https://doi.org/10.1080/00221688509499345

Galappatti, R., 1983. A depth integrated model for suspended transport. Communications on Hydrology - Delft University of Technology, Department of Civil Engineering Report, 83—7.

Gallerano, F., Cannata, G., Lasaponara, F., 2016. A new numerical model for simulations of wave transformation, breaking and long-shore currents in complex coastal regions. Int. J. Numer. Methods Fluids. 80 (10), 571—613. https://doi.org/10.1002/fld.4164

Geiman, J.D., Kirby, J.T., Reniers, A.J.H.M., MacMahan, J.H., 2011. Effects of wave averaging on estimates of fluid mixing in the surf zone. J. Geophys. Res. Oceans 116 (C4). https://doi.org/10.1029/2010JC006678

Gorrick, S., Rodríguez, J.F., 2014. Scaling of sediment dynamics in a laboratory model of a sand-bed stream. J. Hydro-Environ 8 (2), 77—87. https://doi.org/10.1016/j.jher.2013.12.001.

Grasmeijer, B., 2002. Process-Based Cross-Shore Modeling of Barred Beaches Ph.D. Thesis. Utrecht University, Utrecht, The Netherlands.

Hieu, P.D., Phan, V.N., Nguyen, V.T., Nguyen, T.V., Tanaka, H., 2020. Numerical study of nearshore hydrodynamics and morphology changes behind offshore breakwaters under actions of waves using a sediment transport model coupled with the SWASH model. Coast. Eng. J. 62 (4), 553—565. https://doi.org/10.1080/21664250.2020.1828016

Holthuijsen, L.H., Herman, A., Booij, N., 2003. Phase-decoupled refraction-diffraction for spectral wave models. Coast. Eng. 49 (4), 291—305. https://doi.org/10.1016/S0378-3839(03)00065-6

Isobe, M., Horikawa, K., 1982. Study on water particle velocities of shoaling and breaking waves. Coast. Eng. 25 (1), 109—123. https://doi.org/10.1080/05785634.1982.11924340

Johnson, D., Pattiaratchi, C., 2006. Boussinesq modelling of transient rip currents. Coast. Eng. 53 (5—6), 419—439. https://doi.org/10.1016/j.coastaleng.2005.11.005

Karambas, T.V., 2012. Design of detached breakwaters for coastal protection: development and application of an advanced numerical model. Coast. Eng. Proc. 1—6. https://doi.org/10.9753/icce.v33.sediment.115

Karambas, T.V., Koutitas, C., 2002. Surf and Swash Zone Morphology Evolution Induced by Nonlinear Waves. J. Waterw. Port Coast. Ocean Eng. 128 (3), 102—113. https://doi.org/10.1061/(asce)0733-950x(2002)128:3(102)

Karambas, T.V., Samaras, A.G., 2017. An integrated numerical model for the design of coastal protection structures. J. Mar. Sci. Eng. 5 (4), 50. https://doi.org/10.3390/jmse5040050

Katopodi, I., Ribberink, J.S., 1992. Quasi-3D modelling of suspended sediment transport by currents and waves. Coast. Eng. 18 (1—2), 83—110. https://doi.org/10.1016/0378-3839(92)90006-G

Kennedy, A.B., Kirby, J.T., Chen, Q., Dalrymple, R.A., 2001. Boussinesq-type equations with improved nonlinear performance. Wave Motion 33 (3), 225—243. https://doi.org/10.1016/S0165-2125(00)00071-8

Klonaris, G.T., Memos, C.D., Drønen, N.K., 2016. High-Order Boussinesq-Type Model for Integrated Nearshore Dynamics. J. Waterw. Port Coast. Ocean Eng. 142 (6), 04016010. https://doi.org/10.1061/(asce)ww.1943-5460.0000349

Klonaris, G.T., 2016. Morphodynamics in a beach with submerged breakwaters. NTUA Athens, Greece.

Klonaris, G.T., Memos, C.D., Drønen, N.K., Deigaard, R., 2018. Simulating 2DH coastal morphodynamics with a Boussinesq-type model. Coast. Eng. J. 60 (2), 159—179. https://doi.org/10.1080/21664250.2018.1462300

Klonaris, G.T., Metallinos, A.S., Memos, C.D., Galani, K.A., 2020. Experimental and numerical investigation of bed morphology in the lee of porous submerged breakwaters. Coast. Eng. 155, 103591. https://doi.org/10.1016/j.coastaleng.2019.103591

Kobayashi, H., Watanabe, A., Isobe, M., Sato, S., Ishii, T., 2000. Three-dimensional beach deformation model for nonlinear multi-directional waves. In: 2000 — Proceedings of the 27th International Conference on Coastal Engineering. ICCE 2000 https://doi.org/10.1061/40549(276)213

Kobayashi, N., 2016. Coastal Sediment Transport Modeling for Engineering Applications. J. Waterw. Port Coast. Ocean Eng. 142 (6), 03116001. https://doi.org/10.1061/(asce)ww.1943-5460.0000347

Kristensen, S.E., Drønen, N., Deigaard, R., Fredsoe, J., 2016. Impact of groyne fields on the littoral drift: A hybrid morphological modelling study. Coast. Eng. 111, 13—22. https://doi.org/10.1016/j.coastaleng.2016.01.009

Larsen, J., Dancy, H., 1983. Open boundaries in short wave simulations - A new approach. Coast. Eng. 7 (3), 285—297. https://doi.org/10.1016/0378-3839(83)90022-4

Larson, M., Kubota, S., Erikson, L., 2004. Swash-zone sediment transport and foreshore evolution: Field experiments and mathematical modeling. Mar. Geol. 212 (1—4), 61—79. https://doi.org/10.1016/j.margeo.2004.08.004

Larson, M., Wamsley, T.V., 2007. A formula for longshore sediment transport in the Swash. In: Coastal Sediments '07 — Proceedings of 6th International Symposium on Coastal Engeneering and Science of Coastal Sediment Processes. https://doi.org/10.1061/40926(239)151

Leont'yev, I.O., 1996. Numerical modelling of beach erosion during storm event. Coast. Eng. 29 (1—2), 187—200. https://doi.org/10.1016/S0378-3839(96)00029-4

Lesser, G.R., Roelvink, J.A., van Kester, J.A.T.M., Stelling, G.S., 2004. Development and validation of a three-dimensional morphological model. Coast. Eng. 51 (8—9), 883—915. https://doi.org/10.1016/j.coastaleng.2004.07.014

Malej, M., Shi, F., Smith, J. M., 2019. Modeling ship-wake-induced sediment transport and morphological change—sediment module in FUNWAVE-TVD. Technical Note (Engineer Research and Development Center (U.S.)). https://doi.org/10.21079/11681/32911

Madsen, P.A., Sørensen, O.R., Schäffer, H.A., 1997. Surf zone dynamics simulated by a Boussinesq type model. Part I. Model description and cross-shore motion of regular waves. Coast. Eng. 32 (4), 255287. https://doi.org/10.1016/S0378-3839(97)00028-8

Mahmoudof, S.M., Hajivalie, F., 2021. Experimental study of hydraulic response of smooth submerged breakwaters to irregular waves. Oceanologia 63 (4), 448—462. https://doi.org/10.1016/j.oceano.2021.05.002

Masselink, G., Russell, P., Turner, I., Blenkinsopp, C., 2009. Net sediment transport and morphological change in the swash zone of a high-energy sandy beach from swash event to tidal cycle time scales. Mar. Geol. 267 (1—2), 18—35. https://doi.org/10.1016/j.margeo.2009.09.003

Ming, D., Chiew, Y.-M., 2000. Shoreline Changes behind Detached Breakwater. J. Waterw. Port Coast. Ocean Eng. 126 (2), 63—70. https://doi.org/10.1061/(asce)0733-950x(2000)126:2(63)

Nwogu, O., Takayama, T., Ikeda, N., 1992. Living with shore protection structures: A review. Report of Port and Harbour Research Institute 31 (2), 3—19.

Nam, P.T., Larson, M., Hanson, H., 2011. A numerical model of beach morphological evolution due to waves and currents in the vicinity of coastal structures. Coast. Eng. 58 (9), 863—876. https://doi.org/10.1016/j.coastaleng.2011.05.006

Nam, P.T., Larson, M., Hanson, H., Hoan, L.X., 2009. A numerical model of nearshore waves, currents, and sediment transport. Coast. Eng. 56 (11—12), 1084—1096. https://doi.org/10.1016/j.coastaleng.2009.06.007

Nordstrom, K.F., 2014. Living with shore protection structures: A review. Estuar. Coast. Shelf Sci. 50, 11—23. https://doi.org/10.1016/j.ecss.2013.11.003

Postacchini, M., Russo, A., Carniel, S., Brocchini, M., 2016. Assessing the Hydro-Morphodynamic Response of a Beach Protected by Detached, Impermeable, Submerged Breakwaters: A Numerical Approach. J. Coastal Res. 32 (3), 590—602. https://doi.org/10.2112/JCOASTRES-D-15-00057.1

Pranzini, E., Wetzel, L., Williams, A.T., 2015. Aspects of coastal erosion and protection in Europe. J. Coast. Conserv. 19. https://doi.org/10.1007/s11852-015-0399-3

Ranasinghe, R., Larson, M., Savioli, J., 2010. Shoreline response to a single shore-parallel submerged breakwater. Coast. Eng. 57 (11—12), 1006—1017. https://doi.org/10.1016/j.coastaleng.2010.06.002

Razak, M.S.A., Nor, N.A.Z.M., 2018. XBeach Process-Based Modelling of Coastal Morphological Features Near Breakwater. MATEC Web of Conferences. https://doi.org/10.1051/matecconf/201820301007

Ribberink, J.S., 1998. Bed-load transport for steady flows and unsteady oscillatory flows. Coast. Eng. 34 (1—2), 59—82. https://doi.org/10.1016/S0378-3839(98)00013-1

Roelvink, D., Costas, S., 2019. Coupling nearshore and aeolian processes: XBeach and duna process-based models. Environ. Model Softw. 115, 98—112. https://doi.org/10.1016/j.envsoft.2019.02.010

Ruiz-Martínez, G., Mariño-Tapia, I., Baldwin, E.G.M., Casarín, R.S., Ortiz, C.E.E., 2016. Identifying Coastal Defence Schemes through Morphodynamic Numerical Simulations along the Northern Coast of Yucatan. Mexico. J. Coastal Res. 32 (3), 651—669. https://doi.org/10.2112/JCOASTRES-D-15-00009.1

Seabergh, W.C., Kraus, N.C., 2003. Progress in management of sediment bypassing at coastal inlets: Natural bypassing, weir jetties, jetty spurs, and engineering aids in design. Coast. Eng. J. 45 (04), 533—563. https://doi.org/10.1142/S0578563403000944

Servold, K.P., Webb, B.M., Douglass, S.L., 2017. Effects of Low-Crested Living Shoreline Breakwaters on Wave Setup, in: Coastal Structures and Solutions to Coastal Disasters 2015: Resilient Coastal Communities - Proceedings of the Coastal Structures and Solutions to Coastal Disasters Joint Conference 2015. https://doi.org/10.1061/9780784480304.045

Shi, F., Kirby, J.T., Harris, J.C., Geiman, J.D., Grilli, S.T., 2012. A high-order adaptive time-stepping TVD solver for Boussinesq modeling of breaking waves and coastal inundation. Ocean Model. 43, 36—51. https://doi.org/10.1016/j.ocemod.2011.12.004

Smagorinsky, J., 1963. General circulation experiments wiht the primitive equations I. The basic experiment. Mon. Weather Rev. 91.

Smit, P.B., Janssen, T.T., Herbers, T.H.C., 2015. Stochastic modeling of inhomogeneous ocean waves. Ocean Model. 96, 26—35. https://doi.org/10.1016/j.ocemod.2015.06.009

Tang, J., Lyu, Y., Shen, Y., Zhang, M., Su, M., 2017. Numerical study on influences of breakwater layout on coastal waves, wave-induced currents, sediment transport and beach morphological evolution. Ocean Eng. 141, 375—387. https://doi.org/10.1016/j.oceaneng.2017.06.042

Tonelli, M., Petti, M., 2009. Hybrid finite volume - finite difference scheme for 2DH improved Boussinesq equations. Coast. Eng. 56 (5—6), 609—620. https://doi.org/10.1016/j.coastaleng.2009.01.001

Tsiaras, A.-C., Karambas, T., Koutsouvela, D., 2020. Design of Detached Emerged and Submerged Breakwaters for Coastal Protection: Development and Application of an Advanced Numerical Model. J. Waterw. Port Coast. Ocean Eng. 146 (4), 04020012. https://doi.org/10.1061/(asce)ww.1943-5460.0000566

Valsamidis, A., Reeve, D.E., 2017. Modelling shoreline evolution in the vicinity of a groyne and a river. Cont. Shelf Res. 132, 49—57. https://doi.org/10.1016/j.csr.2016.11.010

van Rijn, L., 1993. In: Principles of Sediment Transport in Rivers, Estuaries and Coastal Seas, 1006. Aqua publications, Amsterdam, 11—13.

van Rijn, L.C., 2011. Coastal erosion and control. Ocean and Coastal Manag. 54 (12), 867—887. https://doi.org/10.1016/j.ocecoaman.2011.05.004

van Rijn, L., C., 2013. Design of hard coastal structures against erosion. Accessed online: https://www.leovanrijn-sediment.com/papers/Coastalstructures2013.pdf.

Watanabe, A., 1988. In: Horikawa, K. (Ed.), University of Tokyo Press, Tokyo.

Wei, G., Kirby, J.T., Sinha, A., 1999. Generation of waves in Boussinesq models using a source function method. Coast. Eng. 36 (4), 271—299. https://doi.org/10.1016/S0378-3839(99)00009-5

Zyserman, J.A., Johnson, H.K., 2002. Modelling morphological processes in the vicinity of shore-parallel breakwaters. Coast. Eng. 45 (3—4), 261—284. https://doi.org/10.1016/S0378-3839(02)00037-6

Oceanologia 64 (2022) 535—545

Available online at www.sciencedirect.com

ScienceDirect

journal homepage: www.journals.elsevier.com/oceanologia

ORIGINAL RESEARCH ARTICLE

The decline of Svalbard land-fast sea ice extent as a result of climate change

Jacek A. Urbański[a,*], **Dagmara Litwicka**[b]

[a] *GIS Laboratory, Institute of Oceanography, University of Gdańsk, Gdynia, Poland*
[b] *Institute of Oceanology, Polish Academy of Sciences, Sopot, Poland*

Received 14 July 2021; accepted 24 March 2022
Available online 8 April 2022

KEYWORDS
Svalbard;
Fast ice;
Warming;
Machine learning;
Random Forest

Abstract The Svalbard Archipelago has experienced some of the most severe temperature increases in the Arctic in the last three decades. This temperature rise has accelerated sea-ice melting along the coast of the archipelago, thus bringing changes to the local environment. In view of the importance of the near-future distribution of land-fast sea ice along the Svalbard coast, the available observation data on the ice extent between 1973 and 2018 are used herein to create a random forest (RF) model for predicting the daily ice extent and its spatial distribution according to the cumulative number of freezing and thawing degree days and the duration of the ice season. Two RF models are constructed by using either regression or classification algorithms. The regression model makes it possible to estimate the extent of land-fast ice with a root mean square error (RMSE) of 800 km^2, while the classification model creates a cluster of submodels in order to forecast the spatial distribution of land-fast ice with less than 10% error. The models also enable the reconstruction of the past ice extent, and the prediction of the near-future extent, from standard meteorological data, and can even analyze the real-time spatial variability of land-fast ice. On average, the minimum two-monthly extent of land-fast sea ice along the Svalbard coast was about 12,000 km^2 between 1973 and 2000. In 2005—2019, however, the ice extent declined to about 6,000 km^2. A further increase in mean winter air temperatures by two degrees, which is forecast in 10 to 20 years, will result in a minimum two-monthly land-fast ice extent of about 1,500 km^2, thus indicating a trend of declining land-fast ice extent in this area.

* Corresponding author at: GIS Laboratory, Institute of Oceanography, University of Gdańsk, Gdynia, 81-378, Poland.
E-mail address: jacek.urbanski@ug.edu.pl (J.A. Urbański).
Peer review under the responsibility of the Institute of Oceanology of the Polish Academy of Sciences.

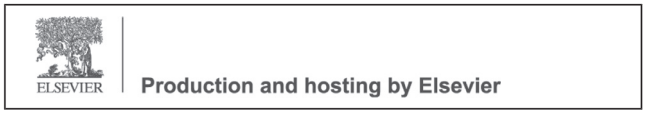

https://doi.org/10.1016/j.oceano.2022.03.008

1. Introduction

The Svalbard Archipelago is the largest land area in the European part of the Arctic. The West Spitsbergen Current and the semi-continuous weather front between the cold masses of Arctic air and the warmer air of the polar cell strongly influence the Svalbard climate. Because of the low air temperature and the highly-indented coastline, the coastal waters of Svalbard are covered every year by land-fast sea ice (referred to hereafter as fast ice), i.e., ice that holds fast to the coastline or the sea bottom. Fast ice usually accumulates in fjords, between islands, and in shallow inshore waters. In the Arctic, fast ice is biologically significant as a breeding and molting site for seals, mainly ringed seals (*Pusa hispida*), which are the principal prey of polar bears (*Ursus maritimus*) (Krafft et al., 2006; Smith and Lydersen, 1991). Moreover, fast ice protects coastal areas from erosion by wave action for as long as it persists. The effects of climate change are intensified in this region, with the Arctic experiencing one of the largest increases in air temperature in the present century (Førland et al., 2011; Isaksen et al., 2016). Since the beginning of the 20th century, meteorological observations have shown that the air temperature has always fluctuated in this region, and the temperature has risen by 4—5°C during the last 40—50 years (Hanssen-Bauer et al., 2019). Although the winter air temperatures between the 1960s and early 1990s were only slightly higher than at the beginning of the 20th century, the temperature increased by the beginning of the 21st century and continues to do so (Nordli et al., 2014, 2020).

The mean annual temperature changes at three meteorological stations in the Svalbard Archipelago between 1975 and 2018 are presented in Figure 1, along with the mean winter temperature changes, which is when land-fast ice predominantly occurs. Current forecasts envisage a mean annual temperature rise in this region of at least 1°C per decade until the mid-21st century (Hanssen-Bauer et al., 2019).

The large-scale permanent monitoring of local sea ice conditions in the fjords and coastal waters of Svalbard began just under 20 years ago using the new technology of high and medium resolution satellite imaging, mainly via C-band Synthetic Aperture Radar (SAR) sensors (Hanssen-Bauer et al., 2019; Johansson et al., 2020; Muckenhuber et al., 2016) and GIS-based automatic or semi-automatic systems for sea ice classification (Zakhvatkina et al., 2019). Since 2005, the Norwegian Ice Service has produced ice charts of the Svalbard area almost daily (Monday—Friday). Since the new methods of ice mapping were introduced, it has been possible gradually to improve the accuracy of the maps. Previously, fast ice conditions in Svalbard were assessed mainly from various observations made as part of several fast-ice related projects (Gerland et al., 2008; Hanssen-Bauer et al., 2019; Zhuravskiy et al., 2012). For example, analyses of the total number of fast-ice days before 1st April (the ring seal pupping date) were performed using satellite data from 1974 to 1988 to reveal a substantial interannual variability of 0—155 days in the fjords of northern Spitsbergen (the largest island of Svalbard), and 38—107 days on the western coast (Smith and Lydersen, 1991).

There have been several reports on local fast ice conditions in the last 20 years. For example, an analysis of the temporal changes in ice cover during 2000—2014 in Isfjorden and Hornsund using SAR and optical images revealed a significant decrease in the extent of fast ice in both fjords (Muckenhuber et al., 2016). Meanwhile, systematic observations in Kongsfjorden since 2003 initially detected substantial interannual variability in the fast ice extent with intervals of 2—3 years or more (Gerland and Renner, 2007), i.e., a similar pattern to that observed in the 1970s and 1980s. However, more recent observations have indicated that the

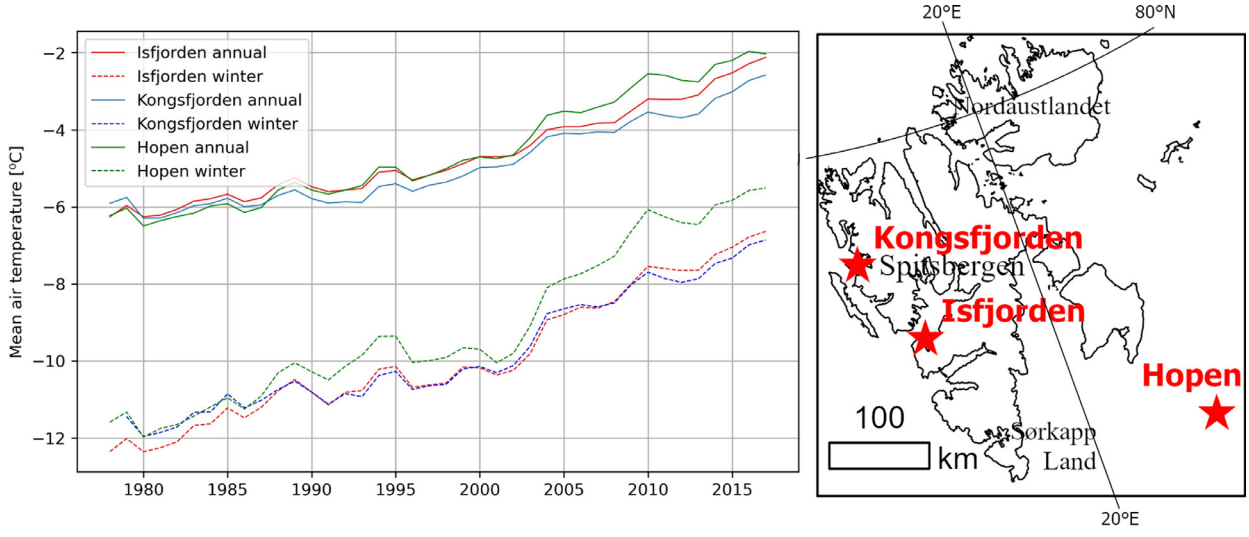

Figure 1 The air temperature changes at three meteorological stations in the Svalbard Archipelago between 1975 and 2018. The solid lines show the annual mean, and the dashed lines show the winter (December—May) means. Eight-year smoothing was used with a rolling yearly mean (left). The locations of the meteorolgical stations: Isfjorden—Barentsburg (78.1°N, 14.3°E), Kongsfjorden—Ny-Ålesund (78.923°N, 11.933°E), and Hopen (76.5°N, 25.067°E) (right).

ice extent is smaller in most years and that the ice season is becoming shorter (Pavlova et al., 2019). In particular, there has been a smaller extent of fast ice near the northern coasts of Svalbard, although occasional observations have shown that the fast ice cover can last from November until July (Wang et al., 2013). It is generally agreed that the duration of fast ice cover around Svalbard has become perceptibly shorter in the last ten years (Dahlke et al., 2020; Hanssen-Bauer et al., 2019; Pavlova et al., 2019). An understanding of this temporal distribution is also vital in studying environmental changes, coastal erosion, and the ecology of many species (Hanssen-Bauer et al., 2019; Krafft et al., 2006; Smith and Lydersen, 1991). Hence, the present project aims to determine the changes in the extent of fast ice and to predict its near-future extent and distribution.

2. Material and methods

2.1. Meteorological data

Two sets of data were used in the present work — one for modeling and the other for assessing the modeling method. In the first case, observational meteorological data from the Hopen, Barentsburg, and Ny-Ålesund stations between 1973 and 2019 were acquired as daily summaries, including minimum, maximum and average air temperatures, from the National Centres for Environmental Information (NCEI) of the National Oceanic and Atmospheric Administration (NOAA) (https://www.ncdc.noaa.gov/cdo-web/datatools/selectlocation) (Menne et al., 2012). In the second case, the Arctic Regional Reanalysis dataset of hourly short-term forecasts of surface meteorological variables at a 2.5-km resolution was used. This dataset was produced using the HARMONIE-AROME regional numerical weather prediction model (https://cds.climate.copernicus.eu/cdsapp#!/dataset/reanalysis-carra-single-levels?tab=overview), and the 2 m daily air temperatures at noon from 1998 to 2019 were downloaded as multivariate rasters for use in the present study.

The mean annual and winter air temperature changes between 1975 and 2018 at the above-mentioned meteorological stations reveal a significant increase in the winter mean temperature between 2000 and 2005 (Figure 1). This time period was therefore used herein to divide the analyzed period into two parts.

2.2. Ice data

The following three sets of sea-ice data were used in the present project: (i) the daily operational ice charts produced by the Norwegian Ice Service in 2005—2018 for the Svalbard Archipelago were downloaded from the archive dataset of the Norwegian Meteorological Institute (https://cryo.met.no/archive/ice-service/icecharts/quicklooks/); (ii) the ice charts for 1973—1998 were downloaded in vector.shp format from the Climate and Cryosphere Historical Ice Chart Archive (http://www.climate-cryosphere.org/resources/historical-ice-chart-archive/gis-data), and (iii) the 10 km x 10 km raster-gridded daily sea ice concentration data for the entire Arctic between 2003 and the present were obtained from the US. National Snow and Ice Data Center (https://nsidc.org/data/G10033/versions/1). The latter data set was created using various methods according to availability over time. Thus, the earliest charts were produced by combining sources such as aerial reconnaissance, surface observations, and airborne and ship reports. Subsequently, infrared and visible-band satellite imagery from the Advanced Very High-Resolution Radiometer (AVHRR) was used, and currently, data from the Synthetic Aperture Radar and Advanced Microwave Scanning Radiometer are used. According to Yu et al. (2014), the relative uncertainty in chart-derived fast ice extent can range from 5% to 25% on average. As this estimation was made for the 25-km resolution National Ice Center charts produced in 1975—2006, the relative uncertainty is assumed to be 5—20% herein. The GIS vector and raster layers with a georeferenced coastline and land-water mask of the Svalbard Archipelago were obtained from the GIS Centre, University of Gdańsk.

2.3. Data pre-processing

The observational meteorological data contained fields with incomplete values of the mean, maximum, and minimum daily air temperatures. The minimum and maximum values contained only occasional gaps, whereas gaps in the mean values were very frequent. The data pre-processing workflow involved the following two steps: (i) a linear regression model was built to estimate the average daily temperature from the minimum and maximum values, then (ii) a regression equation was used to fill gaps in the average daily temperature within each data set. These data are presented in Figure 1 above.

The next step was to calculate the cumulative number of freezing degree days (FDD) and thaw degree days (TDD) by employing Stefan's Law (Leppäranta, 1993):

$$FDD = \int_0^t [T_f - T_0(t)]dt \ \ for\ T_0 < T_f \quad (1)$$

$$TDD = \int_0^t [T_0(t) - T_f]dt \ \ for\ T_0 > T_f \quad (2)$$

where t is time, T_f is the freezing temperature, and $T_0(t)$ is the average daily temperature. The freezing temperature is −1.9°C (the freezing temperature of seawater). The formulas generally use the day as the unit of time. The FDD is also referred to as the sum of negative degree days, and is used to simplify the formula for estimating ice thickness (Leppäranta, 1993) by providing the cumulative sum of below-zero temperatures for each successive day. The TDD is similar, but with respect to temperatures above −1.9°C. Herein, it was assumed that the ice season starts on 1st September and lasts for 300 days until June. The definition of the ice season allows the number of ice seasons and the number of days within a particular ice season (ICSD) to be assigned to each day. Hence, a tidy text format file was created for 13,794 days (1/09/1973—27/06/2019). The following two spatial data models were used to organize the georeferenced data for analysis: (i) a set of 110 randomly distributed points in an area of fast ice localization, and (ii)

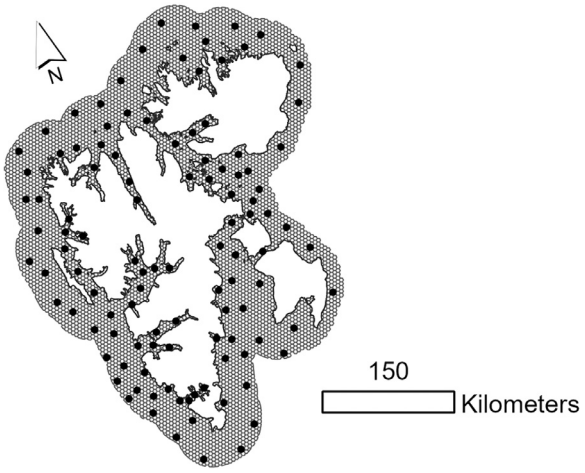

Figure 2 The spatial data models used in the present project: 110 points and a grid of 4782 hexagonal polygons.

a grid of 4782 polygonal cells with areas of 16 km^2. Each model was assigned a unique ID to points and polygons, as indicated in Figure 2. The grid of polygons defines the project area of interest, which is 76512 km^2.

The Arctic Regional Reanalysis dataset of daily air temperature was assigned to the randomly distributed points presented in Figure 2 by extracting its values from rasters. In the resulting tidy text format, the file rows represent days in 110 columns, with the air temperature at each point.

The scanned ice cover maps were manually or automatically digitized to time series of rasters with the following classes: 0 (water), 1 (land), 2 (open water), 3 (very open drift ice), 4 (open drift ice), 5 (close drift ice), 6 (very close drift ice), and 7 (fast ice). The spatial resolution of the rasters was 300 m, and the fast ice classes were used to convert the vector ice charts to the raster format with the same shape and spatial resolution. Combining these two ice sets gives the time series of 1960 rasters for the years 1973—2018, with a gap between 1999 and 2004. It contains, on average, one or two ice concentration maps per week. The tidy text format file of fast ice contains rows representing each map, with a separate column for each hexagon (4782 columns in total), with classes 1 and 0 indicating the presence and absence of fast ice.

The daily sea ice concentration raster gridded data for the entire Arctic was used along with the fast ice class to create an additional text file with two columns representing time and fast ice extent in the area of interest.

2.4. Machine learning modeling

The RF regression and classification models were used to predict the ice cover extent and to classify the hexagonal grid cells for the two classes (ice/no ice) on any day using the FDD, TDD, and ICSD as predictive features. The RF model, introduced by Breiman (2001), has been used in many geophysical and environmental applications (Lutz et al., 2018; Mutanga et al., 2012; Rodriguez-Galiano et al., 2014, 2015). In this method, random decision trees are created by bootstrapping data in which the sample data are drawn and replaced. Then the majority vote or average prediction across all trees is used to generate the result. The main advantages of the RF model are that overfitting can be reduced by averaging several trees and that no statistical assumptions are required regarding normal distribution and data linearity. The model also allows one to measure the relative importance of each feature for the prediction. Furthermore, it is easy to apply, and the few default hyperparameters usually give good results. However, one of the model's shortcomings is that it is impossible to extrapolate beyond the range of values in the training set. As a result, predictions can be made only in the range of values represented by the training data set. In the present study, the range of values in the training set is 0—2800 for the FDD, 1.1—300 for the TDD, and 0—38288 km^2 for the ice cover extent. The typical workflow uses a training set containing the dependent and independent variables to train the RF model, and a test data set to validate the results. The RF modeling was performed using the Python Scikit-learn package (Pedregosa et al., 2011). The following two models were created: (i) a regression model for predicting the total fast ice extent (in km^2) along the coast of Svalbard for every day with available FDD, TDD, and ICSN data, and (ii) a classification model for predicting the presence or absence of fast ice in each hexagonal cell of the grid (by assigning the values 1 or 0) and for building the cluster of independent models in order to predict the spatial distribution of fast ice.

The regression and classification modeling uses a training set to build a model and test sets to validate the model. Both sets are randomly created by splitting the basic set of daily data with known FDD, TDD, and ICSN, along with the total fast ice extents for the regression model and the presence or absence values of each cell in the cluster for the classification model. A standard method for evaluating the accuracy of the model on continuous data (total fast ice extent) is the root mean square error (RMS). However, the error rate is used for evaluating the machine learning classification model, where the error rate is defined as one minus the accuracy, and the accuracy is the ratio of the number of observations with correct classification to the total number of classified observations. The Scikit-learn functionality also allows the tuning of hyperparameters and the analysis of feature importance, the latter being a measure of how the random shuffle of a particular feature influences the result. From 1973 to the present time, the available data range makes the RF method applicable for the present project. In view of the spatial scale (a few hundred square kilometers) and the statistical nature of the models, it is assumed that the FDD and TDD are highly autocorrelated and that the values from one point in Isfjorden can be used. This assumption is discussed in detail later.

The random hyperparameters used in the present work are listed in Table 1. These were tuned by using a field cross-validation grid.

The accuracy of the model was evaluated via the following two steps: (i) the feature importance was evaluated using Scikit-learn, giving accuracies of 60%, 30%, and 10% for the FDD, TDD, and ICESD, respectively, and (ii) the RMS error was calculated as 802 km^2, which is approximately the area of 50 cells in Figure 2. The RF classification model using a cluster of 4782 independent submodels uses the same features as the regression model. The model maps the fast ice distribution in time. The array of fast ice cells can be

Table 1 The hyperparameters tested and used in sklearn.ensemble.RandomForestRegressor (scikit-learn 0.23.2).

Hyperparametres	Hyperparameter grid values tested	Best hyperparameters
Using bootstrap sample when building trees.	True, False	True
The maximum depth of tree.	10, 20, 30, 40, 50, 60, 70, 80, 90, 100, 110, None	80
The number of features considered when looking for the best split.	auto, sqrt	auto
The maximum number of samples required to be at a leaf node.	1,2,4	2
The minimum number of samples required to split an internal mode.	2,5,10	2
The number of trees in the forest.	200, 400, 600, 800, 1000, 1200, 1400, 1600, 1800, 2000	1800

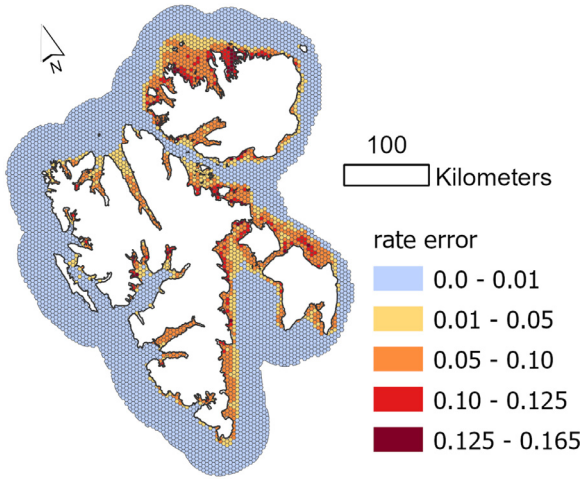

Figure 3 The rate errors in the predicted spatial distribution of fast ice by the classification model.

summed for any day to give the fast ice cover in km^2. The local ice cover depends on, among other things, the water depth, water heat flux, wave action, water circulation, water heat flux, and local microclimate. All these features are irrelevant in the machine learning process if the dependent variable (target) represents a single location. The model uses only basic features from one location and predicts new values only for that particular location. As a result, the robust autocorrelation of features in space is irrelevant. The results of error evaluation for the fast ice distribution model are presented as a rate error map in Figure 3. The rate errors were calculated independently for each cell using the corresponding rows of the validation set. Thus, the classification model exhibits a less than 10% error in predicting the spatial distribution of fast ice for most of the study area. Low error values cover the area, with occasional fast ice only.

3. Results

3.1. Cumulative freezing degree days

The cumulative freezing degree days were previously used by Yu et al. (2014) to explain the changes in fast ice extent in the Arctic because this approach provides a measure of both the changing surface air temperature and its cumulative effect throughout an entire ice growth season. The FDD is the simplest parameter that correlates well with fast ice duration due to its cumulative nature (Leppäranta, 2014). As an ice season straddles two consecutive years, starting in autumn and ending in early summer, all statistics should apply to an ice season rather than a year. The cumulative FDD in each ice season from 1973/74 to 2018/19 in Isfjorden is presented in Figure 4, where the values are assigned to the year when the ice season begins.

3.2. Fast Ice extent in Svalbard

An RF regression model was used to model the changes in fast ice extent in the area of interest, with a total surface of about 76,000 km^2 (Figure 5). The extent of fast ice fluctuates from year to year with 3—4 year cycles of high and low values. Two periods of ice extents larger than 25,000 km^2 appeared before 1990, separated by periods with less extensive fast ice. The winter season fast ice extent is larger than 15,000 km^2 on only a few occasions after 2000, whereas such ice seasons are common before 2000. The modeled extents are compared with the results of Yu et al. (2014) for the period 1975—2007. However, their analysis was performed using data with a spatial resolution of 25 km^2, which may be too coarse for the Svalbard fjords. Nevertheless, the two-time series show several similarities. They both have ice extents of less than 15,000 km^2 for nearly all ice seasons after 2000, and only a few such low extents before. The winters with large extents, such as 1977—1978 and 1981—1982 are also visible in both. However, the maximum fast ice extents reported by Yu et al. (2014) are larger than 40,000 km^2. This is because they occasionally recorded fast ice beyond the area of interest of the present work.

3.3. Distribution of fast ice extent

The cell net classification model makes it possible to estimate the spatial distribution of fast ice for any day. Furthermore, as the created time series is complete, it is easy to calculate statistics for fast ice extent within any time range. For example, the average duration of fast ice in the periods 1973—2000 and 2005—2019 are seen to differ significantly (Figure 6a and b). According to Dahlke et al. (2020), such time ranges emphasize the stationary ice situation be-

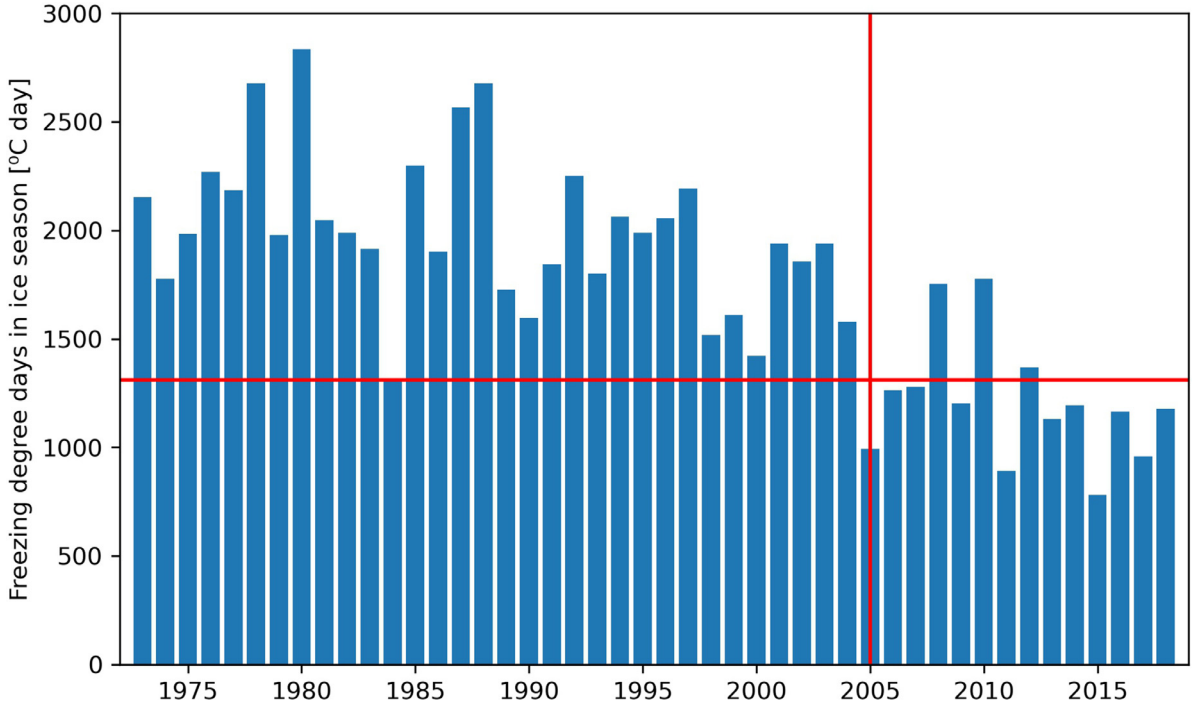

Figure 4 The cumulative freezing degree days (FDD) in Isfjorden during the ice seasons 1973/74 to 2018/19 (assigned to the year when the ice season starts). The vertical red line indicates the year 2005 as the start of warmer winters, and the horizontal line shows the minimum FDD before 2005 (the season 1984/85 was the one that determined this level).

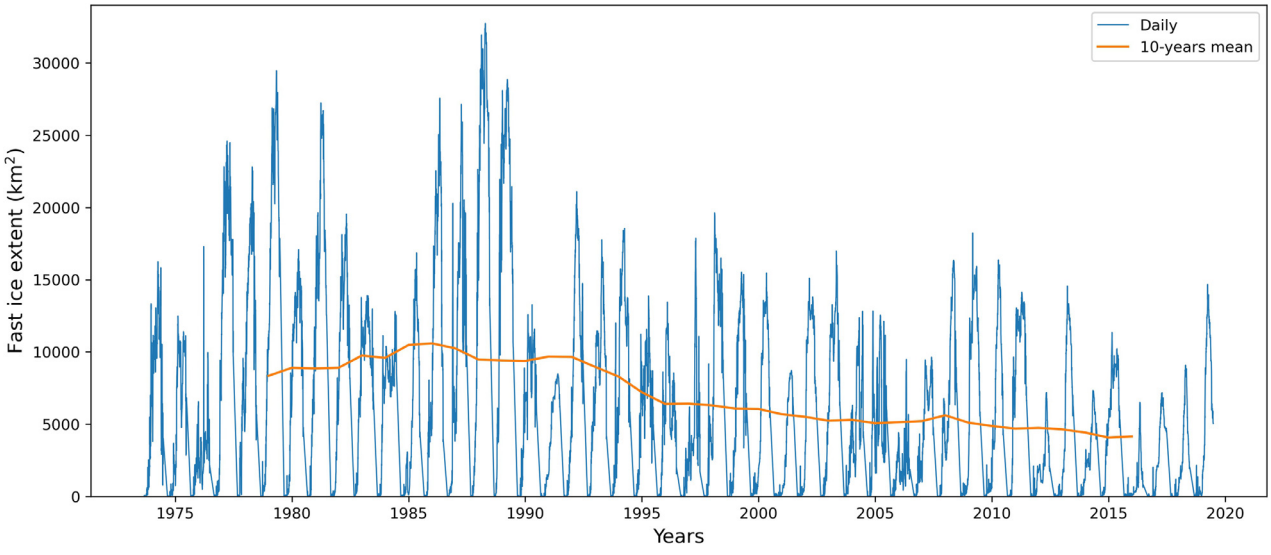

Figure 5 The time series of fast ice extent obtained using the regression model, where the orange line shows 10-year rolling mean.

fore 2000 and the significantly reduced ice cover in recent times.

Between 1973 and 2000, at least half of the surface area of the fjords in west Spitsbergen was covered by fast ice for 4 to 5 months, while the fjords in northern Spitsbergen were entirely covered by fast ice for the same length of time. The northwestern Spitsbergen coast also had fast ice cover for 4–5 months (Figure 6a). The east coast, where there are no fjords, was covered by fast ice, mainly in the bays. Between 2005 and 2019, however, the distribution and duration of fast ice cover changed dramatically. In the fjords of West Spitsbergen, fast ice persisted for four months only at their heads, whereas those in northern Spitsbergen were covered by fast ice for less than half the fjord lengths, usually for two months and only locally for three months (Figure 6b). The most significant differences in duration are in the fjords of Spitsbergen, with the largest changes being in the northern ones. Throughout this area, the duration has been reduced by 3–4 months. Such dramatic changes have occurred only locally; elsewhere, the reduction has

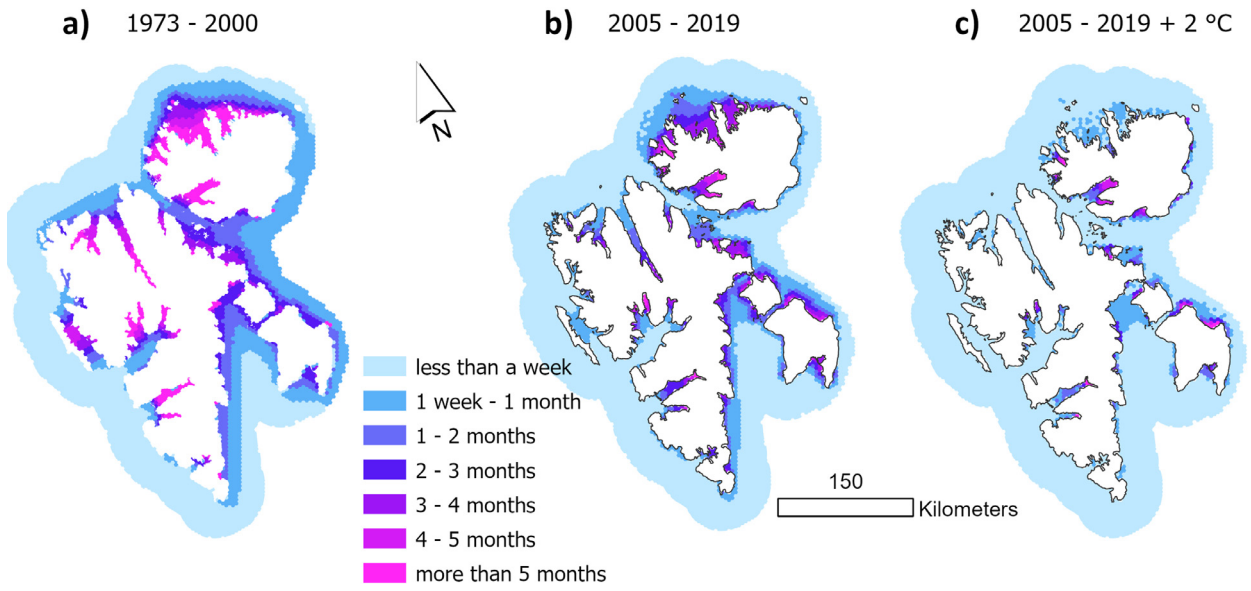

Figure 6 The mean distribution of the fast ice duration in Svalbard (a) during the ice seasons of 1973—2000, (b) during the ice seasons of 2005—2019, and (c) in the near future, assuming a 2°C increase in winter air temperature.

Table 2 The extent of fast ice for various durations of ice cover, with durations of more than 2 months indicated in bold.

Duration of fast ice cover	1973—2000 extent (km^2)	2005—2019 extent (km^2)	2005—2019 + 2°C; near-future extent (km^2)
1 week—1 month	18 059	11 255	6 085
1—2 months	7 464	4 119	1 341
2—3 months	4 467	2 564	712
3—4 months	2 363 **12 320**	2 391 **6 177**	301 **1 522**
4—5 months	1 830	930	356
more than 5 months	3 660	292	153

generally been from 1 to 3 months. In northern Svalbard, the duration of fast ice has decreased by two months; elsewhere, the changes are no greater than one month, and locally no more than two months. The significant changes relate mainly to the fjord's branches (e.g. in Isfjorden), where the fast ice cover before 2000 was long-lasting.

The map in Figure 6c shows the model scenario used in the present study, in which the average fast ice duration for the years 2005—2019 is projected into the future 10—20 years, based on the two-degree increase in the winter air temperature predicted by Hanssen-Bauer et al. (2019). Here, a dramatic decrease in the ice extent is predicted across the entire area. The areas of fast ice extent according to duration are presented in Table 2. However, these total values will differ from the modeled maximum areas because the ice cover may occur at different times. According to the validation procedure described above, the values in Table 2 have an error rate no greater than 10%.

4. Discussion

Although many papers describe the decrease of fast ice extent in Svalbard (e.g., Gerland et al., 2008; Hanssen-Bauer et al., 2019; Zhuravskiy et al., 2012), no prediction was made therein regarding the near future. Nevertheless, given the firm basis of air temperature forecasts, these can be used to model the future fast ice extent. Indeed, the prediction of fast ice extent is vital for the analysis of many physical and biological processes. Among these, the most important physical processes are the terrestrial discharge of freshwater (McClelland et al., 2012) and coastal erosion (Frederick et al., 2016). In addition, changes in the extent of fast ice have significant ecological consequences (Krafft et al., 2006; Smith and Lydersen, 1991).

The important assumption in the present project is that the air temperature changes have strong spatial autocorrelation, thus enabling spatial modeling of the entire area based on the temperature at one point only. The cumulative FDD was previously used by Yu et al. (2014) to understand the long-term changes in fast ice in the Arctic. Hence, the temporal and spatial distributions and their correlation with the FDD were analyzed in the present study using the Arctic Regional Reanalysis dataset of hourly short-term forecasts of surface meteorological variables. As the aim was to use the FDD series from Isfjorden, all series were correlated with this point. Due to the massive amount of data, the FDD was calculated using the air temperature at noon instead of the mean daily air temperature. This is justified because the elevation of the sun doesn't change significantly during the day and, hence, the daily temperature range is small. The analysis was performed using a 110-point

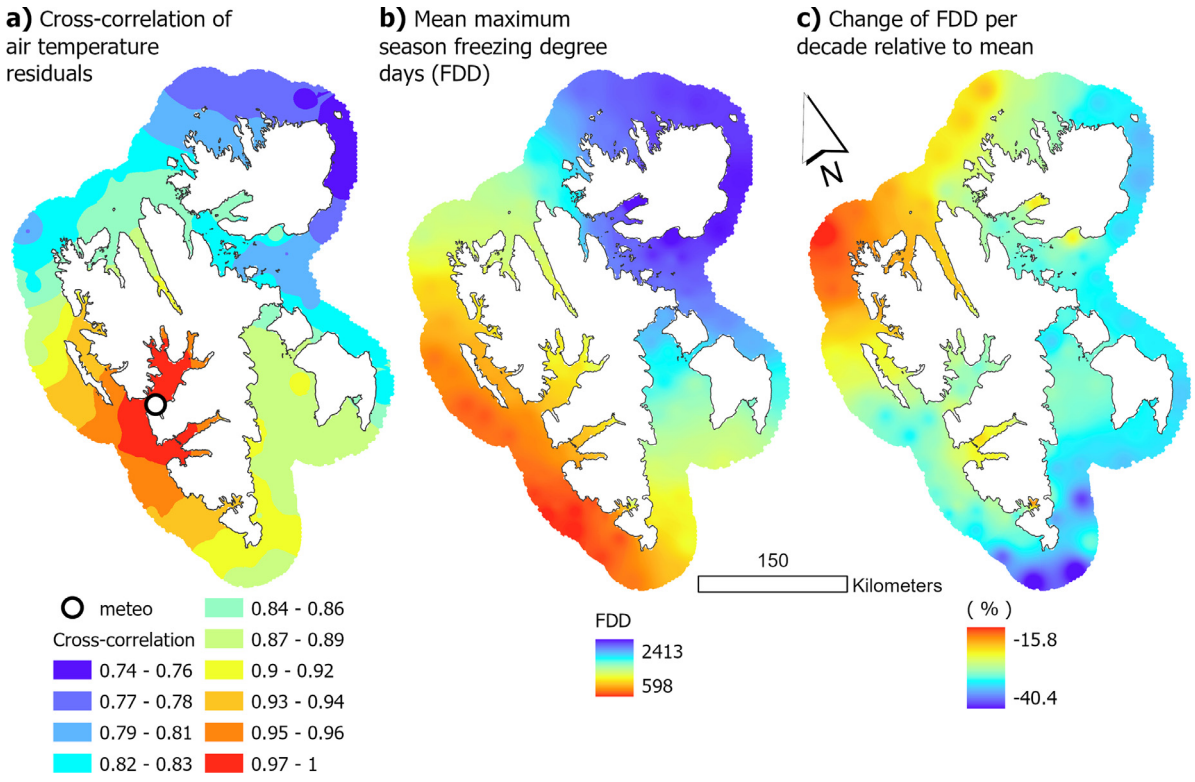

Figure 7 The cross-correlation of air temperature residuals (a). The mean maximum seasonal cumulative freezing degree days (FDD) (b). The decadal change in FDD relative to the mean (c).

time series of daily mid-day air temperatures during 1998–2019 (Figure 2). Because the cross-correlation is impacted by time series dependence, the correlation analyses were performed on temperature residues.

The results of the correlation analyses are presented in Figure 7. For most of the analyzed areas, the correlation coefficients of temperature residues with Isfjorden are higher than 0.8 (Figure 7a). Only in the northern-western parts of Nordaustlandet do the coefficients decrease to 0.74. Despite the influence of various water masses, the west and east coast air temperatures correlate well, with values of about 0.9. This strong correlation is essential when building a total regression model and distributed classification models of fast ice extent based on one-point FDD and TDD values. Meanwhile, the mean maximum ice season FDD is seen to change gradually from the southwest to north-east in the range 600 to 2400 days (Figure 7b), in agreement with the results of Yu et al. (2014) for the years 1977–2007. Further, the results in Figure 7c indicate that the estimated changes in FDD relative to the mean value per decade are higher than 15% for all areas. The fastest changes take place near Sørkapp, with a 40% decrease per decade, while the smallest changes occur at northern-western Spitsbergen.

As detailed in the Materials and methods section, three different data sets were used to create and evaluate a continuous picture of fast ice changes near the coasts of Svalbard (Figure 8). Here, all three data sets contain classified land-fast ice. The reliability of this classification is reflected in the metadata for each dataset, and is not within the scope of the present project.

The time series of FDD was calculated for Isfjorden. As the air temperature in Kongsfjorden is nearly identical, the FDD will be very similar in both fjords. The results in Figure 4 confirm the observed shortening of the fast ice season from 2005/2006 onwards (Pavlova et al., 2019). Prior to that season, the FDD oscillated with a frequency of a few years, varying between 1800 and 2300 days, with an overall decreasing trend. After 2005/2006, the FDD was significantly *higher* than the 1973–2005 (32-season) minimum in only two out of 13 subsequent seasons, but was lower than the minimum (between 900 and 1200 days) in 9 seasons. Interannual variability still occurs, but the decreasing trend in FDD now applies to both the mean and minimum values. The general trends reflected in the above analysis thus confirm the earlier results (Gerland and Hall, 2006; Gerland and Renner, 2007; Pavlova et al., 2019).

Machine learning models have two advantages over the observational mapping of sea ice extents. As noted above, such maps were created using various methods according to availability, thus improving with time. By contrast, the accuracy of estimation using a machine learning model is constant, as determined by the evaluation process. Furthermore, when accurate data are unavailable, better results can be obtained by teaching the model using more accurate contemporary data. In addition, such models can be used for forecasting the future fast ice extent, and the performance of the model can be evaluated by comparing its predictions with observations in the area of interest (the grid of hexagonal polygons in Figure 2). The results of the RF regression and classification models are compared with the Norwegian Ice Service ice-chart data set and the grid data from the US

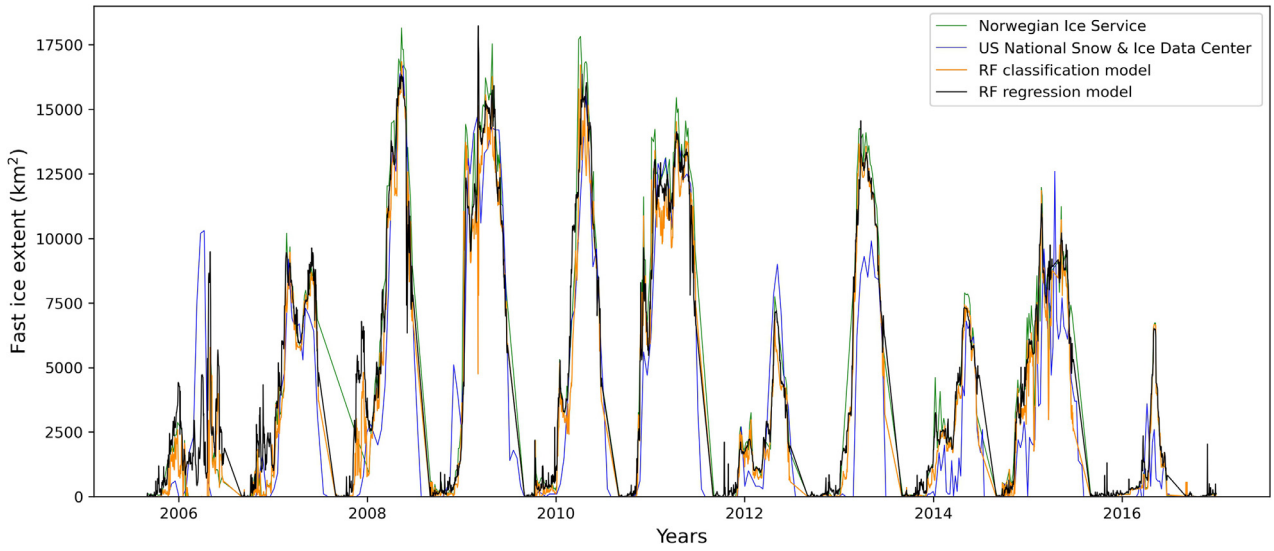

Figure 8 The time series of fast ice extent for project AOI (Figure 2) according to the data from the ice charts produced by the Norwegian Ice Service, the grid data from the US National Snow and Ice Data Center, the random forest classification model results, and the random forest regression model results. The ticks mark link each year to the 1st January of the next year.

National Snow and Ice Data Center in Figure 8. The comparison is for the time window when both data sources were available. A significant similarity between these four time series is observed, although some differences between the two observational datasets exist.

The two main features controlling the model results are the FDD and TDD, although the influence of the FDD is twice that of the TDD. The machine learning models are designed to make the most accurate predictions possible. For example, in the distributed classification model, all local factors such as water temperature or circulation are indirectly included when designing the rules for a particular model cell. The fast ice extent time series obtained using the regression model is presented in Figure 5, and the classification model gives nearly identical results (Figure 8). The characteristic feature is one of fluctuations in the ice extent that are superimposed onto the long-term trend represented by the 10-year rolling mean (orange line on Figure 5). In the latter, the fast ice extent is seen to decrease gradually over time, being halved within the last forty years (a rate of about 100 km^2 per year). This result in in agreement with that of Dahlke et al. (2020), who indicated a decrease of 10—20% per decade in the fjords. In our study, the analysis of spatial change was made using a cluster of local random forest models; this is a new method, but similar solutions have been used by others (e.g., Georganos et al., 2019). The present results show a significant decline in fast ice (Figure 6 and Table 2). The coverage of fast ice lasting more than two months was 12,320 km^2 in 1973—2000, but was halved in 2005—2019. Further, according to the forecast, an increase in temperature by two degrees will decrease the two-month ice coverage four-fold compared to that of 2005—2019.

The amount of fast ice is not a function of air temperature only. The surface air temperature can explain around 25—26% of the fast ice variability (Dahlke, et al., 2020). Many factors have smaller or larger impacts locally. The increased freshwater input from glaciers may alter the fjord fast ice persistence. The temperature and salinity of the water column also play important roles. For example, Kongsfjorden is affected by heat transport in the upper water column, which may impact the ice loss (Cottier et al., 2007; Sundfjord et al., 2017). Also, surface wind stress can cause advecting drift ice, and the mechanical destruction of the existing fast ice may change its extent (King et al., 2017). The snow cover has also important effects on development of fast ice (Wang et al., 2015). As a result, the presence of ice is determined by the unique relationship between air temperature and other factors at each locality. The classification model creates a separate RF model for each locality with an accuracy of greater than 80% (Figure 3). Additionally, the use of air temperature predictions enables these models to predict the future fast ice extent.

5. Conclusions

(1) The quality of ice extent data depends on the time of its acquisition, with older data being less accurate than newer data. However, it is possible to use current observations to model the past via machine learning with errors that are mostly independent of time. Machine learning is also an effective method for modeling the near-future extent and spatial distribution of fast ice. The modeling uses cumulative freezing degree days, thawing degree days, and the total number of days of a particular ice season. Due to the statistical nature of the modeling process, it is possible to use data from a single station if a strong spatial correlation exists.

(2) The most crucial parameter is the cumulative freezing degree days (FDD), with a 60% influence upon the fast ice extent and duration. Since 2005, a significant de-

crease in the FDD has been observed near Svalbard. The changes in air temperature and, hence, the FDD, are strongly correlated in space. The FDD has a significant increasing trend from the southwest to the northeast, with about 400 days across 100 km. As a result of warming, the highest (40%) decrease in FDD per decade is observed near Sørkapp. The lowest (10%) decrease is observed at northwest Spitsbergen.

(3) The maximum winter fast ice extent in the fjords and coastal waters of Svalbard has oscillated from 5,000 to 30,000 km^2 in the last 50 years, with a few-yearly sequence of higher and lower values. The greatest fast ice extent occurred during certain years between 1975 and 1990.
During the last forty years, the mean ice extent has decreased by half at a rate of about 100 km^2 per year.

(4) The most crucial changes in ice extent duration, before and after 2000, are in the western and northern parts of Spitsbergen. The reduction in ice presence is from 1 to 3 months. An increase in mean air temperature by two degrees will reduce the duration of fast ice extent by approximately four times compared to the present.

Declaration of competing interest

The authors declare that they have no known competing financial interests or personal relationships that could have appeared to influence the work reported in this paper.

Acknowledgements

This work was carried out as part of the project ACCES "Deicing of Arctic Coasts: Critical or new opportunities for marine biodiversity and Ecosystem Services?" funded by the Belmont Forum, Call Title: Biodiversity2017 – Scenarios of Biodiversity and Ecosystem Services.

References

Breiman, L., 2001. Random Forests. Mach. Learn. 45, 5–32.

Cottier, F., Nilsen, F., Inall, M., Gerland, S., Tverberg, V., Svendsen, H., 2007. Wintertime warming of an Arctic shelf in response to large-scale atmospheric circulation. Geophys. Res. Lett. 34 (10), 1–5. https://doi.org/10.1029/2007GL029948

Dahlke, S., Hughes, N., Wagner, P, Gerland, S., Wawrzyniak, T., Ivanov, B., Maturilli, M., 2020. The observed recent surface air temperature development across Svalbard and concurring footprints in local sea ice cover. Int. J. Climatol. 40, 5246–5265. https://doi.org/10.1002/joc.6517

Førland, E., Benestad, R., Hanssen-Bauer, I., Haugen, J., Skaugen, T., 2011. Temperature and Precipitation Development at Svalbard 1900 –2100. Adv. Meteorol. 2011. https://doi.org/10.1155/2011/893790

Frederick, J.M., Thomas, M.A., Bull, D.L., Jones, C.A., Roberts, J.D., 2016, The Arctic Coastal Erosion Problem, Sandia Report, SAND2016-9762, 122 pp.

Georganos, S., Grippa, T., Niang Gadiaga, A., Linard, C., Lennert, M., Vanhuysse, S., Mboga, N., Wolff, E., Kalogirou, S., 2019. Geographical random forests: a spatial extension of the random forest algorithm to address spatial heterogeneity in remote sensing and population modelling. Geocarto Int. 36 (2), 1–16. https://doi.org/10.1080/10106049.2019.1595177

Gerland, S., Hall, R., 2006. Variability of fast-ice thickness in Spitsbergen fjords. Ann. Glaciol. 44 (9296), 231–239. https://doi.org/10.3189/172756406781811367

Gerland, S., Renner, A.H.H., 2007. Sea-ice mass-balance monitoring in an Arctic fjord. Ann. Glaciol. 46 (9296), 435–442. https://doi.org/10.3189/172756407782871215

Gerland, S., Renner, A.H.H., Godtliebsen, F., Divine, D., Løyning, T.B., 2008. Decrease of sea ice thickness at Hopen, Barents Sea, during 1966-2007. Geophys. Res. Lett. 35 (6), 1–5. https://doi.org/10.1029/2007GL032716

Hanssen-Bauer, I., Førland, E. J., Hisdal, H., Mayer, S., Sandø, A. B., Sorteberg, A., Adakudlu, M., Andresen, J., Bakke, J., Beldring, S., Benestad, R., Bilt, W., Bogen, J., Borstad, C., Breili, K., Breivik, Ø., Børsheim, K. Y., Christiansen, H. H., Dobler, A., Engeset, R., Frauenfelder, R., Gerland, S., Gjelten, H. M., Gundersen, J., Isaksen, K., Jaedicke, C., Kierulf, H., Kohler, J., Li, H., Lutz, J., Melvold, K., Mezghani, A., Nilsen, F., Nilsen, I. B., Nilsen, J. E. Ø., Pavlova, O., Ravndal, O., Risebrobakken, B., Saloranta, T., Sandven, S., Schuler, T. V, Simpson, M. J. R., Skogen, M., Smedsrud, L. H., Sund, M., Vikhamar-Schuler, D., Westermann, S., Wong, W. K. 2019. Climate in Svalbard 2100, 1/2019, [online]. Available from: https://www.miljodirektoratet.no/globalassets/publikasjoner/M1242/M1242.pdf

Isaksen, K., Nordli, Ø., Førland, E.J., Łupikasza, E., Eastwood, S., 2016. Recent warming on Spitsbergen—Influenceof atmospheric circulation and sea ice cover. J. Geophys. Res. Atmos. 121, 11,913–11,931. https://doi.org/10.1002/2016JD025606

Johansson, A.M., Malnes, E., Gerland, S., Cristea, A., Doulgeris, A.P., Divine, D.V., Pavlova, O., Lauknes, T.R., 2020. Consistent ice and open water classification combining historical synthetic aperture radar satellite images from ERS-1/2, Envisat ASAR, RADARSAT-2 and Sentinel-1A/B. Ann. Glaciol. 61 (82), 1–11. https://doi.org/10.1017/aog.2019.52

King, J., Spreen, G., Gerland, S., Haas, C., Hendricks, S., Kaleschke, L., Wang, C., 2017. Sea-ice thickness from field measurements in the northwestern Barents sea. J. Geophys. Res.-Oceans 122 (2), 1497–1512. https://doi.org/10.1002/2016JC012199

Krafft, B.A., Kovacs, K.M., Andersen, M., Aars, J., Lydersen, C., Ergon, T., Haug, T., 2006. Abundance of ringed seals (Pusa hispida) in the fjords of Spitsbergen, Svalbard, during the peak molting period. Mar. Mammal Sci. 22 (2), 394–412. https://doi.org/10.1111/j.1748-7692.2006.00035.x

Leppäranta, M., 1993. A review of analytical models of sea-ice growth. Atmos.- Oceans 31 (1), 123–138. https://doi.org/10.1080/07055900.1993.9649465

Leppäranta, M., 2014. Freezing of Lakes and the Evolution of their Ice Cover. Springer-Praxis, Heidelberg, 301 pp. https://doi.org/10.1007/978-3-642-29081-7

Lutz, S.R., Krieg, R., Müller, C., Zink, M., Knöller, K., Samaniego, L., Merz, R., 2018. Spatial Patterns of Water Age: Using Young Water Fractions to Improve the Characterization of Transit Times in Contrasting Catchments. Water Resour. Res. 54 (7), 4767–4784. https://doi.org/10.1029/2017WR022216

McClelland, J.W., Holmes, R.M., Dunton, K.H., Macdonald, R.W., 2012. The Arctic Ocean Estuary. Estuar. Coast. 35, 353–368. https://doi.org/10.1007/s12237-010-9357-3

Menne, M.J., I. Durre, B. Korzeniewski, S. McNeal, K. Thomas, X. Yin, S. A. and R. Ray, R.S. Vose, B.E. Gleason, Houston, T. G. 2012. Global Historical Climatology Network – Daily (GHCN-Daily), Version 3.

Muckenhuber, S., Nilsen, F., Korosov, A., Sandven, S., 2016. Sea ice cover in Kongsfjorden and Hornsund, Svalbard (2000-2014) from remote sensing data. Cryosphere 10 (1), 149–158. https://doi.org/10.5194/tc-10-149-2016

Mutanga, O., Adam, E., Cho, M.A., 2012. High density biomass estimation for wetland vegetation using WorldView-2 imagery and random forest regression algorithm. Int. J. Appl. Earth Obs. Geoinf. 18, 399—406. https://doi.org/10.1016/j.jag.2012.03.012

Nordli, Ø., Przybylak, R., Ogilvie, A.E.J., Isaksen, K., 2014. Long-term temperature trends and variability on spitsbergen: The extended svalbard airport temperature series, 1898—2012. Polar Res. 33 (1 SUPPL). https://doi.org/10.3402/polar.v33.21349

Nordli, Ø., Wyszyński, P., Cjelten, H.M.J., Isaksen, K., Łupikasza, E., Niedźwiedź, T., 2020. Revisiting the extended Svalbard Airport monthly temperature series, and the compiled corresponding daily series 1898—2018. Polar Res. 39. https://doi.org/10.33265/polar.v39.3614

Pavlova, O., Gerland, S., Hop, H., 2019. Changes in Sea-Ice Extent and Thickness in Kongsfjorden, Svalbard (2003—2016). In: Hop, H., Wiencke, C. (Eds.), The Ecosystem of Kongsfjorden, Svalbard. Advances in Polar Ecology, vol 2. Springer, Cham. https://doi.org/10.1007/978-3-319-46425-1_4

Pedregosa, F., Varoquaux, G., Gramfort, A., Michel, V., Thirion, B., Grisel, O., Blondel, M., Prettenhofer, P., Weiss, R., Doubourg, V., Vaderplas, J., Passos, A., Cournapeau, D., Brucher, M., Perrot, M., Duchesnay, E., 2011. Scikit-learn: Machine Learning in Python. J. Mach. Learn. Res. 12, 2825—2830.

Rodriguez-Galiano, V., Mendes, M.P., Garcia-Soldado, M.J., Chica-Olmo, M., Ribeiro, L., 2014. Predictive modeling of groundwater nitrate pollution using Random Forest and multisource variables related to intrinsic and specific vulnerability: A case study in an agricultural setting (Southern Spain). Sci. Total Environ. 476—477, 189—206. https://doi.org/10.1016/j.scitotenv.2014.01.001

Rodriguez-Galiano, V., Sanchez-Castillo, M., Chica-Olmo, M., Chica-Rivas, M., 2015. Machine learning predictive models for mineral prospectivity: An evaluation of neural networks, random forest, regression trees and support vector machines. Ore Geol. Rev. 71, 804—818. https://doi.org/10.1016/j.oregeorev.2015.01.001

Smith, T.G., Lydersen, C., 1991. Availability of suitable land-fast ice and predation as factors limiting ringed seal populations, Phoca hispida, in Svalbard. Polar Res. 10 (2), 585—594. https://doi.org/10.1111/j.1751-8369.1991.tb00676.x

Sundfjord, A., Albretsen, J., Kasajima, Y., Skogseth, R., Kohler, J., Nuth, C., Skarðhamar, J., Cottier, F., Nilsen, F., Asplin, L., Gerland, S., Torsvik, T., 2017. Effects of glacier runoff and wind on surface layer dynamics and Atlanticwater exchange in Kongsfjorden, Svalbard; a model study. Estuar. Coast. Shelf Sci. 187, 260—272.

Wang, C., Shi, L., Gerland, S., Granskog, M.A., Renner, A.H.H., Li, Z., Hansen, E., Martma, T., 2013. Spring sea-ice evolution in Rijpfjorden (80°N), Svalbard, from in situ measurements and ice mass-balance buoy (IMB) data. Ann. Glaciol. 54 (62), 253—260. https://doi.org/10.3189/2013AoG62A135

Wang, C., Cheng, B., Wang, K., Gerland, S., Pavlova, O., 2015. Modelling snow ice and suoerimposed ice on landfastsea ice in Kongsfjorden, Svalbard. Polar. Res. 34, 20828. https://doi.org/10.3402/polar.v34.20828

Yu, Y., Fowler, C., Fetterer, F., Maslanik, J., 2014. Interannual Variability of Arctic Landfice Ice between 1976 and 2007. J. Clim. 27 (1), 227—243. https://doi.org/10.1175/JCLI-D-13-00178.1

Zakhvatkina, N., Smirnov, V., Bychkova, I., 2019. Satellite SAR data-based sea ice classification. An overview. Geosci. 9 (4), 3—5. https://doi.org/10.3390/geosciences9040152

Zhuravskiy, D., Ivanov, B., Pavlov, A., 2012. Ice conditions at Gronfjorden Bay, Svalbard, from 1974 to 2008. Polar Geogr. 35 (2), 169—176. https://doi.org/10.1080/1088937X.2012.662535

Oceanologia 64 (2022) 546—552

Available online at www.sciencedirect.com

ScienceDirect

journal homepage: www.journals.elsevier.com/oceanologia

SHORT COMMUNICATION

Effects of air-sea drag coefficient on estimating wind stress using wind statistics

Dag Myrhaug*, **Hong Wang, Lars Erik Holmedal, Bernt J. Leira**

Department of Marine Technology, Norwegian University of Science and Technology (NTNU), Trondheim, Norway

Received 23 November 2021; accepted 17 March 2022
Available online 31 March 2022

KEYWORDS
Wind stress;
Drag coefficient;
North Atlantic;
Northern North Sea;
Wind statistics;
Stochastic method

Abstract This article addresses the effects of the air-sea drag coefficient on estimation of wind stress based on wind statistics. This is achieved by applying the same wind stress parameterizations chosen by Wrobel-Niedzwiecka et al. (2019) together with mean wind speed statistics from three locations in the North Atlantic and one location in the Northern North Sea. The expected values and the variances of the wind stress are provided. This study is complementary to that of Wrobel-Niedzwiecka et al. (2019), also demonstrating different results depending on the drag coefficient formula used.

1. Introduction

Knowledge of the wind stress on the sea surface is important in order to understand the interaction between the atmosphere and the ocean as the air-sea interface represents their coupling by exchanging heat and momentum. This contributes to air-sea mixing processes which occur across the ocean surface, and knowledge about these processes is crucial in climate and ocean studies. The wind shear stress enters in modelling and prediction of, for example, ocean surface waves, ocean currents and ocean circulations. The physical processes in the air-sea mixed layer are usually nonlinear depending on relevant air and sea parameters. Due to the lack of consistent theories on the exchange of the horizontal momentum between the air and the sea, parameterizations in terms of bulk formulae are often used by researchers when undertaking atmospheric and ocean studies.

Wrobel-Niedzwiecka et al. (2019) (hereafter referred to as WN19) studied the effect of some commonly used bulk formulae of the wind shear stress parameterized in terms of a drag coefficient and the mean wind speed (see Eq. (1)). They evaluated the dependence of the average monthly and annual wind stress values on the choice of drag coefficient using actual wind fields representing global satellite data

* Corresponding author at: Department of Marine Technology (NTNU), Otto Nielsen vei 10, NO-7491 Trondheim, Norway.
E-mail address: dag.myrhaug@ntnu.no (D. Myrhaug).
Peer review under the responsibility of the Institute of Oceanology of the Polish Academy of Sciences.

Production and hosting by Elsevier

https://doi.org/10.1016/j.oceano.2022.03.004

from the North Atlantic and the European Arctic. Differences were obtained depending on the drag coefficient formula used. They used the formulae provided by Wu (1969, 1982), Garratt (1977), Yelland and Taylor (1996), Kalnay et al. (1996), Large and Yeager (2004), and Andreas et al. (2012) (see WN19 for more details related to these references as well as a review of the relevant literature).

The purpose of this article is to estimate the wind stress using the same shear stress bulk formulae as in WN19 together with mean wind speed statistics at four locations; three in the North Atlantic (NA) and one in the Northern North Sea (NNS). Thus, this study is complementary to that of WN19, also demonstrating different results depending on the drag coefficient formula used. WN19 found that the area average annual mean values of wind stress were smallest using the Andreas et al. (2012) formula and largest using the Wu (1969) formula which is different from the present results, i.e. the mean wind stress is largest using the Andreas et al. (2012) formula and smallest using the Wu (1969) formula or the Large and Yeager (2004) formula. The reason for this difference is unclear but it is probably related partly to how the wind data is used together with the drag coefficient formulae and partly to the use of global and local wind data. However, further studies are required to investigate this, which is beyond the scope of this article.

The article is organized as follows. This introduction is followed by providing the background of the wind stress bulk formulae used. Then the statistical properties of the wind stress using mean wind speed statistics are derived. Finally, a summary and the main conclusions are given.

2. Background

As referred to, WN19 made a review of some frequently used bulk formulae for the wind shear stress on the sea surface. Due to the lack of consensus on which formulae is the most reliable and as no consistent theory on the exchange of horizontal momentum between the atmosphere and the ocean exist in the literature these bulk formulae are adopted in the present study. For the sake of completeness the formulae are summarized here (see WN19 for more details).

The bulk formula for the wind shear stress on the sea surface is given as

$$\tau = \rho C_D U_{10}^2 \tag{1}$$

where ρ is the air density, C_D is the sea surface drag coefficient, and U_{10} is the mean wind speed 10 m above the sea surface. The friction velocity u_* is defined as $u_*^2 = \tau/\rho$ which combined with Eq. (1) yields

$$u_*^2 = \frac{\tau}{\rho} = C_D U_{10}^2 \tag{2}$$

WN19 considered the following parameterizations of C_D where U_{10} is in m s^{-1} (see WN19 and their Table 1 for more details):

Wu (1969) (W69)

$$C_D \times 10^3 = 0.5\, U_{10}^{0.5}; \quad 1 \le U_{10} \le 15 \tag{3}$$

Garratt (1977) (G77)

$$C_D \times 10^3 = 0.75 + 0.067\, U_{10}; \quad 4 \le U_{10} \le 21 \tag{4}$$

Wu (1982) (W82)

$$C_D \times 10^3 = 0.8 + 0.065\, U_{10}; \quad 1 \le U_{10} \tag{5}$$

Yelland and Taylor (1996) (YT96)

$$C_D \times 10^3 = 0.29 + \frac{3.1}{U_{10}} + \frac{7.7}{U_{10}^2}; \quad 3 \le U_{10} \le 6 \tag{6}$$

$$C_D \times 10^3 = 0.60 + 0.070\, U_{10}; \quad 6 \le U_{10} \le 26 \tag{7}$$

Kalnay et al. (1996) (K96)

$$C_D \times 10^3 = 1.3; \quad 0 \le U_{10} \tag{8}$$

Large and Yeager (2004) (LY04)

$$C_D \times 10^3 = \frac{2.7}{U_{10}} + 0.142 + 0.076\, U_{10}; \quad 0 \le U_{10} \tag{9}$$

Andreas et al. (2012) (A12)

$$C_D \times 10^3 = 0.0583^2 \left(1 - \frac{0.243}{0.0583} U_{10}\right)^2; \quad 0 \le U_{10} \tag{10}$$

All these C_D models are valid for neutral stability of the atmosphere.

In summary, Eq. (2) using Eqs. (3)—(10) is provided in Table 1 by defining $u \equiv U_{10}$ and $T \equiv \tau/\rho$ referred to as models 1—7. More specifically, Eq. (2) using Eq. (3) is referred to as model 1 and is represented as

$$T(u) \times 10^3 = f\, u^g \tag{11}$$

where the coefficients f, g are given in Table 1. Furthermore, Eq. (2) using Eqs. (4)—(10) are referred to as models 2—7, respectively, and are represented as

$$T(u) \times 10^3 = a + bu + cu^2 + du^3 + e\, u^4 \tag{12}$$

where the coefficients a, b, c, d, e are given in Table 1.

3. Estimating wind stress using wind statistics

Parametric models for the cumulative distribution function (*cdf*) (or the probability density function (*pdf*)) of $u = U_{10}$ are provided in the literature, see for example a review by Bitner-Gregersen (2015). In the present study results are exemplified using four *cdfs* of u; one from Johannessen et al. (2001), two from Mao and Rychlik (2017) and one from Li et al. (2015). The first *cdf* of u is based on one-hourly values of u from wind measurements covering the years 1973—1999 from the Northern North Sea (NNS) (see Johannessen et al. (2001) for more details). The next two *cdfs* of u represent the wind speed at two locations along a ship route in the North Atlantic (NA) with coordinates 20°W 60°N (South of Iceland) and coordinates 10°W 40°N (see also Figure 2 in WN19) fitted to 10 years of wind speed data (see Mao and Rychlik (2017) for more details). The last *cdf* of u represents the wind speed obtained as best fit to hindcast wind data from 2001—2010 at the Buoy Cabo Silleiro location 40 km off the North-West Spanish coast (see Li et al. (2015) for more details). All these *cdfs* are given by the two-parameter Weibull model

Table 1 Wind stress formulae and coefficients according to Eq. (11) for model 1 and Eq. (12) for models 2–7.

Model, Eq. number	Authors	a	b	c	d	e	f	g	u_1 [m s^{-1}]	u_2 [m s^{-1}]	u_3 [m s^{-1}]
1, Eq. (11)	W69	-	-	-	-	-	0.5	2.5	1	-	15
2, Eq. (12)	G77	-	-	0.75	0.067	-	-	-	4	-	21
3, Eq. (12)	W82	-	-	0.8	0.065	-	-	-	1	-	∞
4, Eq. (12)	YT96	7.7	3.1	0.29	-	-	-	-	3	6	-
		-	-	0.60	0.070	-	-	-	-	6	26
5, Eq. (12)	K96	-	-	1.3	-	-	-	-	0	-	∞
6, Eq. (12)	LY04	-	2.7	0.142	0.076	-	-	-	0	-	∞
7, Eq. (12)	A12	-	-	0.0034	-0.0283	0.059	-	-	0	-	∞

Table 2 Wind stress results using wind statistics from NA (20°W 60°N) and NNS (the results for $E[T]$ and $E[T] \pm 1\,SD$ are multiplied by 10^3).

Model number	NA (20°W 60°N)					NNS				
	$E[T]$ [m^2 s^{-2}]	$R[T]$	$E[T]-1\,SD$ [m^2 s^{-2}]	$E[T]+1\,SD$ [m^2 s^{-2}]	$\frac{T(E[U_{10}])}{E[T]}$	$E[T]$ [m^2 s^{-2}]	$R[T]$	$E[T]-1\,SD$ [m^2 s^{-2}]	$E[T]+1\,SD$ [m^2 s^{-2}]	$\frac{T(E[U_{10}])}{E[T]}$
1	144	0.78	32	256	1.03	94	1.08	0	196	0.83
2	191	0.88	23	359	0.70	147	1.07	0	304	0.48
3	187	1.02	0	378	0.73	128	1.49	0	319	0.57
4	179	0.999	0	358	0.68	135	1.29	0	309	0.47
5	147	0.82	26	268	0.84	100	1.18	0	218	0.74
6	155	1.04	0	316	0.71	105	1.54	0	267	0.58
7	1213	1.72	0	3299	0.42	807	2.86	0	3115	0.22

$$P(u) = 1 - \exp\left[-\left(\frac{u}{\theta}\right)^{\beta}\right];\quad u \geq 0 \tag{13}$$

with the Weibull scale (θ) and shape (β) parameters as

NNS (Johannessen et al., 2001):

$$\theta = 8.426\,\mathrm{m\,s^{-1}},\quad \beta = 1.708 \tag{14}$$

NA (20°W 60°N) (Mao and Rychlik, 2017):

$$\theta = 10.99\,\mathrm{m\,s^{-1}},\quad \beta = 2.46 \tag{15}$$

NA (10°W 40°N) (Mao and Rychlik, 2017):

$$\theta = 7.11\,\mathrm{m\,s^{-1}},\quad \beta = 2.30 \tag{16}$$

NA (Buoy Cabo Silleiro) (Li et al., 2015):

$$\theta = 7.866\,\mathrm{m\,s^{-1}},\quad \beta = 2.002 \tag{17}$$

According to the summary of the models in Table 1 they are generally valid within a finite interval of u and thus the *pdf* of u follows the truncated Weibull *pdf*:

$$p_t(u) = \frac{1}{N}p(u);\quad u_1 \leq u \leq u_3 \tag{18}$$

$$N = \exp\left[-(\frac{u_1}{\theta})^{\beta}\right] - \exp\left[-(\frac{u_3}{\theta})^{\beta}\right] \tag{19}$$

where

$$p(u) = \frac{dP(u)}{du} = \frac{\beta}{\theta}(\frac{u}{\theta})^{\beta-1}\exp\left[-(\frac{u}{\theta})^{\beta}\right];\quad u_1 \leq u \leq u_3 \tag{20}$$

In the following the expected value, $E[T]$, and the variance, $Var[T]$, of the wind shear stress $T = \tau/\rho$ are calculated based on the given formulae and coefficients in Table 1, and the wind statistics from NNS and NA. For models 1–3 and 5–7 $E[T]$ and $Var[T]$ are calculated from Eqs. (18)–(20) as (Bury, 1975, Ch. 2)

$$E[T(u)] = \int_{u_1}^{u_3} T(u)p_t(u)du \tag{21}$$

$$Var[T(u)] = E\left[T^2(u)\right] - (E[T(u)])^2 \tag{22}$$

$$E\left[T^2(u)\right] = \int_{u_1}^{u_3} T^2(u)p_t(u)du \tag{23}$$

where u_1 and u_3 are given in Table 1. For model 4 the corresponding results are calculated as

$$E[T(u)] = \int_{u_1}^{u_2} T_1(u)p_t(u)du + \int_{u_2}^{u_3} T_2(u)p_t(u)du \tag{24}$$

$$E\left[T^2(u)\right] = \int_{u_1}^{u_2} T_1^2(u)p_t(u) + \int_{u_2}^{u_3} T_2^2(u)p_t(u)du \tag{25}$$

and $Var[T(u)]$ as in Eq. (22). Here $u_1 \leq T_1 \leq u_2$ and $u_2 \leq T_2 \leq u_3$ are as given in Table 1. One should notice that these results can be calculated analytically using the results in Appendix A.

The coefficient of variation is

$$R[T(u)] = \frac{(Var[T(u)])^{1/2}}{E[T(u)]} \tag{26}$$

The results for NNS (Eq. (14)) and NA (20°W 60°N) (Eq. (15)) for models 1–7 are given in Table 2. It should be noted that these two locations are located near the study area of WN19 (i.e. the North Atlantic and the European

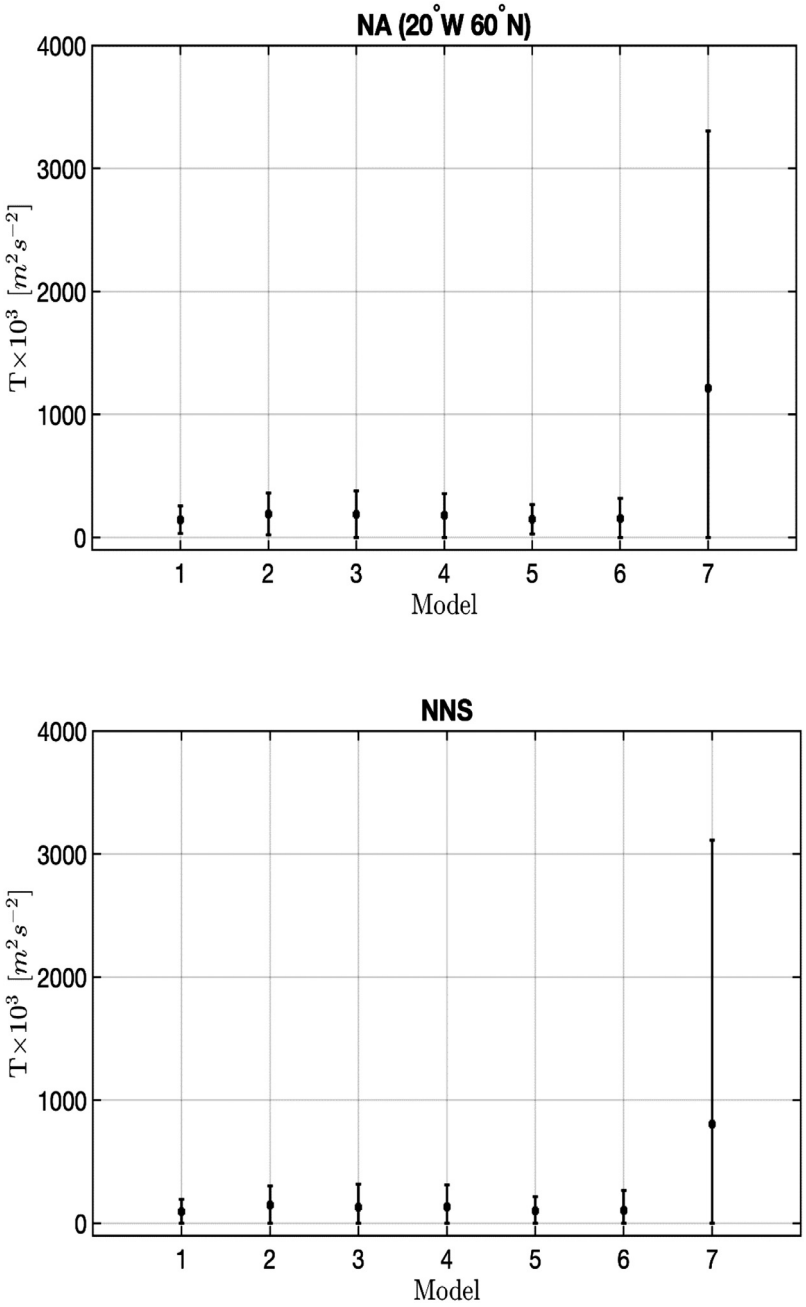

Figure 1 $E[T]$, $E[T] + 1\,SD$ and $E[T] - 1\,SD$ where $SD = (Var[T])^{1/2}$ at the NA (20°W 60°N) and NNS locations.

Arctic, see Figure 2 in WN19). Results are provided for $E[T]$, $R[T]$, $E[T]$ plus and minus one standard deviation (SD), $E[T] \pm 1SD$, where $SD = (Var[T])^{1/2} = E[T] \times R[T]$. It should be noted that the values of $E[T]$ and $E[T] \pm 1SD$ are multiplied by the factor 10^3 and all dimensions are in $m^2\,s^{-2}$. From Table 2 it appears that the wind shear stress is larger at NA (20°W 60°N) than in NNS for all models with the largest value for model 7 and the smallest for model 1 at both locations. At both locations it also appears that the wind shear stress is significantly larger for model 7 compared with the other models. Moreover, the coefficients of variation $R[T]$ for all the models are large; in the range 0.78—1.72 for NA and in the range 1.07—2.86 for NNS, i.e. reflecting large standard deviations.

The values of $E[T] \pm 1\,SD$ are also depicted in Figure 1. It appears from Table 2 and Figure 1 that for models 1—6 at both locations the values of $E[T]$ are within the intervals $E[T] - 1SD$ and $E[T] + 1\,SD$ of the other models. Although $E[T]$ for model 7 is significantly larger than those for the other models, there is overlap between the other models and the interval $E[T] - 1\,SD$ for model 7.

As referred to in the introduction, these results are different from those found by WN19, i.e. as they obtained the smallest wind stress using the Andreas et al. (2012) formula

Table 3 Wind stress results using wind statistics from NA (10°W 40°N) and NA (Buoy Cabo Silleiro) (the results for $E[T]$ and $E[T] \pm 1\,SD$ are multiplied by 10^3).

Model number	NA (10°W 40°N)					NA (Buoy Cabo Silleiro)				
	$E[T]$ [m^2 s^{-2}]	$R[T]$	$E[T]-1\,SD$ [m^2 s^{-2}]	$E[T]+1\,SD$ [m^2 s^{-2}]	$\frac{T(E[U_{10}])}{E[T]}$	$E[T]$ [m^2 s^{-2}]	$R[T]$	$E[T]-1\,SD$ [m^2 s^{-2}]	$E[T]+1\,SD$ [m^2 s^{-2}]	$\frac{T(E[U_{10}])}{E[T]}$
1	69	1.03	0	140	0.72	86	1.05	0	176	0.74
2	81	0.85	12	150	0.58	113	0.997	0.3	226	0.52
3	67	1.04	0	137	0.72	93	1.22	0	206	0.66
4	70	0.89	8	132	0.59	97	1.10	0	204	0.55
5	63	0.87	8	118	0.83	80	0.999	0.1	160	0.79
6	56	0.99	0.6	111	0.75	77	1.21	0	170	0.66
7	229	1.88	0	659	0.38	433	2.26	0	1412	0.30

and the largest wind stress using the Wu (1969) formula. In order to check these results the two *cdfs* in Eqs. (16) and (17) are included representing wind conditions at locations farther south in the North Atlantic than the study area in WN19. It should be noted that the scale parameter θ (Eqs. (16) and (17)) is smaller than those in Eqs. (14) and (15), while the shape parameter β (Eqs. (16) and (17)) have values between those in Eqs. (14) and (15), reflecting different features of the wind data. Thus, similar results to those in Table 2 and Figure 1 are provided in Table 3 and Figure 2 for models 1−7 at these two NA locations (Eqs. (16) and (17)).

From Table 3 it appears that the wind shear stress is larger at NA (Buoy Cabo Silleiro) than at NA (10°W 40°N) for all models with the largest value for model 7 and the smallest for model 6 at both locations, but the wind shear stress at these locations are smaller than those at the two other locations (i.e. Table 2 and Figure 1). It is noticed that the smallest value was obtained for model 1 at the two other locations, which is attributed to the different features of the *cdfs* of the wind speed. Moreover, it also appears that the wind shear stress is significantly larger for model 7 compared with the other models at both locations. The coefficients of variation $R[T]$ are large for all the models; in the range 0.85−1.88 at NA (10°W 40°N) and in the range 0.997−2.26 at NA (Buoy Cabo Silleiro). From Table 3 and Figure 2 it also appears that for models 1−6 the values of $E[T]$ are within the intervals $E[T]-1SD$ and $E[T]+1\,SD$ of the other models at both locations, while there is overlap between the other models and the interval $E[T]-1\,SD$ for model 7.

Thus, the overall results at these two locations exhibit the same main features as those obtained at NA (20°W 60°N) and in NNS, i.e. the wind shear stress is largest using model 7 (Andreas et al., 2012), while WN19 obtained the smallest shear stress using this model. The reason for this difference is unclear, but it is likely that it is partly related to how the wind data is used together with the drag coefficient, and partly to the use of global (WN19) and local (present) wind data. However, more studies are required to investigate this issue, but this is beyond the scope of this article.

An alternative to the stochastic method used here for estimating the wind shear stress is to use a deterministic method, which is to substitute $u = E[U_{10}]$ in Eqs. (11) and (12) for models 1−7, i.e. to calculate $T(E[U_{10}])$. Here $E[U_{10}]$ is obtained using the *cdf* in Eq. (13) giving (Bury, 1975, Ch. 2)

$$E[U_{10}] = \theta\,\Gamma\left(1+\frac{1}{\beta}\right) \tag{27}$$

where Γ is the gamma function. Then, this yields for NNS (Eq. (14)) $E[U_{10}] = 7.52$ m s^{-1};

NA (Eq. (15)) $E[U_{10}] = 9.75$ m s^{-1}; NA (Eq. (16)) $E[U_{10}] = 6.30$ m s^{-1}; NA (Eq. (17)) $E[U_{10}] = 6.97$ m s^{-1}. By using this method together with the results for $E[T]$ in Tables 2 and 3, the deterministic to stochastic method ratios $T(E[U_{10}])/E[T]$ are provided in Table 2 for NNS and NA (20°W 60°N), and in Table 3 for NA (10°W 40°N) and NA (Buoy Cabo Silleiro). At all locations the ratios are smaller than one, except for model 1 at NA (20°W 60°N) where the ratio is slightly larger than one. Overall, the stochastic method should be used as the statistical features of the wind shear stress are taken into account consistently, which is not the case for the deterministic method.

4. Summary and conclusions

A summary and the main conclusion are as follows:

The effect of the air-sea drag coefficient on estimating wind stress based on wind statistics are demonstrated. This was achieved applying the same seven wind stress bulk formulae chosen by Wrobel-Niedzwiecka et al. (2019) together with mean wind speed statistics from three locations in NA and one location in NNS. Results are given in terms of expected values ($E[T]$) and standard deviations (SD) of the wind stress.

The wind stress is larger at NA (20°W 60°N) than in NNS for all formulae with the largest value resulting by using the Andreas et al. (2012) formula and the smallest by using the Wu (1969) formula at both these locations near the study area of Wrobel-Niedzwiecka et al. (2019). Two other data sets from locations farther south in NA are used to check the results, which confirms that the largest wind stress is obtained using the Andreas et al. (2012) formula, while the smallest is obtained using the Large and Yeager (2004) formula. Moreover, at all locations the standard deviations of the wind stress are large; $E[T]$ are within the intervals

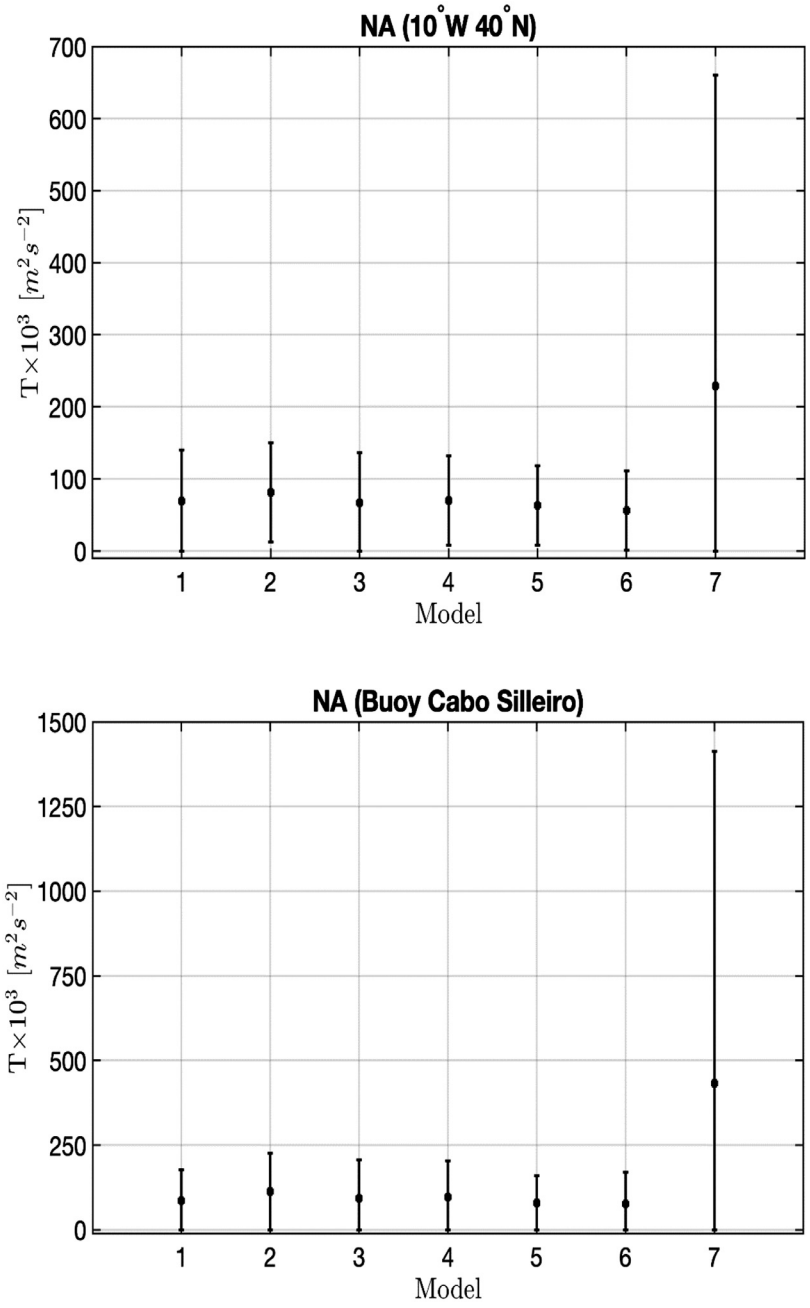

Figure 2 $E[T]$, $E[T] + 1\,SD$ and $E[T] - 1\,SD$ where $SD = (Var[T])^{1/2}$ at the NA (10°W 40°N) and NA (Buoy Cabo Silleiro) locations.

$E[T] - 1\,SD$ and $E[T] + 1\,SD$ using the other formulae, except for the Andreas et al. (2012) formula for which there is overlap between the interval $E[T] - 1\,SD$ and the intervals of the other formulae.

These results are different from those obtained by Wrobel-Niedzwiecka et al. (2019) where the smallest wind stress resulted from using the Andreas et al. (2012) formula and the largest wind stress by using the Wu (1969) formula. The difference is probably attributed to how the wind data is used in combination with the drag coefficient and to the use of global (Wrobel-Niedzwiecka et al., 2019) and local (present) wind data. However, this is not conclusive and needs further investigations.

The present stochastic method should be used rather than the deterministic one since the statistical features of the wind stress are then taken into account in a consistent way.

Appendix A

Let $p_t(u)$ denote the truncated *pdf* in Eqs. (18)—(20). Then $E[T]$ and $Var[T]$ in Eqs. (21)—(25) can be calculated analytically using the results provided in Abramowitz and Stegun (1972, Chs. 6.5 and 26.4).

For models 1 and 2 the calculations contain terms like:

$$E[u^n] = \int_{u_1}^{u_3} u^n p_t(u)du = \frac{1}{N}\theta^n\left\{\Gamma\left[1+\frac{n}{\beta},\left(\frac{u_1}{\theta}\right)^\beta\right]-\Gamma\left[1+\frac{n}{\beta},\left(\frac{u_3}{\theta}\right)^\beta\right]\right\} \quad \text{(A1)}$$

where Γ is the gamma function, $\Gamma(x, y)$ is the incomplete gamma function, n is a real number (not necessarily an integer), $\Gamma(x, 0) = \Gamma(x)$ and $\Gamma(x, \infty) = 0$.

For model 3 the calculations contain terms like (i.e. for $u_3 \to \infty$ in Eq. (A1)):

$$E[u^n] = \int_{u_1}^{\infty} u^n p_t(u)du = \frac{1}{N}\theta^n\Gamma\left[1+\frac{n}{\beta},\left(\frac{u_1}{\theta}\right)^\beta\right] \quad \text{(A2)}$$

For model 4 the calculations contain terms like:

$$E[u^n] = \int_{u_1}^{u_2} u^n p_t(u)du = \frac{1}{N}\theta^n\left\{\Gamma\left[1+\frac{n}{\beta},\left(\frac{u_1}{\theta}\right)^\beta\right]-\Gamma\left[1+\frac{n}{\beta},\left(\frac{u_2}{\theta}\right)^\beta\right]\right\} \quad \text{(A3)}$$

$$E[u^n] = \int_{u_2}^{u_3} u^n p_t(u)du = \frac{1}{N}\theta^n\left\{\Gamma\left[1+\frac{n}{\beta},\left(\frac{u_2}{\theta}\right)^\beta\right]-\Gamma\left[1+\frac{n}{\beta},\left(\frac{u_3}{\theta}\right)^\beta\right]\right\} \quad \text{(A4)}$$

One should notice that in both Eqs. (A3) and (A4), $p_t(u)$ and N are as given in Eqs. (18) and (19), respectively.

For models 5, 6 and 7 the calculations contain terms like (i.e. using the Weibull *pdf* without truncation corresponding to $u_1 = 0,\ u_3 \to \infty$ in Eq. (A1):

$$E[u^n] = \int_0^{\infty} u^n p(u)\,du = \theta^n\Gamma\left(1+\frac{n}{\beta}\right) \quad \text{(A5)}$$

References

Abramowitz, M., Stegun, I.A., 1972. Handbook of Mathematical Functions. Dover Publications, New York, 1046 pp.

Andreas, E.L., Mahrt, L., Vickers, D., 2012. A new drag relation for aerodynamically rough flow over the ocean. J. Atmos. Sci. 69 (8), 2520–2539. https://doi.org/10.1175/JAS-D-11-0312.1

Bitner-Gregersen, E.M., 2015. Joint met-ocean description for design and operations of marine structures. Appl. Ocean Res. 51, 279–292. https://doi.org/10.1016/j.apor.2015.01.007

Bury, K.V., 1975. Statistical Models in Applied Science. John Wiley & Sons, New York, 646 pp.

Garratt, J.R., 1977. Review of drag coefficients over oceans and continents. Mon. Weather Rev. 105 (7), 915–929. https://doi.org/10.1175/1520-0493(1977)105⟨0915:RODCOO⟩2.0.CO;2

Johannessen, K., Meling, T.S., Haver, S., 2001. Joint distribution of wind and waves in the Northern North Sea. In: Chung, J.S., Prevosto, M., Mizutani, N. (Eds.), Proceedings of the 11th Int. Offshore and Polar Engineering Conf., Stavanger, Norway. Int. Soc. Offshore and Polar Engineer (ISOPE), Cupertino, CA, USA, Vol. 3, 19–28.

Kalnay, E., Kanamitsu, M., Kistler, R., Collins, W., Daeven, D., Gandin, L., Iredell, M., Saha, S., White, G., Woollen, J., Zhu, Y., Chelliah, M., Ebisuzaki, W., Higgins, W., Janowiak, J., Mo, K.C., Ropelewski, S., Wang, J., Leetmaa, A., Reynolds, R., Jenne, R., Joseph, D., 1996. The NCEP/NCAR 40-year reanalysis project. Bull. Am. Meteor. Soc. 77 (3), 437–471.

Large, W.G., Yeager, S.G., 2004. Diurnal to decadal globel forcing for ocean and sea-ice models: the data sets and flux climatologies. Technical Note NCAR/TN-460 + STR. NCAR, Boulder, CO.

Li, L., Gao, Z., Moan, T., 2015. Joint distribution of environmental condition at five European offshore sites for design of combined wind and wave energy devices. J. Offshore Mech. Arct. Eng. 137 (3), 031901. https://doi.org/10.1115/1.4029842

Mao, W., Rychlik, I., 2017. Estimation of Weibull distribution for wind speeds along ship routes. Proceedings of the Institution of Mechanical Engineers, Part M: J. Eng. Maritime Environ. 231 (2), 464–480. https://doi.org/10.1177/1475090216653495

Wrobel-Niedzwiecka, I., Drozdowska, V., Piskozub, J., 2019. Effect of drag coefficient formula choice on wind stress climatology in the North Atlantic and the European Arctic. Oceanologia 61 (3), 291–299. https://doi.org/10.1016/j.oceano.2019.02.002

Wu, J., 1969. Wind stress and surface roughness at air-sea interface. J. Geophys. Res. 74 (2), 444–455. https://doi.org/10.1029/JB074i002p00444

Wu, J., 1982. Wind-stress coefficients over sea surface from breeze to hurricane. J. Geophys. Res. 87 (C12), 9704–9706. https://doi.org/10.1029/JC0871iC12p09704

Yelland, M., Taylor, P.K., 1996. Wind stress measurements from the open ocean. J. Phys. Oceanogr. 26 (4), 541–558. https://doi.org/10.1175/1520-0485(1996)026⟨0541:WSMFTO⟩2.0.CO;2